Experimental constraints on the compositions of sulphides and aqueous fluids in the Earth's interior

DISSERTATION

zur Erlangung des akademischen Grades eines Doktors
der Naturwissenschaften (Dr. rer. nat.)
in der Bayreuther Graduiertenschule für Mathematik und Naturwissenschaften
(BayNAT)
der Universität Bayreuth

vorgelegt von

Sumith Abeykoon

aus *Kurunegala (Sri Lanka)*

Bayreuth, 2022

Experimental constraints on the compositions of sulphides and aqueous fluids in the Earth's interior

DISSERTATION

zur Erlangung des akademischen Grades eines Doktors
der Naturwissenschaften (Dr. rer. nat.)
in der Bayreuther Graduiertenschule für Mathematik und Naturwissenschaften
(BayNAT)
der Universität Bayreuth

vorgelegt von

Sumith Abeykoon

aus *Kurunegala (Sri Lanka)*

Bayreuth, 2022

This doctoral thesis was prepared at the Bayerisches Geoinstitut at the University of Bayreuth from May 2018 until October 2022 and was supervised by Prof. Daniel J. Frost and Dr. Andreas Audétat.

This is a full reprint of the thesis submitted to obtain the academic degree of Doctor of Natural Sciences (Dr. rer. Nat.) and approved by the Bayreuth Graduate School of Mathematics and Natural Sciences (BayNAT) of the University of Bayreuth.

Date of submission: 05.10.2022

Date of defense: 25.11.2022

Acting director: Prof. Dr. Hans Keppler

Doctoral committee:

Prof. Dr. Daniel J. Frost	(Reviewer)
Prof. Dr. Hans Keppler	(Reviewer)
PD. Dr. Catherine McCammon	(Chairwoman)
Prof. Dr. David Rubie	

Acknowledgments

I would like to express my deepest appreciation to my supervisor, Prof. Dan Frost for the continuous support throughout my PhD with his immense scientific guidance, motivation, enthusiasm and patience. His guidance helped me enormously in all the times during research, and writing of this thesis. I'm extremely grateful to Dr. Andreas Audétat, for the supervision, encouragement and advice he has provided throughout the PhD. I have been extremely lucky to have both of you who cared so much about my work, and who responded to my questions and queries always. I would like to extend my sincere thanks to PD Dr. Catherine McCammon for her support with Mössbauer measurements and also many insightful discussions, and Dr. Tiziana Boffa Ballaran for her generous support in diffraction data processing and for many perceptive discussions.

I thank my officemate and friend, Dr. Alexander Kurnosov for his help with diffraction data analysis, invaluable discussions and countless support during my entire time in Bayreuth. Many thanks to Dr. Nobuyoshi Miyajima for his support in TEM analysis and Dr. Vera Laurenz for her continuous support since my master's time in BGI. I am also thankful to Prof. Gregor Golabek for his inputs and valuable discussions. I greatly acknowledge all the co-authors for their contributions and collaborations during the PhD projects. My sincere thanks to Dr. Florian Heidelbach for the German translation of the thesis summary and also helping me with EBSD analysis. I would like to extend my sincere thanks to technical staff of BGI, Detlef Krauße, Hubert Schulze, Raphael Njul, Alexander Rother, Stefan Übelhack, Heinz Fischer, Sven Linhardt, Gerald Bauer, Dorothea Wiesner, Ulrike Trenz, Anke Potzel and the administrative staff, Petra Buchert, Janina Scharnagel and Anna Dinius for their countless support in all the time.

Many thanks to Dr. Tatsuya Sakamaki, Dr. Shin Ozawa, Prof. Eiji Ohtani, Prof. Akio Suzuki, Prof. Michihiko Nakamura, Shinobu Okuyama and all the lab members from Tohoku university for providing with great support during my stay in Sendai. Many thanks to all my BGI friends, Caterina, Edith, Adrien, Lianjie, Amrita, Nathan, Elena, Lucas, Lisa, Egor, Iuliia, Tim, Saiana, Artem, Alena. Andrii, Andrea, Narangoo, Matteo, Giacomo, Tommaso, Sourav, Stella, Jia, Anna, Nicki, Kirsten, Johannes, Greta, Enrico, Laura, Laura, Giulia, Niccolo, Marija, Phillip, Pedro, Kirill, Lin, Fei, Esther, Joana, Julia, Pierre, Danilo, (and everyone I missed) for many colourful memories.

I'm grateful to Dr. Geeth Manthilake and his family, Luca and Sula for their continuous caring and support in many ways. I can't thank enough to auntie Monica, and her family for always being

there for me. I'm grateful to my best friends, Channa and Nehara for always encouraging me to pursue my dreams. My special gratitude to Serena, who has always stood by my me with her continued support, understanding and encouragement. Last but not least, this endeavour would not have been possible without my parents, brother and sister, and I'm grateful to them for providing me with unconditional love, support and encouragement.

Experimental constraints on the compositions of sulphides and aqueous fluids in the Earth's interior

Sumith Abeykoon

To my loving Mum and Dad!
මගේ ආදරණීය අම්මටත් සහ අප්පච්චිට!

Abstract

Melts and fluids are transient in the deep Earth's interior and their existence can often only be inferred by the chemical changes that they bring about. Experimental studies are essential for determining the properties and compositions of such liquid phases and for constraining the conditions under which they may exist in the interior. In the course of this study, high-pressure and high-temperature experiments have been performed under three main topics; to determine the composition of aqueous fluids, to examine how the compositions of sulphide melts can be used to determine their formation conditions and to investigate how hydrogen dissolves in sulphide minerals within the Earth's interior.

A new experimental "single-crystal diamond trap (SCDT)" technique, has been developed to determine the composition of fluids at conditions compatible with the Earth's upper mantle. In this technique aqueous fluids, equilibrated with a mineral assemblage at high-pressures and high-temperatures, are trapped in laser-drilled holes within single-crystal diamond plates and, after recovery, are analysed by laser ablation inductively coupled mass spectrometry. The new method was tested first by analysing holes filled with epoxy resins doped with known amounts of chemicals and then on holes filled with known amounts of minerals that were subsequently melted. Finally, the technique was tested using high P–T mineral solubility experiments at 1.0 GPa and 700–900 °C in the quartz–H_2O and olivine–enstatite–H_2O systems, for which reliable reference data exist. In all tests the measured concentrations agree within 1–21% (avg. 13%) with the reference values. In contrast, four mineral solubility experiments that were performed at identical conditions with the classical diamond trap method returned concentrations that deviated by 7–56% (avg. 28%) from the reference value. Furthermore, a strong fractionation effect that has been observed during the ablation of albite + H_2O in a classical diamond trap experiment is efficiently prevented by the single-crystal diamond trap (SCDT) approach.

In a further experimental study, factors controlling the oxygen contents in sulphide melts at mantle conditions have been investigated. A series of multi-anvil experiments were carried out at pressures from 3 to 13 GPa and temperatures from 1300 to 1819 °C, using mainly graphite capsules, to equilibrate sulphide melts with mantle peridotite assemblages with varying Fe and Ni contents. Carbonates were added as a flux and the oxygen fugacity of the experiments was estimated either using the CO_2 contents of the resulting carbonate-silicate melts or by using an added Ir-Fe alloy redox sensor. Recovered sulphide melt oxygen concentrations were in the range 0.2 to 3.7 wt. %, and were found to mainly vary with silicate FeO content, temperature and pressure. Lower oxygen

contents also correlate with increasing sulphide Ni-content, but as this also leads to lower sulphur/metal ratios, the effect of Ni alone cannot be categorically isolated. A preliminary geothermometer expression was developed based on the oxygen content of sulphide melts and the iron oxide concentrations of coexisting olivine and orthopyroxene. With this expression the experimental temperatures are reproduced to within 74 K for Ni-free experiments and within 135 K for Ni- bearing samples. Using measurements of the oxygen contents of sulphide inclusions of peridotite affinity in diamonds from the Lac de Gras kimberlite field, a plausible average entrapment temperature of 1318±48 °C is calculated. Mantle peridotite assemblages would be expected to contain sulphide melts with approximately 0.4–0.6 wt. % oxygen along a typical mantle adiabat down to 200 km depth. It is shown that Mössbauer spectroscopy can be used to determine the oxygen contents of sulphide assemblages, potentially while they are still within the diamond hosts.

In the final study in this thesis *in situ* time-of-flight neutron diffraction measurements were performed to examine the uptake of deuterium in iron monosulphide at pressures up to 11.4 GPa and temperatures to 1300 K, using a multi-anvil device installed at a spallation neutron source. A D_2 fluid was formed in the experiments through the decomposition of ND_3BD_3, resulting in an oxygen fugacity, measured in parallel experiments, of approximately 1.2 log units below the iron-wüstite buffer. This surprisingly high oxygen fugacity is shown to be compatible with recent observations of immiscibility between H_2 and H_2O-rich fluids (Bali et al., 2013). Deuterium positions and site occupancies were determined for the pyrrhotite polytype, referred to as FeS V, at high pressure and temperature conditions using Rietveld refinements of the powder diffraction patterns. The refined structural model indicates that two normally unoccupied sites in the $P6_3/mmc$ FeS V structure, at Wyckoff positions *6h* and *4f*, are partially occupied by D atoms, with the latter being more dominant. The total D site occupancy (x) in $FeSD_X$ increases with both pressure and temperature over the experimental conditions, from 0.148(10) at 2.3 GPa and 787 K to 1.25(5) at 9.7 GPa and 1300 K. The unit-cell volume expansion per deuterium atom is found to be 1.53±0.16 $Å^3$ at 6.9 GPa and 960 K, which is smaller than has been determined for deuteration of metallic iron phases at similar conditions. The variation in unit-cell volume indicates that most deuterium is lost from FeS V upon temperature quenching at high-pressures. By fitting the obtained FeS V deuterium site occupancies to a thermodynamic model, estimates for the hydrogen contents of iron monosulphide at conditions and oxygen fugacities consistent with the base of the cratonic lithosphere can be made that are in the range 1700–2700 ppm. Furthermore, the bulk mantle at these conditions may contain 2–3 ppm H_2 hosted by sulphides, which may increase at greater depths.

Zusammenfassung

Schmelzen und Fluide treten im Erdinnern nur lokal und vorübergehend auf, und ihre Existenz lässt sich oft nur anhand der von ihnen verursachten chemischen Veränderungen ableiten. Experimentelle Untersuchungen sind unerlässlich, um die Eigenschaften und die Zusammensetzung solcher flüssigen Phasen zu bestimmen und die Bedingungen einzugrenzen, unter denen sie im Erdinneren existieren können. Im Rahmen dieser Studie wurden Hochdruck- und Hochtemperaturexperimente zu drei Hauptthemen durchgeführt: zur Bestimmung der Zusammensetzung wässriger Flüssigkeiten, zur Untersuchung, wie die Zusammensetzung von Sulfidschmelzen zur Bestimmung ihrer Entstehungsbedingungen genutzt werden kann, und zur Untersuchung, wie sich Wasserstoff in Sulfidmineralen im Erdinneren löst.

Eine neue experimentelle "Einkristall-Diamantfalle (SCDT)"-Technik wurde entwickelt, um die Zusammensetzung von Fluiden unter Bedingungen zu bestimmen, die mit dem oberen Erdmantel kompatibel sind. Bei dieser Technik werden wässrige Flüssigkeiten, die bei hohem Druck und hohen Temperaturen mit einer Mineraliengruppe im Gleichgewicht sind, in lasergebohrten Löchern in einkristallinen Diamantplatten eingeschlossen und nach dem Experiment mittels induktiv gekoppelter Massenspektrometrie durch Laserablation analysiert. Die neue Methode wurde zunächst an Löchern getestet, die mit Epoxidharzen gefüllt waren, die mit bekannten Mengen von Chemikalien dotiert waren, und dann an Löchern, die mit bekannten Mengen von Mineralien gefüllt waren, die anschließend geschmolzen wurden. Schließlich wurde die Technik anhand von Experimenten zur Löslichkeit von Mineralien bei p,T-Bedingungen von 1,0 GPa und 700-900 °C in den Systemen Quarz-H_2O und Olivin-Enstatit-H_2O getestet, für die zuverlässige Referenzdaten vorliegen. In allen Tests stimmen die gemessenen Konzentrationen innerhalb von 1-21% (durchschnittlich 13%) mit den Referenzwerten überein. Im Gegensatz dazu ergaben vier Minerallösungsexperimente, die unter identischen Bedingungen mit der klassischen Diamantfallenmethode durchgeführt wurden, Konzentrationen, die um 7-56 % (durchschnittlich 28 %) vom Referenzwert abwichen. Darüber hinaus wird ein starker Fraktionierungseffekt, der bei der Ablation von Albit + H_2O in einem klassischen Diamantfallen-Experiment beobachtet wurde, durch den Ansatz der Einkristall-Diamantfalle (SCDT) wirksam verhindert.

In einer weiteren experimentellen Studie wurden die Faktoren untersucht, die den Sauerstoffgehalt in Sulfidschmelzen unter Mantelbedingungen steuern. Eine Reihe von Multi-Anvil-Experimenten wurde bei Drücken von 3 bis 13 GPa und Temperaturen von 1300 bis 1819 °C durchgeführt, wobei hauptsächlich Graphitkapseln verwendet wurden, um Sulfidschmelzen mit Mantelperidotit-

Zusammensetzungen mit unterschiedlichen Fe- und Ni-Gehalten zu equilibrieren. Karbonate wurden als Flussmittel zugesetzt, und die Sauerstoff-Fugazität der Experimente wurde entweder anhand des CO_2-Gehalts der resultierenden Karbonat-Silikat-Schmelzen oder mit Hilfe eines zugesetzten Redox-Sensors aus einer Ir-Fe-Legierung abgeschätzt. Die Sauerstoffkonzentrationen der rückgewonnenen Sulfidschmelzen lagen im Bereich von 0,2 bis 3,7 Gew.-% und variierten hauptsächlich mit dem FeO-Gehalt des Silikats, der Temperatur und dem Druck. Niedrigere Sauerstoffgehalte korrelieren auch mit einem steigenden Ni-Gehalt der Sulfide, aber da dies auch zu niedrigeren Schwefel/Metall-Verhältnissen führt, kann die Wirkung von Ni allein nicht kategorisch isoliert werden. Es wurde ein vorläufiges Geothermometer entwickelt, das auf dem Sauerstoffgehalt von Sulfidschmelzen und den Eisenoxidkonzentrationen von koexistierendem Olivin und Orthopyroxen basiert. Mit dieser Beziehung werden die experimentellen Temperaturen mit einer Genauigkeit von 74 K für Ni-freie Experimente und von 135 K für Ni-haltige Proben reproduziert. Anhand von Messungen des Sauerstoffgehalts von Sulfideinschlüssen mit Peridotit-Zusammensetzung in Diamanten aus dem Lac de Gras-Kimberlitfeld wird eine plausible durchschnittliche Einschlusstemperatur von 1318±48 °C berechnet. Es wird erwartet, dass Peridotit-Zusammensetzungen im Mantel Sulfidschmelzen mit etwa 0,4 - 0,6 Gew.-% Sauerstoff entlang eines typischen Manteladiabats bis in 200 km Tiefe enthalten. Es wird gezeigt, dass die Mössbauer-Spektroskopie zur Bestimmung des Sauerstoffgehalts von Sulfid-Assemblagen verwendet werden kann, möglicherweise noch während sie sich in den Diamanten befinden.

In der letzten Studie dieser Arbeit wurden In-situ-Neutronenbeugungsmessungen mit der time-of-flight Methode durchgeführt, um die Aufnahme von Deuterium in Eisenmonosulfid bei Drücken bis zu 11,4 GPa und Temperaturen bis 1027 °C zu untersuchen, wobei eine an einer Spallationsneutronenquelle installierte Multianvil-Hochdruckpresse verwendet wurde. In den Experimenten bildete sich durch die Zersetzung von ND_3BD_3 eine D_2-Fluid, was zu einer in Parallelexperimenten gemessenen Sauerstoff-Fugazität von etwa 1,2 log-Einheiten unterhalb des Eisen-Wüstit-Puffers führte. Die überraschend hohe Sauerstoff-Fugazität ist nachweislich mit den jüngsten Beobachtungen der Nichtmischbarkeit zwischen H_2 und H_2O-reichen Fluiden vereinbar (Bali et al., 2013). Die Deuteriumpositionen und Platzbelegungen im Kristallgitter wurden für den Pyrrhotit-Polytyp, der als FeS V bezeichnet wird, unter hohen Druck- und Temperaturbedingungen mithilfe von Rietveld-Verfeinerungen der Pulverdiffraktogramme bestimmt. Das verfeinerte Strukturmodell zeigt, dass zwei normalerweise unbesetzte Stellen in der $P6_3/mmc$ FeS V-Struktur an den Wyckoff-Positionen *6h* und *4f* teilweise mit D-Atomen besetzt sind, wobei die letztere Position dominanter ist. Die Gesamtbesetzung der D-Stellen (x) in $FeSD_X$ nimmt sowohl mit dem Druck als auch mit der Temperatur über die untersuchten experimentellen

Bedingungen zu, und zwar von 0,148(10) bei 2,3 GPa und 787 K auf 1,25(5) bei 9,7 GPa und 1300 K. Die Ausdehnung des Einheitszellvolumens pro Deuteriumatom beträgt 1,53±0,16 $Å^3$ bei 6,9 GPa und 960 K und ist damit kleiner als bei der Deuterierung von metallischen Eisenphasen unter ähnlichen Bedingungen ermittelt wurde. Die Variation des Volumens der Einheitszelle deutet darauf hin, dass das meiste Deuterium aus FeS V durch die Abschreckung bei hohen Drücken verloren geht. Durch die Anpassung der erhaltenen Gitterplatzbelegungen des Deuteriums in der FeS V-Phase an ein thermodynamisches Modell können Abschätzungen für den Wasserstoffgehalt von Eisenmonosulfid unter Bedingungen und Sauerstoff-Fugazitäten vorgenommen werden, wie sie an der Basis der kratonischen Lithosphäre vorliegen und im Bereich von 1700-2700 ppm liegen. Darüber hinaus kann der Mantel unter diesen Bedingungen 2-3 ppm H_2 enthalten, die in Sulfiden enthalten sind und mit größerer Tiefe noch zunehmen können.

Contents

1. Introduction..... 1
1.1 Earth's crust and upper mantle – fluids, melts and magma generation..... 4
1.2 The composition of mantle sulphides..... 8
1.3 The role of sulphide melts in fractionation of the Earth's interior..... 12
1.4 Objectives of the PhD thesis..... 19

2. Methods..... 22
2.1 Starting materials..... 22
2.2 High-pressure and high-temperature experiments..... 23
2.2.1 Piston-cylinder apparatus..... 23
2.2.2 Multi-anvil apparatus..... 26
2.2.2.1 The 6-8 type multi-anvil apparatus for ex situ HP-HT experiments..... 26
2.2.2.2 The 6-6 type MA apparatus for in situ HP-HT experiments..... 29
2.2.3 High-pressure and high-temperature in situ neutron diffraction experiments at J-PARC-PLANET beamline..... 32
2.2.4 Rietveld refinements of time-of-Flight (TOF) neutron diffraction data..... 38
2.3 Analytical techniques..... 39
2.3.1 Scanning Electron Microscope..... 39
2.3.2 Electron Probe Micro Analysis..... 41
2.3.3 Transmission Electron Microscope..... 44
2.3.4 Mössbauer spectroscopy..... 46
2.3.5 Laser ablation inductively coupled plasma mass spectrometer..... 48

3. Thesis Synopsis..... 51
3.1 Single-crystal diamond trap technique..... 51
3.2 Oxygen contents of the sulphide melts in the Earth's upper mantle..... 54
3.3 Deuterium content and site occupancy in iron sulphide at high-P-T..... 57

References..... 61

List of Manuscripts and Statements of Author Contributions..... 74

4. The single-crystal diamond trap (SCDT): a new method to determine the composition of high-P–T fluids..... 76
4.1 Introduction..... 77
4.2 Methods..... 79
4.2.1 Piston cylinder experiments..... 81
4.2.2 Capsule opening and sample preparation..... 81
4.2.3 Preparation of test samples..... 85
4.2.4 LA–ICP–MS analyses..... 85
4.3 Results..... 90
4.4 Discussion..... 94
4.5 Conclusions..... 96

References..... 98

5. An experimental investigation of factors controlling the oxygen content of sulphide melts in the Earth's upper mantle…….. 100
5.1 Introduction……..... 101
5.2 Methods…….. 103
5.3 Results ……..... 107
5.4 Discussion……..... 114
5.4.1 Thermodynamic model……. 114
5.4.2 The variation in oxygen content of sulphide melts in the mantle…… 120
5.4.3 The interpretation of oxygen contents of natural sulphide assemblages……. 121
5.5 Summary and Conclusions…….. 124
References……..... 127
6. Deuterium content and site occupancy in iron sulphide at high pressure and temperature using in situ neutron diffraction experiments…….. 133
6.1 Introduction……..... 134
6.2 Methods…….. 136
6.2.1 Sample assemblage……..... 136
6.2.2 High-pressure neutron diffraction……. 137
6.2.3 Powder diffraction analysis……..... 138
6.2.4 Chemical analyses…….. 139
6.3 Results……..... 140
6.3.1 Compressibility of the FeS V phase……... 140
6.3.2 Deuterium incorporation in the FeS V structure……..... 143
6.3.3 Volume variation due to deuteration……. 146
6.4 Discussion……..... 149
6.4.1 P-T behaviour of the FeS V deuterium content and comparison with previous studies…… 149
6.4.2 The oxygen fugacity of the measurements and the nature of the coexisting fluid phase……. 152
6.4.3 A model for the deuterium content of FeS V and extrapolation to mantle conditions……. 155
6.5 Summary…… 158
References…….. 160
Appendix……..... 166
A.1 The single-crystal diamond trap (SCDT): a new method to determine the composition of high-P–T fluids……. 166
A.2 An experimental investigation of factors controlling the oxygen content of sulphide melts in the Earth's mantle…… 171
A.3 Deuterium content and site occupancy in iron sulphide at high pressure and temperature using *in situ* neutron diffraction experiments…….. 175

Figures

1.1 Schematic section showing the internal structure of the Earth……... 3
1.2 Schematic section showing main components in subduction zone…… 5
1.3 Typical geothermal gradients of oceanic, continental and cratonic lithosphere…….. 9
1.4 Classifications of the main diamond formation suites……... 10
1.5 Ternary diagram of the Fe-(Ni+Co+Cu)-S system…… 11
1.6 Co-evolution of the Earth's core, mantle and atmosphere……. 14
2.1 Side view of piston cylinder apparatus……... 24
2.2 High-pressure cell assembly used in piston cylinder experiments……... 25
2.3 The 6-8 type multi-anvil apparatus…… 27
2.4 Cross-section view of the octahedron assembly used for multi-anvil experiments…. 28
2.5 Pressure calibration curves of multi-anvil experiments…….. 29
2.6 Cross-sections view of multi-anvil cubic high-pressure cell assemblies…….. 31
2.7 Six-axes multi-anvil system with 6-6 type cell assembly……. 32
2.8 Neutron scattering power and cross sections…… 34
2.9 Six-axes multi-anvil system with 6-6 type cell assembly at PLANET beamline…….. 37
2.10 Electron beam–sample interactions in electron microscopy instruments……... 40
2.11 Configuration of an electron microprobe…….. 42
2.12 Schematic diagram of a Mössbauer spectrometer…….. 46
2.13 Main components of the laser ablation system with a quadrupole ICP-MS……..... 49
3.1 Single-crystal diamond trap technique……... 53
3.2 Calculated $\Delta G°$ of experiments plotted as a function of the temperature…….. 55
3.3 Final structural model of deuterated FeS V……..... 58
4.1 Capsule set up of the single-crystal diamond trap technique…….. 80
4.2 Photomicrographs of laser-drilled holes in the diamond plates in SCDT……... 83
4.3 LA-ICP-MS signals of SCDT analyses……... 89
4.4 Comparison between measured vs. reference values of SCDT and DT tests……. 93
4.5 Relative deviations of the measured SCDT, DT from the reference values……..... 94
5.1 Overview of an experimental sample with mantle peridotite and sulphide melt……. 108
5.2 Variation of excess anions vs. normalized oxygen content in sulphide……... 109
5.3 Experimental oxygen contents as a function of fo_2 and olivine Fe/(Fe+Mg) ratio…. 112
5.4 Mössbauer spectrum and TEM bright field image of a sulphide assemblage…….. 114
5.5 The distribution coefficient (KD) dependence on the experimental temperature…... 116
5.6 Calculated $\Delta G°$ of experiments plotted as a function of the temperature…….. 118
5.7 Sulphide-silicate distribution coefficient and calculated temperature…….. 119
5.8 Variation in sulphide melt oxygen contents in equilibrium with mantle peridotite…. 121
5.9 Equilibration temperatures of sulphide inclusions in diamonds from Slave craton… 123
6.1 Observed high P, T polymorphs of FeS in the neutron diffraction experiments…… 141
6.2 Unit-cell volumes of FeS V during decompression at room temperature……... 143
6.3 Final structural model of deuterated FeS V……... 145

6.4 Representative Rietveld refinements of neutron diffraction patterns……. 146
6.5 Change in the unit-cell volumes of deuterated and non-deuterated FeS V……. 148
6.6 Absolute unit-cell volumes of experiments plotted as a function of pressure……. 150
6.7 Total site occupancy of D/H in FeS V as a function of pressure……... 152
6.8 Proportion of H_2 in an H_2-H_2O fluid as a function of oxygen fugacity…….. 154

Tables

4.1 Summary of SCDT, DT experiments and obtained results…… 84
5.1 Summary of all experimental run conditions and products…… 105
5.2 Summary of experimental results……... 110
5.3 Thermodynamic model parameters……... 117
6.1 Summary of experimental conditions and run products of the neutron diffraction experiments…….. 140
6.2 Results of Rietveld structure refinements of FeS V……... 149

Chapter 1

Introduction

What we know concerning the structure of the Earth's interior to date has been mainly deduced by combining considerations on how, and from what, the Earth was formed and investigations of rocks from the interior brought to the surface by magmas, with geophysical observations primarily from seismology. Terrestrial planets such as the Earth, were formed by material that condensed from a protoplanetary disk of nebula gas. The condensed dust had a composition similar to CI chondritic meteorites but was depleted in more volatile elements due to incomplete condensation (Wai & Wasson, 1977; Wasson & Chou, 1974). The dust accreted first to form small planetesimals (> 1 km), which through gravitational infalling eventually produced planetary embryos (100–1000 km) that then assembled into terrestrial planets through a series of giant impacts (Greenberg et al., 1978). During accretion high temperatures led to the separation of the Earth's metallic core from the likely liquid silicate mantle. As the mantle cooled a first crust would have formed but there is little evidence left for the nature of this layer, due to reworking or destruction by a late heavy bombardment during the first 500 million years of Earth's history, the so called Hadean eon (Carlson et al., 2019). Melting of mafic crust formed in the late Hadean likely led to the formation of the first continental crustal material but the tectonic setting in which these processes occurred was probably unlike modern plate tectonics, which may have only commenced after approximately one billion years of Earth history (Carlson et al., 2019).

The composition of the upper mantle can be determined from the analysis of mantle xenoliths brought to the surface by magmas from depths of up to approximately 250 km. Some inclusions found in diamonds clearly come from depths of up to 550 km (Beyer & Frost, 2017) and some may come from even greater depths (Nestola, 2017) but this is hard to demonstrate categorically. Seismology, however, provides the primary information for building structural models of the interior (e.g., Dziewonski and Anderson, 1981; Montagner and Kennett, 1996), which have been further interpreted and explored through experiments and geodynamic modelling. The major layers and discontinuities within the Earth are shown in the Figure 1.1. The Earth's crust is approximately 6 km beneath the oceans (White and Klein (2014) and on

average 35 km thick on the continents (Hacker et al., 2015). Beneath the crust the seismically observable Mohorovičić discontinuity marks the transition to the ultramafic mantle (Jarchow & Thompson, 1989). The lithosphere describes the rigid tectonic plates of the Earth that are comprised of the curst and an underlying section of the so-called lithospheric mantle that cools conductively. The boundary with the underlying convectively cooling asthenospheric mantle, i.e. the lithosphere-asthenosphere boundary, has a variable depth range depending on the age of the plate and thickens to a maximum of approximately 140 km beneath oceanic crust and can be extended down to ~ 250 km beneath ancient continents (Rychert et al., 2020). The 410 km discontinuity is caused by the pressure-induced transformation of $(Mg, Fe)_2SiO_4$ olivine to the wadsleyite structure. A further isochemical structural transition occurs around 520 km where wadsleyite transforms to ringwoodite, and one of the most prominent mantle discontinuities is observed at a depth of 660 km, where ringwoodite ($(Mg,Fe)_2SiO_4$) disproportionates to form bridgmanite ($(Mg,Fe)SiO_3$) and ferropericlase ((Mg,Fe)O). The mantle-core boundary is located at a depth of 2900 km but just above this boundary there is a seismically heterogeneous layer of the mantle about 200 km thick, which is known as the D" layer (Kaminsky, 2017). The Earth's core is mainly composed of Fe-Ni alloy but with around 10 % of an as yet unidentified light element, that might be either O, Si, S, C or H or more likely a combination there of. The boundary between the liquid outer core and the solid inner core is located at approximately 5150 km depth.

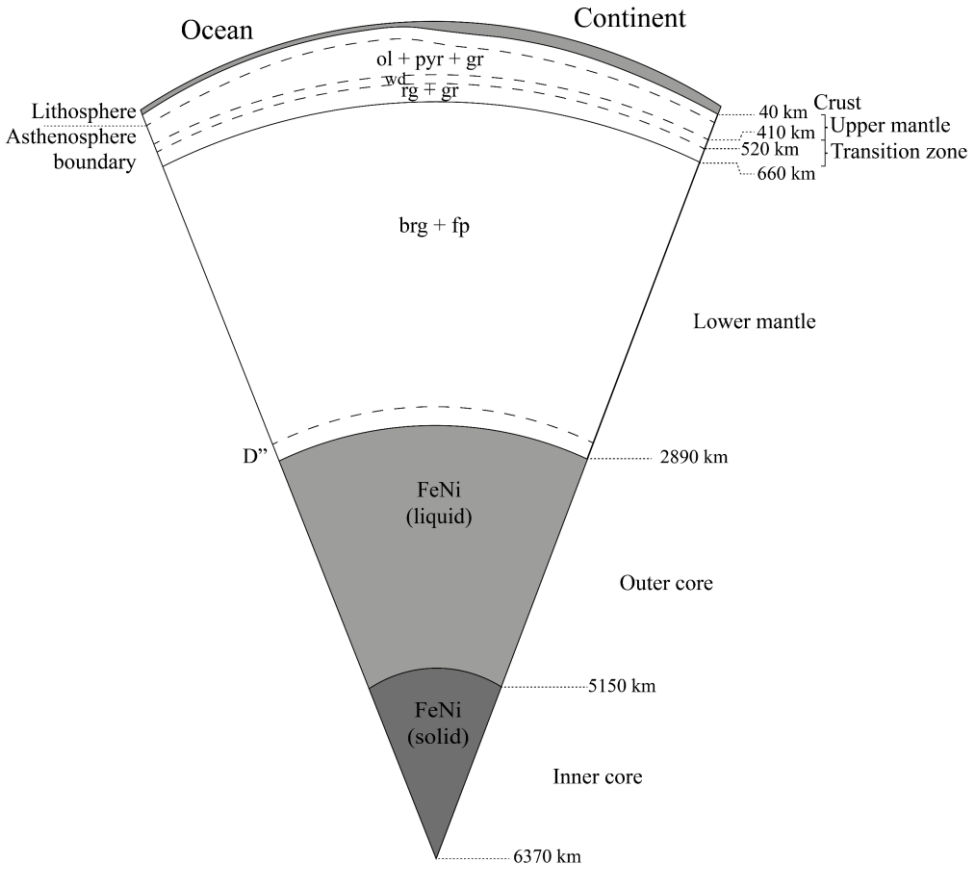

Figure 1.1: Schematic section showing the internal structure of the Earth. Major minerals are olivine (ol), pyroxene (pyr), garnet (gr), wadsleyite (wd), ringwoodite (rg), bridgmanite (brg) and ferropericlase (fp). Modified after (Albarède, 2009). The dimensions are not to scale.

Distinctive properties of Earth's layers mean that they play essential roles in sustaining the inimitable habitability of the planet as a whole (Stevenson, 2009). While the bulk composition of the Earth is comparable to the undifferentiated meteorites (chondrites), each layer has evolved to an characteristic average present-day composition (Hart & Zindler, 1986; McDonough, 2001; McDonough & Sun, 1995) through dynamic processes that not only drive chemical fractionation but interconnect each layer of the Earth and sustain a continual geochemical exchange. Plate tectonic processes have dominated the geodynamic and chemical evolution of the crust and upper mantle, through magmatism in different tectonic settings and through the transport of material from the surface to the interior by subduction (Fountain & Christensen, 1989; Green, 1972). Plate tectonics is part of the cooling process of the Earth's interior, where heat is lost through the creation of new oceanic lithosphere, which cools conductively at the surface, thus becoming denser with time and then sinks back into the

interior at subduction zones (Bercovici, 2003; Bickle, 1978; Silver & Behn, 2008). Such processes have led to chemical differentiation in the crust and mantle, but a complete understanding of this chemical diversity is hindered by the fact that samples from the interior become rarer and less representative as depths increase. Although seismology provides information on the physical properties of the interior, these properties are averaged over very large regions and cannot provide information on small scale processes, that can still cause important variations in geochemistry. Other processes are obscured by extreme time and the fact that we can only see the end result of these events. Important gaps in our spatial and temporal understand of the Earth's differentiation processes can be filled by reproducing them in high-pressure and high-temperature laboratory experiments. State-of-the-art experimental capabilities can reproduce a wide range of conditions comparable to planetary interiors, allowing the investigations of various geological processes (Liebermann, 2011; Mao & Hemley, 1996). This cumulative PhD thesis includes three projects, where in each a specific study of a process in the Earth's interior has been examined using high-pressure and high-temperature experiments combined with appropriate analytical techniques. The following sub-sections of this chapter are an overview of Earth's interior dynamics relevant to the topics presented in the subsequent chapters.

1.1. Earth's crust and upper mantle – fluids, melts and magma generation

The movement and interaction of tectonic plates is the main driving force for magma differentiation and the creation of geochemical diversity within the Earth's crust and mantle (Fig. 1.2). At divergent plate boundaries, partial melting at mid-ocean ridges creates new oceanic lithosphere, in the most continuous and voluminous magmatic process on Earth. The oceanic lithosphere loses heat through conduction and with time becomes cold and denser than the underlying asthenospheric mantle (Stein & Stein, 1996). At this point it sinks back into the mantle at a convergent plate boundary, and this subduction process leads to arc magmatism on the overriding plate. Melting of oceanic crust at mantle pressures and temperatures appears to be the main mechanism through which continental crust has been formed (Collins et al., 2020). However, models of current geothermal gradients (Rüpke et al., 2004; Syracuse et al., 2010) in subduction zones imply that temperatures are not high enough for melting of subducted oceanic crust to generate magmas. Subduction zone magmatism occurs from decompressive melting of the asthenosphere, that rises in response to mantle overlying the subducting slab being dragged

down (Stern, 2002). There are multiple lines of evidence, however, which infer that a hydrous fluid flux from the subducting slab also plays a role in arc magma genesis (e.g., Gaetani and Grove, 1998; Grove et al., 2012). This explains, for example, the generally more volatile rich-nature of arc magmas (Müntener et al., 2021; Scaillet & Pichavant, 2003), the relatively high degrees of partial melting (Ulmer, 2001) and their trace element signature, that shows an enrichment in fluid mobile elements such as light rare earths and large ion lithophiles, relative to high field strength elements (Bau & Knittel, 1993; Kessel et al., 2005; Kushiro, 1990; Leybourne et al., 1999; Ulmer, 2001; Zheng, 2019). Slab-derived aqueous fluids produced by the breakdown of hydrous minerals such as amphiboles, phengite, lawsonite and serpentine can migrate upwards to metasomatize the overlying mantle source of arc magmas, lowering the melting point and increasing the degree of mantle melting (Rüpke et al., 2004; Schmidt & Poli, 1998; Ulmer & Trommsdorff, 1995). Furthermore, fluid released in the forearc region can dissolve significant amounts of material and transport it into the overlying lithospheric plate (McCulloch & Gamble, 1991).

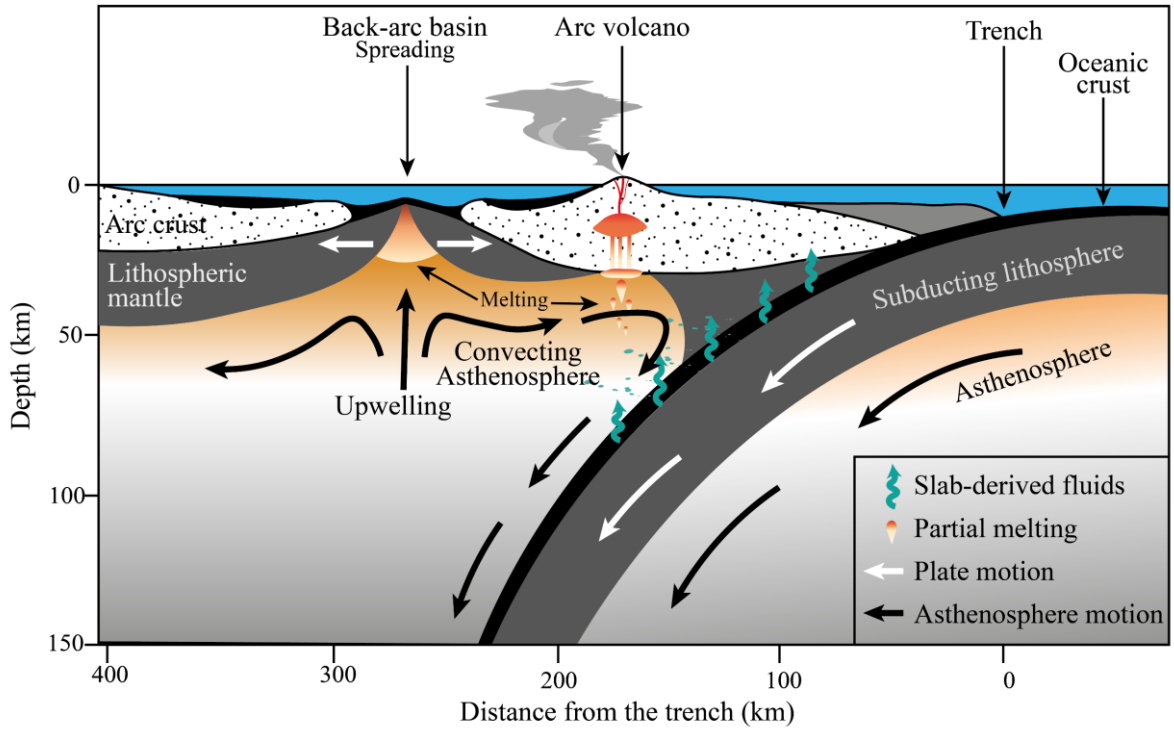

Figure 1.2: Schematic section showing the main crustal and upper mantle components associated in a typical subduction zone, modified after (Stern, 2002). Slab-derived aqueous fluids metasomatize the asthenospheric mantle where magma is produced beneath the arc.

The factors controlling the composition of the fluids such as mineral solubilities and element partitioning between fluids and minerals, are important for any quantitative modelling of transport processes in subduction zones. The fluids in the subduction zones commonly contain a dissolved silica component due to their interaction with the surrounding minerals. Usually the fluid contains several weight percent of dissolved silicates and the silicate source could be the MORB/eclogite layer or the peridotite mantle wedge (Manning, 1994; Newton & Manning, 2002). In some specific cases, very high-silica contents in supercritical fluids may be possible, when fluids interact with a subducted sediment layer (Keppler, 2017).

Experimental methods for determining the composition of high pressure and temperature water-rich fluids in equilibrium with minerals/rocks are important for understanding fluid transport processes in the mantle. In general, performing and analysing fluid- or melt-bearing experiments is challenging. Also, analysing the fluid composition is difficult because the composition of the fluid changes during quenching due to precipitation of solid phases (Keppler, 2017). Using a double-capsule technique, Manning (1994) determined quartz solubility by measuring the weight loss of a clean, polished single crystal during high-pressure and temperature piston cylinder experiments. In this technique, a perforated Au inner capsule enclosing a quartz single crystal is used, such that the dissolved SiO_2 is focused in the outer Pt capsule and does not precipitate on the single-crystal quartz during the quench. Therefore, the solubility of SiO_2 can be estimated directly using the weight loss of the quartz crystal measured after the experiment. This technique can be used only for very simple systems, however, such as quartz solubility in water (Manning, 1994) and forsterite + enstatite + water (Newton & Manning, 2002). Large disagreements have been found when applying this technique to the solubility of accessory minerals such as rutile + H_2O: weight loss experiments by Ayers and Watson (1993) returned rutile solubilities in water up to 1.9 wt. % at 1 GPa and 1100 °C, whereas a later study by Tropper and Manning (2005) reported a maximum of < 400 ppm by weight at 1000–1100 °C and 1–2 GPa. The large overestimation by Ayers and Watson (1993) (by about a factor 270) was caused by a considerable temperature gradient in their piston-cylinder experiments and a misidentification of crystals formed by material transport during the run as quench crystals. High field strength element (Nb, Ta, Zr, Hf, Ti) oxides such as rutile and zircon seem to be more susceptible to re-distribution in temperature gradients than major elements such as SiO_2 (Bernini et al., 2013; Rustioni et al., 2021; Tropper & Manning, 2005). Therefore, the applicability of weight-loss experiments depends on the type of compositional

system studied and requires very accurate control on temperature gradients within piston cylinder assemblies (Keppler, 2017).

The fluid composition in high-pressure, high-temperature experiments can be also determined using the diamond trap technique (e.g., Kessel et al. 2004; Aerts et al. 2010; Tiraboschi et al. 2018). The diamond trap method has originally been developed by Ryabchikov et al. (1989), and has also been used for determining the composition of high-pressure, high-temperature partial melts (Baker & Stolper, 1994; Kushiro & Hirose, 1992). In this method, a layer of diamond powder (20–50 µm grain size) is placed at the centre of the experimental capsule, into which fluids/melts infiltrate during the experiment and precipitate dissolved solids during quenching. Subsequently, the diamond layer is analysed by laser ablation–inductively coupled plasma–mass spectrometry (LA–ICP–MS) analysis. Stalder et al. (2001) allowed the remaining aqueous fluid present in the diamond trap to evaporate prior to analysis. However, Kessel et al. (2004) found that dissolved ions were preferentially lost during this approach. As a solution, they developed a technique in which the whole sample capsule is kept frozen during opening and subsequent LA-ICP-MS analysis.

In the above described diamond trap experiments, the basic assumption is made that everything that is present within the diamond trap after the experiment was originally dissolved in the fluid and was in equilibrium with the residual solid assemblage at the time of quenching. However, this assumption is not always valid. For instance, if an experiment is started with a silicate glass, then high solubilites can be reached metastably in the aqueous solution during heating, resulting in the precipitation of crystalline phases in the diamond trap. Precipitation of such phases during dissolution of a piece of metastable andesitic glass in water, was directly observed in an externally heated diamond anvil cell experiment by Keppler (2017). Subsequent LA-ICP-MS analysis of the diamond trap would include these crystalline phases, leading to an overestimation of the true fluid solute content.

Overall, the above summary demonstrates that there are considerable limitations in the existing approaches to determine the compositions of fluids in high- pressure and temperature experiments. Therefore, innovations in both experimental and analytical techniques are required to refine the accuracy and reproducibility of mineral solubility and fluid/mineral partitioning experiments at upper mantle conditions.

1.2. The composition of mantle sulphides

Direct information on the mineralogy and geochemistry of the Earth's mantle can be obtained from a number of sources.

- Regions where the mantle is exposed at the Earth's surface known as ultramafic massifs, e.g., Serranía de Ronda peridotite massif, in southern Spain (e.g., Pereira et al., 2003); Lanzo Massif in Western Italian Alps (e.g., Vitale Brovarone et al., 2017).
- Direct samples transported from the mantle to the surface as xenoliths (e.g., Bohrson and Clague, 1988; Haggerty and Sautter, 1990) or as inclusions trapped in xenocrysts (e.g., Varela et al., 1997; Aulbach et al., 2004).
- Surface exposures of mafic and rare ultramafic magmas produced by partial melting in the mantle (e.g., Huppert et al., 1985).
- Direct samples from the mantle captured as inclusions in diamonds (Alvaro et al., 2022), found in xenoliths brought to the surface by kimberlitic magmas.

Amongst samples from the Earth's deep mantle, inclusions in diamonds are particularly valuable. Diamonds can in principle host pristine inclusions due to their chemically inert nature and together with the very old ages, they are important for studying the origin and evolution of the lithospheric mantle (Griffin et al., 2003; Heaman & Pearson, 2010) and the migration of carbon. The chemical and morphological data of various inclusions can provide direct information on processes operating in the interior (e.g., Navon et al., 1988; Pearson et al., 2014; Angel et al., 2015, 2022; Smith et al., 2018; Anzolini et al., 2020). Furthermore, inclusions not only allow the age of diamond formation to be determined through geochronology (e.g., Pearson et al., 1999; Harvey et al., 2016), but by interpreting their compositions using the results of laboratory experiments, it is possible to perform geothermometry (e.g., Davies et al., 2004) and geobarometry (Beyer & Frost, 2017; Eggler & Lorand, 1993) measurements. The pressure and temperature conditions of diamond formation within the upper mantle are easily achieved in experiments, which allow processes that lead to the mobility of carbon in the interior to be studied.

With the exception of some rare super deep diamonds that come from the mantle transition zone and possibly the lower mantle (Boyd & Gurney, 1986; Stachel et al., 2005), the subcratonic lithosphere, that can extend to depths of approximately 250 km, is the main source of natural diamonds (Fig. 1.3). Diamond formation appears to be favourable at relatively low

temperatures and thus in regions with low geothermal gradients (Tappert & Tappert, 2011). Such low gradients occur in ancient continental blocks known as cratons (Janse, 1991; Rudnick & Nyblade, 1999), which have remained stable for at least 2.5 billion years (Stachel & Harris, 2009).

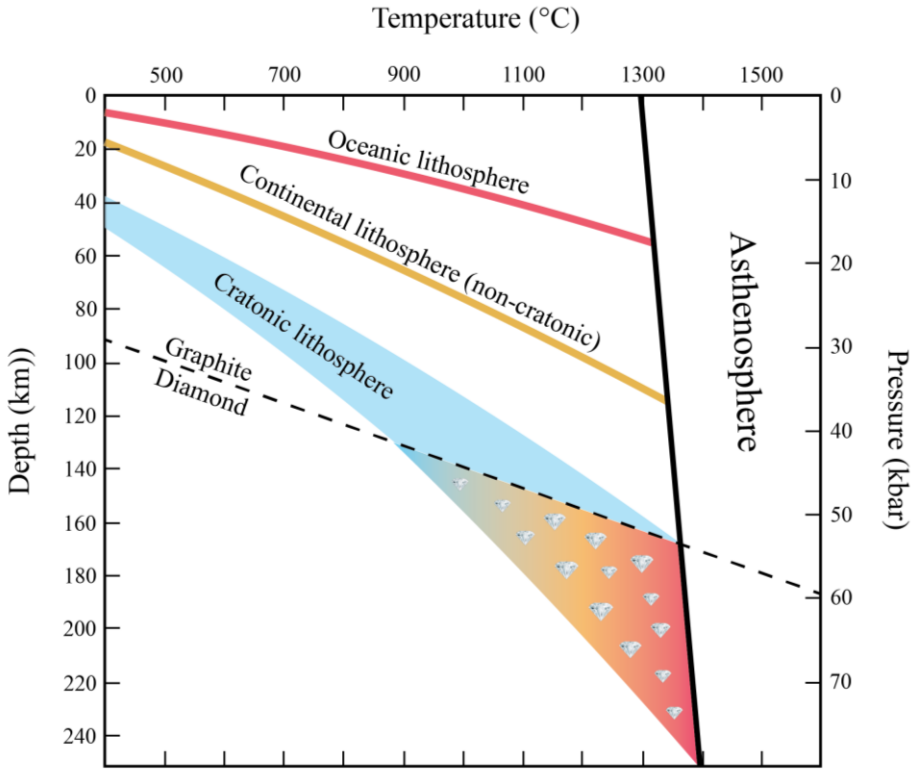

Figure 1.3: Typical geothermal gradients of oceanic, continental and cratonic lithosphere. Diamonds are found in xenoliths brought to the surface by kimberlitic magmas in regions where thick cratonic lithosphere extends to depths beyond the graphite-diamond transition (modified after Tappert and Tappert, 2011).

Diamonds are found within three main groups of rocks, peridotites, eclogites and websterites. Peridotites are the main rocks forming the upper mantle and can be further subdivided based on the type and proportion of pyroxene (see the ultramafic rock classification in the figure 1.4 and also more details can be found in, Stachel and Harris, 2009), eclogites appear to have mainly formed from metamorphosed basaltic rocks (Jacob, 2004) and websterites, which are comprised of near equal proportions of clino- and orthopyroxene, have bulk compositions that are intermediate between eclogites and peridotites (Aulbach et al., 2002). Based on the chemistry of single inclusions found within diamonds, however, they can also be associated with these rock types, in which case they are proposed to have either peridotitic, eclogitic or websteritic parageneses. The proportions of these different parageneses are shown in the Figure

1.4 (left), based on a compilation of silicate and oxide inclusions from a total of 2844 natural diamonds by Stachel and Harris (2009). The most significant paragenesis is peridotitic (65 % of inclusion bearing diamonds), followed by eclogitic (33 %), with only a minor proportion of websteritic (2 %) diamonds (Fig. 1.4).

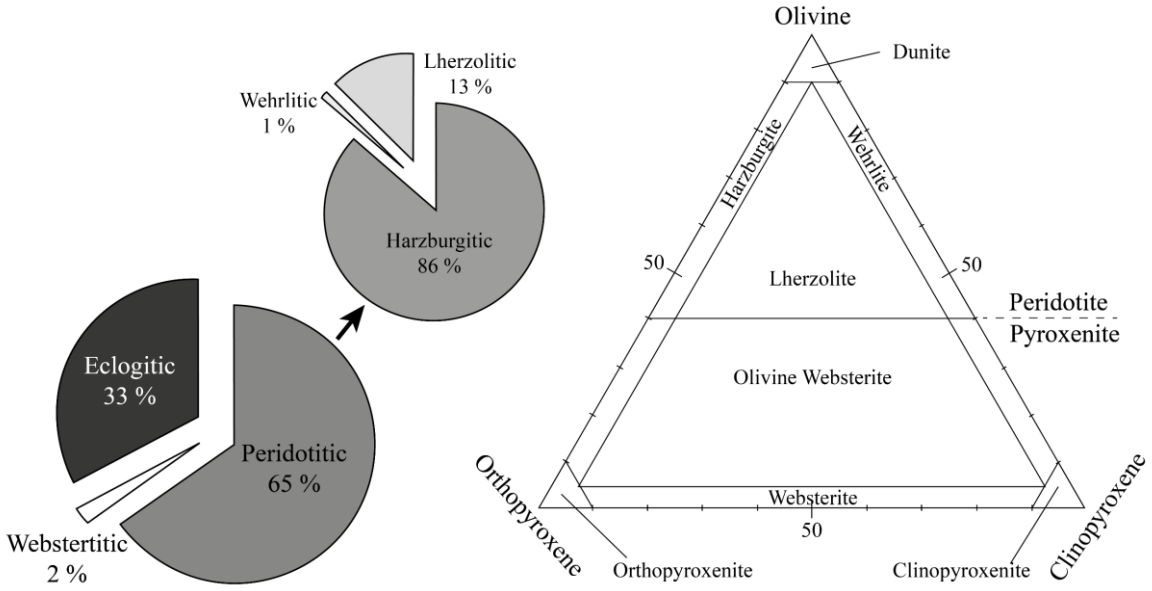

Figure 1.4: Left: relative abundances of the main diamond suites based on 2844 inclusion bearing diamonds. The peridotitic suite is further subdivided into harzburgitic, lherzolitic and wehrlitic based on the proportion and nature of pyroxene minerals (from: Stachel and Harris, 2009). Right: The ultramafic rock classification diagram, showing the subdivision of peridotitic and pyroxenitic suites.

The most common type of inclusions in lithospheric diamonds are sulphides, which contain variable amounts of base metals, such as Ni, Co and Cu (Pearson et al., 1998; Richardson et al., 2004; W. E. Sharp, 1966; L. A. Taylor & Liu, 2009). Due to the common occurrence in both peridotitic and eclogitic diamonds, it has been argued that sulphides may be involved in the diamond forming process (Bulanova, 1995; Gunn & Luth, 2006; Palyanov et al., 2007; Shushkanova & Litvin, 2008). Sulphide inclusions are generally multiphase mineral assemblages formed on cooling of an initially trapped single phase. The most common minerals found are pyrrhotite ($Fe_{1-X}S$) and pentlandite ($(Fe,Ni)_9S_8$), but pyrite (FeS_2), chalcopyrite ($CuFeS_2$), cubanite ($CuFe_2S_3$), and heazlewoodite (Ni_3S_2) are also found (Bulanova et al., 1996; Deines & Harris, 1995). The paragenesis of sulphide inclusions is based on their Ni contents as being either peridotitic (>12 wt. % Ni), pyroxenitic (8–12 wt. % Ni) or eclogitic (< 8 wt. % Ni) (Aulbach et al., 2009; Deines & Harris, 1995; Yefimova et al., 1983). Compositions of

single sulphide mineral inclusions among different diamondiferous kimberlites from Koffiefontein, Orapa, Premier, Roberts Victor, Jagersfontein, Sierra Leone, Star, and Mwadui are plotted in a ternary (Fe–(Ni+Co+Cu)–S) diagram in Figure 1.5.

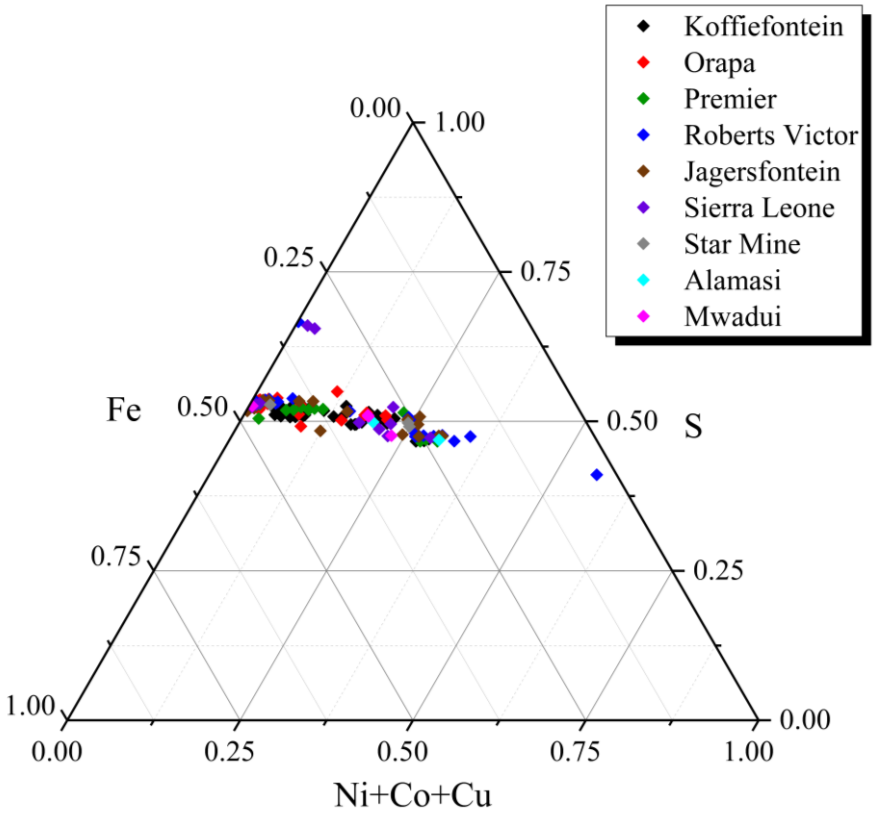

Figure 1.5: Ternary diagram of the Fe–(Ni+Co+Cu)–S system, showing atomic fractions of sulphide minerals from South African diamond inclusions. Different symbols indicate inclusions in diamonds from different kimberlite fields; Koffiefontein, Orapa, Premier, Roberts Victor, Jagersfontein, Sierra Leone, Star mine, Alamasi and Mwadui. (Deines & Harris, 1995).

Various hypotheses have been put forward to explain the common occurrence of sulphide inclusions in diamonds and their possible connection with diamond formation (Haggerty, 1986; Marx, 1972; Palyanov et al., 2007), yet the ideas are still debated. However, diamond inclusions allow the compositions of deep lithospheric sulphides to be examined, which might potentially be used to understand the conditions and protoliths in which diamonds are formed. In addition to Fe, Ni and Cu, other elements such as oxygen and carbon have been shown experimentally to be present in sulphide melts (Terasaki et al., 2005; Zhang & Hirschmann, 2012) and oxide minerals are also found in natural sulphide inclusion assemblages (Bulanova et al., 1996; Jacob et al., 2016). These minor components have been shown to influence

properties of sulphide melts. One example is the effect of oxygen on the dihedral angle between Fe-O-S melt and silicate minerals (Gaetani & Grove, 1999; Terasaki et al., 2005; Zhang et al., 2018). Also, it has been shown that dissolved oxygen lowers the melting temperature of FeS significantly (Naldrett, 1969; Zhang & Hirschmann, 2016). Moreover, oxygen contents have been reported in natural sulphide inclusions in diamonds (Bulanova et al., 1996; Davies et al., 1999, 2004; Jacob et al., 2016). However, there has been no previous experimental study reported that investigated the factors controlling the oxygen content in mantle sulphides, particularly in relation to the observed diamond inclusions. Due to the inert nature of diamonds, we can expect that the oxygen concentrations of diamond sulphide inclusions represent the original mantle values, unless they were exposed and altered. It is plausible that at least some diamond sulphides were in equilibrium with typical mantle assemblages at the time of entrapment and the oxygen concentration may therefore reveal information concerning the conditions at which this occurred. Although there have been many previous studies examining various aspects of sulphide melt stability and chemistry (Fonseca et al., 2008; Naldrett, 1969; Terasaki et al., 2005; Zhang et al., 2018b), non were conducted in equilibrium with typical mantle mineral assemblages. What is required is a systematic study to examine how the oxygen concentration in sulphides may be influenced, not only by the pressure and temperature, but by other factors such as the coexisting mineral assemblage, oxygen fugacity and major element sulphide composition.

1.3. The role of sulphide melts in fractionation of the Earth's interior

Core formation was the most significant differentiation event to affect the Earth, which influenced the evolution of the mantle, crust and the atmosphere. During this process iron metal equilibrated with the silicate mantle at an oxygen fugacity (fO_2) below the iron-wüstite (IW) buffer, i.e., the fO_2 imposed by the equilibrium $2Fe + O_2 = 2FeO$. This would have left very little ferric iron in the silicate portion of the Earth. Some of the oldest magmas on Earth, however, reveal a mantle fO_2 that was similar to that of the modern mantle, which is 4–5 times higher than that of the IW buffer (Frost & McCammon, 2008), and close to the level described by the fayalite-magnetite-quartz (FMQ) oxygen buffer (O'Neill, 1987). The atmospheres of the terrestrial planets were mainly sourced through magmatic degassing (Elkins-Tanton, 2008; Gaillard & Scaillet, 2014; Hirschmann, 2012). If the mantle had remained at an fO_2 compatible with core-mantle equilibration, reduced volatile species such as H_2, CO, CH_4, H_2S would have degassed, creating an anoxic atmosphere that would have been incompatible with the eventual

development of an oxygenated atmosphere (Gaillard & Scaillet, 2009; Hirschmann, 2012). The increase in the oxidation state of the mantle, however, allowed H_2O and CO_2 to degas from the interior so that an oxygenated atmosphere could eventually form (Kasting, 1993). The mantle oxidation mechanism was, therefore, a key step in the evolution of the Earth into a habitable planet.

The fO_2 of the present-day mantle can be calculated using the Fe^{3+}/Fe^{2+} ratios of primitive magmas, such as mid-ocean ridge basalt (MORB) glasses (e.g., Bézos and Humler, 2005; Cottrell and Kelley, 2011; Zhang et al., 2018a). Using thermodynamic-based oxy-thermobarometry calibrations (e.g., Gudmundsson and Wood, 1995), the fO_2 of spinel peridotite residues from mantle melting can also be determined (e.g., Davis et al., 2017). Both types of studies show that mantle fO_2 varies within the range ±1.5 log units of FMQ (Frost & McCammon, 2008).

As stated previously the fO_2 of the mantle seems to have increased quite rapidly after the Earth was formed and may have occurred either during or just after core formation had finished (Kasting, 1993; Trail et al., 2011). Evidence for this can be found in the oxidation state of some of the earliest mantle-derived magmas, which date back to the Archean eon. Using experimental calibration of the partitioning of redox sensitive elements such as chromium (e.g, Delano, 2001) and vanadium (Canil, 1997), it has been show that the fO_2 levels of Archean komatiites, dating back to at least 3500 Ma and possibly even 3960 Ma (Canil, 1997), were similar to present day mantle melts. The oxidation state of magmas from which the oldest minerals on Earth crystallised, detrital zircons approximately ~ 4400 Myr old (Ridley, 1998; Hopkins et al., 2008), has also been estimated using zircon/melt partitioning calibrations, and implies magmatic fO_2 conditions similar to FMQ (Trail et al., 2011). Other methods based, for example, on the V/Sc ratio of ancient basalts (Li & Lee, 2004) and vanadium distribution in peridotites (Lee et al., 2003), further support that the transition from a reducing mantle (set by metal-silicate equilibrium) to the present-day oxidized levels must have occurred rapidly after the core formation. However, the mechanism, or mechanisms through which the mantle oxidation state was raised after core formation, are unclear.

Figure 1.6 shows a cartoon summarizing the co-evolution of the Earth's core, mantle and atmosphere through the processes described in this section 1.3.

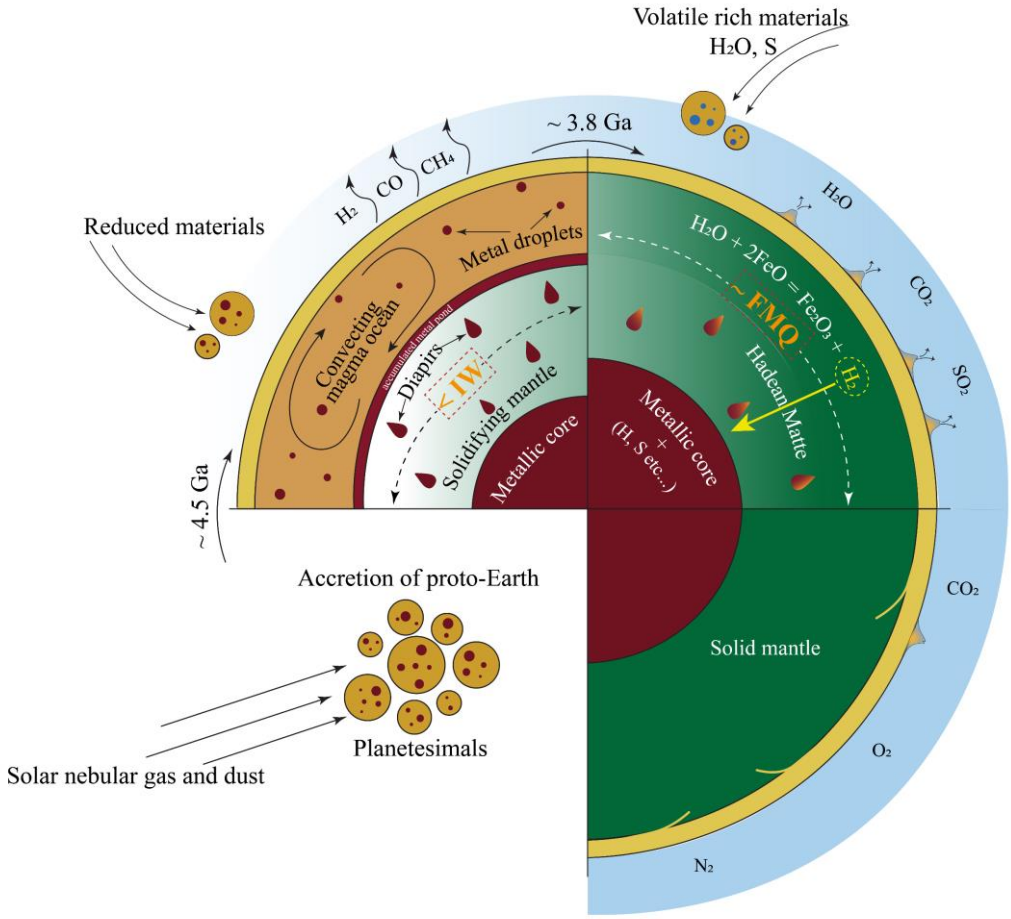

Figure 1.6: Co-evolution of the Earth's core, mantle and atmosphere. Schematic sections show specific periods of Earth throughout its evolution: (*i*) accretion of planetesimals from dust condensed from the solar nebular (~4.5 Ga); (*ii*) core formation stage where metal-silicate equilibration occurs under reducing conditions fO_2 < IW) (4.5 – 3.8 Ga) where any initial atmosphere would have been composed of reduced gases (e.g. H_2, CH_4, CO); (*iii*) rapid mantle oxidation through the addition of volatile-rich materials during the final stage of the core formation, more oxidised volcanic gases for the atmosphere (e.g. H_2O, CO_2), at this stage the core has accreted with main constituents plus volatile elements (e.g. H, S); (*iv*) In the final stage photosynthesis causes the rise in O_2 of the atmosphere.

The addition of oxidized and water-rich material during the later stages of accretion (O'Neill, 1991; Wood et al., 2006) could have increased the oxidation state of the mantle. This mechanism would have been closely related to the establishment of the highly siderophile element (HSE – elements that partition very strongly into iron metal) concentration in the mantle. In such a scenario the planetesimals and planetary embryos that accreted during the early phases of Earth's formation were reduced, i.e., contained very little FeO, and volatile

poor (O'Neill, 1991). Core formation during this phase of accretion would have removed all siderophile elements from the mantle, and even nominally lithophile elements such as V, Cr and Si. The final 10–20 % of accretion would have been characterized by the addition of more oxidized and volatile-rich material that would have established the mantle's current FeO content (e.g. Ballhaus et al., 2017; Kubik et al., 2021; Li, 2022). As no or little iron metal would have been present in this material the added siderophile elements would have remained in the mantle. Although this can explain the abundance of nominally siderophile elements in the mantle such as Co and Ni, it would have led to an overabundance of highly siderophile elements. There must, therefore, have been a further stage of core formation that involved the separation of sulphide melt, that would still be stable at the higher oxygen fugacities of this accretion stage. Further core formation through the separation of the so called "Hadean matte" (O'Neill, 1991; Righter et al., 2019, 2020; Rubie et al., 2016) would have removed the highly siderophile elements from the mantle, but because of its relatively small abundance, the nominally siderophile element ratios in the mantle would have remained unchanged. The final mantle concentrations of HSEs would have been established in a concluding stage of accretion, called the late veneer, where no subsequent core formation occurred (Laurenz et al., 2016; Rubie et al., 2016).

In this scenario water in the material accreted in the later stages could have oxidised the mantle through the following reaction (Sharp et al., 2013);

$$2FeO + H_2O \rightarrow Fe_2O_3 + H_2 \quad (1.1)$$

However, the oxidation process would not be sustained up to the fO_2 of the present-day mantle unless the produced hydrogen was removed from the mantle. Hydrogen is a strong reducing agent and it would simply reverse the oxidation reaction if it passed though material that had already been oxidised. Removal of hydrogen by degassing of H_2 to the space was proposed by Sharp et al., (2013), but was probably not an effective mechanism (Elkins-Tanton, 2008; Gaillard & Scaillet, 2014; Hirschmann, 2012). Firstly, as the oxidation state of the mantle material increased the degassing species would become H_2O rather than H_2, that would have a negligible effect on mantle redox state (Hirschmann, 2012). Secondly, in order to degas H_2, the silicate melt should have been hydrogen-supersaturated to nucleate H_2 bubbles (Elkins-Tanton, 2008, 2012). This supersaturation levels may not be feasible due to relatively low abundance of molecular H_2 in shallow levels of the magma ocean at the pressures below 3 GPa (Hirschmann, 2012).

A further more plausible possibility would be that the hydrogen could have been removed by incorporation into the core. As discussed earlier, the main core-segregating phase as the oxidation state of the mantle increased would have been iron sulphide melt (Hadean matte). The sulphur concentration at sulphide saturation (SCSS) defines the maximum sulphur concentration of a magma ocean that is in equilibrium with FeS melt. If the magma ocean sulphur content reached the SCSS level at certain conditions, then FeS melt would have exsolved from the magma ocean. The SCSS in peridotite melts decreases with increasing pressure and decreasing temperature (Blanchard et al., 2021; Mavrogenes & O'Neill, 1999). This implies that, as the magma ocean cools down, FeS would have inevitably exsolved from the magma and would have segregated to the core due to the higher density. This is also supported by experimentally reproduced superchondritic abundances of HSE in the mantle (Laurenz et al., 2016; Rubie et al., 2016).

The issue remains, however, as to whether sufficient hydrogen can dissolve in core-forming FeS at suitable oxygen fugacities to facilitate the oxidation of the mantle by H_2O. Currently there are no experimental data through which to assess this. Previous studies have indicated that H_2 is soluble in liquid metallic iron, which could bring a significant amount of hydrogen to the core (Iizuka-Oku et al., 2017; Ikuta et al., 2019; Machida et al., 2014, 2019; Okuchi, 1997). One major problem in studying this is that Fe-metal melt crystallises on quenching and the solid phases produced do not preserve the original H_2 concentration, making H_2 analysis on the recovered samples meaningless. In previous studies (Okuchi, 1997) iron liquid H_2 concentrations were, therefore, estimated from the volumes of H_2 bubbles that were quenched into the Fe-metal, with an accuracy that is hard to assess as it depends on the exact conditions of quenching and the equation of state of H_2. As discussed earlier, however, if the mantle started to oxidise towards the end of accretion, Fe metal would no longer be a stable, and could not, therefore, remove H_2 to the core.

Previous studies have also implied that FeS melt can dissolve H_2O, that exsolves upon quench crystallisation leaving vesicular pore spaces (Mungall & Brenan, 2003; Wykes & Mavrogenes, 2005). Higher-pressure (up to 16.5 GPa) experiments (Shibazaki et al., 2011) also indicate a significant decrease of the melting temperature of FeS caused by either H_2O or hydrogen solubility. To evaluate the possibility of FeS liquids dissolving H_2 requires information on the partitioning of H_2 between sulphide melts and a magma ocean as a function of oxygen fugacity.

The first step in being able to determine quantitatively the amount of hydrogen in FeS liquid would be to determine how much can actually be quenched into solid FeS phases. There is reasonably good evidence from *in situ* X-ray diffraction experiments that hydrogen is soluble in solid FeS minerals at high-pressure and high-temperature conditions (Shibazaki et al., 2011). The unit-cell volume of FeS in the presence of H_2 is higher compared to the nominally H_2-free FeS equation of state. Assuming the unit-cell volume expansion behaviour is similar to iron hydrides, Shibazaki et al. (2011) calculated the hydrogen content to be x = 0.2 – 0.4 (in $FeSH_x$ stoichiometry) between 3 GPa and 16 GPa. However, the uncertainties of this calculated hydrogen contents could be large, because Fe metal and FeS are structurally and chemically different. Furthermore, FeS undergoes a pressure-induced iron high-spin to low-spin phase transition, at pressures below ~7 GPa at 500 K and below 12.5 GPa at 1200 K (Fei et al., 1995; Urakawa et al., 2004). This causes abnormal compressibility behaviour, and therefore, unit-cell volume-based calculations for determining hydrogen contents in FeS will result in high-uncertainties as no simple P-V-T relation exists for the pressure interval of the spin transition. Although the hydrogen content of FeS likely increases with pressure at high-temperature, samples recovered to room pressure most likely lose this hydrogen, as observed for other hydride phases (Antonov et al., 1998; Fukai & Suzuki, 1986; Iizuka-Oku et al., 2017; Okuchi, 1997), so that *in situ* measurements are the only way to perform reliable hydrogen measurements.

An alternative more reliable approach to determine the hydrogen content in FeS is to use *in situ* neutron diffraction. Neutron diffraction is a powerful tool that provides structural information on a mineral phase, including site occupancies, and is sensitive to elements with a small atomic number. In neutron diffraction, the scattering power of an element is not dependent on the atomic number and both heavy and light elements can scatter similarly, in X-ray diffraction the scattering power simply increases with atomic number making light elements like hydrogen invisible (for more details, see the chapter 2). Through an analysis of neutron diffraction intensities, information on the sites in the FeS structure that are occupied by hydrogen can be obtained. Importantly, this method is completely independent from the determination of the unit-cell volume and it can therefore be used to validate the accuracy of previous X-ray diffraction unit-cell volume-based determinations of the hydrogen content of FeS. As FeS likely loses hydrogen on quenching to low pressure, however, neutron diffraction measurements have to be performed at high-pressure and temperature conditions. Due to the limitations in volume in the high-pressure experiments and in the ability to change the

orientation of the sample, it is necessary to perform power neutron diffraction measurements rather than single-crystal measurements.

In a recent study that used high pressure and temperature *in situ* neutron diffraction measurements (Iizuka-Oku et al., 2021), it was claimed that hydrogen incorporation in FeS is negligible. However, this study consists of experiments on hydrogen partitioning in a relatively complex system, with a starting material that comprised an iron-silicate-water-sulphur mixture. The resulting diffraction patterns were over-crowded with mostly overlapping reflections from multiple phases. In fact, the diffraction patterns show only 3 reflections of FeS that are not overlapping with other phases. It is therefore questionable as to whether the Rietveld refinement is of sufficient quality to determine the hydrogen concentration. This underlines the importance of obtaining a reliable systematic assessment of hydrogen incorporation in FeS at high-pressure and high-temperature. The first step should in fact be to determine the FeS hydrogen solubility, i.e., in equilibrium with pure H_2 gas. It is also essential to obtain clean diffraction patterns without overlapping reflections in order to refine multiple parameters such as, unit-cell dimensions, hydrogen occupancy, thermal parameters simultaneously. In such a study, once the total hydrogen content is obtained using Rietveld refinement, the volume increase of FeSHx on hydrogenation (ΔV_H) can also be calculated. This would, in addition, allow previous x-ray diffraction volume determinations of FeSHx (Shibazaki et al., 2011) and possibly neutron diffraction volumes by Iizuka-Oku et al., (2021) to be more accurately inverted to determine the hydrogen content. Once the maximum concentration of hydrogen under particular conditions are known it should be possible to perform measurements where the fo_2 is varied and the hydrogen activity is lowered. It would also be possible to perform partitioning experiments at lower hydrogen activities, where FeS liquid is quenched to a solid assemblage at conditions where the hydrogen concentration is below saturation in the solid and can, therefore, be reliably measured while the sample is still under high-pressure conditions.

If the mechanism of Earth's mantle oxidation indeed could be explained by oxidation by H_2O and the removal of H_2 through sulphide segregation to the core, this would also provide an important constraint in understanding of the composition of the Earth's core. Seismological observations show that both the inner and outer core are less dense than the main constituent Fe–Ni alloy (Birch, 1952, 1964; Ringwood, 1977). At the relevant high-pressure and high-temperature conditions density measurements on Fe or Fe-Ni alloy imply that the density of the core is only matched if some lighter element or elements are also present (Kantor et al.,

2007; Lin et al., 2003; Morrison et al., 2019). The candidate light elements are carbon, oxygen, sulphur, silicon and hydrogen due to their cosmochemical abundances (Birch, 1964; Poirier, 1994). However, up to now models that proposes the presence of just one of these elements fail to match both the density of the core and P and S seismic wave velocities (Hirose et al., 2021; Li et al., 2018; Umemoto & Hirose, 2020). It is most likely that the presence of not only just one, but a mixture of light elements in the core is responsible for the density deficit (Hirose et al., 2021). If multiple light elements are present then there may be too few geophysical constraints to independently determine the core's composition and additional constraints from an understanding of the core-formation process may be required (Badro et al., 2015). If sulphide segregation is indeed associated with the transport of a significant amount of hydrogen to the core, it may be possible to constrain the proportions of these two light elements (S and H) in an inter-dependant manner in core formation models.

Finally, as iron-rich monosulphides are accessory phases in the upper mantle and are the main inclusions found in diamonds it is important to also determine if they could host H_2 at plausible mantle oxygen fugacities as this could potentially influence their thermodynamic properties and melting temperatures. Sulphide minerals and melts may also be an additional, although potentially minor, host for hydrogen in the interior.

1.4. Objectives of the PhD thesis

This thesis consists of three experimental projects (presented in chapters 4, 5 and 6) each aimed at addressing a specific scientific question, as described below.

The first objective was to develop a new experimental method to determine the composition of high-pressure and temperature fluids in equilibrium with mineral assemblages. As discussed in section 1.1, high P-T fluid associated experiments are often challenging, and several recent studies have pointed out some inconsistencies in experimentally determined mineral solubilities using the often-applied classical diamond trap method. In the classical method fluids reside in an open network within a porous diamond powder layer sandwiched between layers of mineral/rock grains. The new method is aimed at improving this by separating the location where the fluid is captured from the region where mineral equilibrium occurs. The fluid is then captured in multiple traps so the homogeneity of the fluid composition can be assessed. This allows rigorous testing of the reproducibility and accuracy of data. High fluid/solid ratios in the experiment promotes growth of large single crystals, which can be

easily analysed to determine fluid-mineral partition coefficients. Another important aspect is to minimize the strong element fractionation during LA-ICP-MS analysis that has been observed in the classical diamond trap method.

The second part of this thesis was aimed at understanding the factors controlling the oxygen contents of mantle sulphide melts in equilibrium with peridotite mineral assemblages. As described in section 1.2, some natural sulphide inclusions found in diamonds show measurable oxygen concentrations, which might have originated as a component of a sulphide melt in the mantle. In the experimental work presented in chapter 5, the main goal was to measure oxygen concentrations of sulphide melts, in order to constrain the effects of pressures, temperatures, chemical composition and oxygen fugacity conditions relevant to upper mantle diamond formation. With the results of this study, a thermodynamic model is derived that can explain the variation in oxygen concentration in sulphide liquids of the upper mantle. Furthermore, the experimental results may be used to interpret the conditions of origin from the measured oxygen concentrations in natural sulphide diamond inclusions. An additional objective is to test a non-destructive method of measuring the oxygen concentration in sulphides using Mössbauer spectroscopy.

The main goal of the final chapter of this thesis is to determine the deuterium contents and site occupancy in iron sulphide at high-pressure and high-temperature using *in situ* neutron diffraction experiments. Deuterium is used as a proxy for hydrogen as it has a strong, positive neutron scattering length, but otherwise behaves similarly. As outlined in section 1.3, the capacity of FeS liquids to accommodate hydrogen (deuterium in the experiments) is relevant to various planetary formation and differentiation processes. Although hydrogen appears to dissolve in FeS minerals and melts at high-pressure and temperature, they most likely do not retain hydrogen in their structure during the P/T quench. The potentially most conclusive approach is to use *in situ* neutron diffraction analysis at high pressures and temperatures, to examine deuterium solubility in FeS minerals. This provides at least a starting point for understanding the likely hydrogen contents in sulphide liquids. Further thermodynamic treatments could provide information on the potential storage of hydrogen in sulphide relevant to planetary mantles and inner cores. Therefore, in this study high pressure and temperature experiments were made in the solubility of deuterium in a polytype of pyrrhotite (NiAs-type $Fe_{(1-x)}S$), referred to as FeS V, using a multi-anvil press installed at the J-PARC spallation neutron source in Japan. Powder time-of-flight neutron diffraction measurements were made

that can provide structural information on atomic positions and site occupancies of deuterium in FeS V when analysed using Rietveld structure refinements. Further experiments were performed to determine the oxygen fugacity imposed by the deuterium source and a model is used to determine the likely hydrogen content of FeS V at the higher oxygen fugacities of cratonic lithosphere conditions and diamond formation.

Chapter 2

2 Methods

This chapter describes the experimental and analytical techniques used in this thesis. Some of the techniques included here will be described in slightly more detail in the following chapters.

2.1 Starting materials

All starting materials were synthesized using reagent grade oxides carbonates and metal powders. Specific compositions of the starting mixtures will be described in the following chapters relevant to each project. As a general procedure, starting materials consisting of more than one component were prepared by mixing them in an agate mortar after weighing each component in appropriate proportions. The mixture of each composition was grounded under ethanol for at least 40 minutes to ensure homogeneity. In some instances, the mixing procedure was repeated more than one time, when for example, the starting powders contained trace amounts of components that must be distributed homogeneously.

Required contents of oxides in the silicate starting materials were obtained either using the exact oxide composition (e.g. Al_2O_3, MgO) or for particularly hydroscopic components through decarbonation of the carbonate (e.g. $CaCO_3 \rightarrow CaO + CO_2$). Iron was added to starting materials using the most stoichiometric oxide, Fe_2O_3, which was then reduced in a gas mixing furnace at an appropriate oxygen fugacity. For this, a small amount (~ 0.5 g) of the starting powder was pressed into a pellet using a hydraulic pellet press and then hung inside the vertical tube of the gas mixing furnace inside a Pt cage. By using a cage of thin Pt wires, contact and thus iron loss, to the Pt was minimized. The required oxygen fugacity was obtained by mixing CO and CO2 gas flow through the vertical tube of the furnace at a temperature of 1100 °C. The proportion of $CO:CO_2$ required to arrive at a particular oxygen fugacity is determined using look-up tables that are based on the equilibrium,

$$2CO + O_2 \rightleftharpoons 2CO_2 \quad (2.1)$$

Quenched pellets were ground in an agate mortar for another 10–20 minutes and all the

prepared starting materials were stored in a desiccator to prevent oxidation/hydration before use in the high-pressure and temperature experiments.

2.2 High-pressure and high-temperature experiments

Mainly two high-pressure (*HP*) and high-temperature (*HT*) experimental techniques for *ex situ* experiments were used. Overall, experiments at pressures lower than 3 GPa were conducted using the piston-cylinder apparatus (sub-section 2.2.1) which has the advantage of being able to synthesize relatively large sample volumes (up to ~ 600 mg) under well controlled thermal environments. Experiments at higher pressures (>3 GPa) were performed using a multi-anvil apparatus (6-8 type) operating with a large volume press (LVP). The multi-anvil has the advantage of being able to generate pressures up to 25 GPa and temperatures up to 2500 K (sub-section 2.2.2.1) i.e. conditions that encompass those down to the top of the lower mantle. Sample sizes decrease with pressure although even at the highest-pressures, samples of a few milligrams can be obtained. All *in situ HP-HT* neutron diffraction experiments at J-PARC were performed using a 6-6 type multi-anvil apparatus, described in detail in sub-section 2.2.2.2.

2.2.1 Piston-cylinder apparatus

The piston cylinder press (Boyd & England, 1960) has been used for high *P*, high *T* experiments at conditions that typically encompass the lower crust up to the top of the upper mantle (~3 GPa and ~2000 °C), although higher pressures (up to ~ 5 GPa) are possible (Boyd & England, 1960; Perkins et al., 1981). Relatively large sample sizes can be employed in the piston cylinder apparatus (~200 mm^3 in 1/2" assembly) compared to the multi-anvil type LVP. A stack of three main pieces, i.e., bridge, pressure vessel and top plate, comprise a cylindrical-shaped setup, where the high-pressure and high-temperature experiments are carried out. A typical end-loaded set up is shown in the Figure 2.1. The pressure vessel (bomb), is made of a series of outer steel rings that surround and confine an inner tungsten carbide (WC) core with a cylindrical cavity at the centre for the high-pressure assembly. The master ram transfers the pressure to the sample (enclosed in the high-pressure cell assembly) through a WC piston which moves inside the WC core of the pressure vessel. A second hydraulic ram provides the end-load pressure during an experiment to support the pressure vessel from the opposite side of the master ram (Fig. 2.1). In general, pressurization is first performed using two hand-pumps (one for each ram with a maximum oil pressure of 2000 bars), and then a programmed pressure profile can be executed through a pressure controller system, which is driven by two automatic

pumps. Some of the experiments were performed using fully manual type piston cylinder presses, in which the pressure is generated only using the hand pumps. After compression, electrical power is supplied via copper electrodes on the top plate and the bridge, which creates an electrical circuit through a resistive graphite heater that generates high temperatures in the assembly. During heating, the pressure vessel is cooled using circulating water (~5 – 8 L/min), which stops high-temperatures building up within the concentric rings and core of the bomb and within the pressurising oil, allowing pressures to remain stable for long durations (up to several weeks).

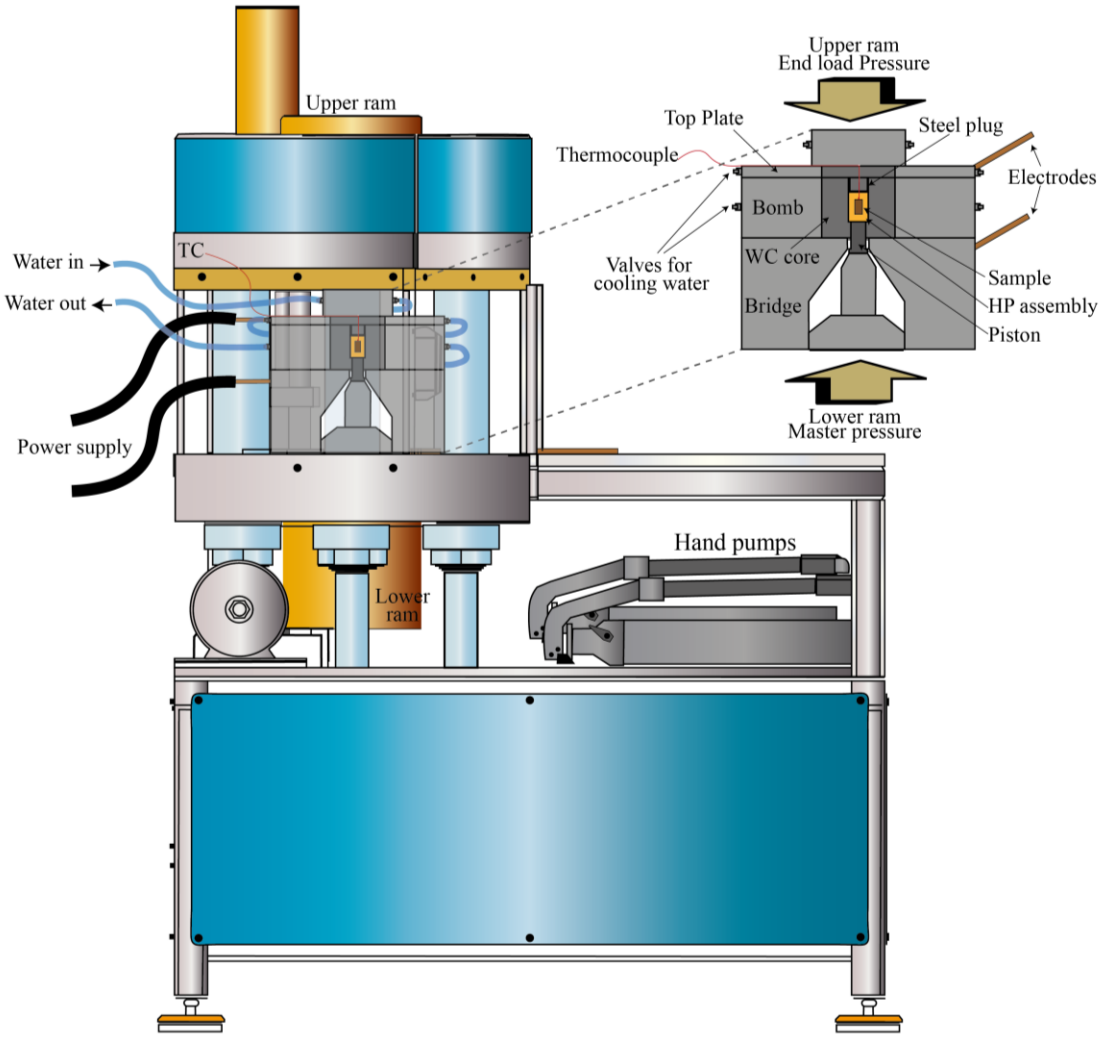

Figure 2.1: Side view of piston cylinder press (MavoPress from Max Voggenreiter GmbH) and the components of the end-loaded set up. The copper electrodes are connected to the "Eurotherm" power supply for heating the experiments. The water in and out is connected to a central cooling water supply which circulates around the stack of metal cylinders and sample-containing bomb during the heating period of experiments for cooling.

The high-pressure assembly (Fig. 2.2) is placed inside the cylindrical cavity within the tungsten carbide core of the pressure vessel (Fig. 2.1). A steel plug with an outer pyrophyllite sleeve is inserted within the carbide core (on top of the assembly) to prevent the assembly from being extruded upon pressurizing. The high-pressure assembly used for the experiments described in this thesis was made out of an outer NaCl sleeve, inner polycrystalline MgO sleeve and a stepped graphite resistance heater (referred to as an "NaCl+MgO" assembly, Fig. 2.2). The sample capsule placed at the centre of the assembly surrounded by an MgO sleeve and two MgO plugs on both sides. The electrical connection to the graphite heater is maintained through the steel plug on the top and a graphite and steel disk at the bottom of the assembly. The experimental temperature is monitored using a thermocouple (S type in this study – Pt/Pt_{90}-Rh_{10}), inserted axially such that the welded junction is in close contact with the top of the capsule. Even though the primary load applied is uniaxial, the sample capsule is pressurized quasi-hydrostatically once the pressure-medium materials of the assembly are heated up. Calculation of the pressure (P) of piston cylinder experiments is based on the relationship between applied force (F) and area (A), i.e., P = F/A, and could be determined based on the surface area of the piston. The pressure experienced by the sample, however, depends on the extent to which force is lost due to frictional sliding of the piston and within the assembly parts. This requires a "friction correction" to be made which varies for different cell assemblies but is determined through pressure calibration experiments.

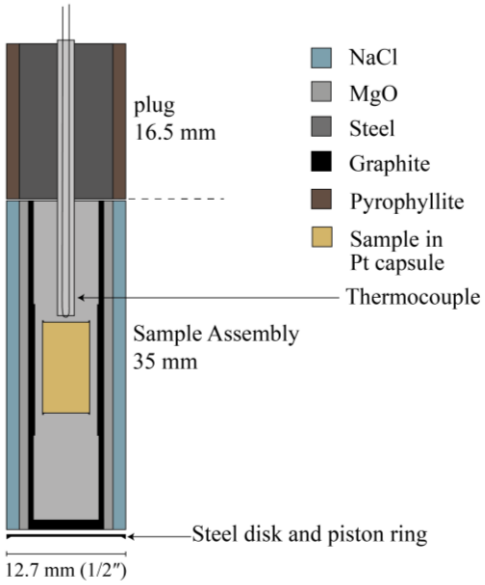

Figure 2.2: A schematic diagram of the high-pressure cell assembly and base plug on top used in piston cylinder experiments. Type S (Pt/Pt–Rh) thermocouple inserted axially was employed for the temperature measurements.

2.2.2 Multi-anvil apparatus

The multi-anvil apparatus is capable of generating pressures and temperatures corresponding to the conditions up to the top of Earth's lower mantle (~25 GPa, 2500 K), while maintaining a relatively large sample volume of the order of ~10 mm^3. A multi-anvil press consists of hydraulically driven ram that compresses two opposing guide blocks, each containing three hardened steel primary stage anvils. The outer anvils are shaped to compress a cubic array of eight second stage tungsten-carbide (WC) anvils, resulting in a so called 6-8 type multi-anvil apparatus. Each second stage anvil has a corner truncation such that when the eight cubes are assembled into a larger single cube, an octahedral shaped cavity is created at the centre. An octahedral high-pressure ceramic cell assembly is placed in this cavity, containing the sample separated from a resistance heater by further ceramic parts. Recent technical advances have allowed pressures up to 50 GPa to be reached by using sintered diamond cubes as second stage anvils and boron-doped diamond as a heater material (Xie et al., 2021). Experiments presented in the following chapters of this thesis, were performed using two main types of multi-anvil, i.e. 6-8 type and 6-6 type multi-anvil apparatuses.

2.2.2.1 The 6-8 type multi-anvil apparatus for ex situ HP-HT experiments

The 6-8 setup uses a set of 8 WC second stage cubic anvils, each with at least one triangular corner truncation. When the 8 cubes are assembled, the corner truncations create an octahedral chamber, in which the HP sample assembly is placed. Pyrophyllite gaskets are glued along the sides of the WC cube truncations to confine the HP chamber in which the cell assembly is placed. A set of eight WC cubes with the octahedral HP cell in the centre is placed in the lower of two steel guide blocks, each containing three outer hardened steal anvils that together form a cubic chamber. One of the guide blocks is fixed, while the other is moved using a hydraulic ram. The sizes of the octahedral cell assembly and the truncation edge length (TEL) of the WC anvils controls the pressure generation on the sample (placed in the centre of the octahedron) for a given uniaxial load generated by the hydraulic powered guide blocks. The 6-8 type multi-anvil setup is sketched in Figure 2.3 and further details can be found in Rubie (1999).

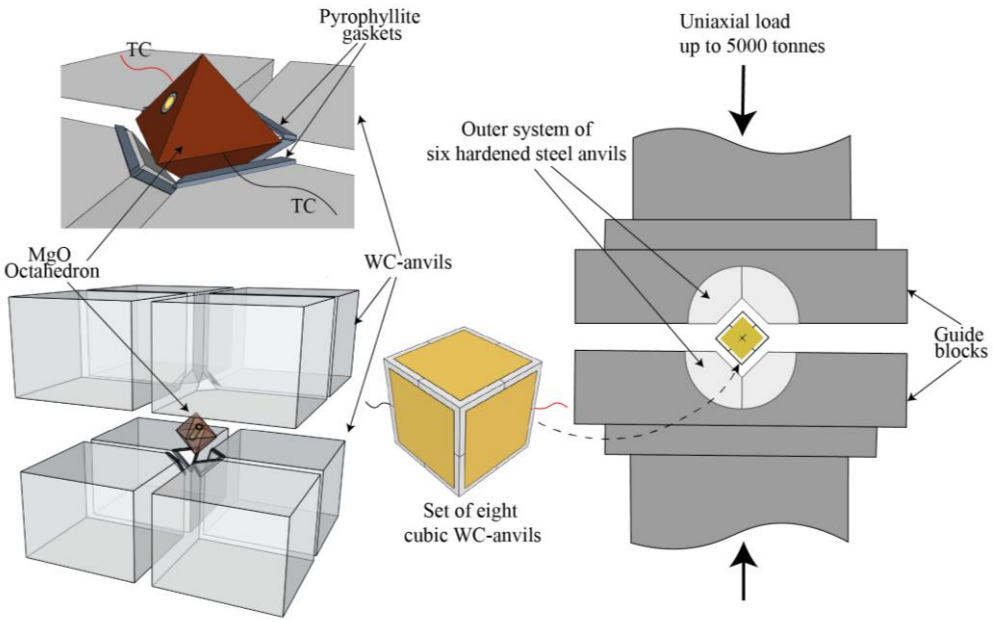

Figure 2.3: The 6-8 type multi-anvil apparatus (modified after Rubie, 1999). TC–thermocouple, WC - tungsten carbide.

The octahedral shaped high-pressure sample cell assembly is made out of Cr_2O_3-doped MgO (pressure medium). The pressure medium contains about 5 % of Cr_2O_3 that lowers the thermal conductivity of MgO. Figure 2.4 shows a cross-section through the 18/11 (i.e., 18 mm edge length of the octahedra and 11 mm truncation edge length of the WC anvils) assembly. Prior to the experiments, assembly parts made of MgO and $LaCrO_3$ were baked at 1000°C for a few hours to remove water and organic binders. The octahedron contains a cylindrical hole (6.8 mm in diameter – 18/11 assembly) in which a furnace surrounded by a thermally insulating ZrO_2 sleeve is place. A resistive heater made of $LaCrO_3$ (for experiments above ~8 GPa) or graphite (for experiments below ~8 GPa) is employed, separated into three stepped cylindrical parts, with different wall thicknesses, designed to minimize the thermal gradient over the sample. The upper heater component encloses an MgO tube that serves to accommodate the thermocouple, while a solid MgO cylinder is inserted inside the bottom section of the heater. The middle part of the stepped heater accommodates the sample capsule inside a thin MgO sleeve and has a thicker wall in order to create a smaller axial thermal gradient. The starting materials used in each experiment and the sample environment (including the type of furnace, capsule material, type of the thermocouple, etc.) will be described in detail in the relevant chapters. Two disks made of either molybdenum (with $LaCrO_3$ heater) or graphite (with graphite heater) are placed both on the top and bottom of the octahedron assembly to ensure

optimal electrical connection between the resistive heater and the truncated faces of the WC cubes during the experiment. To monitor the temperature during the experiments, a thermocouple is placed on the top of the sample capsule. Thermocouples made of $W_{97}Re_3$ and $W_{75}Re_{25}$ alloy wires (type D), with a crossed junction at one end of a four-hole dense alumina tube were inserted vertically from the top of the cell assembly. Estimated uncertainty of the temperature measurements is about ± 50 K (Rubie, 1999).

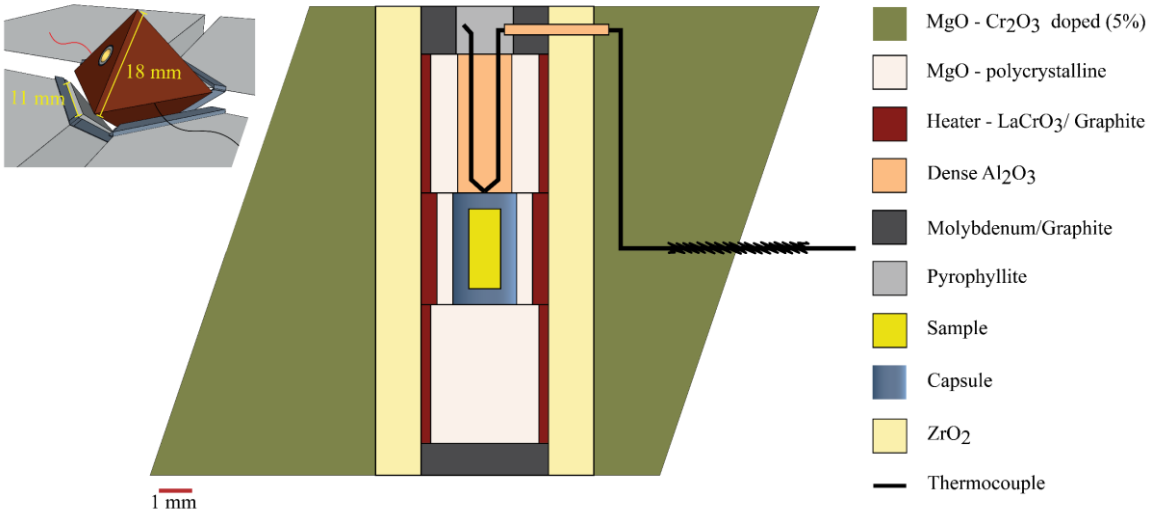

Figure 2.4: Cross-section through the 18/11 (18mm edge length of the octahedra and 11mm truncation of WC anvils – as shown in the top left corner) assembly, all other sizes of assemblies used in the experiments follow a similar design.

The pressure calibration in the multi-anvil apparatus is performed using the known pressures of certain mineral phase transformations. The pressure calibration curves used at the Bayerisches Geoinstitut (BGI) are shown in Figure 2.5, where pressure (in GPa) is plotted vs. applied force (in tonnes). Different combinations of octahedral assembly size/truncation edge length (e.g., 18/11, 10/4 etc.) are noted next to the respective curves. Details of the various phase transformations used for the pressure calibration can be found in Keppler and Frost (2015).

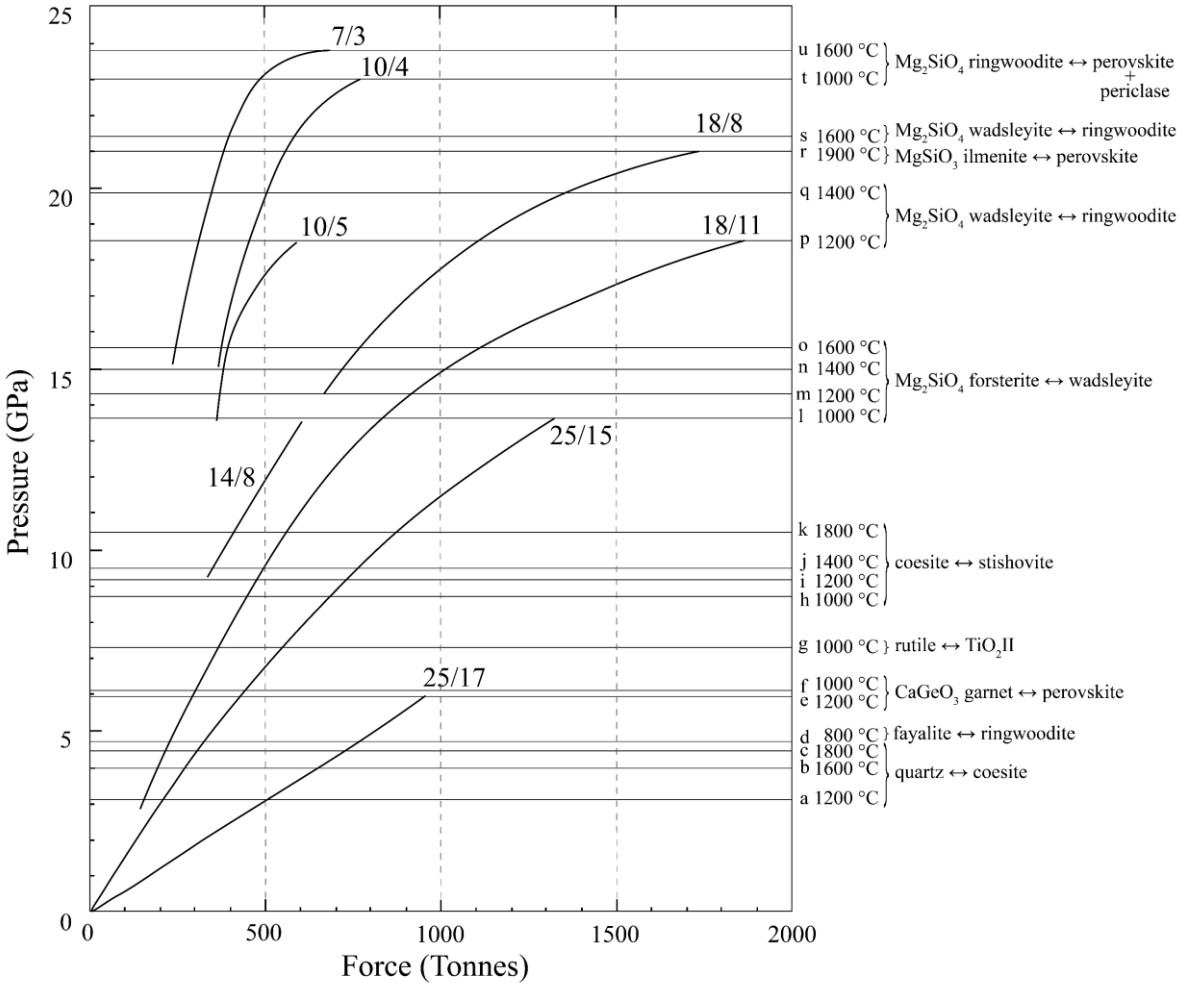

Figure 2.5: Pressure calibration curves used at the BGI, performed in 1200 tonne split-sphere and 5000 tonne split-cylinder multi-anvil presses (modified after Keppler and Frost, 2015). Major phase transformations used for the calibrations are shown at the right side of the figure, and the additional details and references can be found in Keppler and Frost (2015).

2.2.2.2 The 6-6 type MA apparatus for *in situ HP-HT* experiments

A similar 6-6 type multi-anvil device to that installed at the Bayerisches Geoinstitut exists at the PLANET beamline of the J-PARC spallation neutron diffraction source, for *in situ* neutron powder diffraction measurements. The system consists of six independently movable rams attached directly to square-faceted hardened steel first-stage anvils. Within the cubic cavity created as the 6 first-stage anvils are advanced, sits a second stage of 6 inner steel-supported WC anvils, which also have square-shaped facets that compress a cubic high-pressure cell assembly. The high-pressure cubic cell assembly is made of polycrystalline Cr_2O_3-doped MgO,

which serves as a quasi-hydrostatic pressure medium, at high-temperature. Capsules made of NaCl were used (further discussed in Chapter 6), which is well known for efficiently sealing hydrogen at high *P* and *T* (Fukai et al., 2003; Machida et al., 2014; Sakamaki et al., 2009; Shibazaki et al., 2011). The dry powders of the sample and the deuterium source are pressed to dense pellets using pellet presses of appropriate sizes (3 or 4 mm in diameter), without any binding agent. Inside the NaCl capsules, pellets of the sample are placed in the centre with the deuterium source on the top and the bottom. The capsule with an NaCl lid is enclosed within a cylindrical graphite sleeve. The graphite sleeve with lids of graphite on the top and bottom serves as a box resistance heater and is placed inside a cylindrical hole drilled at the centre of the cubic pressure transmitting medium. End caps, made out of ZrO_2 (OZ8C) wrapped with molybdenum foil (for electrical conduction), are then placed in contact with both sides of the graphite resistance heater. Cubes with edge lengths (CEL) of 15.0 mm and 10.5 mm (Fig. 2.6) were used for experiments at $P \leq 7$ GPa and $P > 7$ GPa respectively. The MgO cube was truncated along the edges ("edge-cut") in order to fit perfectly inside the second stage anvils. Pyrophyllite gaskets were glued along the edges of the second stage anvils using "Cemedine CA-141 Photo Glue". This glue may contain a small amount of hydrogen, and therefore, very small amounts were used and placed only at the edge of the truncations. The gaskets were baked at 750 °C, for a minimum of 30 minutes before the experiment to remove the moisture, chemically bonded water (as stoichiometric OH groups) and organic impurities. The cell assembly was compressed between six tungsten carbide second stage anvils (TEL – truncation edge length = 10 mm with CEL 15 assembly, and 7 mm with CEL 10.5 assembly), using six independently operated rams attached to the first-stage anvils, where each can apply a force of up to 500 tonnes.

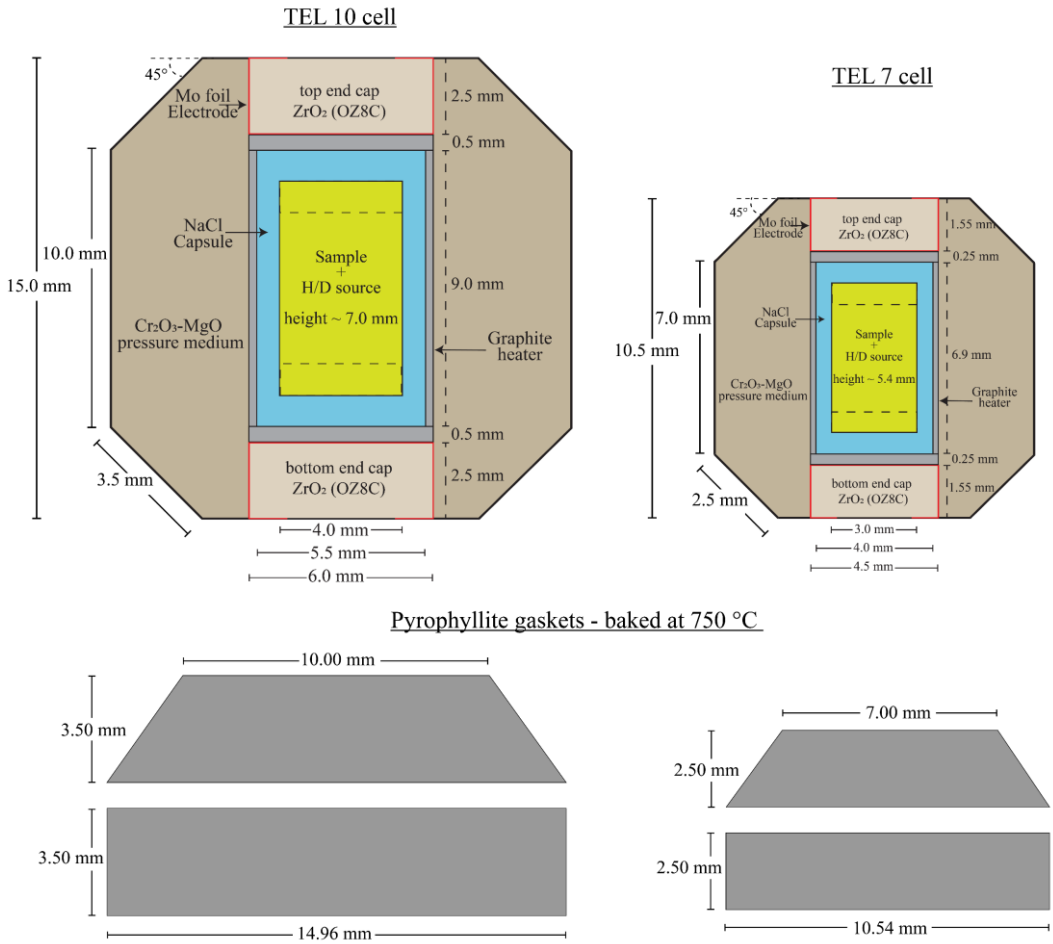

Figure 2.6: Cross-sections through the high-pressure cell assemblies; TEL 10 cell (CEL 15.0 mm) used for experiments at P ≤ 7 GPa and the TEL 7 cell (CEL 10.5 mm) used for the experiments at P > 7 GPa. The deuterium source, is placed on the top and bottom of the sample pellet inside the NaCl capsule. Pyrophyllite gaskets are baked at 750 °C at least for 30 minutes before the experiments in order to remove the moisture and organic impurities.

Figure 2.7 shows a sketch of the cubic MgO cell assembly placed at the centre of the first stage anvils surrounded by the independently movable rams of the apparatus. A frame made of aluminium (alignment frame) facilitates the alignment of the second-stage-anvils imposes symmetrical movement (each anvil moves perpendicular to the six faces of the MgO cube) during the initial sample compression, while maintaining small spaces between anvils (anvil gap) to provide sufficient room for compression. These anvil gaps provide an additional important advantage of using 6-6 type apparatus for *in situ* neutron diffraction experiments (will be described in the next section), where the neutron beam needs a sufficient access to travel from the neutron source through the sample and then to the detector in *time-of-flight*

powder neutron diffraction measurements. Further details concerning the beamline setup and *in situ* measurements are described in Chapter 6 and in the following section.

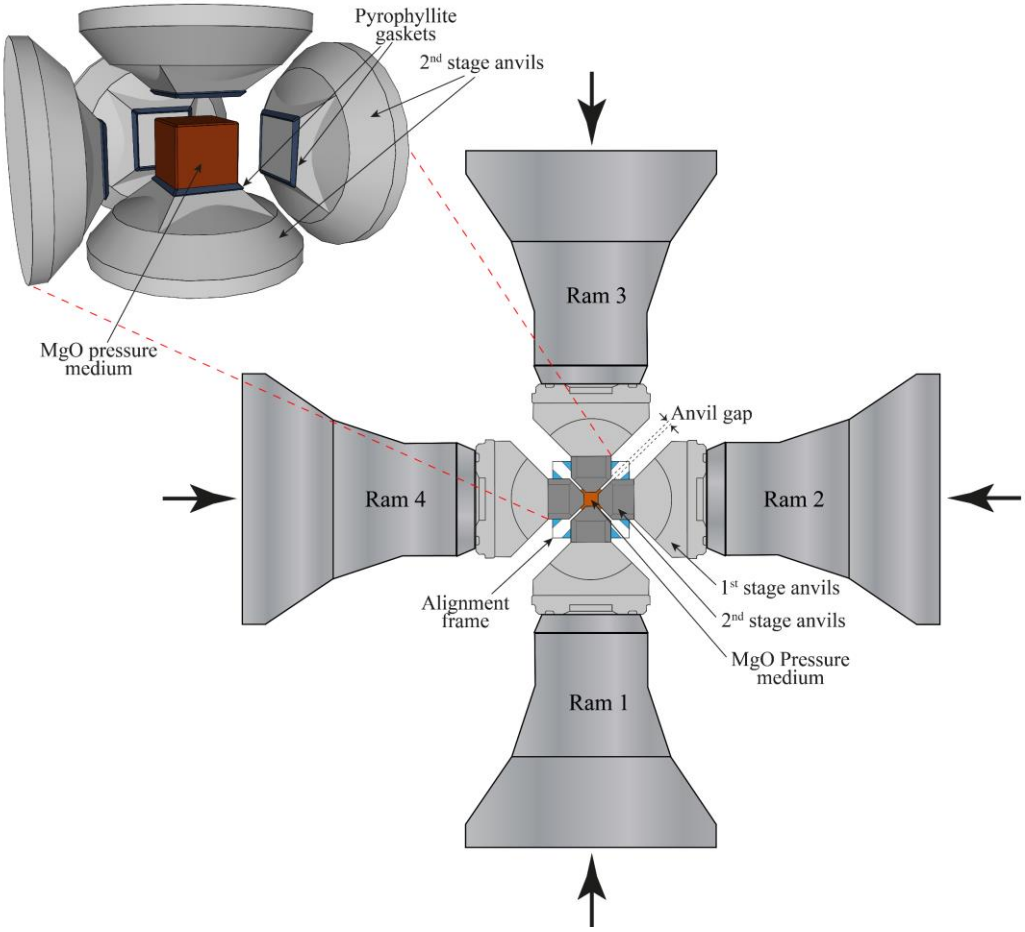

Figure 2.7: The six-ram multi-anvil system with a 6-6 type cell assembly. The sketches are show a side view of the second stage anvils made of tungsten carbide with Ni binder (TMS05 from FUJILLOY - https://www.fujidie.co.jp/) with the cubic high-pressure cell assembly sits in the middle (top left), and a section view from the top of the six-ram press. The first stage anvils are attached on the top of each ram, and are made of tungsten carbide with a Co binder (F10 from FUJILLOY - https://www.fujidie.co.jp/) surrounded by tool steal retainment rings.

2.2.3 High-pressure and high-temperature *in situ* neutron diffraction experiments at the *J-PARC* PLANET beamline

Neutron diffraction is the only tool capable of resolving the crystallographic position of hydrogen and other light elements in the frameworks of heavier atoms. Due to the comparatively weak interaction of neutrons with matter and the low flux of neutron sources compared to X-rays, neutron diffraction measurements require relatively large sample

volumes. If measurements are to be performed at high-pressures, this requires the use of large volume presses such as the multi-anvil apparatus described in the previous section.

Neutrons are uncharged subatomic particles which make up approximately 50% of the mass of an atom, in a proportion which gradually increases with atomic number. Although they have a mass of 1.0087 atomic mass units, i.e. slightly greater than a proton, they exhibit wave-like behaviour, with wavelengths that can be similar to the interatomic distances in condensed matter. This allows neutron diffraction to be used to investigate atomic structures of condensed matter. Free neutrons were first produced through fission reactions inside a nuclear reactor. Later spallation sources were developed from which higher neutron fluxes can be obtained. At a spallation source, neutrons are emitted when an accelerated high energy proton beam (~3 GeV) hits a high-density metal target. Mercury is often the metal of choice as its liquid state allows more effective cooling. The free neutrons produced by both reactor and spallation sources have kinetic energies in the MeV range, which need to be lowered, often referred to as "cooled", in order for the wavelengths to approach those of interatomic distances. This is done by passing the beam through a moderator, such as D_2O or H_2O, at near room temperature. The resulting "thermal" neutron spectrum has energies of the order of 0.025 eV, and a wavelength distribution in the range 0.3-6 Å. The initial proton accelerator can be pulsed, which allows the target to cool but more importantly creates a neutron beam with the same pulse rate, generally in the range 10-50 Hz, which facilitates neutron time of flight measurements, as discussed later. As neutrons cannot be easily focused, different instruments at neutron facilities are generally arranged radially around the moderator. The neutrons travel to the instrument along a neutron guide, which reduces the loss of neutrons by allowing small angle reflections (Abele et al., 2006).

Although the principal of neutron diffraction is similar to when X-rays are used, the difference arises in the way that neutrons interact with condensed matter. While X-rays are scattered through interactions with the electron cloud of an atom, neutrons interact with the atomic nucleus. The extent of X-ray scattering is proportional to the number of electrons in the electron cloud, which means the scattering factor increases uniformly with increasing atomic number (Fig. 2.8-a). Consequently, X-rays are not very sensitive to the presence of light elements such as hydrogen and do not differentiate well between elements of similar atomic number. The strength of neutron scattering, characterised by the neutron scattering length, b measured in femtometres, or using the equivalent scattering cross section, σ measured in barns (1 barn =

10^{-24} cm^2), shows a seemingly random variation with atomic number and can vary strongly even between isotopes of the same element (Fig. 2.8-b). A large difference exists, for example, between the scattering lengths of hydrogen (-3.74 fm) and deuterium (+6.67 fm). The negative scattering amplitude of hydrogen contributes to strong incoherent scattering in hydrogen-rich materials, which leads to a large isotropic background in neutron diffraction data. This can be overcome by substituting hydrogen for deuterium, for which the coherent scattering cross section, which gives rise to Bragg diffraction, dominates over the incoherent. Neutrons not only have the advantage of being scattered quite strongly by light elements, but they also have large penetration depths for certain materials, which is a useful property when studying samples that are confined in order to reach high pressure and temperature conditions.

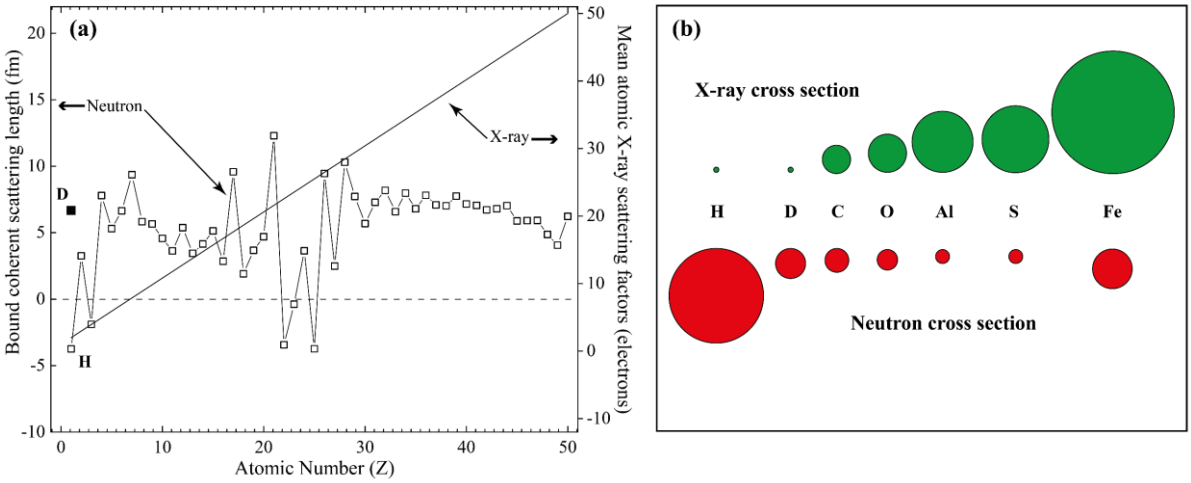

Figure 2.8: (a) Variation of scattering power expressed as bound coherent scattering length for neutrons (in left-axis) and as mean atomic X-ray scattering factor (in the right-axis) as a function of the atomic number. **(b)** Representation of the relative total scattering cross sections of selected elements and isotopes for neutrons and X-rays. Hydrogen has large scattering power for neutrons (Neumann 2006; Courtesy of Muhammad Arif, NIST)

Neutron detection is made challenging by the fact that they do not directly ionize materials and free neutron beams have low intensities, compared to X-rays. Neutron detectors generally employ ^3He in a cell filled with another gas, such as Ar, and with a cathode, often as the wall of the cell, and an anode at the centre. Neutrons are absorbed in a nuclear reaction i.e. n + ^3He = ^1H + ^3H + 0.77 MeV, which causes ionization of the gas and a current to flow between the electrodes. It is also possible to create position sensitive detectors that determine the position

along the detector tube's length where the reaction occurs and current flows between the electrodes.

As in an x-ray diffraction measurement, the Bragg equation,

$$2d_{hkl}\sin(\theta) = \lambda \tag{2.2}$$

can be used to determine d_{hkl}, the d-spacing of a crystallographic reflection with a given hkl Miller indices, either by fixing the wavelength λ in a monochromatic measurement and measuring θ, half the angle between the incident and diffracted beam, or by using a white neutron beam comprised of a collection of energies i.e. wavelengths, and determining λ of a diffracted beam at a fixed diffraction angle. For high pressure LVP measurements angular access to diffracted neutrons from the sample is limited and angle dispersive measurements would be challenging, also for the detector array. Neutron diffraction energy dispersive measurements are, therefore, performed utilising the time of flight technique (TOF). The relationship between wavelength λ of a neutron and its momentum can be described by the de Broglie equation,

$$\lambda = \frac{h}{mv} \tag{2.3}$$

where, h is Planck's constant (6.626×10^{-34}Js) and m is the mass of the neutron (1.675×10^{-27}kg). Thus, the velocity, *v*, of the neutron is inversely proportional to its wavelength. If a white neutron beam is pulsed, then over a fixed path length, *L*, from the moderator to the detector and over one cycle, neutrons with different λ and therefore different v will arrive at different times *t*, and λ can be determined from,

$$\lambda = \frac{ht}{mL} \tag{2.4}$$

Combining with the Bragg equation,

$$\lambda = \frac{ht}{mL} = 2d\ sin\theta \tag{2.5}$$

shows that *d*-spacing can be determined as a function of time at fixed or known values of θ. TOF powder diffraction patterns are plotted with time on the x-axis, which is directly proportional to the *d*-spacing. This is different from energy dispersive or angle-dispersive x-

ray diffraction methods, where *d*-spacing is inversely proportional to the relevant x-axis of energy(keV) or angle (2θ).

The powder neutron diffraction experiments presented in chapter 6 were performed at the Materials and Life science experimental Facility (MLF), J-PARC, Japan. The PLANET beamline (BL 11) is equipped with a six-ram multi-anvil press, capable of performing experiment up to ~15 GPa pressure and temperatures up to 2000 K. Another main advantages of using 6-6 multi-anvil system for *in situ* experiments at synchrotron facilities (J-PARC in this study) is that the six-axis set-up (Fig. 2.9) can maintain wide windows between anvils allowing the collimator devices to be positioned close to the sample. This is particularly useful in neutron diffraction experiments, since the intensity of neutron sources are relatively weak (compared to X-ray), and therefore wide detector windows and large sample sizes are essential. The six-ram multi-anvil press (ATSUHIME) installed at BL-11 (Sano-Furukawa et al., 2014) provides an excellent set-up for high *P, T* neutron diffraction experiments. Large sample sizes can be accommodated (up to ~ 60 mm^3) in the high-pressure assemblies used, and the neutron diffraction data are collected with a 90-degree geometry between the incident beam and two vertical detector arrays on each side for the diffracted signal (Fig. 2.9-c). The detector arrays are position sensitive in the horizontal direction, so that neutrons collected at known angles a few degrees either side of the 90-degree geometry can also be integrated into the measurements.

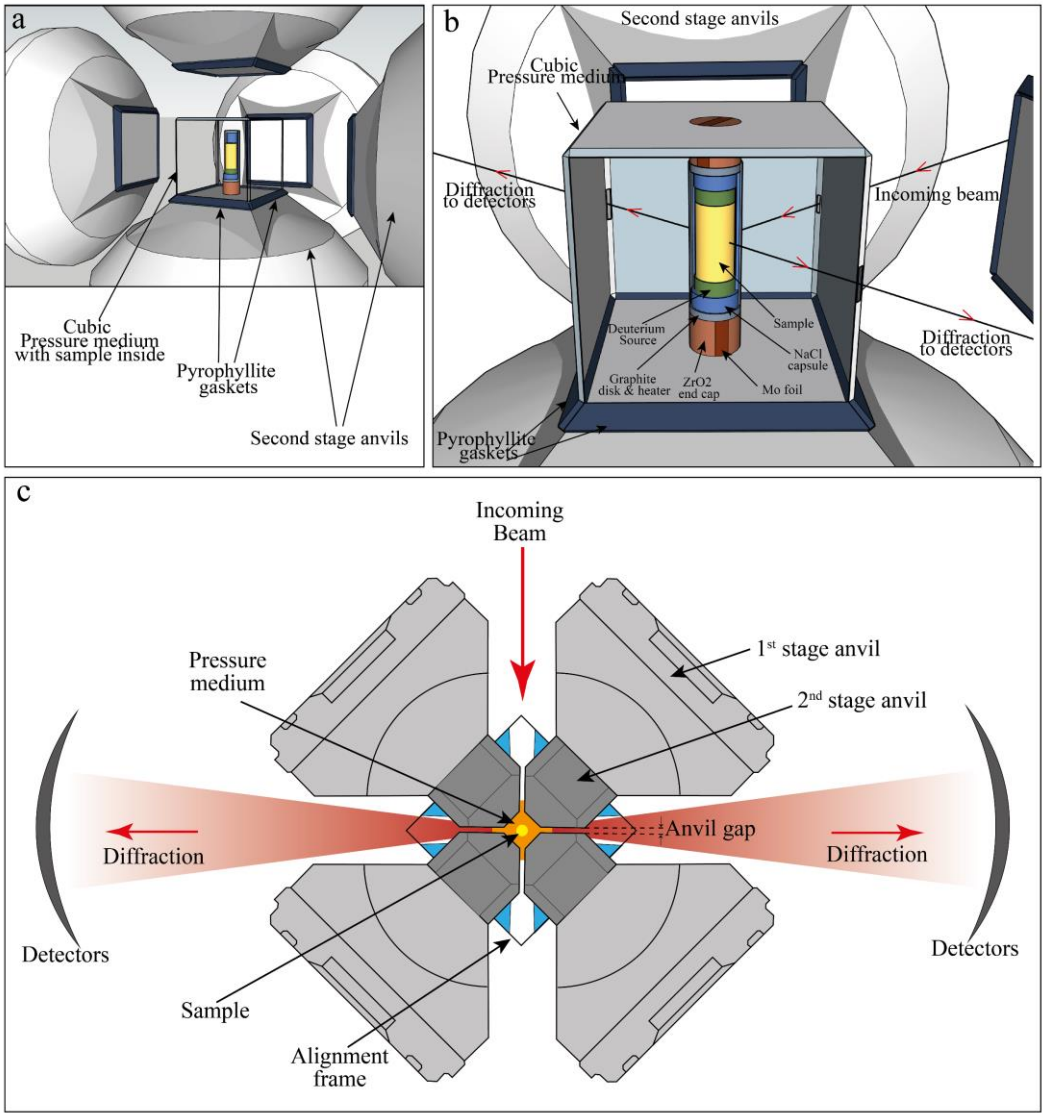

Figure 2.9: Six-ram multi-anvil system with a 6-6 type cell assembly. **(a)** A view from the side of the second stage anvils with the cubic *HP* cell assembly placed at the center. Pyrophyllite gaskets are glued along the truncations of each second-stage anvil **(b)** A close up view of the *HP* cell assembly. **(c)** A view from the top of the six-ram press installed in BL11 at J-PARC, Japan (modified after Sano-Furukawa et al., 2014). The 90-degree geometry between incoming and diffracted beams through the sample is shown, with the beam path between the anvil gaps of the 6-6 two stage anvil configuration indicated. As the detectors are position sensitive in this plane, diffracted neutrons from a few degrees either side of the 90-degree geometry can be integrated into the diffraction measurement. A frame made of aluminium (alignment frame - blue colour) aligns the second-stage-anvils to impose an initial spacing and symmetrical movement (each anvil moves perpendicular to the six faces of the MgO cube) during initial sample compression.

The powder TOF neutron diffraction patterns collected at *HP-HT* conditions were analysed using the Rietveld refinement method in order to determine the position of deuterium in the crystal structure examined.

2.2.4 Rietveld refinements of time-of-Flight (TOF) neutron diffraction data

A time-of-flight (TOF) powder neutron diffraction pattern comprises intensity data as a function of time (proportional to lattice plane d-spacing), that reveals a series of crystallographic reflections (diffraction peaks) with particular intensities. Information on the symmetry of the crystal structure and unit-cell parameters are encoded in the diffraction peak positions. The peak intensities encode information on the atom positions, site occupancies and thermal parameters, although they can also be influenced by preferred orientation within the sample. Peak widths are influenced by factors such as defects within the structure, lattice strains, grain sizes and instrumental characteristics. Peak overlaps due to multiple phases can result in certain reflections being obscured or hidden, which causes a reduction in information if the pattern is analysed by examining individual peaks in turn. In 1969 Hugo Rietveld introduced a new method to overcome this problem, which is known as the Rietveld structure refinement method (Rietveld, 1969). The basic concept is to model a calculated powder diffraction pattern that includes contributions from each phase present along with a background function and then to minimize the misfit between this model and the actual pattern by refining properties of the crystal structure. The powder pattern for each phase is described by a set of parameters, the most important being the crystal symmetry, unit cell parameters, atomic positions and occupancies and instrumental characteristics. Further factors such as the effect of a preferred orientation of the powdered sample on the intensities of reflections can also be included in the model and in fact should be tested in any model. The set of defined parameters are refined using a least-squares method until the calculated pattern intensities match those of the experimentally obtained diffraction pattern. When the calculated and experimental patterns agree satisfactorily, the structure is considered to be refined. The goodness of the fit between calculated and experimental diffraction patterns is evaluated using reduced chi square χ^2 or "goodness of the fit" which is defined by the minimization function,

$$\chi^2 = \frac{M}{N_{\text{obs}} - N_{\text{var}}} \tag{2.6}$$

where M is sum of the components of the minimization function ($M = f_h \sum M_h$), N_{obs} is the total number of observations in all histograms and N_{var} is the number of variables in the least-squares refinement (Larson & Dreele, 2004).

Another way of examining the quality of a least squares refinement is by determining residual functions which cover the entire pattern, defined as,

$$R_p = \sum |I_o - I_c| \,/\, \sum I_o \tag{2.7}$$

and,

$$R_{wp} = \sqrt{\sum \mathrm{w}(I_o - I_c)^2 / \sum \mathrm{w} I_0^2} \tag{2.8}$$

where I_o is the observed intensity and I_c is the calculated intensity and *w* are weights which are derived from an error propagation during the refinement (Larson & Dreele, 2004).

2.3 Analytical techniques

High pressure and temperature experiments produce relatively small samples of the order of a millimetre and individual crystals often of the order of micrometres. Microbeam analysis techniques are therefore required to characterise the mineralogy and chemistry. The following are short descriptions of the techniques used in the course of this thesis. More details can be found in the respective chapters.

2.3.1 Scanning Electron Microscope

Scanning electron microscopy (SEM) is an instrument which can produce magnified, high spatial resolution images by scanning the surface of a sample with an electron beam. Observation of the experimental run products was performed using a conventional field-emission scanning electron microscope, Zeiss LEO 1530 FE-SEM for high resolution imaging, identification of mineral phases and semi-quantitative chemical analyses of the polished sections of the high-P-T experimental run products. The typical SEM spatial resolution is ~10 nm in topographic mode, and up to 100 nm in compositional mode (Reed, 2005). To prevent electrical charging, a conductive sample surface was made by coating a thin layer of carbon with ~12 nm thickness.

Electrons are produced by an electron gun, normally a heated tungsten filament, and are accelerated down a column towards an anode by a potential difference in the range 10-30 kV.

The electron beam is focused on the sample surface by passing through a series of lenses and apertures. The entire column and the sample chamber are evacuated and kept under high-vacuum (vacuum pressure below 10^{-5} mbar/10^{-8} atm) to prevent deterioration of the filament and to avoid interaction of the electron beam with other particles. Electromagnetic condenser lenses are used to focus and shape the electron beam and a final scanning coil is used to deflect the beam so that it can be scanned over a two-dimensional area. As a result of interaction of the incident electron with the sample (interaction volume), different types of signals arising from either electrons or X-rays are emitted (Fig. 2.10). Secondary electrons (SE), are ejected when the incident beam ionizes atoms in the sample. SE are of low energy and need to be accelerated before they can be detected with a scintillator coupled to a photomultiplier placed at a low angle to the sample. Variations in the topography of the sample modify the number of ejected secondary electrons and therefore, details of the sample topology can be obtained. Backscattered electrons (BSE) are higher energy electrons produced when the incident beam is reflected or back-scattered through elastic interaction with the atoms in the sample. They are detected by either solid state or scintillation detectors placed above the sample. The number of back-scattered electrons produced is controlled by the atomic number of atoms in the sample such that heavy atoms produce more flux and appear brighter on the electron image produced. Thus, the variation of BSE contrast in the sample image produced can be used to investigate the compositional variation within the sample.

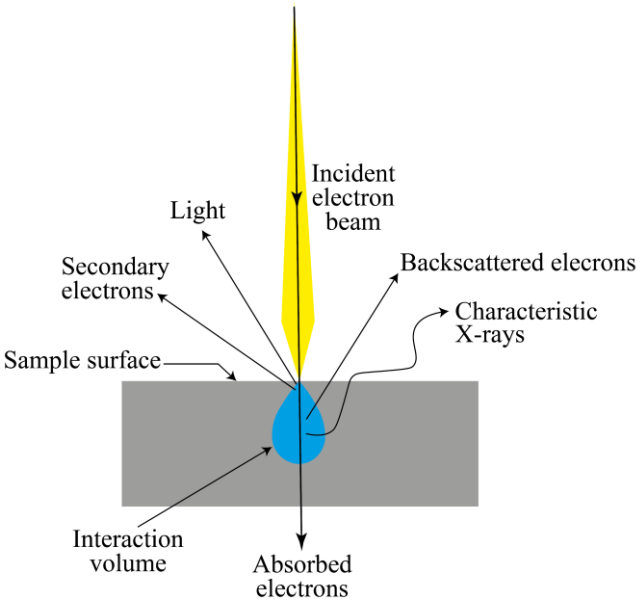

Figure 2.10: Incident electron beam and sample interactions in electron microscopy instruments.

Electrons of sample atoms can be removed through ionisation when the incident electron beam hits the sample. When the created vacancy is refilled by an electron in the outer shells of the same atom, the energy difference is released as a characteristic X-ray. The distinctive X-ray spectrum, containing lines characteristic to each element present in the sample, can be collected using an energy dispersive X-ray spectrometer (EDS), which provides qualitative, and semi-quantitative chemical analyses. For more precise quantitative chemical composition analyses, the electron probe micro analyser (EPMA) is used and basic instrumentation of which is closely related to the SEM.

2.3.2 Electron Probe Micro Analysis

The electron probe micro analyser (EPMA) is a commonly used technique for chemical composition analyses of micron-sized areas. The main components of the electron microprobe are shown in Figure 2.11. The electron gun and the alignment components of the electron beam are similar to that of the SEM. As described for the SEM, when incident electrons eject electrons from target atoms, characteristic X-rays with energies unique to the particular element are produced as electrons fall back from higher energy levels to fill the vacancies. A quantitative measurement of the proportion of a particular element present can be made by determining the intensity of a particular characteristic X-ray energy. A wavelength-dispersive spectrometer (WDS) is used for this purpose, which is comprised of two main components, the diffracting crystal and the X-ray detector. The diffracting crystal distinguishes X-rays with a specific wavelength when Bragg's law is satisfied and the resulting diffraction intensities are measured at a specific angle by the detector. The sample i.e. the X-ray source, the diffracting crystal and the detector lie on the circumference of an imaginary circle (Rowland circle). The crystal is curved with the same circumference and moving the crystal and the detector along the same Rowland circle ensures the same focusing geometry at the detector. Due to special limitations of the geometry, the full range of wavelength cannot be covered by a single diffracting crystal. Therefore, multiple diffracting crystals with differing d-spacings, e.g., LiF (lithium fluoride – $2d$=4.026 Å), PET (pentaerythritol – $2d$=8.742 Å) or TAP (thallium acid phthalate – $2d$=25.9 Å), are employed in several spectrometers that can operate in parallel. This has the further benefit that the intensities of different X-ray wavelengths, corresponding to different chemical elements, can be analysed simultaneously. The analyses presented in this

thesis were performed using the Jeol JXA 8200 equipped with 5-wavelength dispersive spectrometers (channels).

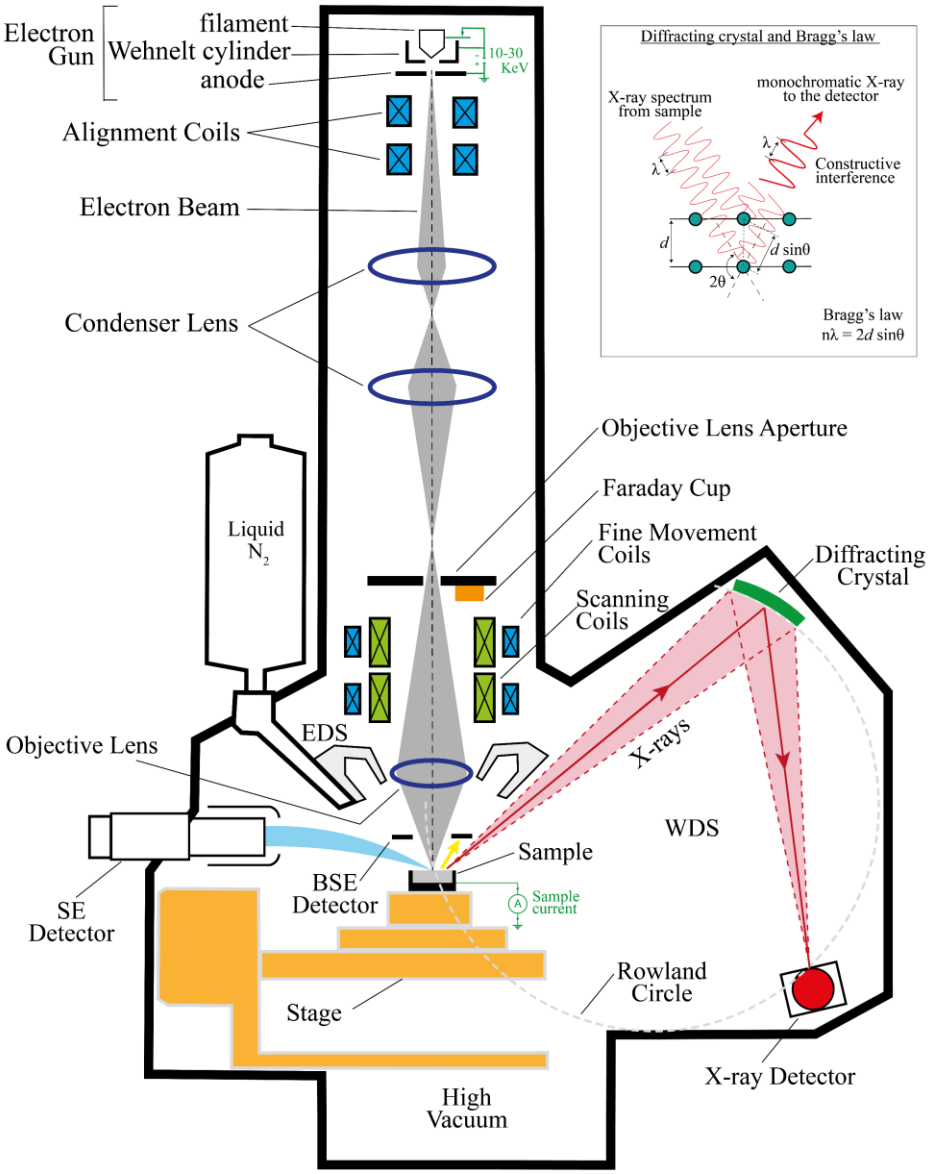

Figure 2.11: Configuration of an electron microprobe (source: UCLA.org). As shown in the inset, constructive interference in the diffracting crystal occurs at a determined 2θ angle, when X-rays with a particular wavelength satisfy Bragg's law.

As explained in the previous section (2.3.1), the X-ray spectrum containing characteristic lines for all elements present in the sample can be identified qualitatively from their wavelength. In order to make accurate quantitative measurements, the intensities of the emitted X-rays are compared with those emitted from standard reference materials containing known concentrations of the chemical element in question.

The main concept behind the EPMA is based on the X-ray intensity ratio of a given element between the sample and the standard, which is called the "*K* ratio".

$$K_M = \frac{I_M^{\text{sample}}}{I_M^{\text{standard}}} \tag{2.9}$$

where, *K* is the "*K* ratio" for element *M* and *I* is the X-ray intensity. The concept was first introduced by Raimond Castaing in 1951 and to a first approximation the composition *C* of element M of the unknown sample can be defined as,

$$C_M^{\text{sample}} \approx \frac{I_M^{\text{sample}}}{I_M^{\text{standard}}} \times C_M^{\text{standard}} \tag{2.10}$$

$$C_M^{\text{sample}} \approx K_M \times C_M^{\text{standard}} \tag{2.11}$$

Under this approximation, if we consider that the $C_M^{\text{standard}} = 1$, in the case of a pure element standard, the unknown sample concentration should be equal to the *K* ratio. But in reality, there is a difference between actual composition and the *K* ratio. This deviation is dependent on the sample matrix and therefore, a correction needs to be added to the raw X-ray intensity data which referred as the "matrix correction". The matrix corrections include, Z – atomic number effects, A – absorption effects, and F – fluorescence effects, and are collectively referred to as a ZAF correction (equation 2.12). Sometime later, the Phi-rho-Z correction was introduced, in which the Z and A are merged into one correction.

$$C_M^{\text{sample}} = K_M \times \frac{ZAF_M^{\text{sample}}}{ZAF_M^{\text{standard}}} \times C_M^{\text{standard}} \tag{2.12}$$

The correction is dependent on the proportions of each element and results in a shift in the concentration ratios that accounts for the different matrix effects. Therefore, technically the matrix correction cannot be calculated until the true composition is known, which itself depends on the true correction factors. The routine starts with a first approximation that the relative intensities measured are equal to the apparent mass concentrations. From this composition a set of ZAF correction factors are then calculated, which are then used to further re-calculate the concentrations. This iterative process terminates, when there is no further significant improvement in the concentrations.

This process is performed for all the elements until convergence is achieved. In general, the iteration is terminated either after ten-cycles or until the calculation error is reduced to within 0.001mass% (Jeol instrument manual, 2001). In order to obtain accurate, quantitative data, some further critical aspects need to be fulfilled, e.g. both the samples and standards need to be polished smoothly and have a similar thicknesses of carbon coating applied. The sample and standard material raw data (counts) must also be acquired in the same instrument and with the same operating conditions (acceleration voltage and beam current). Quality control of the obtained chemical compositions can be evaluated by analysing secondary standards in each session. This is particularly important for the analysis of light elements such as oxygen, where the oxygen-free background levels are checked by analysing secondary, oxygen-free standards. More details will be discussed about the oxygen analyses in its relevant chapter.

2.3.3 Transmission Electron Microscope

The transmission electron microscope (TEM) uses a beam of electrons transmitted through a thinned sample (< 200 nm) to form an image at the sub-micrometre scale. An electron beam is produced from a high energy electron gun, which operates with a potential difference typically in the range 300 – 400 kV. The main imaging components of the TEM are contained inside a vertical column under vacuum, with the electron gun at the top of the column. The electron beam is accelerated and focused on the sample through a system of condenser and objective lenses. Underneath the sample there are objective and imaging lenses together with a set up to record and view images including a fluorescent screen and CCD camera. Through different types of interaction between the electron beam and the sample, different applications of imaging, spectroscopy and electron diffraction can be performed to gather morphological, compositional and crystallographic information on the sample.

For phase identification of the experiments presented in the chapter 5 we used, bright field TEM images, high-angle annular dark field (HAADF) scanning TEM images, selected area electron diffraction (SAED), and energy dispersive X-ray (EDX) element maps, using a 200 kV analytical transmission electron microscope (ATEM, FEI Titan G2 80-200 S/TEM) equipped with an energy-dispersive X-ray spectrometer (EDXS, Bruker QUANTAX silicon drift detector).

Bright field images are the most commonly used in the TEM. The difference between dark and bright field images are based on the selection of electrons which are used to produce the image.

Depending on the inhomogeneities within the sample some areas may absorb or scatter incident electrons (e.g., crystalline materials), while other areas transmit the electrons (e.g., amorphous materials). In bright field image mode, an aperture is positioned in the back focal plane of the objective lens which allows only the direct beam to pass through. The sample-beam interaction results weakening of the direct beam, which lead to the formation of bright field image. The main contribution factors for the image formation are, the mass-thickness and diffraction contrast, where thick areas, heavy atom enriched areas and crystalline areas appear with dark contrast. In contrast, in the dark field images, the direct electrons are blocked while one or more diffracted beams are allowed to pass the aperture. Therefore, the crystalline features of the sample that scatter the beam can be observed in the resulting dark field image such as, crystal defects, stacking faults, dislocations etc. In the proximity of defects, certain lattice planes bend and can be made to satisfy the Bragg diffraction conditions by tilting the single crystal sample to an angle where undeformed lattice planes do not diffract, this causes an increase in the locally diffracted beam intensity, that illuminates the defect in the dark field image.

High-angle scattered electrons are used for HAADF scanning images, where the scattered angles are higher than the diffraction maxima and the angular range is ~50–200 mrad (Goodhew, 2001). These electrons are scattered elastically (no detectable energy change), mainly by interaction with atomic nuclei i.e. Rutherford scattering. Due to the low probability of electrons being scattered to a high-angle, the number of electrons is low. Nonetheless, the main advantage of this method of imaging is that the scattered electrons are strongly dependant on the atomic number of the nuclei and less sensitive to structure and orientation. Therefore, the local variation of HAADF intensity reflects changes in chemical composition, where the intensity is directly related to the average atomic number at the level of pixel resolution of the image.

Selected area electron diffraction (SAED) provides information about the structure of a restricted illuminated region of a sample being analysed. The spatial distribution of the electrons scattered by the sample lattice forms an electron diffraction pattern. Using a selected area diffraction (SAD) aperture to define the area from which the diffraction pattern is collected, typically 0.5-1 μm, phase identification can be performed based on the diffraction pattern. A single crystal will show a discrete set of diffraction spots in an SAED pattern, created through Bragg diffraction from atomic planes parallel to the incident electron beam, from which the symmetry and spacing of the particular lattice planes can be determined. A

polycrystalline sample produces numerous small spots making up rings. Any amorphous materials where there is no order of atoms would result in diffuse rings.

Energy dispersive X-ray (EDX) element maps is one of the useful tools for phase identification specially when combined with high resolution capability in the TEM. The highly energetic electron-sample interaction results in the emission of characteristic X-rays, as described in section 2.3.1. Measuring the energy (wavelength) of each characteristic X-ray is used to identify the elements present and the semi-quantitative information on the proportions of elements can be obtained from the intensities. EDX analyses at the qualitative level can be used to create an elemental distribution. EDX analyses have limitations in the detection of light elements, peak separation and peak to background ratio detection (Goodhew et al., 2001).

2.3.4 Mössbauer spectroscopy

Mössbauer spectroscopy is used in numerous fields to provide information on the chemical, structural and magnetic environments of specific isotopes in materials and is widely used to determine the oxidation and spin state of Fe. In the work presented within the chapter 5, Mössbauer spectroscopy was used to determine the phase proportions in an experimental sample containing quenched FeS melt and magnetite.

Mössbauer spectroscopy uses the recoil-free emission and absorption of gamma (γ) radiation by nuclei in a solid matrix (Mössbauer effect), which was first discovered by Rudolf Mössbauer (Mössbauer, 1958). A typical Mössbauer spectrometer consists of a source, absorber and a detector (Fig. 2.12). The current set up at BGI employs monochromatic γ radiation with an energy of 14.41 keV from a radioactive ^{57}Co point source with a half-life of 270 days (McCammon et al., 1997, 1998) and a specific activity of ≥2000 mCi/cm^2.

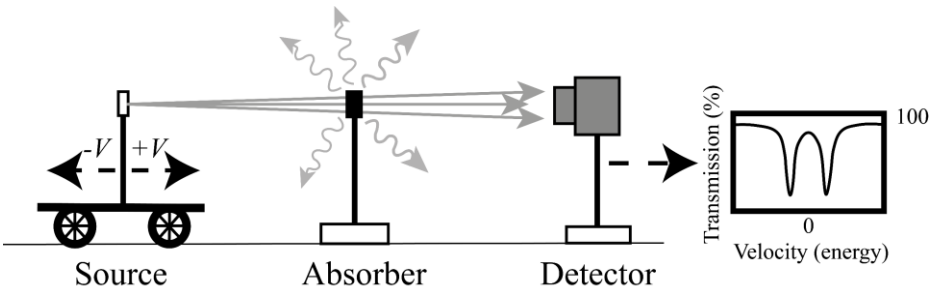

Figure 2.12: Schematic diagram of a Mössbauer spectrometer. Source: McCammon (2004).

By moving the source relative to the sample/absorber at different velocities, the energy of the monochromatic radiation is varied through the Doppler effect. The γ rays that pass through the sample without interacting are recorded by the detector as a count rate as a function of source velocity (mm/sec). The γ-rays are absorbed at velocities corresponding to resonant energy levels of the sample and are re-emitted in different directions so that they are not recorded by the detector. The resulting spectrum consists of dips in the counts, at specific energies that were absorbed. The subsequent spectrum as a function of energy (source velocity in mm/sec) can be used to probe hyperfine interactions in ^{57}Fe.

The hyperfine interactions between nuclei and electrons, and also magnetic fields, lead to sets of peaks (actually minima) in the Mössbauer spectrum, characteristics of which are sensitive to the electronic environment of the Fe nuclei in the sample investigated, i.e. number of electrons, coordinating anions and the symmetry of the site. The spectrum is deconvoluted by fitting sets of peaks, where each set corresponds to an iron nucleus in a specific environment. Characteristics of these peaks define three types of hyperfine parameters. The isomer or centre shift is a shift of the peak energy absorbed, relative to alpha-iron, and is sensitive to s electron density in the sample. It assumes values in well-defined ranges as a result of the coordination, valence state, and spin state of iron. Ferric iron has a lower isomer shift than ferrous iron due to the former having a greater s-electron density at the nucleus. The quadrupole splitting is a split of a single peak into a doublet, and reflects an asymmetry of valence electron charge distribution, as well as non-cubic symmetry in a crystalline lattice (McCammon, 2004). It is also sensitive to valence state, spin state, site symmetry, and coordination. Magnetic hyperfine splitting occurs due to interaction between the nucleus and either an external or internal magnetic field, which causes the nuclear energy levels to split into a sextet due to the so-called Zeeman-effect. Fitting a spectrum involves its deconvolution into its component Lorentzian doublets and sextets, which are each then assigned to iron in different oxidation and coordination states depending on their determined hyperfine parameters. In general, the relative site populations within a spectrum are determined by calculating ratios of respective peak areas. However, some correction may apply based on the influence of line shape, thickness effects and differing recoil-free fractions on relative areas (McCammon, 2004).

In this work, the resulting Mössbauer spectrum of an experimental sample consisting of FeS and magnetite were both fitted using two magnetic sextets. The intensity ratio of the two sextets was then used to calculate the abundance of iron in each phase. The fitting and analysis of the

collected Mössbauer spectra were performed using the MossA software package (Prescher et al., 2012).

2.3.5 Laser ablation inductively coupled plasma mass spectrometer (LA-ICP-MS)

The combination of laser ablation (LA) with an inductively coupled plasma mass spectrometer (ICP-MS) has been commonly used to perform major and trace multi-element analyses, including the determination of isotopic ratios, on solid or liquid materials with a high spatial resolution. A typical LA-ICP-MS system consists of three main components as illustrated in the Figure 2.13. The following description is relevant to the system installed at the BGI, which was used to perform the major and minor element analyses of experimental products, as described in Chapter 4 of this thesis.

During laser ablation analyses, a sample is placed in the ablation cell and a very small portion is vaporized using a pulsed high-energy laser beam. The laser ablation component of the device comprises a Coherent GeolasPro (USA) system equipped with an argon fluoride (ArF) excimer laser. The use of a shorter (193 nm) wavelength ultra-violet laser results in less thermal alteration of the sample and produces small particles (< 1µm) during the ablation process. The laser beam is shaped using optical lenses to have a "flat-top"-type homogeneous energy distribution, for more controlled ablation of the sample and correspondingly less elemental fractionation. The final size of the laser beam, which corresponds to the pit-size within the analysed sample, is controlled by a mask, which can be varied from 5 µm to 200 µm in diameter. The pulsed laser beam is focused on the sample through a modified petrographic microscope, which is also used to observe the sample. The sample can be monitored using a CCD (charge-coupled device) camera mounted on the microscope that can be used to precisely position the laser spot. The ablation behaviour (amount of material removed) depends on the energy of the laser, which can be regulated, and the nature of the sample analysed. The aerosol, which contains a mixture of excited atoms, ions, molecules and solid particles, is transported by helium gas flow (0.4 l/min) to the plasma of the ICP-MS. A small amount of H_2 (5 ml/min) is also added after the sample chamber to increase the signal sensitivity. The argon plasma torch is produced through inductive coupling. A high frequency electric current passed through an induction coil causes sustained ionization of argon gas passing through the coil due to collision excitation by argon ions and electrons accelerated by the varying magnetic field. The aerosol is ionized by the plasma at temperatures of up to 6000 K (Todolí, 2019). The ions are

electrostatically directed into a mass analyser, where they are separated according to their mass-to-charge (m/z) ratio and subsequently sent to a detector. The use of a helium and argon mixture (Ar is added after the ablation cell – see Figure 2.13) to carry the aerosol to the ICP, enhances the sensitivity and increases intensity and stability (Günther & Heinrich, 1999).

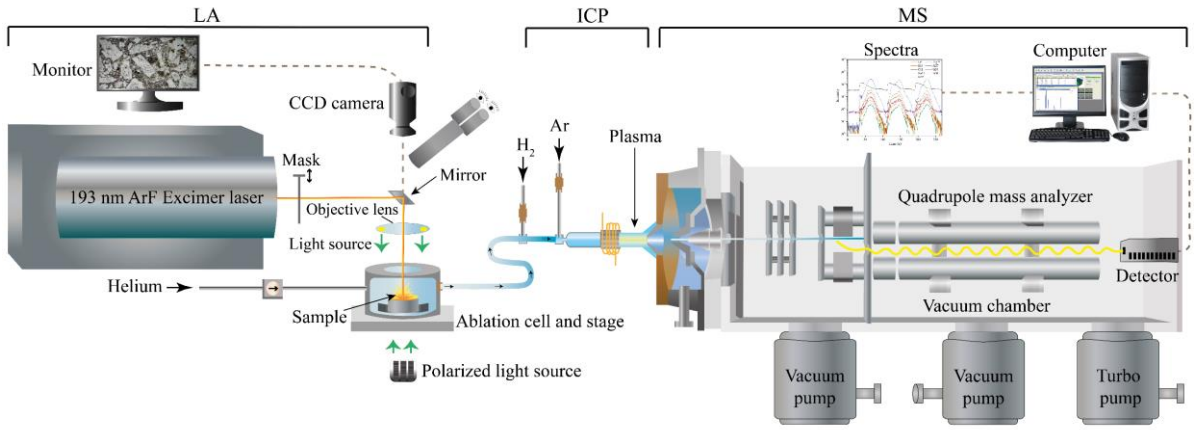

Figure 2.13: Main components of the laser ablation system combined with a quadrupole ICP-MS (modified after Abduriyim & Kitawaki, 2006). The laser beam is focused on the solid sample inside the ablation cell and the laser ablated aerosol is transported to the ICP-MS by a carrier gas (He). The aerosol is ionized in the ICP and the resulting ions are separated in the mass spectrometer according to their mass-to-charge ratio. The quadrupole mass analyser allows only specific isotopes to reach the detector depending on the applied voltage.

The laser ablation system at the BGI is attached to a Perkin Elmer ELAN DRC-e quadrupole ICP-MS (Canada). This most commonly used quadrupole mass analyser in ICP-MS systems, consists of four parallel metal rods set-up in a square. Each opposite pair of rods is supplied with both AC (alternating current) and DC (direct current) electrical potentials. By applying a certain combination of AC and DC potential values, only selected ions with a characteristic m/z ratio are allowed to pass through the rods to the detector. By regulating different combinations of AC, DC voltages, one can detect an array of different ions sequentially. In general, during an analysis of a sample, first the background is measured for about 30s - 40s and then sequential measurements of different isotopes are carried out.

The resulting spectrum, consisting of relative intensities of various isotopes, only provides a semi quantitative chemical analysis. A calibration must be carried out in order to obtain accurate chemical data. This is achieved firstly, by using an external standard of known composition. Measured signals for all elements of interest in the sample are compared with the

signals from the standard material, which contains independently determined concentrations of the same elements. In general, the use of external standards with a similar matrix to the analysed sample gives the best results, but in practice it is often not possible to find matrix matched standards for all the analysed samples (Abduriyim & Kitawaki, 2006). One of the most widely used external standard materials are NIST (National Institute of Standards and Technology) glasses, which have been used successfully for analysing major and trace elements in silicates and carbonates. There are other standards such as USGS GSE-1G, GeoReM (http://georem.mpch-mainz.gwdg.de/) that are also frequently used for analysis of geological materials. Commonly analysed isotopes include ^{7}Li, ^{11}B, ^{12}C, ^{23}Na, ^{25} Mg, ^{27}Al, ^{29}Si, ^{30}Si, ^{31}P, ^{35}Cl, ^{39} K, ^{43}Ca, ^{49}Ti, ^{53}Cr, ^{55}Mn, ^{57}Fe, ^{59}Co, ^{62}Ni, ^{65}Cu, ^{66}Zn, ^{85}Rb, ^{88}Sr, ^{89}Y, ^{90}Zr, ^{133}Cs, ^{137}Ba, ^{139}La, ^{140}Ce, ^{157}Gd, ^{175}Lu, ^{208}Pb, ^{232}Th, and ^{238}U, for which dwell times (the period of time over which the signal of each isotope is accumulated) of 10–20 ms are used. The two main interferences in ICP-MS analyses are caused by 1) formation of doubly-charged ions and 2) formation of polyatomic compounds after the ICP, most notably oxides. To monitor the abundances of these species, the formation rate of ThO and the doubly–charged ^{42}Ca ions are routinely quantified at 0.5–1.5 % and 0.15–0.30 % respectively, based on measurements on NIST SRM 610 glass (Jochum et al., 2011). The second step in obtaining the concentration of the analysed elements from the obtained isotope ratios, is to use an internal standard i.e. an element in the sample for which the absolute concentration is known independently. That concentration can be determined either by another analytical method, or by compositional constraints from the sample, e.g. in the case of silicates by summing up all the major + minor element oxides to 100 wt. %. In addition to the commonly used internal standard method, a new quantification method has been developed based on the carbon signal produced during the laser ablation of epoxy resin added to the sample before the analysis. Details of this new approach are described in the chapter 4.

Chapter 3

3 Thesis Synopsis

This chapter provide a brief overview of key findings in the projects presented in chapter 4, 5 and 6, following the scientific questions outlined in the introduction. Chapter 4 has been published as Abeykoon and Audétat (2022), and chapter 5 is under review for publication as Abeykoon et al. Chapter 5 of this thesis has been prepared for publication as Abeykoon et al.

3.1 Single-crystal diamond trap technique

The diamond trap (DT) method is a commonly used method to study the compositions fluids or small degree partial melts in high P-T piston-cylinder experiments (Kessel et al., 2004; Kushiro & Hirose, 1992; Ryabchikov et al., 1989; Tiraboschi et al., 2018). In the classical diamond trap method, fluid infiltrates into the pore space of a layer of diamond powder at high P-T, and it is assumed that any material present in this pore space after the quenching at the end of the experiments was dissolved in the fluid. The diamond trap is analyzed by LA-ICP-MS, typically by slowly moving the laser beam over the frozen sample. The signals are relatively constant for some elements, but highly variable for some other elements. Recently, significant discrepancies between mineral solubilities determined in classical DT experiments versus weight-loss experiments have been reported (Rustioni et al., 2021) (more details in the chapter 4). Therefore, an alternative experimental method, employing a single-crystal diamond trap (SCDT), was developed to quantify the composition of high P-T fluids. In the SCDT method the high P-T fluids are trapped in laser-drilled holes within single-crystal diamond plates and later analysed by LA-ICP-MS. In contrast to the classical DT method, where the fluid resides in a large, open network, in the SCDT technique the fluid is trapped in isolated and well-defined holes (Fig. 3.1-b). This permits a more rigorous testing of the data reproducibility and, therefore, to identify whether material was dissolved and re-precipitated during the high-P-T experiments. The experiments were prepared using two synthetic diamond plates placed on top of each other, such that the holes that were drilled into one of the plates were covered by the other plate. The whole stack was then loaded into a small Pt capsule, which subsequently was closed by welding. After tightly shrinking the Pt capsule around the

diamonds, and one end of the capsule was cut off with a razor blade to render the diamonds accessible to the fluid. This small, diamond-containing Pt capsule was then loaded together with H_2O and crushed minerals into a larger Pt capsule and then sealed (Fig. 3.1-a). The high P–T mineral solubility experiments were conducted in a piston-cylinder apparatus at 1.0 GPa and 700–900 °C in the quartz–H_2O and olivine–enstatite–H_2O systems. After the experiments the SCDT capsules were cut open at room temperatures using a razor blade, and the diamond plate in which the aqueous solution is trapped within the holes was recovered. The solution in the holes was allowed to evaporate, and then the solid residue was melted with a small amount of added $Li_2B_4O_7$ powder inside an 1 atm box furnace at 1000 °C for 10 min. This step was necessary to melt the precipitates within the holes and quench them in to a homogeneous glass, in order to obtain smooth LA-ICP-MS signals and minimizing element fractionation during analysis. Due to this melting procedure a partial loss of the internal standard elements (Rb, Cs) occurs, which are normally used for quantification of the LA-ICP-MS signals. We thus developed a new quantification procedure that does not require the use of any internal standard in the fluid but instead uses the carbon signal produced by epoxy filled into the holes before LA-ICP-MS analysis (Fig. 3.1-c).

Testing of this new method was performed using room P-T test experiments, by 1) filling the holes in the diamond plate with epoxy resins doped with known concentrations of chemicals, and 2) by filling the holes with known amounts of minerals that were subsequently melted. Tests were also performed through mineral solubility experiments at 1.0 GPa and 700–900 °C in the quartz–H_2O and olivine–enstatite–H_2O systems. These two systems were selected owing to the availability of reliable reference data based on weight-loss experiments (Manning, 1994; Newton & Manning, 2002). A total of 15 experiments, i.e., room P-T tests using fine grained Al_2O_3, TiO_2, $BaCO_3$, CaF_2, garnet, epidote, tourmaline, and high P-T runs in quartz–H_2O; olivine–enstatite–H_2O systems, conducted using the SCDT method resulted measured concentrations agree within 1-21% (avg. 13%) with the reference values. In contrast, four mineral solubility experiments that were performed at identical conditions with the classical diamond trap method returned concentrations that deviated by 7-56% (avg. 28%) from the reference values.

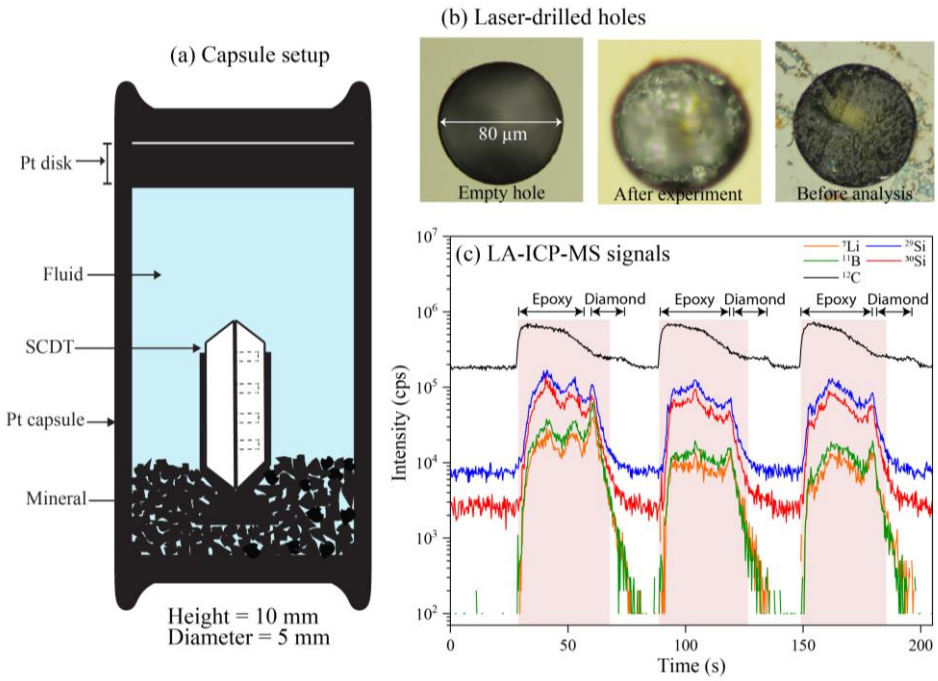

Figure 3.1: The single-crystal diamond trap technique. **(a)** Schematic drawing of the capsule setup, showing the inner capsule (SCDT) sitting on a bead of crushed minerals inside a fluid-filled Pt capsule. **(b)** Photomicrographs of laser-drilled holes in the diamond plates – from right to left: empty hole before the experiment, after a high P–T quartz solubility experiment, containing precipitated SiO_2 and after filling with epoxy resin, ready to be analysed with LA–ICP–MS. **(c)** LA–ICP–MS signals of three different holes containing on average 12.0 ± 1.6 wt. % of SiO_2 from a quartz + water experiment at 1.0 GPa, 900 °C. Shaded areas show the signal integration intervals of each hole.

A test performed by Rustioni et al. (2021) with an albite-doped classical diamond trap revealed strong element fractionation during the laser-ablation of the diamond + albite + ice/liquid H_2O mixture, resulting in a SiO_2/Al_2O_3 ratio that deviated by a factor of two compared to the albite starting material. A similar test performed using the new SCDT method (albite powder filled in to holes in diamonds, melted and analysed) show that the fractionation effect during LA-ICP-MS analyses is minimized (improved ablation behaviour compared to the classical DT method) indicated by the SiO_2, Na_2O and Al_2O_3 concentrations that agree within 2% with those of the albite starting material. However, the same test shows a gain of about 3.8 wt. % K_2O, which may indicate a possible mobility of alkalies during the melting step in the SCDT approach. On the other hand, the new method can be used at very high fluid/solid ratios, which promotes the growth of large crystals that are needed to measure fluid–mineral partition

coefficients for highly incompatible trace elements. Overall, we show that the new SCDT method is a viable alternative to the classical diamond trap technique.

3.2 Oxygen contents of sulphide melts in the Earth's upper mantle

The most common type of inclusion found in diamonds are Fe and Ni-rich sulphides (Pearson et al., 1998; Richardson et al., 2004; Sharp, 1966), which are also found as accessory phases in most upper mantle rocks (Alard et al., 2011; Aulbach et al., 2004b; Delpech et al., 2012). Some naturally occurring sulphide assemblages have oxygen contents that likely originated as a component dissolved in a sulphide melt (Bulanova et al., 1996; Davies et al., 1999; Davies et al., 2004b; Jacob et al., 2016). To determine what factors may control the O contents of sulphide melts in the upper mantle, and particularly under conditions where lithospheric diamonds may form, high-pressure (3 – 13 GPa) and high-temperature (1300 – 1819 °C) experiments were performed on sulphide melts in equilibrium with peridotite assemblages in mainly graphite capsules. In some experiments, 1-5 wt. % of Ir was added to allow the oxygen fugacity to be directly calculated using Fe-Ir alloy in run products. In most experiments carbonates (1-10 wt. %) were added as a flux to aid in the attainment of equilibrium between mineral phases and the sulphide melt. This also enabled oxygen fugacities to be estimated from the CO_2 contents of the resulting melts in equilibrium with the graphite capsules (Stagno et al., 2010). The FeO concentration in the silicate portion and the Ni concentration in the sulphide melt (added as either Ni metal or NiS) were varied. Factors were examined such as pressure, temperature, oxygen fugacity, silicate iron oxide content, sulphide Ni content and metal/sulphur ratio, to see how they influence the sulphide O contents and a preliminary model for describing sulphide melt O contents in equilibrium with upper mantle peridotite assemblages was formulated. Phases in the recovered experiments were analysed using the electron probe micro-analyser.

Sulphide melt O concentrations in the recovered experiments were in the range 0.2 to 3.7 wt. %, which is in qualitative agreement with the range reported for some sulphide inclusion assemblages in diamonds (Davies et al. 1999; 2004). The coexisting silicate assemblage comprised mainly olivine and orthopyroxene crystals with olivine Fe/(Fe+Mg) ratios in the range 0.04 - 0.25 depending on the FeO concentration of the starting material. The measured O contents do not correlate with fo_2, over the range from 1.8 to 4.0 log units below the FMQ buffer, which is a plausible range of conditions for diamond formation in the subcratonic lithosphere (Stagno et al., 2013). Ni-free experiments indicate that the sulphur to metal cation

ratio does not affect the sulphide melt O content. The presence of Ni in the sulphide appears to lower the O content, although all Ni-bearing experiments, including those in the literature, also have lower sulphur/metal ratios, which makes it hard to distinguish the effect of Ni alone on the O content of the melt and thus creates some uncertainty. The results show that the main factors controlling the sulphide melt O contents in addition to Ni are the FeO content of coexisting silicates, temperature and pressure.

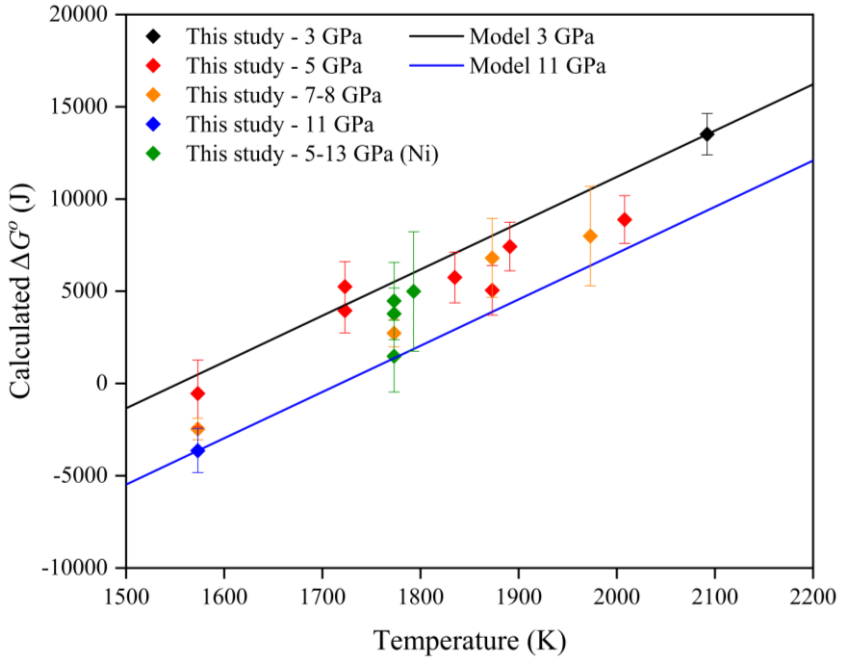

Figure 3.2: Calculated standard state Gibbs free energy, ΔG^{o}, of experiments plotted as a function of the temperature. The lines show the T dependency of the thermodynamic model at 3 and 11 GPa. The uncertainties are calculated from the 1σ errors on the sulphide FeO mole fraction determinations.

A preliminary thermodynamic model was developed based on the exchange of FeO between olivine, orthopyroxene and sulphide melt; Fe_2SiO_4 (olivine) = $FeSiO_3$ (orthopyroxene) + FeO (sulphide). The calculated standard state Gibbs free energy, ΔG^{o}, for this equilibrium shows a clear correlation with temperature and also pressure (Fig. 3.2). The observed decrease in the sulphide melt O content in Ni-bearing experiments was accounted for by considering a non-ideal FeO–NiS interaction parameter in the thermodynamic model.

Using this model, the O content of a sulphide melt in equilibrium with a typical peridotite assemblage is calculated, along a mantle adiabat between 100 and 200 km depth, to be in the range 0.4–0.6 wt. %. This relatively small variation in O content is mainly caused by changes

in the NiS content of the sulphide melt due to pressure-dependent changes in partitioning with the silicate assemblage (Zhang et al., 2018). The variation in the O content of the sulphide melt can be used as a geothermometer and using the thermodynamic model the experimental temperatures are reproduced to be within 74 K for Ni-free experiments and within 135 K for Ni- bearing samples. Using reported O contents of sulphide inclusions in diamonds from the Lac de Gras kimberlite field in the central Canadian Slave Craton (Davies et al., 1999; Davies et al., 2004b), a plausible average entrapment temperature of 1318±48 °C is calculated for peridotite affinity sulphides, which is in excellent agreement with the upper limit of temperature (1300 °C) calculated using garnet – clinopyroxene inclusions from the same diamonds (Davies et al. 2004). However, some of the peridotitic inclusions with high O concentrations, and also high Ni and Co contents, i.e. Ni/(Fe+Ni+Co)>0.6, result in unrealistically high calculated temperatures. This may be due to the sulphides having fractionally crystallised from melts that were no longer in equilibrium with mantle peridotite. However, clarifying the O contents of high Ni-bearing sulphides which do not also have low sulphur/metal ratios would help to clarify this.

Temperatures for eclogitic sulphide inclusions also found in diamonds from the same locality (Davies et al., 1999; Davies et al., 2004b) were calculated by using the same thermodynamic relation but determining fictive olivine and orthopyroxene iron contents from a typical eclogitic garnet iron content using published Fe-Mg partitioning data. These calculations give calculated entrapment temperatures of, 978 ±50 °C, which is far below the sulphide solidus temperature. It is possible that other components such as H_2 or H_2O may have lowered the sulphide solidus or that these inclusions were in equilibrium with assemblages with lower iron contents, i.e. more similar to peridotites, that would yield temperatures above the sulphide solidus.

Although the temperatures calculated for some sulphide assemblages from diamonds appear reasonable, this could simply be a coincidence and the inclusions themselves may contain O as a result of post entrapment (epigenetic) alteration or the O analyses might not be representative of the entire inclusion as a result of a heterogeneous distribution of phases. Although the estimation of temperatures from sulphide inclusion O contents is shown to be promising, the most important future direction would be to study more closely sulphide inclusions in diamonds, to determine if the O contents are produced through post entrapment alteration and to obtain O analyses that are clearly representative of the entire inclusion. Mössbauer spectroscopy is shown to be a useful non-destructive method for making qualitative

determinations of the O content of sulphide inclusions, by determining the magnetite/iron sulphide ratio, potentially while they are still trapped inside the host diamonds.

3.3 Deuterium content and site occupancy in iron sulphide at high-P-T

Previous high P and T experimental studies have indicated that iron sulphide minerals and melts may contain significant amounts of hydrogen (Piet et al., 2021; Shibazaki et al., 2011). As sulphides are accessory minerals in the upper mantle and the main inclusion found in diamonds, their capacity to host hydrogen may have an influence on their stability and thermodynamic properties, in addition to them being a potential host for hydrogen in the interior. As sulphide melts were likely involved in the formation of planetary cores, it would also be important to study whether hydrogen partitioned into such core-forming melts. Similar to many metal hydrides (Antonov et al., 1998; Fukai & Suzuki, 1986; Iizuka-Oku et al., 2017; Okuchi, 1997), however, hydrogen is likely lost from sulphide minerals and melts during quenching and can most likely not be recovered to ambient conditions for analysis. Measurements made at high pressures and temperatures are therefore necessary for determining sulphide hydrogen contents.

In situ time-of-flight (TOF) neutron powder diffraction measurements were performed to study the solubility of deuterium in FeS from 2.3 – 11.4 GPa, and temperatures from 787 – 1300 K. Deuterium solubility should be the same as hydrogen and was employed as a proxy to reduce the background in the neutron diffraction data, caused by incoherent scattering of hydrogen. Experiments were performed using a multi-anvil apparatus installed at the PLANET beamline of the J-PARC spallation neutron source. Compressed powders of FeS were employed, sandwiched between pellets of a ND_3BD_3, which releases D_2 on heating.

Time of flight neutron diffraction measurements were collected for up to 19 hours at high temperatures and pressures on the NiAs-structured $Fe_{(1-x)}S$ pyrrhotite polytype, referred to as FeS V (Urakawa et al., 2004). Unit-cell volumes measured for quenched FeS V during decompression to room pressure show an anomalous increase starting at approximately 6.5 GPa. This behaviour is likely due to a pressure-induced iron spin transition, i.e., from low-spin to high-spin on decompression (Kobayashi et al., 1997; Kusaba et al., 1998; Rueff et al., 1999; Urakawa et al., 2004).

The powder diffraction data were analysed by Rietveld refinement using the FeS V structural model (Brand & Briest, 1965; Shibazaki et al., 2011) with Fe at the *2a* $\{0, 0, 0\}$ and S at the *2c* $\{1/3, 2/3, 1/4\}$ Wyckoff positions of the $P6_3/mmc$ space group. Significant discrepancies were found between the observed high pressure and temperature patterns and those calculated with this model. A difference Fourier map was then generated that showed nuclear densities at two positions, that after refinement could be identified as the *6h*: $\{0.46(2), 0.54(2), 3/4\}$ and *4f*: $\{1/3, 2/3, 0.03(3)\}$ Wyckoff positions (Fig. 3.3). The partial deuterium occupancy in both sites could be refined with the latter showing a greater occupancy.

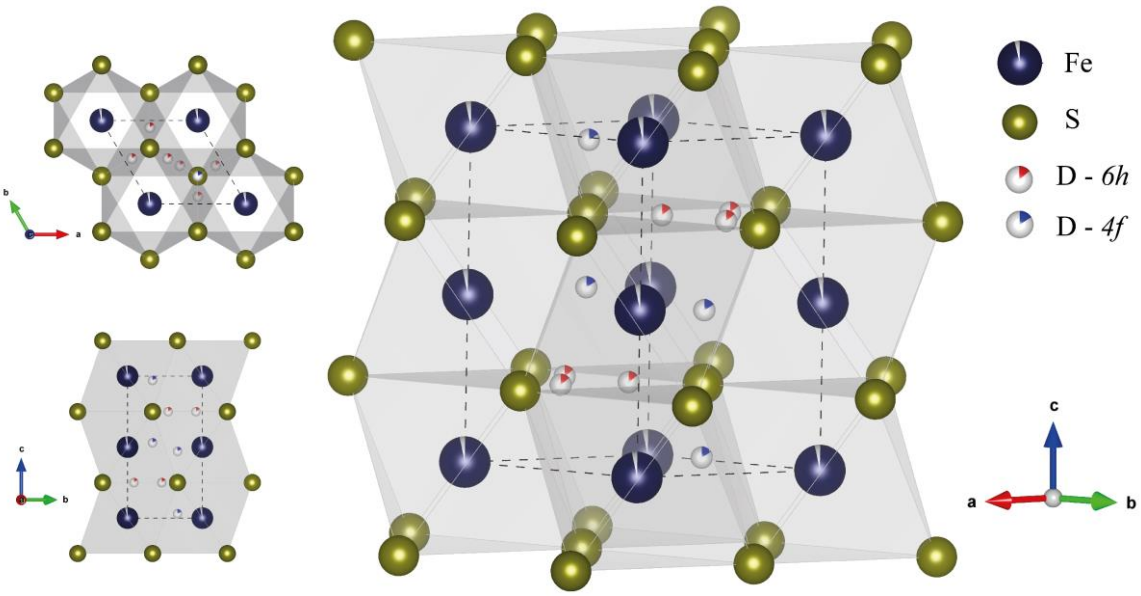

Figure 3.3: Final structural model of deuterated FeS V ($P6_3/mmc$, Z=2) at 6.9 GPa and 960 K. The dashed lines mark the unit-cell of FeS V, and section view along the *c*-axis and the *a*-axis of the structure are shown in the left side.

Expansion of the unit cell parameter of FeS V at 6.9 GPa and 960 K due to the incorporation of deuterium was monitored in a series of diffraction measurements and occurred over five hours. The extent of the unit cell expansion was confirmed by a deuterium-free experiment at nearly the same conditions that showed no comparable expansion. The difference in unit-cell volumes at these conditions is approximately 4.3% and the unit-cell volume expansion per deuterium atom, $\Delta V(D)$, is 1.53±0.16 $Å^3$, which is smaller compared to that previously reported for Fe-metal hydrides at similar conditions (2.21±0.04 $Å^3$–Machida et al., 2014). Our structural model shows that both deuterium positions are much closer to the S atoms than to the Fe atoms, which implies that S and D may be covalently bonded. If this is the case, it might explain the smaller $\Delta V(D)$ value compared to Fe-metal hydrides. Previously reported hydrogen contents

in FeS V, by Shibazaki et al. (2011) by means of X-ray diffraction volume relations are likely underestimated, due to the use of a ΔV(H) value estimated from results on hydrogenated Fe-metal phases. However, the general trend of increasing D occupancy with pressure observed by Shibazaki et al. (2011) agrees with the present study.

Refinements of all diffraction patterns collected indicate that the D content in FeS V increases with both pressure and temperature. The total deuterium content, X in FeSDx, increases from 0.148(10) at 2.3 GPa and 787 K to 1.25(5) at 9.7 GPa and 1300 K. A comparison between FeSDx and FeHx/FeDx shows that there is a general agreement in the magnitude of H/D occupancy with increasing pressure. The deuterium dissolved in FeS V at high-temperature is mainly lost during temperature quenching at high-pressure, as indicated by the decrease in unit-cell volumes of the quenched experiments.

A parallel multi-anvil experiment was conducted to determine the oxygen fugacity of samples exposed to the D_2 fluid produced by the breakdown of ND_3BD_3. In this experiment the FeS sample was replaced by a sample comprised of $Fe_{0.2}Mg_{0.8}O$ plus Fe-metal. From the extent of reduction of the oxide an oxygen fugacity of 1.2 ± 0.2 log units below the iron wüstite (IW) oxygen buffer was calculated. This is much higher than would be expected for a O-H fluid dominated by H_2 if ideal mixing of H_2–H_2O is assumed. However, a recent high pressure and temperature study (Bali et al., 2013) shows that non-ideal mixing can create immiscible H_2 and H_2O-rich fluids and if non-ideal mixing terms compatible with this previous study are assumed it is shown to be plausible to have a D_2 dominated fluid at IW-1.2 log units.

The experimentally determined deuterium contents in FeS V are fitted to a thermodynamic model assuming deuterium fugacities calculated for H_2 using the equation of state of Belonoshko & Saxena (1991), which allows the results to be extrapolated to different pressures, temperatures and oxygen fugacities. Although the model is somewhat simplified, it confirms that FeS V deuterium contents should drop to low levels on temperature quenching at high-pressure. It can also be used to show that at oxygen fugacities compatible with the base of the cratonic lithosphere, where diamond formation occurs, FeS V, which forms the main type of inclusion in diamonds, could contain significant amounts of hydrogen, in the range 1700–2700 ppm. It is proposed that loss of hydrogen from diamond hosted FeS V during decompression, could play a role in the development of the rosette like fracture systems often observed around sulphide inclusions in diamonds (Harris, 1972). Based on an average mantle sulphur content of 400 ppm (Gehlen, 1992), then at the base of the cratonic lithosphere a bulk mantle H_2 content

of 2–3 ppm could be hosted by mantle sulphides, at typical mantle oxygen fugacities for this depth. At greater depths lower oxygen fugacities and melting of FeS V may lead to higher hydrogen contents in sulphides.

References

Abduriyim, A., & Kitawaki, H. (2006). Applications of laser ablation-inductively coupled plasma-mass spectrometry (LA-ICP-MS) to gemology. *Gems and Gemology*, *42*(2), 98–118.

Abele, H., Dubbers, D., Häse, H., Klein, M., Knöpfler, A., Kreuz, M., Lauer, T., Märkisch, B., Mund, D., Nesvizhevsky, V., Petoukhov, A., Schmidt, C., Schumann, M., & Soldner, T. (2006). Characterization of a ballistic supermirror neutron guide. *Nuclear Instruments and Methods in Physics Research Section A: Accelerators, Spectrometers, Detectors and Associated Equipment*, *562*(1), 407–417.

Aerts, M., Hack, A. C., Reusser, E., & Ulmer, P. (2010). Assessment of the diamond-trap method for studying high-pressure fluids and melts and an improved freezing stage design for laser ablation ICP-MS analysis. *American Mineralogist*, *95*(10), 1523–1526.

Alard, O., Lorand, J. P., Reisberg, L., Bodinier, J. L., Dautria, J. M., & O'reilly, S. Y. (2011). Volatile-rich metasomatism in montferrier xenoliths (Southern France): Implications for the abundances of chalcophile and highly siderophile elements in the subcontinental mantle. *Journal of Petrology*, *52*(10), 2009–2045.

Albarède, F. (2009). Geochemistry: An Introduction. In *Cambridge University Press*. Cambridge University Press.

Alvaro, M., Angel, R. J., & Nestola, F. (2022). Inclusions in diamonds probe Earth's chemistry through deep time. *Communications Chemistry*, *5*(1), 5–7.

Angel, R. J., Alvaro, M., & Nestola, F. (2022). Crystallographic Methods for Non-destructive Characterization of Mineral Inclusions in Diamonds. *Reviews in Mineralogy & Geochemistry*, *88*, 257–306.

Angel, R. J., Nimis, P., Mazzucchelli, M. L., Alvaro, M., & Nestola, F. (2015). How large are departures from lithostatic pressure? Constraints from host-inclusion elasticity. *Journal of Metamorphic Geology*, *33*(8), 801–813.

Anzolini, C., Marquardt, K., Stagno, V., Bindi, L., Frost, D. J., Pearson, D. G., Harris, J. W., Hemley, R. J., & Nestola, F. (2020). Evidence for complex iron oxides in the deep mantle from FeNi(Cu) inclusions in superdeep diamond. *Proceedings of the National Academy of Sciences of the United States of America*, *117*(35), 2108–21094.

Aulbach, S., Griffin, W. L., Pearson, N. J., O'Reilly, S. Y., Kivi, K., & Doyle, B. J. (2004a). Mantle formation and evolution, Slave Craton: Constraints from HSE abundances and Re-Os isotope systematics of sulfide inclusions in mantle xenocrysts. *Chemical Geology*, *208*(1–4), 61–88.

Aulbach, S., Griffin, W. L., Pearson, N. J., O'Reilly, S. Y., Kivi, K., & Doyle, B. J. (2004b). Mantle formation and evolution, Slave Craton: Constraints from HSE abundances and Re-Os isotope systematics of sulfide inclusions in mantle xenocrysts. *Chemical Geology*, *208*(1–4), 61–88.

Aulbach, S., Stachel, T., Creaser, R. A., Heaman, L. M., Shirey, S. B., Muehlenbachs, K., Eichenberg, D., & Harris, J. W. (2009). Sulphide survival and diamond genesis during formation and evolution of Archaean subcontinental lithosphere : A comparison between the Slave and Kaapvaal cratons. *Lithos*, *112*, 747–757.

Aulbach, S., Stachel, T., Viljoen, K. S., Brey, G. P., & Harris, J. W. (2002). Eclogitic and websteritic diamond sources beneath the Limpopo Belt - Is slab-melting the link? *Contributions to Mineralogy and Petrology*, *143*(1), 56–70.

Ayers, J. C., & Watson, E. B. (1993). Rutile solubility and mobility in supercritical aqueous fluids. *Contributions to Mineralogy and Petrology*, *114*(3), 321–330.

Badro, J., Brodholt, J. P., Piet, H., Siebert, J., & Ryerson, F. J. (2015). Core formation and core composition from coupled geochemical and geophysical constraints. *Proceedings of the National Academy of Sciences of the United States of America*, *112*(40), 12310–12314.

Baker, M. B., & Stolper, E. M. (1994). Determining the composition of high-pressure mantle melts using diamond aggregates. *Geochimica et Cosmochimica Acta*, *58*(13), 2811–2827.

Ballhaus, C., Fonseca, R. O. C., Münker, C., Rohrbach, A., Nagel, T., Speelmanns, I. M., Helmy, H. M., Zirner, A., Vogel, A. K., & Heuser, A. (2017). The great sulfur depletion of Earth ' s mantle is not a signature of mantle – core equilibration. *Contributions to Mineralogy and Petrology*, *172*(68).

Bau, M., & Knittel, U. (1993). Significance of slab-derived partial melts and aqueous fluids for the genesis of tholeiitic and calc-alkaline island-arc basalts: Evidence from Mt. Arayat, Philippines. *Chemical Geology*, *105*(4), 233–251.

Bercovici, D. (2003). The generation of plate tectonics from mantle convection. *Earth and Planetary Science Letters*, *205*(3–4), 107–121.

Bernini, D., Audétat, A., Dolejš, D., & Keppler, H. (2013). Zircon solubility in aqueous fluids at high temperatures and pressures. *Geochimica et Cosmochimica Acta*, *119*, 178–187.

Beyer, C., & Frost, D. J. (2017). The depth of sub-lithospheric diamond formation and the redistribution of carbon in the deep mantle. *Earth and Planetary Science Letters*, *461*, 30–39.

Bézos, A., & Humler, E. (2005). The Fe3+/ΣFe ratios of MORB glasses and their implications for mantle melting. *Geochimica et Cosmochimica Acta*, *69*(3), 711–725.

Bickle, M. J. (1978). Heat loss from the Earth: a constraint on Archaean tectonics from the relation between geothermal gradients and the rate of plate production. *Earth and Planetary Science Letters*, *40*(3), 301–315.

Birch, F. (1952). Elasticity and Constitution of the Earth'S Interior*. *Journal of Geophysical Research*, *57*(2), 227–286.

Birch, F. (1964). Density and Composition of Mantle and Core. *Journal of Geophysical Research*, *69*(20), 4377–4388.

Blanchard, I., Abeykoon, S., Frost, D. J., & Rubie, D. C. (2021). Sulfur content at sulfide saturation of peridotitic melt at upper mantle conditions. *American Mineralogist*, *106*(11), 1835–1843.

Bohrson, W. A., & Clague, D. A. (1988). Origin of ultramafic xenoliths containing exsolved pyroxenes from Hualalai Volcano, Hawaii. *Contributions to Mineralogy and Petrology*, *100*(2), 139–155.

Boyd, F. R., & England, J. L. (1960). Apparatus for phase-equilibrium measurements at pressures up to 50 kilobars and temperatures up to 1750°C. *Journal of Geophysical*

Research, *65*(2), 741–748.

Boyd, F. R., & Gurney, J. J. (1986). Diamonds and the african lithosphere. *Science*, *232*(4749), 472–477.

Brand, V. P., & Briest, J. (1965). Das quasi-binäre System NiAs-Ni1,5Sn. *Zeitschrift Für Anorganische Und Allgemeine Chemie*, *337*(3–4), 209–213.

Bulanova, G. P. (1995). The formation of diamond. *Journal of Geochemical Exploration*, *53*(1–3), 1–23.

Bulanova, G. P., Griffin, W. L., Ryan, C. G., Shestakova, O. Y., & Barnes, S. J. (1996). Trace elements in sulfide inclusions from Yakutian diamonds. *Contributions to Mineralogy and Petrology*, *124*(2), 111–125.

Canil, D. (1997). Vanadium partitioning and the oxidation state of Archaean komatiite magmas. *Nature*, *389*(6653), 842–845.

Carlson, R. W., Garçon, M., O'Neil, J., Reimink, J., & Rizo, H. (2019). The nature of Earth's first crust. *Chemical Geology*, *530*, 119321.

Collins, W. J., Murphy, J. B., Johnson, T. E., & Huang, H. Q. (2020). Critical role of water in the formation of continental crust. *Nature Geoscience*, *13*(5), 331–338.

Cottrell, E., & Kelley, K. A. (2011). The oxidation state of Fe in MORB glasses and the oxygen fugacity of the upper mantle. *Earth and Planetary Science Letters*, *305*(3–4), 270–282.

Davies, R. M., Griffin, W. L., O'Reilly, S. Y., & Doyle, B. J. (2004). Mineral inclusions and geochemical characteristics of microdiamonds from the DO27, A154, A21, A418, DO18, DD17 and Ranch Lake kimberlites at Lac de Gras, Slave Craton, Canada. *Lithos*, *77*(1–4), 39–55.

Davies, R. M., Griffin, W. L., Pearson, N. J., Andrew, A. S., Doyle, B. J., & O'Reilly, S. Y. (1999). Diamonds from the deep: pipe DO27, Slave craton, Canada. In J. J. Gurney, J. L. Gurney, M. D. Pascoe, & S. H. Richardson (Eds.), *7th international Kimberlite conference* (pp. 148–155). Red Roof Designs.

Davis, F. A., Cottrell, E., Birner, S. K., Warren, J. M., & Lopez, O. G. (2017). Revisiting the electron microprobe method of spinel-olivine-orthopyroxene oxybarometry applied to spinel peridotites. *American Mineralogist*, *102*(2), 421–435.

Deines, P., & Harris, J. W. (1995). Sulfide inclusion chemistry and carbon isotopes of African diamonds. *Geochimica et Cosmochimica Acta*, *59*(15), 3173–3188.

Delano, J. W. (2001). Redox history of the Earth's interior since ~3900 Ma: Implications for prebiotic molecules. *Origins of Life and Evolution of the Biosphere*, *31*(4–5), 311–341.

Delpech, G., Lorand, J. P., Grégoire, M., Cottin, J. Y., & O'Reilly, S. Y. (2012). In-situ geochemistry of sulfides in highly metasomatized mantle xenoliths from Kerguelen, southern Indian Ocean. *Lithos*, *154*, 296–314.

Dziewonski, A. M., & Anderson, D. L. (1981). Preliminary reference Earth model*. *Physics of the Earth and Planetary Interiors*, *25*, 297–356.

Eggler, D. H., & Lorand, J. P. (1993). Mantle sulfide geobarometry. *Geochimica et Cosmochimica Acta*, *57*(10), 2213–2222.

Elkins-Tanton, L. T. (2008). Linked magma ocean solidification and atmospheric growth for Earth and Mars. *Earth and Planetary Science Letters*, *271*(1–4), 181–191.

Elkins-Tanton, L. T. (2012). Magma oceans in the inner solar system. *Annual Review of Earth and Planetary Sciences*, *40*, 113–139.

Fei, Y., Charles, T., Prewitt, C. T., Mao, H., & Bertka, C. M. (1995). Structure and Density of FeS at High Pressure and High Temperature and the internal Structure of Mars. *Science*, *268*, 1892–1894.

Fonseca, R. O. C., Campbell, I. H., O'Neill, H. S. C., & Fitzgerald, J. D. (2008). Oxygen solubility and speciation in sulphide-rich mattes. *Geochimica et Cosmochimica Acta*, *72*(11), 2619–2635.

Fountain, D. M., & Christensen, N. I. (1989). Composition of the continental crust and upper mantle: A review. *Geophysical Framework of the Continental United States*, *172*, 711–742.

Frost, D. J., & McCammon, C. A. (2008). The Redox State of earth's mantle. *Annual Review of Earth and Planetary Sciences*, *36*, 389–420.

Fukai, Y., Mori, K., & Shinomiya, H. (2003). The phase diagram and superabundant vacancy formation in Fe-H alloys under high hydrogen pressures. *Journal of Alloys and Compounds*, *348*(1–2), 105–109.

Gaetani, G. A., & Grove, T. L. (1998). The influence of water on melting of mantle peridotite. *Contributions to Mineralogy and Petrology*, *131*(4), 323–346.

Gaetani, G. A., & Grove, T. L. (1999). Wetting of mantle olivine by sulfide melt: Implications for Re/Os ratios in mantle peridotite and late-stage core formation. *Earth and Planetary Science Letters*, *169*(1–2), 147–163.

Gaillard, F., & Scaillet, B. (2009). The sulfur content of volcanic gases on Mars. *Earth and Planetary Science Letters*, *279*(1–2), 34–43.

Gaillard, F., & Scaillet, B. (2014). A theoretical framework for volcanic degassing chemistry in a comparative planetology perspective and implications for planetary atmospheres. *Earth and Planetary Science Letters*, *403*, 307–316.

Gehlen, K. von. (1992). Sulfur in the Earth's Mantle—A Review. *Early Organic Evolution*, 359–366.

Goodhew, P. (2001). General Introduction to Transmission Electron Microscopy (TEM). *Aberration-Corrected Analytical Transmission Electron Microscopy*, 1–19.

Goodhew, P. J., Humphreys, J., & Beanland, R. (2001). Electron Microscopy and Analysis. In *Taykor and Francis*.

Green, D. H. (1972). Magmatic activity as the major process in the chemical evolution of the earth's crust and mantle. In *Developments in Geotectonics* (Vol. 4, pp. 47–71). Elsevier.

Greenberg, R., Wacker, J. F., Hartmann, W. K., & Chapman, C. R. (1978). Planetesimals to planets: Numerical simulation of collisional evolution. *Icarus*, *35*(1), 1–26.

Griffin, W. L., O'Reilly, S. Y., Abe, N., Aulbach, S., Davies, R. M., Pearson, N. J., Doyle, B. J., & Kivi, K. (2003). The origin and evolution of Archean lithospheric mantle. *Precambrian Research*, *127*(1–3), 19–41.

Grove, T. L., Till, C. B., & Krawczynski, M. J. (2012). The role of H2O in subduction zone magmatism. *Annual Review of Earth and Planetary Sciences*, *40*, 413–439.

Gudmundsson, G., & Wood, B. J. (1995). Experimental tests of garnet peridotite oxygen barometry. *Contributions to Mineralogy and Petrology*, *119*(1), 56–67.

Gunn, S. C., & Luth, R. W. (2006). Carbonate reduction by Fe-S-O melts at high pressure and high temperature. *American Mineralogist*, *91*(7), 1110–1116.

Günther, D., & Heinrich, C. A. (1999). Enhanced sensitivity in laser ablation-ICP mass spectrometry using helium-argon mixtures as aerosol carrier. *Journal of Analytical Atomic Spectrometry*, *14*(9), 1363–1368.

Hacker, B. R., Kelemen, P. B., & Behn, M. D. (2015). Continental Lower Crust. *Annu. Rev. Earth Planet. Sci*, *43*, 167–205. https://doi.org/10.1146/annurev-earth-050212-124117

Haggerty, S. E. (1986). Diamond genesis in a multiply-constrained model. *Nature*, *320*, 34–38.

Haggerty, S. E., & Sautter, V. (1990). Ultradeep (Greater Than 300 Kilometers), Ultramafic Upper Mantle Xenoliths. *Science*, *248*(4958), 993–996.

Harris, J. W. (1972). Black material on mineral inclusions and in internal fracture planes in diamond. *Contributions to Mineralogy and Petrology*, *35*(1), 22–33.

Hart, S. R., & Zindler, A. (1986). In search of a bulk-Earth composition. *Chemical Geology*, *57*(3–4), 247–267.

Harvey, J., Warren, J. M., & Shirey, S. B. (2016). Mantle Sulfides and their Role in Re-Os and Pb Isotope Geochronology. *Reviews in Mineralogy & Geochemistry*, *81*, 579–649.

Heaman, L. M., & Pearson, D. G. (2010). Nature and evolution of the Slave Province subcontinental lithospheric mantle. *Canadian Journal of Earth Sciences*, *47*(4), 369–388.

Hirose, K., Wood, B., & Vočadlo, L. (2021). Light elements in the Earth's core. *Nature Reviews Earth and Environment*, *2*(9), 645–658.

Hirschmann, M. M. (2012). Magma ocean influence on early atmosphere mass and composition. *Earth and Planetary Science Letters*, *341–344*, 48–57.

Hopkins, M., Harrison, T. M., & Manning, C. E. (2008). Low heat flow inferred from >4 Gyr zircons suggests Hadean plate boundary interactions. *Nature*, *456*(7221), 493–496.

Huppert, H. E., Stephen, R., & Sparks, J. (1985). Cooling and contamination of mafic and ultramafic magmas during ascent through continental crust. *Earth and Planetary Science Letters*, *74*(4), 371–386.

Iizuka-Oku, R., Gotou, H., Shito, C., Fukuyama, K., Mori, Y., Hattori, T., Sano-Furukawa, A., Funakoshi, K. I., & Kagi, H. (2021). Behavior of light elements in iron-silicate-water-sulfur system during early Earth's evolution. *Scientific Reports*, *11*(1), 12632.

Iizuka-Oku, R., Yagi, T., Gotou, H., Okuchi, T., Hattori, T., & Sano-Furukawa, A. (2017). Hydrogenation of iron in the early stage of Earth's evolution. *Nature Communications*, *8*(14096).

Ikuta, D., Ohtani, E., Sano-Furukawa, A., Shibazaki, Y., Terasaki, H., Yuan, L., & Hattori, T. (2019). Interstitial hydrogen atoms in face-centered cubic iron in the Earth's core.

Scientific Reports, *9*(1), 1–8.

Jacob, D. E. (2004). Nature and origin of eclogite xenoliths from kimberlites. *Lithos*, *77*(1-4 SPEC. ISS.), 295–316.

Jacob, D. E., Piazolo, S., Schreiber, A., & Trimby, P. (2016). Redox-freezing and nucleation of diamond via magnetite formation in the Earth's mantle. *Nature Communications*, *7*, 11897.

Janse, A. J. A. (1991). Is Clifford's Rule still valid? Affirmative examples from around the world. *International Kimberlite Conference: Extended Abstracts*, *5*, 196–198.

Jarchow, C. M., & Thompson, G. A. (1989). The nature of the Mohorovicic discontinuity. *Annual Review of Earth and Planetary Sciences*, *17*, 475.

Jeol instrument manual. (2001). *Basic sotware/ Quantitative analysis program - XM-17330/27330* (pp. 1–101). Jeol.

Jochum, K. P., Weis, U., Stoll, B., Kuzmin, D., Yang, Q., Raczek, I., Jacob, D. E., Stracke, A., Birbaum, K., Frick, D. A., Günther, D., & Enzweiler, J. (2011). Determination of reference values for NIST SRM 610-617 glasses following ISO guidelines. *Geostandards and Geoanalytical Research*, *35*(4), 397–429.

Kaminsky, F. V. (2017). *The Earth's Lower Mantle*. Springer Geology.

Kantor, A. P., Kantor, I. Y., Kurnosov, A. V., Kuznetsov, A. Y., Dubrovinskaia, N. A., Krisch, M., Bossak, A. A., Dmitriev, V. P., Urusov, V. S., & Dubrovinsky, L. S. (2007). Sound wave velocities of fcc Fe-Ni alloy at high pressure and temperature by mean of inelastic X-ray scattering. *Physics of the Earth and Planetary Interiors*, *164*(1–2), 83–89.

Kasting, J. F. (1993). Earth's Early Atmosphere. *Science*, *259*(5097), 920–926.

Keppler, H. (2017). Fluids and trace element transport in subduction zones. *American Mineralogist*, *102*(1), 5–20.

Keppler, H., & Frost, D. J. (2015). Introduction to minerals under extreme conditions. *Mineral Behaviour at Extreme Conditions*, *7*, 1–30.

Kessel, R., Schmidt, M. W., Ulmer, P., & Pettke, T. (2005). Trace element signature of subduction-zone fluids, melts and supercritical liquids at 120-180 km depth. *Nature*, *437*(7059), 724–727.

Kessel, R., Ulmer, P., Pettke, T., Schmidt, M. W., & Thompson, A. B. (2004). A novel approach to determine high-pressure high-temperature fluid and melt compositions using diamond-trap experiments. *American Mineralogist*, *89*(7), 1078–1086.

Kobayashi, H., Sato, M., Kamimura, T., Sakai, M., Onodera, H., Kuroda, N., & Yamaguchi, Y. (1997). The effect of pressure on the electronic states of FeS and Fe7S8 studied by Mössbauer spectroscopy. *Journal of Physics Condensed Matter*, *9*(2), 515–527.

Kubik, E., Siebert, J., Blanchard, I., Agranier, A., Mahan, B., & Moynier, F. (2021). Earth's volatile accretion as told by Cd, Bi, Sb and Tl core–mantle distribution. *Geochimica et Cosmochimica Acta*, *306*, 263–280.

Kusaba, K., Syono, Y., Kikegawa, T., & Shimomura, O. (1998). High pressure and temperature behavior of FeS. *Journal of Physics and Chemistry of Solids*, *59*(6–7), 945–950.

Kushiro, I. (1990). Partial melting of mantle wedge and evolution of island arc crust. *Journal of Geophysical Research*, *95*(B10), 929–939.

Kushiro, I., & Hirose, K. (1992). Experimental determination of composition of melt formed by equilibrium partial melting of peridotite at high pressures using aggregates of diamond grains. *Proceedings of the Japan Academy*, 63–68.

Larson, A. C., & Dreele, R. B. Von. (2004). General Structure Analysis System (GSAS). *Los Alamos National Laboratory Report LAUR*, *86–748*.

Laurenz, V., Rubie, D. C., Frost, D. J., & Vogel, A. K. (2016). The importance of sulfur for the behavior of highly-siderophile elements during Earth's differentiation. *Geochimica et Cosmochimica Acta*, *194*, 123–138.

Lee, C. T. A., Brandon, A. D., & Norman, M. (2003). Vanadium in peridotites as a proxy for paleo-fO2 during partial melting: Prospects, limitations, and implications. *Geochimica et Cosmochimica Acta*, *67*(16), 3045–3064.

Leybourne, M. I., Van Wagoner, N., & Ayres, L. D. (1999). Partial melting of a refractory subducted slab in a Paleoproterozoic island arc: Implications for global chemical cycles. *Geology*, *27*(8), 731–734.

Li, C. H. (2022). Late veneer and the origins of volatiles of Earth. *Acta Geochimica*, *41*(4), 650–664.

Li, Y., Vočadlo, L., & Brodholt, J. P. (2018). The elastic properties of hcp-Fe alloys under the conditions of the Earth's inner core. *Earth and Planetary Science Letters*, *493*, 118–127.

Li, Z.-X. A., & Lee, C.-T. A. (2004). The constancy of upper mantle fO2 through time inferred from V/Sc ratios in basalts. *Earth and Planetary Science Letters*, *228*(3–4), 483–493.

Liebermann, R. C. (2011). Multi-anvil, high pressure apparatus: A half-century of development and progress. *High Pressure Research*, *31*(4), 493–532.

Lin, J. F., Struzhkin, V. V., Sturhahn, W., Huang, E., Zhao, J., Hu, M. Y., Alp, E. E., Mao, H. kwang, Boctor, N., & Hemley, R. J. (2003). Sound velocities of iron- nickel and iron-silicon alloys at high pressures. *Geophysical Research Letters*, *30*(21), 1–4.

Machida, A., Saitoh, H., Hattori, T., Sano-Furukawa, A., Funakoshi, K. ichi, Sato, T., Orimo, S. ichi, & Aoki, K. (2019). Hexagonal Close-packed Iron Hydride behind the Conventional Phase Diagram. *Scientific Reports*, *9*(1), 1–9.

Machida, A., Saitoh, H., Sugimoto, H., Hattori, T., Sano-Furukawa, A., Endo, N., Katayama, Y., Iizuka, R., Sato, T., Matsuo, M., Orimo, S. I., & Aoki, K. (2014). Site occupancy of interstitial deuterium atoms in face-centred cubic iron. *Nature Communications*, *5*, 2–5.

Manning, C. E. (1994). The solubility of quartz in H2O in the lower crust and upper mantle. *Geochimica et Cosmochimica Acta*, *58*(22), 4831–4839.

Mao, H.-K., & Hemley, R. J. (1996). Experimental studies of Earth's deep interior: accuracy and versatility of diamond-anvil cells. *Philosophical Transactions of the Royal Society of London. Series A: Mathematical, Physical and Engineering Sciences*, *354*(1711), 1315–1332.

Marx, P. C. (1972). Pyrrhotine and the origin of terrestrial diamonds. *Mineralogical Magazine*, *38*, 636–638.

Mavrogenes, J. A., & O'Neill, H. S. C. (1999). The relative effects of pressure, temperature and oxygen fugacity on the solubility of sulfide in mafic magmas. *Geochimica Et Cosmochimica Acta*, *63*(7/8), 1173–1180.

McCammon, C. A. (2004). Mössbauer spectroscopy : Applications. In *EMU Notes in Mineralogy* (Vol. 6, pp. 369–398).

McCammon, C. A., Chin, I. L., Gurney, J. J., & Mccallum, M. E. (1998). Ferric iron content of mineral inclusions in diamonds from George Creek , Colorado determined using Mössbauer spectroscopy. *Contributions to Mineralogy and Petrology*, *133*, 30–37.

McCammon, C. A., Mccammon, C., Hutchison, M., & Harris, J. (1997). Ferric Iron Content of Mineral Inclusions in Diamonds from São Luiz : A View into the Lower Ferric Iron Content of Mineral Inclusions in Diamonds from São Luiz : A View into the Lower Mantle. *Science*, *278*(5337), 434–436.

McCulloch, M. T., & Gamble, J. A. (1991). Geochemical and geodynamical constraints on subduction zone magmatism. *Earth and Planetary Science Letters*, *102*(3–4), 358–374.

McDonough, W. F. (2001). Chapter 1 The composition of the earth. *International Geophysics*, *76*, 3–23.

McDonough, W. F., & Sun, S. s. (1995). The composition of the Earth. *Chemical Geology*, *120*(3–4), 223–253.

Montagner, J. P., & Kennett, B. L. N. (1996). How to reconcile body-wave and normal-mode reference earth models. *Geophysical Journal International*, *125*(1), 229–248.

Morrison, R. A., Jackson, J. M., Sturhahn, W., Zhao, J., & Toellner, T. S. (2019). High pressure thermoelasticity and sound velocities of Fe-Ni-Si alloys. *Physics of the Earth and Planetary Interiors*, *294*, 106268.

Mössbauer, R. L. (1958). Kernresonanzfluoreszenz von Gammastrahlung in Ir191. *Zeitschrift Für Physik*, *151*(2), 124–143.

Mungall, J. E., & Brenan, J. M. (2003). Experimental evidence for the chalcophile behavior of the halogens. *Canadian Mineralogist*, *41*(1), 207–220.

Müntener, O., Ulmer, P., & Blundy, J. D. (2021). Superhydrous arc magmas in the Alpine context. *Elements*, *17*(1), 35–40.

Naldrett, A. J. (1969). A portion of the system Fe-S-O between 900 and 1080 °C and its application to sulfide ore magmas. *Journal of Petrology*, *10*(2), 171–201.

Navon, 0, Hutcheon, I. D., Rossman, G. R., & Wasserburg, G. J. (1988). Mantle-derived fluids in diamond micro-inclusions. *Nature*, *335*, 784–789.

Nestola, F. (2017). Inclusions in super-deep diamonds : windows on the very deep Earth. *Rendiconti Lincei*, *28*(4), 595–604.

Neumann, D. A. (2006). Neutron scattering and hydrogenous materials. *Materials Today*, *9*(1), 34–41.

Newton, R. C., & Manning, C. E. (2002). Solubility of enstatite + forsterite in H2O at deep crust/upper mantle conditions: 4 to 15 kbar and 700 to 900°C. *Geochimica et Cosmochimica Acta*, *66*(23), 4165–4176.

O'Neill, H. S. C. (1987). Quartz-fayalite-iron and quartz-fayalite-magnetite equilibria and the free energy of formation of fayalite (Fe2Si04) and magnetite (Fe304). *American Mineralogist*, *72*, 67–75.

O'Neill, H. S. C. (1991). The origin of the moon and the early history of the earth-A chemical model. Part 2: The Earth. *Geochimica et Cosmochimica Acta*, *55*, 1159–1172.

Okuchi, T. (1997). Hydrogen partitioning into molten iron at high pressure: Implications for earth's core. *Science*, *278*(5344), 1781–1784.

Palyanov, Y. N., Borzdov, Y. M., Bataleva, Y. V, Sokol, A. G., Palyanova, G. A., & Kupriyanov, I. N. (2007). Reducing role of sulfides and diamond formation in the Earth's mantle. *Earth and Planetary Science Letters*, *260*(1–2), 242–256.

Pearson, D. G., Brenker, F. E., Nestola, F., McNeill, J., Nasdala, L., Hutchison, M. T., Matveev, S., Mather, K., Silversmit, G., Schmitz, S., Vekemans, B., & Vincze, L. (2014). Hydrous mantle transition zone indicated by ringwoodite included within diamond. *Nature*, *507*(7491), 221–224.

Pearson, D. G., Shirey, S. B., Bulanova, G. P., Carlson, R. W., & Mllledge, H. J. (1999). Re-Os isotope measurements of single sulfide inclusions in a Siberian diamond and its nitrogen aggregation systematics. *Geochimica et Cosmochimica Acta*, *63*(5), 703–711.

Pearson, D. G., Shirey, S. B., Harris, J. W., & Carlson, R. W. (1998). Sulphide inclusions in diamonds from the Koffiefontein kimberlite, S Africa: Constraints on diamond ages and mantle Re-Os systematics. *Earth and Planetary Science Letters*, *160*(3–4), 311–326.

Pereira, M. D., Shaw, D. M., & Acosta, A. (2003). Mobile trace elements and fluid-dominated processes in the Ronda peridotite, southern Spain. *Canadian Mineralogist*, *41*(3), 617–625.

Perkins, D., Holland, T. J. B., & Newton, R. C. (1981). The Al2O3 Contents of Enstatite in Equilibrium with Garnet in the System MgO-Al203-SiO2 at 15-40 kbar and 900° - 1,600 °C. *Contributions to Mineralogy and Petrology*, *78*, 99–109.

Poirier, J. P. (1994). Light elements in the Earth's outer core: A critical review. *Physics of the Earth and Planetary Interiors*, *85*(3–4), 319–337.

Prescher, C., McCammon, C., & Dubrovinsky, L. (2012). MossA: A program for analyzing energy-domain Mössbauer spectra from conventional and synchrotron sources. *Journal of Applied Crystallography*, *45*(2), 329–331.

Reed, S. J. M. (2005). *Electron Microprobe Analysis and Scanning Electron Microscopy in Geology*. Cambridge University Press.

Richardson, S. H., Shirey, S. B., & Harris, J. W. (2004). Episodic diamond genesis at Jwaneng, Botswana, and implications for Kaapvaal craton evolution. *Lithos*, *77*(1–4), 143–154.

Ridley, W. I. (1998). Earth's mantle geochemistry. In *Geochemistry* (pp. 162–168). Springer Netherlands.

Rietveld, H. M. (1969). A profile refinement method for nuclear and magnetic structures. *Journal of Applied Crystallography*, *2*(2), 65–71.

Righter, K., Pando, K., Ross, D. K., Righter, M., & Lapen, T. J. (2019). Effect of silicon on activity coefficients of Bi , Cd , Sn , and Ag in liquid Fe-Si , and implications for

differentiation and core formation. *Meteoritics & Planetary Scienc*, *54*(6), 1379–1394.

Righter, K., Schönbächler, M., Pando, K., Ii, R. R., Righter, M., & Lapen, T. (2020). Ag isotopic and chalcophile element evolution of the terrestrial and martian mantles during accretion : New constraints from Bi and Ag metal-silicate partitioning. *Earth and Planetary Science Letters*, *552*.

Ringwood, A. E. (1977). Composition of the core and implications for origin of the earth. *Geochemical Journal*, *11*, 111–135.

Rubie, D. C. (1999). Characterising the sample environment in multianvil high-pressure experiments. *Phase Transitions*, *68*(3), 431–451.

Rubie, D. C., Laurenz, V., Jacobson, S. A., Morbidelli, A., Palme, H., Vogel, A. K., & Frost, D. J. (2016). Highly siderophile elements were stripped from the Earth's mantle by iron sulfide segregation. *Science*, *353*(6304), 1141–1144.

Rudnick, R. L., & Nyblade, Andre. A. (1999). The thickness and heat production of Archean lithosphere: constraints from xenolith thermobarometry and surface heat flow. *Mantle Petrology: Field Observations and High Pressure Experimentation: A Tribute to Francis R.(Joe) Boyd*, *6*(6), 3–12.

Rueff, J. P., Kao. C. C., Struzhkin, V. V., Badro, J., Shu, J., Hemley, R. J., & Mao, H. K. (1999). Pressure-induced high-spin to low-spin transition in FeS evidenced by X-ray emission spectroscopy. *Physical Review Letters*, *82*(16), 3284–3287.

Rüpke, L. H., Morgan, J. P., Hort, M., & Connolly, J. A. D. (2004). Serpentine and the subduction zone water cycle. *Earth and Planetary Science Letters*, *223*(1–2), 17–34.

Rustioni, G., Audétat, A., & Keppler, H. (2021). A systematic assessment of the diamond trap method for measuring fluid compositions in high-pressure experiments. *American Mineralogist*, *106*(1), 28–37.

Ryabchikov, I. ., Orlova, G. ., Kalenchuk, G. Y., Ganeyev, I. I., Udovkina, N. G., & Nosik, L. P. (1989). Reactions of spinel lherzolite with H2O-CO2 fluids at 20 kbar and 900 °C. *Geochemistry International*, *26*, 56–62.

Rychert, C. A., Harmon, N., Constable, S., & Wang, S. (2020). The Nature of the Lithosphere-Asthenosphere Boundary. *Journal of Geophysical Research: Solid Earth*, *125*(10).

Sakamaki, K., Takahashi, E., Nakajima, Y., Nishihara, Y., Funakoshi, K., Suzuki, T., & Fukai, Y. (2009). Melting phase relation of FeHx up to 20 GPa: Implication for the temperature of the Earth's core. *Physics of the Earth and Planetary Interiors*, *174*(1–4), 192–201.

Sano-Furukawa, A., Hattori, T., Arima, H., Yamada, A., Tabata, S., Kondo, M., Nakamura, A., Kagi, H., & Yagi, T. (2014). Six-axis multi-anvil press for high-pressure, high-temperature neutron diffraction experiments. *Review of Scientific Instruments*, *85*(11).

Scaillet, B., & Pichavant, M. (2003). Experimental constraints on volatile abundances in arc magmas and their implications for degassing processes. *Geological Society, London, Special Publications*, *213*(1), 23–52.

Schmidt, M. W., & Poli, S. (1998). Experimentally based water budgets for dehydrating slabs and consequences for arc magma generation. *Earth and Planetary Science Letters*, *163*(1–4), 361–379.

Sharp, W. E. (1966). Pyrrhotite: a common inclusion in South African diamonds. *Nature*, *211*(5047), 402–403.

Sharp, Z. D., McCubbin, F. M., & Shearer, C. K. (2013). A hydrogen-based oxidation mechanism relevant to planetary formation. *Earth and Planetary Science Letters*, *380*, 88–97.

Shibazaki, Y., Ohtani, E., Terasaki, H., Tateyama, R., Sakamaki, T., Tsuchiya, T., & Funakoshi, K. ichi. (2011). Effect of hydrogen on the melting temperature of FeS at high pressure: Implications for the core of Ganymede. *Earth and Planetary Science Letters*, *301*(1–2), 153–158.

Shushkanova, A. V, & Litvin, Y. A. (2008). Experimental evidence for liquid immiscibility in the model system CaCO3-pyrope-pyrrhotite at 7.0 GPa: The role of carbonatite and sulfide melts in diamond genesis. *Canadian Mineralogist*, *46*(4), 991–1005.

Silver, P. G., & Behn, M. D. (2008). Intermittent plate tectonics? *Science*, *319*(5859), 85–88.

Smith, E. M., Shirey, S. B., Richardson, S. H., Nestola, F., Bullock, E. S., Wang, J., & Wang, W. (2018). Blue boron-bearing diamonds from Earth's lower mantle. *Nature*, *560*(7716), 84–87.

Stachel, T., Brey, G. P., & Harris, J. W. (2005). Inclusions in Sublithospheric Diamonds: Glimpses of Deep Earth. *Elements*, *1*(2), 73–78.

Stachel, T., & Harris, J. W. (2009). Formation of diamond in the Earth's mantle. *Journal of Physics Condensed Matter*, *21*(364206).

Stagno, V., Ojwang, D., McCammon, C. A., & Frost, D. J. (2013). The oxidation state of the mantle and the extraction of carbon from Earth's interior. *Nature*, *493*(7430), 84–88.

Stalder, R., Ulmer, P., Thompson, A., & Günther, D. (2001). High pressure fluids in the system MgO–SiO2–H2O under upper mantle conditions. *Contributions to Mineralogy and Petrology*, *140*(5), 607–618.

Stein, S., & Stein, C. A. (1996). Thermo-mechanical evolution of oceanic lithosphere: Implications for the subduction process and deep earthquakes. *Washington DC American Geophysical Union Geophysical Monograph Series*, *96*, 1–17.

Stern, R. J. (2002). Subduction zones. *Reviews of Geophysics*, *40*(4), 3-1-3–38.

Stevenson, D. J. (2009). Earth formation and evolution. In D. J. Stevenson & G. Schubert (Eds.), *Evolution of the Earth: Treatise on Geophysics* (1st ed., pp. 1–11). Elsevier.

Syracuse, E. M., van Keken, P. E., Abers, G. A., Suetsugu, D., Bina, C., Inoue, T., Wiens, D., & Jellinek, M. (2010). The global range of subduction zone thermal models. *Physics of the Earth and Planetary Interiors*, *183*(1–2), 73–90.

Tappert, R., & Tappert, M. C. (2011). Diamonds in nature: A guide to rough diamonds. In *Diamonds in Nature: A Guide to Rough Diamonds*.

Taylor, L. A., & Liu, Y. (2009). Sulfide inclusions in diamonds: not monosulfide solid solution. *Russian Geology and Geophysics*, *50*(12), 1201–1211.

Terasaki, H., Frost, D. J., Rubie, D. C., & Langenhorst, F. (2005). The effect of oxygen and sulphur on the dihedral angle between Fe-O-S melt and silicate minerals at high pressure: Implications for Martian core formation. *Earth and Planetary Science Letters*, *232*(3–4),

379–392.

Tiraboschi, C., Tumiati, S., Sverjensky, D., Pettke, T., Ulmer, P., & Poli, S. (2018). Experimental determination of magnesia and silica solubilities in graphite-saturated and redox-buffered high-pressure COH fluids in equilibrium with forsterite + enstatite and magnesite + enstatite. *Contributions to Mineralogy and Petrology*, *173*(1), 1–17.

Todolí, J. L. (2019). Atomic mass spectrometry | inductively coupled plasma mass spectrometry. In *Encyclopedia of Analytical Science* (Third Edit, Vol. 1, Issue July 2018). Elsevier.

Trail, D., Watson, E. B., & Tailby, N. D. (2011). The oxidation state of Hadean magmas and implications for early Earth ' s atmosphere. *Nature*, *480*(7375), 79–82.

Tropper, P., & Manning, C. E. (2005). Very low solubility of rutile in H_2O at high pressure and temperature, and its implications for Ti mobility in subduction zones. *American Mineralogist*, *90*(2–3), 502–505.

Ulmer, P. (2001). Partial melting in the mantle wedge - The role of H_2O in the genesis of mantle-derived 'arc-related' magmas. *Physics of the Earth and Planetary Interiors*, *127*(1–4), 215–232.

Ulmer, P., & Trommsdorff, V. (1995). Serpentine stability to mantle depths and subduction-related magmatism. *Science*, *268*(5212), 858–861.

Umemoto, K., & Hirose, K. (2020). Chemical compositions of the outer core examined by first principles calculations. *Earth and Planetary Science Letters*, *531*(1997), 116009.

Urakawa, S., Someya, K., Terasaki, H., Katsura, T., Yokoshi, S., Funakoshi, K., Utsumi, W., Katayama, Y., Sueda, Y., & Irifune, T. (2004). Phase relationships and equations of state for FeS at high pressures temperatures and implications for the internal structure of Mars. *Physics of the Earth and Planetary Interiors*, *143*(1–2), 469–479.

Vanderhaeghe, O., Laurent, O., Gardien, V., Moyen, J. F., Gébelin, A., Chelle-Michou, C., Couzinié, S., Villaros, A., & Bellanger, M. (2020). Flow of partially molten crust controlling construction, growth and collapse of the Variscan orogenic belt: The geologic record of the French Massif Central. *BSGF - Earth Sciences Bulletin*, *191*, 0–56.

Varela, M. E., Bjerg, E. A., Clocchiatti, R., Labudia, C. H., & Kurat, G. (1997). Fluid inclusions in upper mantle xenoliths from Northern Patagonia, Argentina: Evidence for an upper mantle diapir. *Mineralogy and Petrology*, *60*(3–4), 145–164.

Vitale Brovarone, A., Martinez, I., Elmaleh, A., Compagnoni, R., Chaduteau, C., Ferraris, C., & Esteve, I. (2017). Massive production of abiotic methane during subduction evidenced in metamorphosed ophicarbonates from the Italian Alps. *Nature Communications*, *8*(February).

Wai, C. M., & Wasson, J. T. (1977). Nebular condensation of moderately volatile elements and their abundances in ordinary chondrites. *Earth and Planetary Science Letters*, *36*, 1–13.

Wasson, J. T., & Chou, C. (1974). Fractionation of moderately volatile elements in ordinary chondrites. *Meteoritics*, *9*(1), 69–84.

White, W. M., & Klein, E. M. (2014). Composition of the Oceanic Crust. In H. D. Holland & K. K. Turekian (Eds.), *Tretise on Geochemistry* (2nd ed.). Elsevier Ltd.

Wood, B. J., Walter, M. J., & Wade, J. (2006). Accretion of the Earth and segregation of its core. *Nature*, *441*(7095), 825–833.

Wykes, J. L., & Mavrogenes, J. A. (2005). Hydrous sulfide melting: Experimental evidence for the solubility of H2O in sulfide melts. *Economic Geology*, *100*(1), 157–164.

Xie, L., Chanyshev, A., Ishii, T., Bondar, D., Nishida, K., Chen, Z., Bhat, S., Farla, R., Higo, Y., Tange, Y., Su, X., Yan, B., Ma, S., & Katsura, T. (2021). Simultaneous generation of ultrahigh pressure and temperature to 50 GPa and 3300 K in multi-anvil apparatus. *Review of Scientific Instruments*, *92*(10).

Yefimova, E. S., Sobolev, N. V, & Pospelova, L. N. (1983). Sulfide inclusions in diamonds and specific features of their paragenesis. *Zapiski Vsesoyuznogo Mineralogicheskogo Obshchestva*, *112*(3), 300–310.

Zhang, H. L., Cottrell, E., Solheid, P. A., Kelley, K. A., & Hirschmann, M. M. (2018a). Determination of $Fe^{3+}/\Sigma Fe$ of XANES basaltic glass standards by Mössbauer spectroscopy and its application to the oxidation state of iron in MORB. *Chemical Geology*, *479*(January), 166–175.

Zhang, Z., & Hirschmann, M. M. (2012). Carbon Solubility of Molten Sulfides at 2-3 GPa. *American Geophysical Union, Fall Meeting 2012*, abstract id. DI13D-2454. https://ui.adsabs.harvard.edu/abs/2012AGUFMDI13D2454Z/abstract

Zhang, Z., & Hirschmann, M. M. (2016). Experimental constraints on mantle sulfide melting up to 8 GPa. *American Mineralogist*, *101*(1), 181–192.

Zhang, Z., von der Handt, A., & Hirschmann, M. M. (2018b). An experimental study of Fe–Ni exchange between sulfide melt and olivine at upper mantle conditions: implications for mantle sulfide compositions and phase equilibria. *Contributions to Mineralogy and Petrology*, *173*(19).

Zheng, Y. F. (2019). Subduction zone geochemistry. *Geoscience Frontiers*, *10*(4), 1223–1254.

List of Manuscripts and Statements of Author Contributions

- **Abeykoon, S.**, Audétat, A. The single-crystal diamond trap (SCDT): a new method to determine the composition of high-P–T fluids. *Contrib Mineral Petrol* **177**, 24 (2022). https://doi.org/10.1007/s00410-021-01882-6

S. Abeykoon performed high-pressure high-temperature experiments and prepared the samples for analysis with the help of A. Audétat. Sample analysis by LA–ICP–MS were carried out by A. Audétat and data processing was done by S. Abeykoon. Both authors discussed the results and a first draft of the manuscript, figures and graphs were prepared by S. Abeykoon. The manuscript was further refined by A. Audétat before the submission for publication.

- **Abeykoon, S.**, Laurenz, V., Frost, D. J., Miyajima, N., McCammon, C. An experimental investigation of factors controlling the oxygen content of sulphide melts in the Earth's upper mantle. *Contrib Mineral Petrol* **178**, 13 (2023). https://doi.org/10.1007/s00410-023-01992-3

S. Abeykoon carried out high-pressure and temperature experiments and sample analysis by EPMA and SEM, with the help of V. Laurenz. A Mössbauer spectroscopy measurement and fitting was done by C. McCammon and TEM work by N. Miyajima. Thermodynamic modelling was developed by D. J. Frost. All co-authors discussed the results and a first draft of the manuscript was prepared by S. Abeykoon followed by further improvements by D. J. Frost, and all co-authors before the submission for publication.

- **Abeykoon, S.,** Howard, C., Dominijanni, S., Eberhard, L., Kurnosov, A., Frost, D. J., Boffa–Ballaran, T., Terasaki, H., Sakamaki, T., Suzuki, A., Ohtani, E., Sano-Furukawa, A., Abe, J. Deuterium content and site occupancy in iron sulphide at high-pressure and high-temperature using *in situ* neutron diffraction experiments. Under review in *J. Geophys. Res. Solid Earth.*

The project proposal to the PLANET beamline was conceived by D.J. Frost with advice from E. Ohtani, T. Sakamaki and H. Terasaki. High-pressure, high-temperature *in situ* experiments were prepared and performed by S. Abeykoon, S. Dominijanni, L. Eberhard, and C. Howard

with the support of A. Sano-Furukawa and J. Abe. During the experiments D. J. Frost, H. Terasaki, T. Sakamaki and A. Suzuki made preliminary assessments of the collected data. Rietveld refinements of the neutron diffraction data and calculations were performed by S. Abeykoon with the assistance of T. Boffa-Ballaran, A. Kurnosov, C. Howard, A. Sano-Furukawa and S. Dominijanni. Thermodynamic modelling was conceived by D. J. Frost. The first draft of the manuscript, with figures and tables, was prepared by S. Abeykoon. The manuscript was further improved by D. J. Frost, T. Boffa-Ballaran, A. Kurnosov and C. Howard.

Chapter 4

The single-crystal diamond trap (SCDT): a new method to determine the composition of high-P–T fluids

Sumith Abeykoon[1]✉, Andreas Audétat[1]

[1]Bayerisches Geoinstitut, University of Bayreuth, 95440 Bayreuth, Germany
✉ sumith.abeykoon@uni-bayreuth.de

This chapter has been published as:

Abeykoon, S., Audétat, A. The single-crystal diamond trap (SCDT): a new method to determine the composition of high-P–T fluids. *Contrib Mineral Petrol* **177**, 24 (2022). https://doi.org/10.1007/s00410-021-01882-6

Abstract

In view of recently reported discrepancies in mineral solubility results obtained with the classical diamond trap method, an alternative approach to quantify the composition of high P–T fluids was developed. In this approach the high P–T fluids are trapped in laser-drilled holes within single-crystal diamond plates and subsequently analyzed by LA–ICP–MS using the same pit size as the one that was used to drill the holes, which allows more rigorous testing of the data reproducibility than in the case of the classical diamond trap, where the fluid resides in a large, open network. To reduce the spikiness of the LA–ICP–MS signals and minimize element fractionation, the aqueous solution within the holes was allowed to evaporate, and the solid residue was melted to a glass. Because this results in the partial loss of the internal standard elements that are usually used for quantifying the LA–ICP–MS signals we developed a new quantification procedure that works without any internal standard in the fluid but instead uses the carbon signal produced by the epoxy that was filled into the holes after melting the precipitates. The new method was first tested on holes filled with epoxy resins doped with known amounts of chemicals, then on holes filled with known amounts of minerals that were subsequently melted, and finally on real high P–T mineral solubility experiments at 1.0 GPa and 700–900 °C in the quartz–H_2O and olivine–enstatite–H_2O systems, for which reliable

reference data exist. In all 15 experiments the measured concentrations agree within 1–21% (avg. 13%) with the reference values. In contrast, four mineral solubility experiments that were performed at identical conditions with the classical diamond trap method returned concentrations that deviated by 7–56% (avg. 28%) from the reference value. Furthermore, a strong fractionation effect that has been observed during the ablation of albite + H_2O in a classical diamond trap is efficiently prevented in our single-crystal diamond trap (SCDT) approach. On the downside, we observe significant mobility of alkalies during the melting step in our approach.

4.1 Introduction

Various experimental techniques have been used to study the composition of aqueous fluids at ≥1 GPa and ≥500 °C, including: (i) measuring the weight of single crystals before and after the experiment (e.g., quartz solubility in H_2O; Manning 1994), (ii) constraining the fluid composition via phase relations (e.g., enstatite–forsterite–H_2O system; Zhang and Frantz 2000), (iii) in-situ observation of dissolving minerals in the hydrothermal diamond anvil cell (e.g., rutile solubility in water; Audétat and Keppler 2005), (iv) trapping fluids in the form of synthetic fluid inclusions and subsequently analyzing them by laser ablation–inductively coupled plasma–mass spectrometry (LA–ICP–MS), which allows only elements that are not abundant in the host mineral to be quantified (e.g., Spandler et al. 2007), (v) in-situ synchrotron–radiation XRF in the hydrothermal diamond anvil cell (e.g., Schmidt et al. 2007), and (vi) the diamond trap method (e.g., Kessel et al. 2004). Of those, the diamond trap method (in the following called "classical diamond trap method") is the most versatile method, because it can be applied in compositionally complex systems, has virtually no limitation with respect to accessible P–T conditions, and has also very little limitation with respect to the type and concentration of measurable elements. The diamond trap method was originally developed by Ryabchikov et al. (1989) and was subsequently modified and improved by Kushiro and Hirose (1992), Baker and Stolper (1994), Stalder et al. (2001) and Kessel et al. (2004). This method employs a layer of diamond powder in the experimental capsule, into which fluids/melts infiltrate during the experiment and precipitate dissolved solids during quenching. The diamond layer can subsequently be analyzed by bulk techniques, or–more commonly–by means of in situ LA–ICP–MS analysis. The latter approach has been substantially improved by introducing the “freezing technique" (Kessel et al. 2004), in which the sample capsule is kept frozen during the opening and the subsequent analysis by LA–ICP–MS. This approach

avoids spatial fractionation of elements that remain dissolved in the fluid after quenching, such as Cs that is commonly used as internal standard for LA–ICP–MS signal quantification.
A basic assumption behind the diamond trap experiments is that everything analyzed within the diamond trap was dissolved in the fluid at the time of quenching and was in equilibrium with the solid assemblage/mineral. However, this assumption may not always be valid. For example, if the solid starting material is added in the form of a silicate glass, then the aqueous solution will likely get supersaturated during heating and precipitate crystalline phases that may remain in the system during the whole experiment. This phenomenon was documented by in-situ observation of the dissolution of a piece of andesitic glass in water during heating in a diamond anvil cell (Keppler 2017). Minerals that precipitate within the diamond trap during this process will be misinterpreted as dissolved fluid components. Minerals can also form within the diamond trap in response to temperature gradients if the temperature of the diamond trap is lower than that of the surrounding material. High field strength elements (HFSE; Nb, Ta, Zr, Hf, Ti) oxides such as rutile and zircon appear to be particularly sensitive to this effect (Tropper and Manning 2005; Bernini et al. 2013; Rustioni et al. 2021).

Commonly, the LA–ICP–MS signal obtained during slow movement of a laser beam of 50–80 µm size over a frozen diamond trap is relatively constant for some elements, but highly variable for some other elements, such as high field strength elements, for example. The frequency of the signal peaks of the latter elements suggests that local accumulations occur at the scale of 100–200 µm, which is relatively large compared to the grain size of the diamond trap (15–25 µm). This observation raises the question whether these local accumulations represent de-localized solute precipitates that formed during the quench, or whether they reflect material that precipitated already during the run and thus should not be included in the signal interval.
Another potential problem of the classical diamond trap method is elemental fractionation during LA–ICP–MS analysis. Rustioni et al. (2021) analyzed a frozen diamond trap that contained small albite grains and H_2O (and was pressurized, but was never heated) and obtained SiO_2/Al_2O_3 ratios that were about twice as high as the theoretical value of albite. In contrast, analyses on a larger piece of the same albite starting material that was analyzed on the same day with the same laser settings returned the correct SiO_2/Al_2O_3 ratio. This suggests that in certain mineral–fluid systems severe element fractionation may occur during LA–ICP–MS analysis.

We are aware of only three studies that performed accuracy tests on the diamond trap technique. Aerts et al. (2010) report an accuracy of 3% and a precision of 5% based on a single quartz

solubility experiment in H_2O performed at 0.88 GPa and 700 °C, using the solubility data of Manning (1994) as reference. Tiraboschi et al. (2018) report an accuracy of 5% for a single forsterite+enstatite solubility experiment in H_2O conducted at 1.0 GPa and 800 °C, using the solubility data of Newton and Manning (2002) as reference. In contrast, in a more extensive test series based on the solubilities of quartz, forsterite+enstatite, corundum, rutile in H_2O, and supercritical H_2O–albite fluids at 700–800 °C and 1.0–2.0 GPa, Rustioni et al. (2021) found deviations from reference values ranging from 3% to more than a factor of two, even among identical experiments. The reason for the large discrepancies in some experiments is not clear, but the data suggest that the accuracy of the method can vary dramatically from experiment to experiment, and potentially also from laboratory to laboratory, if, e.g., the temperature distribution or pressure correction in piston cylinder experiments varies. Therefore, it is important to test alternative approaches that may lead to more reproducible results.

Here we present a new method that aims at minimizing the potential problem of mineral precipitation within the diamond trap during the experiment by trapping the high P–T fluid in pre-drilled holes in single diamond crystals, which allows more rigorous testing of the reproducibility of the results than analyzing small parts of the open pore network in a classical diamond trap. Furthermore, with the new method we try to reduce elemental fractionation effects arising from the ablation of spatially unconfined liquid+solid mixtures by letting the liquid to evaporate from the pre-drilled holes and then melting the residue to a glass.

4.2 Methods

For our single-crystal diamond trap (SCDT) method we used polished, synthetic diamond plates of about 2.5 mm side length and 0.8–1.0 mm height purchased from Chenguang Machinery & Electric Equipment Co. Ltd., China (~10 € per piece). Two such diamond plates were used in each experiment. Into one of them we drilled 9–16 holes (80 µm diameter; 50–70 µm depth) using a 193 nm ArF Excimer laser that provides a fluence of ~25 J/cm^2 at the sample surface (Fig. 4.1a). The two diamond plates were then placed on top of each other such that the holes that were drilled into one of the plates were covered by the other plate, and the whole stack was then loaded into a small Pt capsule of 3.5 mm O.D., 3.2 mm I.D. and 5.4 mm length. The Pt capsule was then welded shut, placed into a cold-seal pressure vessel filled with H_2O, and then pressurized to 0.15–0.20 GPa, such that the Pt capsule shrunk tightly around the diamond plates (Fig. 4.1b). This step is necessary to keep the diamonds tightly together during the subsequent high P–T experiment. After removing the capsule from the vessel it was dried,

and then one end of the capsule was cut off with a razor blade to render the diamonds accessible to the fluid. This small, diamond-containing Pt capsule was then loaded together with H_2O and crushed minerals (63–160 µm fraction) into a larger Pt capsule of 5.0 mm O.D., 4.6 mm I.D. and 10 mm length that was sealed using the method described in Audétat and Bali (2010) (Fig. 4.1b, c). In a few classical diamond trap experiments that were conducted for comparison purpose, the same mineral starting materials were loaded together with a central layer of diamond powder (1:1 ratio of 10–20 µm and 40–60 µm grain size) and aqueous solution containing 200 µg/g of Cs and Rb into Pt capsules of the same size. The fluid was added to these capsules in several steps following the approach of Rustioni et al. (2021). Finished capsules were checked for leaks by measuring their weights before and after placing them for 2–3 hours in a drying oven at 150 °C.

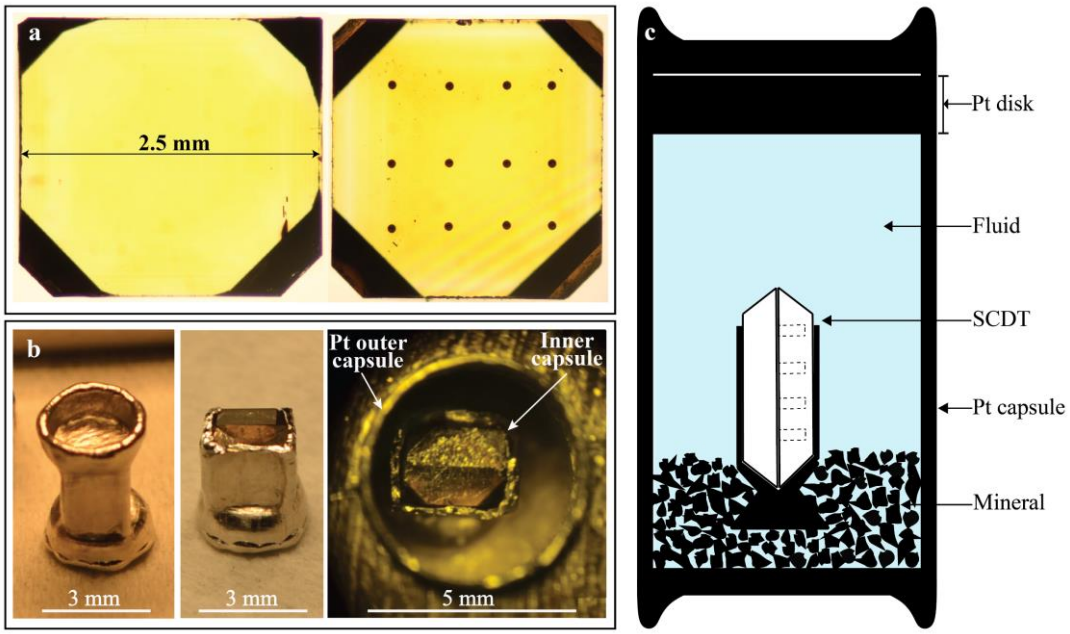

Figure 4.1: (a) Photomicrographs of an undrilled (left) and a drilled (right) diamond plate. The holes measure ~80 µm in diameter and are ~50–70 µm deep; **(b)** sealed and shrunk inner capsule (left); one-side cut-open inner capsule (middle); and an inner capsule sitting inside a platinum outer capsule before filling with fluid; **(c)** a schematic drawing of the capsule setup, showing the cut-open inner capsule sitting on a bead of crushed minerals. The Pt disk was used to seal the fully fluid-filled Pt capsule of 5.0 mm diameter and 10.0 mm height.

4.2.1 Piston cylinder experiments

High pressure and high-temperature experiments were conducted in an end-loaded piston cylinder apparatus using ½ inch NaCl–MgO assemblies with a stepped graphite furnace. A constant friction correction of 0.12 GPa was applied based on calibrations involving the quartz-coesite transition at 790 °C and 2.93 GPa and the densities of synthetic fluid inclusions trapped 800 °C and 0.37–9.58 GPa in quartz and corundum single crystals. Temperatures were measured using type S (Pt/Pt–Rh) thermocouples. After pressurization close to the target value, the sample was heated at a rate of 100 °C/min to the target temperature. In a final step, pressure was raised to the target temperature (i.e., hot piston in). Run durations varied depending on the studied system (Table 4.1), and the experiments were quenched by switching off the electrical power, which resulted in quenching to below 200 °C within 4–6 seconds. Once the sample had cooled to room temperature, the remaining pressure was released within 15–30 min. The recovered capsules were checked for leaks by visual observation under the binocular and by checking their weights in intervals of several minutes. About one out of six capsules leaked during the experiment. Intact capsules were immediately opened and prepared in the case of the SCDT experiments, whereas in the case of the classical diamond trap experiments they were kept in a freezer at -20 °C until the day of the LA–ICP–MS analysis.

4.2.2 Capsule opening and sample preparation

SCDT capsules were cut open at room temperatures using a razor blade. Once opened, part of the liquid residing in the capsule was sucked up with a pipette. The inner capsule was then removed, and the diamond stack was recovered by cutting off some Pt wrapped around them, while the two diamonds remained contacting each other. Special care was taken to keep the diamonds wetted by liquid at all times, including the stage at which the upper diamond was slid off the lower, drilled diamond, as otherwise part of the liquid within the holes is dragged out by surface tension forces during the separation of the diamonds. Permanent wetting was achieved by adding liquid from the pipette. After separating the diamonds, excess liquid on the lower, drilled diamond plate was quickly scratched off with a clean razor blade, and the holes were allowed to dry. In some cases, the surface was once more cleaned with the razor blade after drying. Attempts to directly fill the holes with epoxy and subsequently analyze them by LA–ICP–MS were not successful, because (i) the precipitates within the holes are commonly loose and ablate very fast, which leads to very spiky signals, and (ii) because elements, such as Rb and Cs, which we wanted to use as internal standard, dissolved into the epoxy. As described

further below, we thus completely refrained from using an internal standard and quantified the analyses based on the carbon signal of the epoxy filling instead.

To solve the problem with the spiky signals we developed a way to melt the precipitates within the holes and to quench them to a glass without losing too many elements through vaporization. For this purpose, a high-purity, MnO-containing $Li_2B_4O_7$ glass was prepared. Addition of MnO was necessary, because pure $Li_2B_4O_7$ glass is difficult to ablate with the laser. One gram of $Li_2B_4O_7$ (Alfa Aesar, 99.998 % purity) was thus mixed with 2 wt. % MnO (Alfa Aesar, 99.99% purity) and melted at 1200 °C for 12 minutes in a crimped Pt capsule. The capsule was then quenched in distilled water and the recovered glass was finely ground in an agate mortar. To add small amounts of this glass to each hole in the SCDT without losing solid precipitates, the fine glass powder was mixed into a ~2:1 acetone–ethanol solution. One drop of this suspension was then placed onto the drilled diamond plate and allowed to dry, resulting in a fine layer of precipitated glass powder evenly spread across the entire surface. Glass powder that precipitated between the holes was then cleaned away using a razor blade. Subsequently, the diamond was covered with a small piece of gold foil (0.2 mm thickness) that was held in place and slightly pushed down with the help of two SiO_2 glass cylinders that fit neatly into a sintered Al_2O_3 tube. The whole setup was then heated for 10 min at 1000 °C inside an 1 atm box furnace. As a result, the precipitates within the holes in the diamond melted and formed a thin glass layer (Fig. 4.2c). Finally, the holes were filled with epoxy resin (EPOFIX resin mixed with hardener from Struers GmbH, Germany; making sure that no air bubbles were trapped), and excess epoxy was cut away using a razor blade before the epoxy reached full hardness (Fig. 4.2d).

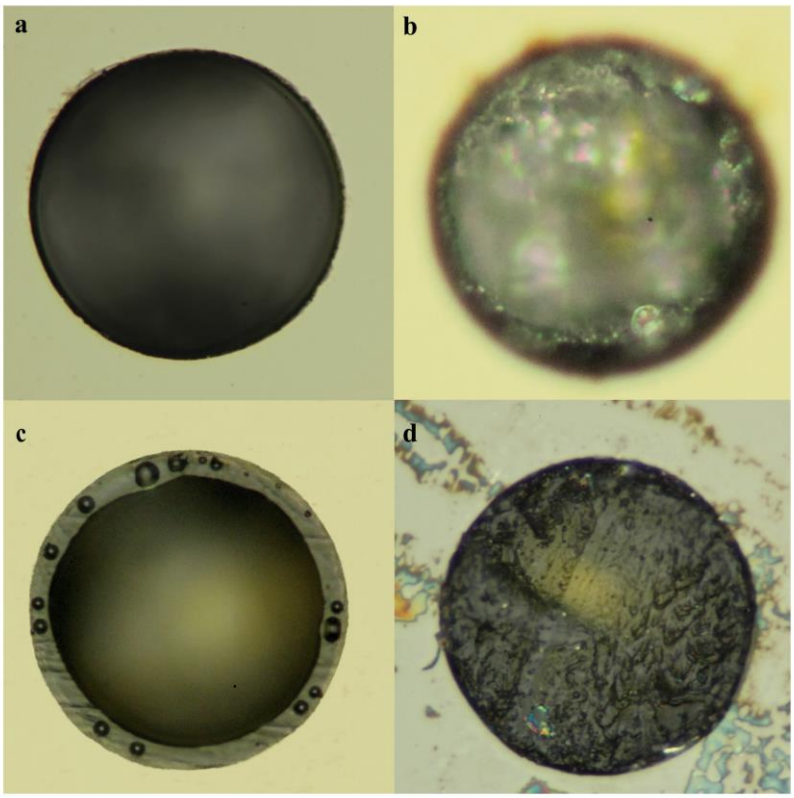

Figure 4.2: Photomicrographs of laser-drilled holes in the diamond plates: **(a)** empty hole before the experiment; **(b)** after a high P–T quartz solubility experiment, containing precipitated SiO_2; **(c)** after adding $Li_2B_4O_7$ powder and melting at 1000 °C; **(d)** after filling with epoxy resin, ready to be analyzed with LA–ICP–MS. The diameter of each hole is 80 µm. Images a and d were taken in reflected light; images b and c in transmitted light.

Table 4.1: Summary of experiments and obtained results

Experiment	P (GPa)	T (°C)	Dura-tion (h)	Average $Li_2B_4O_7$ (wt. %)	Refe-rence value (wt. %)	Reference	Density of original solvent (g/cm^3)	Reference value if solvent was H_2O with 1.0 g/cm^3 (wt. %)	Result with 100 wt. % C as internal standard (wt. %)	Density of precipit ate (g/cm^3)	% less volu me of epoxy	corrected result 1st iteration (wt. %)	corrected result 3rd iteration (wt. %)	% devi atio n
$BaCO_3$ in epoxy[a]				0	0.35	weigh-in	1.15	0.40	0.4 ± 0.1	4.3	0.1	0.40	0.40±0.05	-1
Al_2O_3 in epoxy[a]				0	0.47	"	1.15	0.54	0.4 ± 0.1	4.0	0.2	0.44	0.44±0.04	-19
Al_2O_3 in epoxy[a]				0	5.30	"	1.15	6.05	5.0 ± 0.4	4.0	1.7	4.92	4.92±0.33	-19
TiO_2 in epoxy[a]				0	2.10	"	1.15	2.41	2.2 ± 0.3	4.0	0.7	2.22	2.22±0.28	-8
TiO_2 in epoxy[a]				0	0.32	"	1.15	0.37	0.4 ± 0.1	4.0	0.1	0.40	0.40±0.09	9
TiO_2 in epoxy[a]				0	0.48	"	1.15	0.55	0.6 ± 0.1	4.0	0.2	0.60	0.60±0.12	9
CaF_2 in epoxy[a]				0	0.52	"	1.15	0.60	0.6 ± 0.2	3.2	0.3	0.62	0.62±0.16	3
Epidote in CrystalBond[b]				5.2	17.0	"	1.31	21.18	23.1 ± 5.3	2.6	14.6	19.7	20.1±5.3	-5
Garnet in CrystalBond[b]				2.3	18.5	"	1.31	22.92	21.0 ± 2.1	4.1	8.0	19.3	19.4±2.1	-15
Tourmaline in CrystalBond[b]				3.9	17.0	"	1.31	21.16	19.9 ± 2.3	3.2	10.4	17.8	18.0±2.3	-15
Epidote in CrystalBond[b]				6.0	17.0	"	1.31	21.18	20.4 ± 2.5	2.6	14.1	15.6	17.9±1.7	-16
SCDT – Quartz solubility in water – SA24	1.0	800	3	0	7.0	Manning (1994)	0.89	6.3	7.0 ± 1.3	2.2	4.2	6.7	6.7±1.3	8
SCDT – Quartz solubility in water – SA39	1.0	900	2	5.0	12.6	"	0.85	10.8	13.4 ±1.9	2.2	10.9	11.9	12.0±1.6	11
SCDT – Forsterite + Enstatite solubility in water – SA31	1.0	800	5	0.7	1.8	Newton & Manning (2002)	0.89	1.6	2.0 ± 0.2	2.2	1.6	1.9	1.9±0.2	21
SCDT – Forsterite + Enstatite solubility in water – SA36	1.0	900	4	15.9	3.1	"	0.85	2.6	2.6 ± 0.8	2.2	8.9	2.3	2.3±0.7	-11
DT – Quartz solubility in water – SA40	1.0	900	5	0	12.6	Manning (1994)	-	-	-	-	-	-	5.5±0.7	-56
DT – Quartz solubility in water – SA41	1.0	800	7	0	7.0	"	-	-	-	-	-	-	5.6±0.5	-20
DT – Forsterite + Enstatite solubility in water – SA42	1.0	900	8	0	3.1	Newton & Manning (2002)	-	-	-	-	-	-	3.3±0.7	7
DT – Forsterite + Enstatite solubility in water – SA43	1.0	800	10	0	1.8	"	-	-	-	-	-	-	1.3±0.2	-31
SCDT – Eclogite + H_2O	2.8	700	15	0	-	-	-	-	-	-	-	-	-	-

A fictive carbon content of 15 wt. % in the calcite was used for all quantifications, DT classical diamond trap experiments, SCDT Single-crystal diamond trap experiments
[a] Carefully weighed amounts of fine-grained chemicals were mixed into epoxy and filled into the holes. [b] Carefully weighed amounts of pigments were mixed into molten Crystalbond 509. After the mixture was filled into the holes, the Crystalbond was dissolved away in a 2:1 acetone:ethanol mixture.

4.2.3 Preparation of test samples

To calibrate the new quantification approach based on the carbon signal of the epoxy and to test the analytical accuracy of the SCDT method we prepared test samples with known amounts of chemicals or minerals that were placed into the drilled holes in the diamonds. For this purpose, fine-grained Al_2O_3 (< 3 µm), TiO_2 (<1 µm), $BaCO_3$ (<5 µm) and CaF_2 (<2 µm) chemicals were carefully mixed into epoxy resin in weight proportions of 0.32–5.3 wt. % and filled into the holes. Excess epoxy was cut away using a razor blade. The LA–ICP–MS data were used to calibrate the standardless quantification via the carbon signal (see below). To test the validity of the entire experimental approach including the partial melting step with the added $Li_2B_4O_7$ it was necessary to add known amounts of solids into the holes without simultaneously adding epoxy. This was achieved by mixing relatively coarse-grained garnet (~5 µm), epidote (~5 µm) and tourmaline (~5 µm) pigments (Enogu mineral pigments series from Kremer Pigments, Aichstetten, Germany) into molten Crystalbond 509, which, after filling the mixture into the holes and cutting excess material away with a razor blade, was subsequently dissolved away using a 2:1 acetone–ethanol solution. The holes were then doped with MnO-bearing $Li_2B_4O_7$ as described above and melted at 1000 ° C. Finally, the holes were filled with epoxy, and LA–ICP–MS analysis were performed after the epoxy had hardened overnight. The purity of the MnO-doped $Li_2B_4O_7$ and the epoxy was checked by LA–ICP–MS analyses. The MnO-doped $Li_2B_4O_7$ contains 0.37±0.03 wt. % SiO_2 (probably from grinding and mixing the two components in an agate mortar) but otherwise is very pure (supplementary Table A.1.1), and also the epoxy is very pure (supplementary Table A.1.2). The concentrations and detection limits listed in supplementary Table A.1.1 are representative of the detection limits that can be reached in the analyses of real experimental run products (i.e., less than a few µg/g for most trace elements). The small amount of SiO_2 present in the lithium tetraborate does not significantly affect the calculated solute contents, because even at an extraordinarily high $Li_2B_4O_7$: solute SiO_2 weight ratio of five it causes only a (5/6*0.0037)/(1/6*1.0) = 1.85 % increase in the calculated SiO_2 content of a SiO_2–dominated fluid.

4.2.4 LA–ICP–MS analyses

Initially we performed the experiments with Rb- and Cs-doped solutions, with the aim to use these elements as internal standard for quantifying the LA–ICP–MS analyses. A test experiment performed at ambient conditions by filling the holes with a 5 wt. % Na_2SiO_3

solution doped with 100 µg/g each of Rb and Cs, returned reproducible and accurate results (4.9 ± 0.1% relative) for all elements. However, subsequent high P–T experiments performed on model systems (solubility of quartz or enstatite+olivine in H_2O, and supercritical H_2O–albite fluids) with Rb- and Cs-doped aqueous solutions were plagued by poor reproducibility and in average either too high or too low values, which seemed to be at least partly due to problems with the internal standard. Opening the capsules in frozen state and then allowing the ice within the laser holes to melt and slowly dry out in a controlled fashion did not solve the problem. Rather, tests with simple NaCl–KCl–Rb–Cs–Ba–B–Pb solutions (element concentrations ranging from 1 wt.% to 200 µg/g) revealed that freezing amplified the problem, probably because a part of the solution did not freeze and thus remained mobile at the temperature of -20 to -30 °C prevailing in the freezing chamber. Another big problem was the very short, spiky nature of the LA–ICP–MS signals.

To overcome these issues, we started to fill the holes with epoxy resin after they dried out. This increased the length of the LA–ICP–MS signals, but it did not solve the problems with the spiky nature of the signals and the internal standard. During these tests it was observed that the ablation of epoxy produces a much higher carbon signal than the ablation of diamond (because the ablation rate in epoxy is much faster), which opens up the possibility to use the epoxy filling instead of a fluid component as the internal standard. However, such an approach is fundamentally different from the normal way of using internal standards: the carbon signal of the epoxy can only be used to quantify the weight of the precipitates relative to the weight of the epoxy that fills out the rest of the hole. To transform this value into the amount of solids dissolved within the fluid, it is thus necessary to make corrections for the density difference between epoxy and fluid, and for the space occupied by the precipitates + $Li_2B_4O_7$ (see below).

In the case of the few comparison runs performed with the classical diamond trap technique the capsules were first dropped into liquid nitrogen before opening them longitudinally with a sturdy razor blade in an opening device that had a temperature of ca. -30 to -60 °C . One half of the frozen capsule was then quickly transferred to a LA–ICP–MS sample chamber that was cooled to ca. -30 °C (according to tests with H_2O–ethanol solutions) by means of a Peltier cooling element to keep the sample frozen also during the measurement (Kessel et al. 2004, Aerts et al. 2010). In those experiments, the Cs concentration in the starting solution was used as the internal standard for calculating absolute element concentrations, accounting for the lowering of the original concentration due to the dissolution of solids.

The LA–ICP–MS analyses were performed with a 193 nm ArF Excimer laser (GeolasPro system; Coherent; USA) attached to a quadrupole mass spectrometer (Elan DRC-e; Perkin Elmer; Canada). To increase the length of the LA–ICP–MS signals the epoxy-filled holes were ablated with a lower repetition rate (5 Hz) and a lower energy (40–65 mJ) than the external standards (10 Hz, 90–110 mJ). For ablating the epoxy-filled holes in the diamonds we used the same laser diameter (80 µm) as the one that had previously been used to drill the holes. The sample chamber was flushed with He gas at a rate of 0.4 l/min, to which 5 ml/min H_2 was added on the way to the ICP–MS. The latter was tuned to a ThO production rate of 0.5–1.5% and a production rate of doubly–charged ^{42}Ca ions of 0.15–0.30 based on measurements on NIST SRM 610 glass. Analyzed isotopes include ^{7}Li, ^{11}B, ^{12}C, ^{23}Na, ^{25}Mg, ^{27}Al, ^{29}Si, ^{30}Si, ^{31}P, ^{35}Cl, ^{39}K, ^{43}Ca, ^{49}Ti, ^{53}Cr, ^{55}Mn, ^{57}Fe, ^{59}Co, ^{62}Ni, ^{65}Cu, ^{66}Zn, ^{85}Rb, ^{88}Sr, ^{89}Y, ^{90}Zr, ^{133}Cs, ^{137}Ba, ^{139}La, ^{140}Ce, ^{157}Gd, ^{175}Lu, ^{208}Pb, ^{232}Th, and ^{238}U, using dwell times of 10–20 ms. For external standardization we used either NIST SRM 610 (Jochum et al. 2011) or USGS GSE-1G as reference material (for the latter we used the GeoReM preferred values of 7/2018), plus a natural calcite crystal from Iceland as a calibrant for the carbon signal. Signal integration, spike removal, and numerical calculations were done using two in-house Excel spreadsheets. The quantification spreadsheet allows two external standards to be used simultaneously. As internal standard we used in a first stage the carbon signal of the ablated epoxy. Attempts to dope the epoxy with trace elements and use one of these elements as internal standard failed, because we did not manage to manufacture epoxy in which the trace elements are homogeneously distributed at the micrometer scale. Due to the different ablation behavior of epoxy relative to minerals, it is not possible to take the actual carbon content of the epoxy as internal standard. Instead, we used a fictive carbon concentration of 100 wt.% and changed via the "goal seek" analysis tool in Excel the carbon content of the calcite until the best average result was obtained for the experiments in which the holes were filled with known amounts of Al_2O_3, TiO_2, $BaCO_3$ and CaF_2 using very fine-grained mixtures in epoxy. The same could have been done using the correct carbon concentration for calcite and finding via the goal seek function a fictive carbon concentration in the epoxy, but for the calculations the former approach is more practical. In either case, the fictive carbon value that is found via the goal seek function likely depends on ICP–MS instrument and laser ablation settings and thus has to be calibrated for each laboratory individually based on test samples as described above. However, it does not seem to be necessary to re-calibrate the fictive carbon in each analytical session, as test samples analyzed on 15 different measuring days spread over a 5 months period using a constant fictive carbon value for the calcite (15 wt. % in our case) returned consistent results.

Another important difference to the normal way of internal standardization is that corrections need to be made to account for the difference in the density of epoxy vs. the density of the medium in which the solutes were dissolved or immersed originally. For example, if, e.g., SiO_2 was originally dissolved in a high P–T H_2O fluid with a density of 0.89 g/cm^3, and the holes are then filled with pure epoxy with a density of 1.15 g/cm^3, then a correction of (1.15/0.89)–1.0 = +29% has to be applied to the concentration values determined based on epoxy. Because we used calibrants with various densities (epoxy with 1.15 g/cm^3, Crystalbond 509 with 1.31 g/cm^3, and aqueous solutions with 0.85–0.89 g/cm^3) we decided to normalize all concentrations to a solvent density of 1.00 g/cm^3 before determining the fictive carbon concentration of the calcite (Table 4.1). This means that for any new solubility measurement the results are first obtained for an assumed solvent density of 1.0 g/cm^3, and then a correction needs to be applied to account for the actual solvent density.

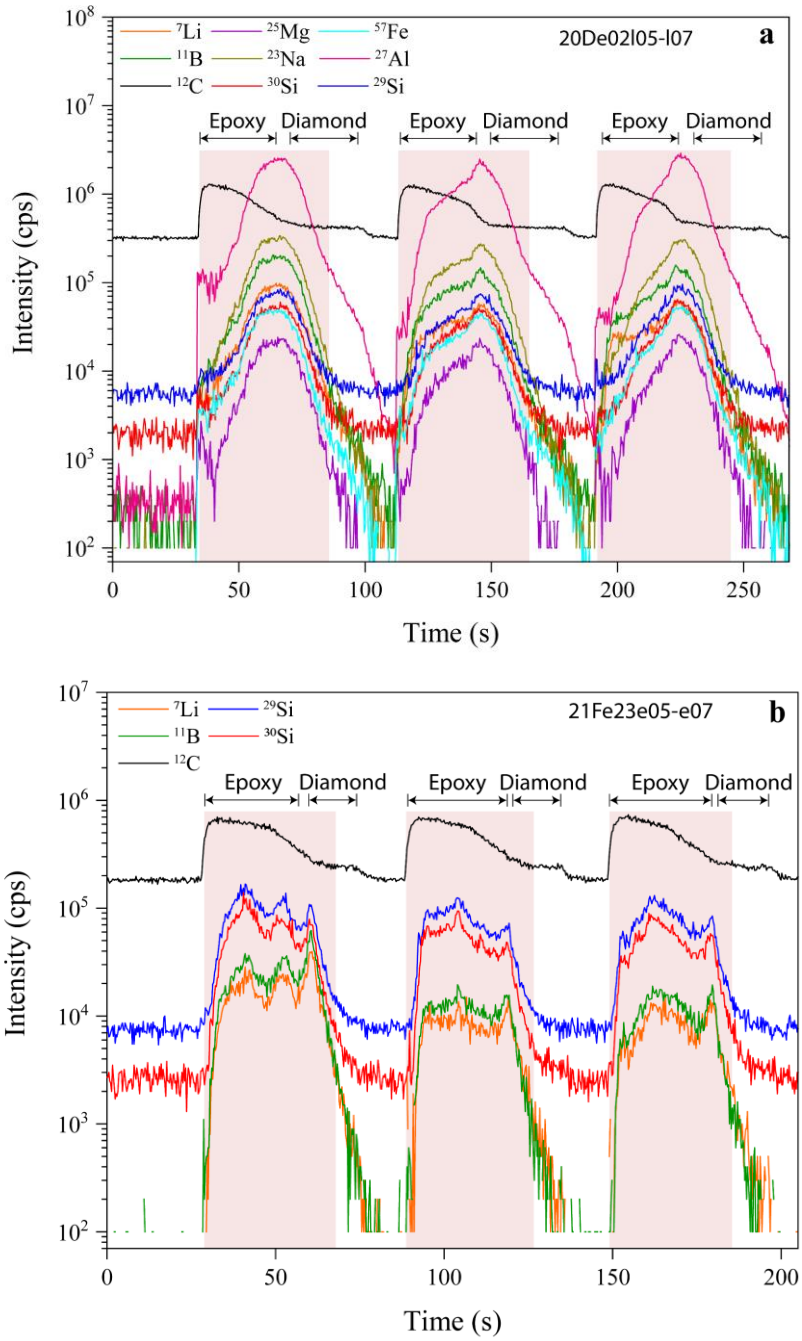

Figure 4.3: LA–ICP–MS signals of SCDT analyses; **(a)** signal of three different holes containing 18.0±2.3 wt. % of tourmaline pigment; **(b)** three analyzed holes of the quartz + water experiment at 1.0 GPa, 900 °C containing in average 12.0±1.6 wt. % of SiO_2. The shaded areas show the signal integration intervals of each hole.

A last issue concerns the difference between the density of the solvent vs. the density of the bulk fluid (i.e., solvent + solute). At solute contents of less than a few weight percent the difference between the two values is negligible, but at higher solute content it becomes significant, such that an additional correction is required. A visual way to deal with this issue

is to think in terms of space occupied by the precipitated solutes (plus added $Li_2B_4O_7$) vs. space occupied by the remaining solvent (now filled with epoxy). If, e.g., one-third of the hole is filled with precipitates (plus added $Li_2B_4O_7$) instead of with epoxy, then the result calculated on the basis of an internal carbon concentration of 100 wt.% will turn out 33% too high. If the density of the epoxy, the weight percentage of the precipitates and the average density of the latter are known, then the amount of overestimation equals to:

$$\%\ overestimation = \left[\frac{wt.\%\ solute}{density\ of\ precipitates} + \frac{wt.\%\ added\ Li_2B_4O_7}{density\ of\ Li_2B_4O_7}\right] \times \left[\frac{density\ of\ epoxy}{100/density\ of\ epoxy}\right] \times 100$$

However, the weight percentage of solute is what we are actually looking for, hence the correct value can only be found iteratively. In the first step, it is assumed that the entire hole is filled with epoxy, which gives a certain weight percent solute. That value is then used to calculate a corrected weight percent value, which is then used to calculate a further refined value. After three iterations a stable result (<1% difference relative to the previous iteration) value is obtained even for high solute contents of 20–30 wt. %. It should be stressed that the magnitude of this final correction procedure is small: for 10 wt. % solute it amounts to ≤6% (the exact value depending on the fluid density, and thus on the P–T conditions), i.e., the value of 10 wt. % needs to be correct down to 9.4 wt. % at most. An Excel spreadsheet with the full calculation details of experiment SA31 is provided in the electronic supplementary material.

4.3 Results

Representative LA–ICP–MS signals obtained from SCDT experiments are shown in Fig. 4.3. Figure 4.3a shows the signals of three holes analyzed from a test experiment performed with 17 wt. % tourmaline pigment, whereas Fig. 4.3b shows the signals of three holes analyzed from a quartz solubility experiment in water at 1.0 GPa, 900 °C (the reference solubility value for the latter experiment is 12.6 wt. % SiO_2; Manning 1994). The net carbon signal obtained from the ablation of epoxy is about 6 times higher than the net signal obtained during the ablation of diamond, hence even if part of the chosen signal interval extends into the diamond domain (Fig. 4.3a) the bulk of the net carbon signal is still heavily dominated by the epoxy. The reason why the signal of the melted solids within the holes commonly extends beyond the signal of the epoxy is that the glass tends to accumulate at the bottom of the hole.

After calibrating the new method based on holes filled with epoxy that was doped with known amounts of chemicals (Al_2O_3, TiO_2, $BaCO_3$, CaF_2), the sample melting procedure with the added MnO–doped $Li_2B_4O_7$ was tested with a series of experiments in which known amounts of mineral pigments (garnet, epidote, tourmaline) were filled into the holes with the help of Crystalbond 509 that was subsequently dissolved away. The expected values (calculated from the weights of pigments mixed into Crystalbond) for the garnet, epidote, tourmaline tests are 22.9, 21.2 and 21.2 wt. %, respectively, and the obtained results agree with these reference values within 5–16 %. In addition, the measured compositions of the melted minerals agree well (within 1 wt. % absolute) with those obtained through LA–ICP–MS analysis of densely pressed pellets produced from the same pigment powders, except for the Al_2O_3 content of the tourmaline, which turned out 7 wt. % too high, and the K_2O content of one of the two tests performed with epidote, which was 2 wt. % too high (supplementary Table A.1.3). Whereas the reason for the higher Al_2O_3 content of the melted tourmaline is not clear, gains of K_2O during the melting procedure were relatively common and appear to have been caused by contamination of the furnace or some other parts of the melting assembly (see below).

A more detailed check for potential losses or gains of elements during the melting procedure was performed by loading small amounts of crushed GSE-1G reference glass plus Mn-doped $Li_2B_4O_7$ at a weight ratio of ca. 2:1 into the laser-drilled holes in a diamond, melting them in the usual manner (i.e., at 1000 °C; with the holes covered by an Au foil), and then filling the remaining space of the holes with epoxy before the LA–ICP–MS analysis. The results (supplementary Table A.1.4) reveal that most of the major and minor element concentrations remained unmodified, except for Na_2O and K_2O, which experienced gains of 50 % and 130 %, respectively (1.8 wt. % Na_2O and 3.4 wt. % K_2O on an absolute basis). The results with respect to changes in trace element concentrations are varied: six out of 19 analyzed trace changed by less than 10%; nine elements decreased by 10–25%; and Cs, Cu, Ag and Cd decreased by 35 to >147% (supplementary Table A.1.4).

A final test to investigate potential losses or gains of elements during the melting procedure was performed by adding variable amounts of albite powder into the holes (the exact amounts being unknown, but visually estimated to be in the range of 1–20 wt. %) and melting them as described above. The LA–ICP–MS analyses revealed SiO_2, Na_2O and Al_2O_3 concentrations that agree within 2% with those of the starting material, but about 3.8 wt. % K_2O were gained (supplementary Table A.1.3). Remember that a similar test performed on an albite-doped classical diamond trap returned a SiO_2/Al_2O_3 concentration ratio that was wrong by a factor of

two (Rustioni et al. 2021), apparently due to element fractionation occurring during the ablation of the diamond + albite + ice/liquid H_2O mixture (Rustioni et al. 2021). The present test thus suggests that the SCDT method greatly helps to reduce fractionation effects occurring during the LA–ICP–MS analysis of classical diamond traps, but alkalies may be significantly gained (or lost) during the melting procedure.

Finally, the experiments were expanded to real solubility measurements at high pressure and temperature in the well-studied H_2O–SiO_2 and H_2O–enstatite–olivine systems, for which reliable reference data exist (Manning 1994; Newton and Manning 2002). A summary of all the previously described tests and the high *P, T* runs is provided in Table 4.1 and Fig. 4.4. With regard to quartz solubility in water we performed two SCDT experiments at 1.0 GPa pressure and 800 °C and 900 °C, respectively, plus two classical diamond trap experiments at the same conditions for comparison. Previous experimental studies returned consistent results within this range of P–T conditions (Anderson and Burnham 1965, Fournier and Potter 1982, Manning 1994), allowing us to use these data as a reference. Our experiments at 800 °C and 900 °C agree with the reference values within +8% and +11%, respectively. The same experiments performed using the classical diamond trap method show 20% deviation at 800 °C and 56% deviation at 900 °C. Aerts et al. (2010) report only -3% deviation for a classical diamond trap experiment performed at 0.88 GPa and 700 °C, whereas Rustioni et al. (2021) performed two experiments (also using the classical approach) at 1.0 GPa and 800 °C and found +3% discrepancy in one of them, and -40% discrepancy in the other. The reason for the large discrepancies in some of these experiments is not clear. If it was due to erroneous temperature reading due to thermal gradients between thermocouple and sample, then these gradients would have to be nearly 100 °C, which seems unlikely (see below). Run duration should not have been the problem either, as our SCDT experiments were run only for 2–3 hours and returned already good agreement, whereas our classical diamond trap experiments were run for 5–7 hours, and those of Rustioni et al. (2021) for 16–18 hours. One potential explanation would be preferential loss of H_2O during the experiment, which would lead to an increase in the Cs concentration in the remaining fluid and thus in an underestimation of the SiO_2 solubility. Another potential explanation is that during the opening of the frozen diamond trap some Cs-rich, residual solution was expelled onto the diamond trap surface.

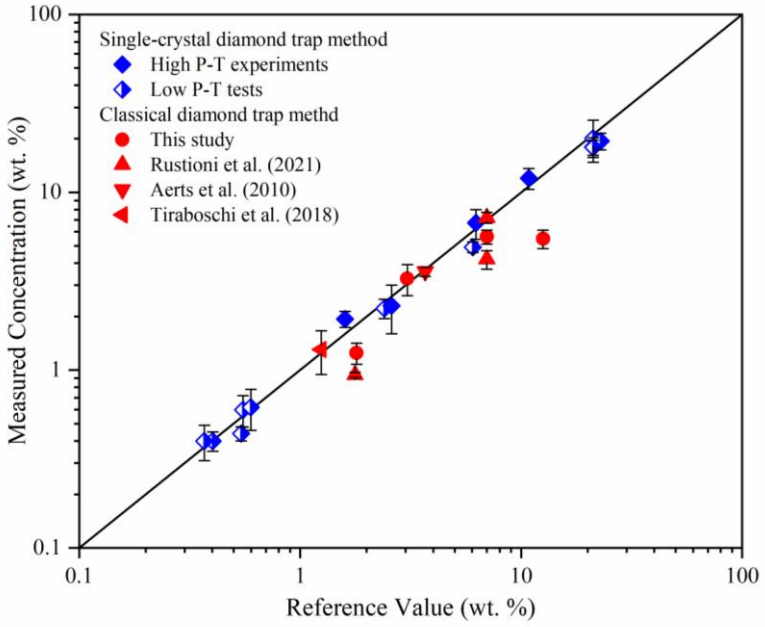

Figure 4.4: Comparison between measured weight percentages and reference values for tests and experiments conducted with the SCDT method (blue diamonds) versus experiments conducted with silicate materials using the classical diamond trap method (red circles and triangles). The black line represents the 1:1 line, i.e., perfect agreement between measured and reference values.

The solubility of SiO_2 in the forsterite–enstatite–water system was measured at 1.0 GPa and 800 to 900 °C. Our SCDT results agree with the Newton and Manning (2002) data within +21% at 800 °C, and within -11% at 900 °C. In comparison, the results of our classical DT experiments agree with the literature values within -31% at 800 °C, and within +7% at 900 °C. A classical diamond experiment performed by Rustioni et al. (2021) at 1.0 GPa and 800 °C resulted in 47% underestimation of the SiO_2 solubility, whereas Tiraboschi et al. (2018) obtained an agreement within +5% at the same conditions. Again, run time is unlikely to be responsible for the discrepancies, as our SCDT experiments were run for 4–5 hours, whereas our classical diamond trap experiments were run for 8–10 hours, that of Rustioni et al. (2021) for 20 hours, and that of Tiraboschi et al. (2018) for ~48 hours. Considering all experiments and test runs, the new SCDT method produced results that deviate maximal 21% from the reference values (average deviation 13%), whereas identical experiments using the classical diamond trap method deviate by up to 56 % (average deviation 28%; Fig. 4.5). The large negative deviations of some classical diamond trap experiments are unlikely to be caused by short run times, because other classical diamond trap experiments of similar duration returned

correct results and because the SCDT experiments lasted only half as long. We tried to avoid unnecessarily long experimental run times, because this promotes the dissolution and re-precipitation of minerals in thermal gradients and thus may cause positive deviations from reference values. One advantage of the new SCDT method over the classical diamond trap method is that it allows use of very high fluid/solid ratios. This facilitates the growth of large crystals during the experiments and thus the determination of fluid–mineral partition coefficients of trace elements. For example, we conducted a SCDT experiment with a crushed eclogite as starting material and recovered large crystals of pyroxene, garnet and mica after a run duration of only 15 hours (supplementary Figure A.1.1).

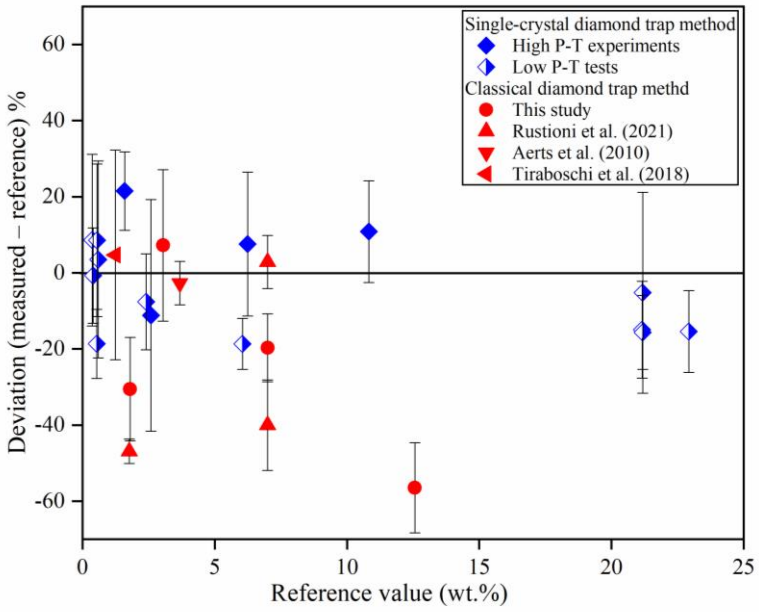

Figure 4.5: Relative deviation (in %) of the measured weight percentages from the reference values as a function of the absolute weight percentages. Blue diamonds denote the SCDT method, whereas red circles and triangles denote the classical diamond trap method.

4.4 Discussion

According to the results presented above the new SCDT method provides more reliable mineral solubility data at high *P–T* conditions than corresponding data obtained with the classical diamond trap technique in our lab. However, as with any experimental or analytical technique, the results can be affected by a number of sources of uncertainty. In decreasing order of estimated relevance these are: (1) temperature differences between the thermocouple and the

diamond trap; (2) loss or addition of material from/to the holes during sample preparation after the experiments; (3) fractionation effects during LA–ICP–MS analysis; (4) gains or losses of alkalies during the melting procedure, (5) wrong assumptions made in the quantification approach (e.g., regarding the density of the precipitates); and (6) day–to–day variations in the sensitivity of the carbon relative to other elements.

Recent experiments to quantify temperature gradients within Pt capsules of piston cylinder experiments revealed that with the standard 1/2" assemblies used at BGI (a talc-pyrex-crushable Al_2O_3 assembly and a MgO–NaCl assembly; the latter being used in the present study) temperature gradients between thermocouple and the center of the Pt capsule can easily reach ±50 °C, depending on how the graphite heater deforms during initial pressurization (Audétat et al. 2020). A temperature offset of ±50 °C at our experimental conditions results in a SiO_2 solubility difference of ±0.5 wt. % in the forsterite–enstatite–H_2O system, and ±1–3 wt. % in the quartz–H_2O system, corresponding to errors of 28 % and 14–43 %, respectively.

Loss or addition of material from/to the holes during sample preparation can occur due to shaky hands. In addition, excess minerals may form within some holes due to dissolution–reprecipitation in response to temperature gradients, or due to metastability effects during heating (Keppler, 2017). However, in contrast to the classical diamond trap method, these effects can be readily noticed in SCDT experiments by anomalous results obtained from certain holes. Indeed, in five of our fifteen SCDT experiments some holes were strongly anomalous and thus were not considered in the calculation of the average (see the calculations of experiment SA31 in the supplementary material as an example). This is perhaps the biggest advantage of the SCDT method over the classical approach, as each sample volume is clearly defined, whereas in the classical approach it is up to the user how to choose the integration intervals.

Our tests with mineral pigments and albite added to unheated single-crystal diamond traps suggest that fractionation effects during laser ablation are small. In particular, the test with the albite revealed an agreement with the theoretical values within 6%, which is a major improvement compared to a similar test performed by Rustioni et al. (2021) with the classical diamond trap, in which a discrepancy of a factor of two was noticed. The analyses of garnet, epidote, tourmaline albite and silicate glass powders that were filled into the holes in the diamond and subsequently melted in the presence of lithium tetraborate revealed SiO_2, Al_2O_3, MgO, FeO_{tot} and TiO_2 concentrations that generally agree within 1 wt. % with the compositions

of the starting materials, except for Na_2O and K_2O, which in some tests were gained in appreciable amounts (supplementary Tables A.1.3 and A.1.4).

The standardless quantification approach requires input of the density of the precipitates within the holes after the experiment, and that of the solvent at run conditions. The former can only be estimated. In our high P–T runs the bulk of dissolved matter was dominated by SiO_2. For simplicity we thus assumed that the precipitates after the experiment consist of SiO_2 glass, and that the density of SiO_2 dissolved in the fluid was the same as that of SiO_2 glass (although the latter is not perfectly true, e.g., Hunt and Manning 2012). In this case the density of the solvent corresponds to the density of H_2O, which was calculated based on Saul and Wagner (1987). Since the amount of dissolved matter in our high P–T runs was relatively low (≤12 wt. %) the calculated concentrations are rather insensitive to the assumptions regarding the density of the precipitates and the density of dissolved matter in the fluid: changing the value by 30% causes the calculated concentration of dissolved matter to change by only 2–3%. Finally, since the standardless quantification is based on the carbon signal, which shows a high background value (Fig. 4.3), day–to–day or within–day variations in the sensitivity of carbon relative to other elements may represent another source of uncertainty. However, within 15 measuring days spread out over 5 months we did not notice any systematic shift in the fictive carbon value of the calcite that was required to obtain optimal agreement between measured concentration values and the reference values. We thus believe that variations in the sensitivity of carbon do not represent a large source of uncertainty in the SCDT approach, at least if the ICP–MS is used in a similar fashion as in the current study.

4.5 Conclusions

Our newly developed SCDT method for studying fluid compositions in high-P and high-T experiments offers the following advantages over the classical diamond trap approach:

- The use of spatially separated holes to retain the high-pressure fluids during quench allows a more reliable testing of the reproducibility of solubility data. Outliers caused by growth of minerals within certain holes during the run, or gain/loss of mineral precipitates during the sample preparation can be readily identified and be excluded from the data set.
- At least in the present study the SCDT method produced better reproducible and more accurate results than the classical diamond trap approach.
- Less element fractionation (i.e., test with albite)

- No freezing stage is necessary to analyze the diamond trap.
- The method can (but does not necessarily have to) be used with very high fluid/solid ratios, which promotes the growth of large crystals that are required to determine fluid–mineral partition coefficients for mineral-incompatible trace elements.

The main disadvantages of the SCDT method are the following:

- Both the sample preparation before the experiments (drilling of diamonds; preparation of inner capsules) and the sample preparation after the experiments (addition of $Li_2B_4O_7$; melting; filling of the residual space with epoxy) is more time consuming and requires clean, careful handling without shaky hands.
- Compared to the classical diamond trap approach also the quantification procedure of the LA–ICP–MS signals is more difficult and time consuming. On the other hand, the fact that no internal standard in the fluid is necessary may prove helpful in experiments in which none of the available elements behaves incompatibly enough to be used as internal standard.
- Alkalies may be gained or lost during the melting step.
- Finally, one needs to purchase single-crystal diamond plates. However, they cost only 10–20 € each, depending where one buys them.

Overall, we believe that the SCDT method is a viable alternative to the classical diamond trap method and provides reliable mineral solubility data in high P–T fluids.

Acknowledgments

We would like to thank Raphael Njul and Alexander Rother for help with epoxy and test filling materials preparation, Stefan Übelhack and Sven Linhardt for manufacturing the Peltier element-cooled ablation cell and other devices. Sincere thanks also to Othmar Müntener, Bob Luth and an anonymous reviewer for their thorough reviews, which greatly helped to improve the manuscript. This study was conducted under the “Deep volatile cycles – International Research Training Group” funded by German Research Foundation (Deutsche Forschungsgemeinschaft – DFG, GRK 2156/1).

Supplementary materials

See appendix A.1 for supplementary figures and tables. Electronic supplementary materials are available at: https://doi.org/10.1007/s00410-021-01882-6

References

Aerts M, Hack AC, Reusser E, Ulmer P (2010) Assessment of the diamond-trap method for studying high-pressure fluids and melts and an improved freezing stage design for laser ablation ICP–MS analysis. Am Mineral 95:1523–1526. https://doi.org/10.2138/am.2010.3356

Anderson GM, Burnham CW (1965) Solubility of quartz in supercritical water. Am J Sci 263:494–511

Audétat A, Bali E (2010) A new technique to seal volatile-rich samples into platinum capsules. Eur J Mineral 22:23–27. https://doi.org/10.1127/0935-1221/2010/0022-1982

Audétat A, Keppler H (2005) Solubility of rutile in subduction zone fluids, as determined by experiments in the hydrothermal diamond anvil cell. Earth Planet Sci Lett 232:393–402. https://doi.org/10.1016/j.epsl.2005.01.028

Audétat A, Krupp A, Putra R (2020) Mapping the temperature distribution within piston cylinder sample capsules. Annual report Bayerisches Geoinstitut pp 146-147

Baker MB, Stolper EM (1994) Determining the composition of high-pressure mantle melts using diamond aggregates. Geochim Cosmochim Acta 58:2811–2827. https://doi.org/10.1016/0016-7037(94)90116-3

Bernini D, Audétat A, Dolejš D, Keppler H (2013) Zircon solubility in aqueous fluids at high temperatures and pressures. Geochim Cosmochim Acta 119:178–187. https://doi.org/10.1016/j.gca.2013.05.018

Fournier RO, Potter RW (1982) An equation correlating the solubility of quartz in water from 25 482 °C to 900 °C at pressures up to 10,000 bars. Geochim Cosmochim Acta 46:1969–1973. https://doi.org/10.1016/0016-7037(82)90135-1

Hunt JD, Manning CE (2012) A thermodynamic model for the system SiO_2-H_2O near the upper critical end point based on quartz solubility experiments at 500-1100 °C and 5-20kbar. Geochim Cosmochim Acta 86:196–213. https://doi.org/10.1016/j.gca.2012.03.006

Jochum KP, Weis U, Stoll B, et al (2011) Determination of reference values for NIST SRM 610-617 glasses following ISO guidelines. Geostand Geoanalytical Res 35:397–429. https://doi.org/10.1111/j.1751-908X.2011.00120.x

Keppler H (2017) Fluids and trace element transport in subduction zones. Am Mineral 102:5–20. doi: 10.2138/am-2017-5716. http://dx.doi.org/10.2138/am-2017-5716

Kessel R, Ulmer P, Pettke T, Schmidt MW, Tompson AB (2004) A novel approach to determine high-pressure high-temperature fluid and melt compositions using diamond-trap experiments. Am Mineral 89:1078–1086. https://doi.org/10.2138/am-2004-0720

Kushiro I, Hirose K (1992) Experimental determination of composition of melt formed by equilibrium partial melting of peridotite at high pressures using aggregates of diamond

grains. In: Proc Jpn Acad pp 63–68

Manning CE (1994) The solubility of quartz in H_2O in the lower crust and upper mantle. Geochim Cosmochim Acta 58:4831–4839. https://doi.org/10.1016/0016-7037(94)90214-3

Newton RC, Manning CE (2002) Solubility of enstatite + forsterite in H_2O at deep crust/upper mantle conditions: 4 to 15 kbar and 700 to 900°C. Geochim Cosmochim Acta 66:4165–4176. https://doi.org/10.1016/S0016-7037(02)00998-5

Rustioni G, Audétat A, Keppler H (2021) A systematic assessment of the diamond trap method for measuring fluid compositions in high-pressure experiments. Am Mineral 106:28–37. https://doi.org/10.2138/am-2020-7453

Ryabchikov I, Orlova G, Kalenchuk GY, Ganeyev II, Udovkina NG, Nosik LP (1989) Reactions of spinel lherzolite with H_2O-CO_2 fluids at 20 kbar and 900 °C. Geochemistry international 26:56–62

Saul A, Wagner W (1987) International equation for the saturation properties of ordinary water substance. J Phys Chem Ref Data 16:893–901. https://doi.org/10.1063/1.555787

Schmidt C, Rickers K, Bilderback DH, Huang R (2007) In situ synchrotron-radiation XRF study of REE phosphate dissolution in aqueous fluids to 800 °C. Lithos 95:87–102. https://doi.org/10.1016/j.lithos.2006.07.017

Spandler C, Mavrogenes J, Hermann J (2007) Experimental constraints on element mobility from subducted sediments using high-P synthetic fluid/melt inclusions. Chem Geol 239:228–249. https://doi.org/10.1016/j.chemgeo.2006.10.005

Stalder R, Ulmer P, Thompson AB, Günther D (2001) High pressure fluids in the system MgO-SiO_2-H_2O under upper mantle conditions. Contrib Mineral Petrol 140:607–618. https://doi.org/10.1007/s004100000212

Tiraboschi C, Tumiati S, Sverjensky D, Pettke T, Ulmer P, Poli S (2018) Experimental determination of magnesia and silica solubilities in graphite-saturated and redox-buffered high-pressure COH fluids in equilibrium with forsterite+enstatite and magnesite+enstatite. Contrib to Mineral Petrol 173:1–17. https://doi.org/10.1007/s00410-017-1427-0

Tropper P, Manning CE (2005) Very low solubility of rutile in H_2O at high pressure and temperature, and its implications for Ti mobility in subduction zones. Am Mineral 90:502–505. https://doi.org/10.2138/am.2005.1806

Zhang YG, Frantz JD (2000) Enstatite-forsterite-water equilibria at elevated temperatures and pressures. Am Mineral 85:918–925. https://doi.org/10.2138/am-2000-0705

5. Chapter 5

An experimental investigation of factors controlling the oxygen content of sulphide melts in the Earth's upper mantle

Sumith Abeykoon[1]✉, Vera Laurenz[1], Daniel J. Frost[1], Nobuyoshi Miyajima[1], Catherine McCammon[1]

[1]Bayerisches Geoinstitut, University of Bayreuth, 95440 Bayreuth, Germany
✉ sumith.abeykoon@uni-bayreuth.de

This chapter has been published as:

Abeykoon, S., Laurenz, V., Frost, D. J., Miyajima, N., McCammon, C. An experimental investigation of factors controlling the oxygen content of sulphide melts in the Earth's upper mantle. *Contrib Mineral Petrol* **178**, 13 (2023).
https://doi.org/10.1007/s00410-023-01992-3

Abstract

To determine the factors that control the oxygen content of sulphide melt in the upper mantle, sulphides were equilibrated with mantle peridotite assemblages, with varying FeO and NiO contents, between 3 and 13 GPa and 1300 to 1819 °C. Carbonates were added as a flux and oxygen fugacities were estimated for most of the experiments. Sulphide melt oxygen concentrations were found to be in the range 0.2 to 3.7 wt. %, coexisting with silicate assemblages with olivine Fe/(Fe+Mg) ratios between 0.04 and 0.25. Except in Ni-bearing experiments, variations in the sulphur/metal cation ratio did not affect the sulphide melt oxygen contents, which also appeared to be independent of oxygen fugacity. The silicate FeO contents, temperature and pressure were found to be the main controls on oxygen contents. Nickel lowers the oxygen content, although all Ni-bearing experiments produced sulphides with lower sulphur/metal ratios, making it difficult to categorically separate the effect of Ni alone. A preliminary geothermometer expression was developed based on the oxygen content of the

sulphide melts and the iron oxide concentrations of coexisting olivine and orthopyroxene. With this expression the experimental temperatures are reproduced to within 74 K for Ni-free experiments and within 135 K for Ni- bearing samples. Using measurements of the oxygen contents of sulphide inclusions of peridotite affinity in diamonds from the Lac de Gras kimberlite field, a plausible average entrapment temperature of 1318±48 °C is calculated. Mantle peridotite assemblages would be expected to contain sulphide melts with approximately 0.4 – 0.6 wt. % oxygen along a typical mantle adiabat down to 200 km depth.

5.1 Introduction

Base metal, iron-nickel sulphides are found as accessory phases in most upper-mantle rocks and also form the most common inclusions in diamonds (Pearson et al., 1998; Richardson et al., 2004; W. E. Sharp, 1966). Sulphides exert an important control over the distribution of highly siderophile elements in the mantle (Kiseeva et al., 2017; Pearson et al., 1998; Z. Zhang et al., 2018), are commonly employed in geochronology due to their high Re and Pb contents (Harvey et al., 2016a; Pearson et al., 1999; Rudnick et al., 1993; Smit et al., 2016; Wiggers de Vries et al., 2013), and are also, used to estimate mantle sulphur fugacities (Eggler & Lorand, 1993). Along a typical adiabat, mantle sulphides should remain molten, or at least partially molten, up to pressures of 8 GPa, i.e. approximately up to 250 km depth (Bockrath et al., 2004; Z. Zhang & Hirschmann, 2016). Some mantle sulphides found as inclusions in xenoliths have textures consistent with them being molten at some point (e.g. Aulbach et al. 2004; Harvey et al. 2016). Upon cooling, however, they undergo a relatively complex crystallisation process. This starts with the crystallisation of $(Fe,Ni)_{(1-x)}S$ monosulphide solid solution (MSS) and ends, after a series of crystallisation and exsolution reactions, with the formation of pentlandite ($(Fe,Ni)_9S_8$), chalcopyrite ($CuFeS_2$) and pyrrhotite ($Fe_{1-x}S$) (Bulanova et al., 1996; Harvey et al., 2016a; Holwell & Mcdonald, 2010). It is often assumed that sulphide inclusions in diamond were trapped as MSS, from which a similar sulphide assemblage forms through solid state exsolution during cooling (L. A. Taylor & Liu, 2009). Geothermometry estimates for cratonic geotherms and diamond formation yield temperatures mainly below the solidus of MSS (Shirey et al., 2013; Z. Zhang & Hirschmann, 2016). The common occurrence of sulphide inclusions in diamond, however, has led many researchers to propose a link between sulphide melts and diamond formation, either through the provision of a carbon-saturated source or by acting as a reducing agent for carbonate melts (Bulanova, 1995; Gunn & Luth, 2006; Palyanov et al., 2007; Shushkanova & Litvin, 2008). Furthermore, some cratonic lithosphere regions appear to

encompass conditions where sulphide melts would be stable (Ashchepkov et al., 2010; Shirey et al., 2013; Z. Zhang & Hirschmann, 2016) and more Fe-metal-rich sulphide-bearing melts certainly appear to have played a role in the formation of some sublithospheric diamonds (E. E. Smith et al., 2016). The extent to which other components, such as Cu, O or H, may lower MSS melting temperatures is also unclear.

One potential indicator for the initial entrapment of sulphide melt is the presence of magnetite in recovered sulphide assemblages (Bulanova et al., 1996), which is an indicator of dissolved O in sulphide melt. While oxygen appears to be slightly soluble in MSS at high temperatures, concentrations are relatively low (<0.4 wt. % O) in comparison to sulphide melts (Graham et al., 1987; Graham & McKenzie, 1987; Z. Zhang & Hirschmann, 2016). The 1 bar Fe-FeO-FeS ternary eutectic melt, for example, contains approximately 7.5 wt. % oxygen and is essentially a binary composition of 62 mol % FeS and 38 mol % FeO, with a melting temperature of 915 °C, i.e. approximately 270 °C lower than the FeS liquidus (Naldrett, 1969). In equilibrium with silicate melts, sulphide liquid oxygen contents have been reported from approximately 1 to over 10 wt. % (Boujibar et al., 2019; Brenan, 2015; Doyle & Naldrett, 1987; Terasaki et al., 2005; Wendlandt, 1982). A number of factors are likely important in controlling sulphide liquid oxygen contents such as pressure, temperature, fO_2, fS_2 and Ni contents (Doyle & Naldrett, 1987; Fonseca et al., 2008; Wendlandt, 1982). As yet, however, no model exists for determining the O contents of sulphide melts in equilibrium with mantle assemblages. The O content may be an important factor controlling the mobility and geochemistry of sulphides. Oxygen exerts the main influence on the dihedral angle between sulphide melts and olivine, such that high O-bearing melts may potentially form interconnected networks (Gaetani and Grove 1999; Terasaki et al. 2005; Zhang et al. 2018). Kiseeva and Wood (2015) showed that sulphide melt O contents also control the partitioning of many chalcophile elements with coexisting silicate melts.

Although rarely reported, O contents of sulphide melts hosted by olivine xenocrysts range up to approximately 16 wt. %, with samples showing O concentrations higher than around 4 wt. % generally also showing signs of alteration (Alard et al., 2011; Aulbach et al., 2004b; Delpech et al., 2012). Olivine is unlikely to be an inert container with respect to sulphide O contents, however, which may well reequilibrate during ascent to the surface and cooling. Diamonds, on the other hand, should provide a more unreactive host, as long as they remain crack-free. Oxygen concentrations of sulphide inclusions in diamonds are rarely measured, however, either because studies focus more on the sulphide trace element concentrations, or radiogenic

isotopes, or because analyzing the bulk composition is challenging, due to the initially homogeneous sulphides recrystallizing into the previously described phases on cooling (McDonald et al., 2017). The presence of magnetite in diamond sulphide inclusion assemblages has been reported, however, (Bulanova et al., 1996; Jacob et al., 2016) and measurements of the bulk oxygen contents do exist. Davies et al. (1999, 2004) measured oxygen concentrations in the range of 0.2 – 12 wt. % for sulphide diamond inclusions of both peridotitic and eclogitic associations. Sulphide inclusion Ni contents are used to characterize this association as either peridotite (>12 wt. % Ni), pyroxenitic (8–12 wt. % Ni) or eclogitic (< 8 wt. % Ni) (Aulbach et al., 2009; Deines & Harris, 1995; Yefimova et al., 1983). On the other hand, Bulanova et al. (1996) found magnetite to be rare in sulphide inclusions within a suite of Yakutian diamonds and, in what can be viewed as a cautionary note, observed that assemblages that did contain magnetite appeared to be associated with cracks, implying an epigenetic origin.

In an attempt to clarify what factors may control the O contents of sulphide assemblages in the mantle, and particularly under conditions where lithospheric diamonds may form, we have performed high-pressure and high-temperature experiments on sulphide melts in equilibrium with a peridotite assemblage. We examine how factors such as pressure, temperature, oxygen fugacity, silicate iron oxide content, sulphide Ni content and metal/sulphur ratio influence the O contents and, with the aid of further studies from the literature, we propose a preliminary model for describing sulphide oxygen contents in mantle peridotite assemblages. Finally, we also demonstrate that Mössbauer spectroscopy could be used as a non-destructive method to determine the O content of sulphide inclusions in diamonds, potentially while the inclusions are still hosted in the diamonds (McCammon et al., 1997, 1998).

5.2 Methods

Starting materials were prepared using reagent-grade oxide and carbonate powders. The silicate bulk composition employed is close to KLB-1 peridotite (Davis et al., 2009), but the FeO content was varied between 8.1 and 17.6 wt. % (supplementary Table A.2.1). Each silicate mixture was ground under ethanol in an agate mortar for 30–40 minutes and subsequently reduced and decarbonated for 24 hours in a 1 atm $CO:CO_2$ gas mixing furnace using a Pt cage at 1100 °C and an oxygen fugacity 2 log units below the Fayalite-Magnetite–Quartz buffer (FMQ; O'Neill 1987).

Sulphides were added to the silicate material as reagent grade FeS powder in a 30:70 weight proportion of sulphide to silicate. In order to recreate natural sulphide inclusion compositions Ni and Cu were added as metals (mixed with the sulphide) to some experiments. Additionally, we added Ir metal powder as a redox sensor to calculate the oxygen fugacity of the experiments (Stagno & Frost, 2010). In order to saturate the sulphide phase and have a coexisting Fe-Ir alloy, the Ir content of some experiments had to be raised up to 5 wt. %. To promote equilibrium between sulphide melt and silicate mineral phases, between 1 and 10 wt. % of either $Mg(OH)_2$ or $MgCO_3$ were added to most of the starting materials as a flux to stabilise the formation of a silicate-bearing melt phase. Details of the starting mixtures employed in each experiment are reported in Table 5.1.

Experiments were performed using a 1000 tonne and a 5000 tonne multi-anvil press. A Cr_2O_3-doped MgO octahedron pressure medium was used with an edge length of 18 mm. Stepped graphite (<6 GPa) or $LaCrO_3$ (>6 GPa) resistive heaters were used inside a thermally insulating sleeve of ZrO_2. Samples were placed in a 2 mm outer and 1 mm inner diameter graphite or single crystal MgO (above 8 GPa) capsule, with a 1.5 mm sample length, which was inserted into the furnace inside an MgO sleeve. A type D ($W_{97}Re_3$–$W_{75}Re_{25}$) thermocouple inserted axially was in contact with a thin (~ 0.3 mm) MgO disk placed on the top of the sample capsule. The MgO disk prevents damage to the soft graphite capsule by the thermocouple. The estimated uncertainty of the temperature measurements due to the length of the sample is ±50K (Rubie 1999; Hernlund et al. 2006). A sketch of the high-pressure assembly is given in the supplementary Figure A.2.1.

Following the compression to targeted pressures between 3 and 13 GPa, samples were heated up to target temperatures (1300 – 1819 °C) by increasing the electric power to the heater. When using graphite capsules, experiments were first heated to 800–900 °C for 4 hours in order to sinter the graphite capsules, before being raised to the target temperature. This step helps to prevent the escape of sulphide melt during the experimental run. Run times of experiments at target temperature ranged from 2–24 hours depending on the temperature. Details of the experimental conditions are given in Table 5.1. The experiments were quenched by switching off the electrical power to the heater and then decompressed overnight to room pressure. Recovered samples were mounted in epoxy resin and ground and polished for chemical analysis.

Table 5.1: Summary of all experimental run conditions and products.

Run No.	*P* (GPa)	*T* (°C)	Capsule material	Starting materials			Run time (hrs.)	Coexisting phases [b]
				Silicate	Sulphide	Flux		
H4662	3	1819[a]	Graphite	A	FeS, Ir(1)	$Mg(OH)_2$(1)	6	sul., ol., sil.
Z1761	5	1735[a]	Graphite	A	FeS, Ir(1)	$Mg(OH)_2$(1)	2	sul., ol., opx., sil.
Z1775	5	1450	Graphite	B	FeS, Ir(2)	$MgCO_3$(10)	5	sul., ol., opx., sil.
Z1780	5	1450	Graphite	B	FeS, Ir(5)	$MgCO_3$(10)	5	sul., ol., opx., sil., aly.
Z1788	5	1300	Graphite	B	FeS, Ir(5)	$MgCO_3$(10)	5	sul., ol., opx., gt., aly.
Z1789	5	1600	Graphite	B	FeS, Ir(5)	$MgCO_3$(5)	5	sul., ol., opx., sil.
Z1793	5	1562[a]	Graphite	C	FeS, Ir(5)	-	5	sul., ol., opx., gt., sil., aly.
Z1864	5	1618[a]	Graphite	D	FeS, Ir(5)	-	5	sul., ol., opx., sil., aly.
H4958	5	1600	Graphite	B	FeS, Mo, Cu, Ni	$MgCO_3$(1)	5	sul., ol., cpx.
H4960	5	1480	Graphite	B	FeS, Mo, Cu, Ni	$MgCO_3$(1)	5	sul., ol., cpx.
Z1960	5	1320	Graphite	B	FeS, Mo, Cu, Ni	$MgCO_3$(1)	7	sul., ol., opx.
H5560-1	5	1500	Graphite	B	FeS, NiS(10)	$MgCO_3$(5)	5	sul., ol., cpx., sil.
H5560-2	5	1500	Graphite	B	FeS, NiS(50)	$MgCO_3$(5)	5	sul., ol., opx., sil.
H5561	5	1500	Graphite	B	NiS	$MgCO_3$(5)	6	sul., ol., opx, sil.
Z2207	5	1500	Graphite	F	FeS, NiS(50)	-	24	sul., ol., opx., sil.
Z1778	7	1600	Graphite	B	FeS, Ir(2)	$MgCO_3$(10)	6	sul., ol., opx., sil.
Z1869	8	1700	Graphite	C	FeS, Ir(5)	-	5	sul., ol., sil.
Z1885	8	1500	Graphite	B	FeS, Ir(5)	$MgCO_3$(5)	5	sul., ol., opx., gt., sil.
Z1912	8	1300	MgO	B	FeS	$MgCO_3$(1)	10	sul., ol., gt.
Z1915	11	1300	MgO	B	FeS	$MgCO_3$(1)	24	sul., ol., gt.
Z1999	13	1520	MgO	E	FeS, Ni	-	12	sul., ol., cpx.

A, B, C, D – Silicate composition, modified KLB-1 after Davis et al. (2009) with variable FeO content.
E – simplified olivine + clino-enstatite composition
F – Fe rich olivine $(Mg_{0.7}Fe_{0.3})_2SiO_4$ + 5 % SiO_2 starting mixture
Full details of A, B, C, D, E and F compositions are given in the supplementary Table A.2.1.
Numbers within brackets are added amounts (in wt. %) of $Mg(OH)_2$ and $MgCO_3$ flux in silicates, and Ir, NiS in FeS. Amount of added metals are ~1 wt. % of Mo, ~3 wt. % of Cu and ~20 wt. % of Ni in sulphide.
[a] Temperatures were determined using olivine-melt-thermometer (Putirka, 2008; Putirka et al., 2007) due to issues with thermocouple measurements during experiments.
[b] Sulphide melt–sul., olivine–ol., spinel–sp., clinopyroxene–cpx., orthopyroxene–opx., garnet–gt., ferropericlase–fp., silicate melt–sil., Fe-Ir alloy–aly.

Chemical analyses were performed with a JEOL JXA 8200 electron probe micro analyser (EPMA) in wavelength dispersive X-ray spectroscopy (WDS) mode. For silicate phases a 15 kV accelerating voltage and 15 nA probe current was employed. Sulphides and Ir-Fe alloy were analysed with a 20 kV acceleration voltage and 20 nA probe current. Oxygen in the sulphides was measured using a LDE 1 (Kα) crystal in the WD spectrometer. Counting times were 20 s for major elements and 60 s for minor elements, with half of each counting time used for the respective backgrounds. We used a focused electron beam to analyse the mineral phases, and

a defocused beam with a diameter of 10 –30 µm for the sulphide and silicate melt, which commonly show a spatially inhomogeneous quench texture. The beam diameter was varied for different samples depending on the size of the quench textures. Standards employed were natural silicate minerals and oxides for silicate analyses and pure metals and sulphides for sulphide and alloy phases (supplementary Table A.2.2). In order to check the oxygen-free background level, we performed analyses of freshly polished oxygen-free standards of FeS_2, pyrrhotite, Fe metal and FeSi alloy, following the methodology of Fonseca et al. (2008). In contrast to Fonseca et al. (2008), however, we found background oxygen levels of 0.06 ± 0.04 wt. % and so applied no correction to the oxygen analyses to account for an apparent oxygen contribution from the background. We also analysed a series of secondary standards during each session in order to ensure internal consistency. Matrix corrections were performed using the "φρ-z" method for silicates, whereas the "ZAF" method was used for sulphide melt and alloy phases.

A Mössbauer spectroscopy measurement was performed on a mass of quenched sulphide melt with a diameter of approximately 200 µm separated from sample Z1778 (7 GPa, 1600 °C). The biggest sulphide mass in the sample (approximately 200 µm diameter) was liberated from the rest of the silicate assemblage and mounted in epoxy resin. The separated sulphide was then parallel polished to create a section that was approximately 100 µm thick. A 25 µm thick Ta foil was placed over the section with the sample exposed through a 200 µm diameter hole. The Ta foil absorbs more than 99% of the 14.4 keV gamma rays, which acts as a collimator. A point source Mössbauer spectrometer (McCammon et al. 1997; 1998) (specific activity ≥2000 mCi/cm^2) was employed with a collection time of just over 6 days.

Transmission electron microscopy (TEM) measurements were also performed on a quenched sulphide melt sample synthesized at 3 GPa and 1400 °C using similar methods as described above (Sample number V1045; Armstrong 2018). A thick section (~30 µm) of the sample was glued onto a 3 mm sized Mo grid and subsequently thinned to electron transparency using Ar ion milling. The sample was observed in a 200 kV analytical transmission electron microscope (ATEM, FEI Titan G2 80-200 S/TEM) equipped with an energy-dispersive X-ray spectrometer (EDXS, Bruker QUANTAX silicon drift detector). For phase identification, selected area electron diffraction (SAED), bright field TEM images, high angle annular dark field (HAADF) scanning TEM images, and EDX element maps were obtained.

5.3 Results

The experimental run products consisted of silicate mineral phases, mainly olivine and orthopyroxene, quenched silicate melt and quenched sulphide melt. In some experiments an Fe-Ir alloy was also present. A complete list of phases in each experiment is given in Table 5.1. Olivine Fe/(Fe+Mg) ratios (X_{Fe}^{ol}) vary between the experiments from approximately 0.04 to 0.25. The iron contents of coexisting orthopyroxene are in excellent agreement with the predictions of previous models (Von Seckendorff and O'Neill 1993), with the olivine - orthopyroxene Fe-Mg exchange coefficient ($K_D^{Fe-Mg} = [X_{Fe}^{Ol}\, X_{Mg}^{Opx}]/[X_{Fe}^{Opx}\, X_{Mg}^{Ol}]$) showing very little variation with either pressure or temperature over the conditions of this study. Proportions of silicate melt fractions varied with temperature and with the amount of flux added to the experiments. In most samples, silicate melt accumulated in the upper section of the capsule but as shown in Figure 5.1-a, the capsule length was <1.5 mm so thermal gradients were likely to be <50 °C (Hernlund et al., 2006; Rubie, 1999).

Quenched sulphides generally formed rounded melt globules, which become more irregular in shape when surrounded by silicate minerals (Fig. 5.1-c). Quenched sulphide melts viewed in backscattered electron images (Fig. 5.1-b) are heterogenous and contain regularly spaced regions of a lighter grey, often elongated, sulphide phase separated by dark grey interstitial oxygen-rich material. If sufficient Ir was added to the experiments an additional Fe-Ir alloy phase formed, which can be distinguished from quenched alloy originally dissolved in the sulphide melt because it forms euhedral crystals with sizes up to 30 µm (Fig. 5.1-a). This alloy phase was, nonetheless, generally always found in contact with blobs of sulphide melt (Fig. 5.1-a). To capture the average composition of the heterogeneously quenched sulphide melt globules, they were analysed with a defocused beam, generally of 10-20 µm diameter. By using a defocused beam, average compositions of the quenched melts were obtained, with the choice of beam diameter (10-20 µm) depending on the grain size of the quenched crystals within the sulphides. The same method was applied to the silicate melt analyses, where in some cases the beam diameter was increased up to 30 µm. Sulphide blobs smaller than 10 µm were avoided because they could potentially have re-equilibrated with surrounding silicates during quenching (O'Neill et al., 1998). The standard deviation (1σ) reported for each sulphide melt composition is determined from the average of at least 14 but up to 69 individual melt analyses (supplementary Table A.2.4). Carbon contents in sulphide melt have been measured by Zhang and Hirschmann (2012) from experiments performed under similar conditions. They reported

negligible C concentrations for sulphide melts with S contents >20 wt. %. Sulphur contents in the present study were above 30 wt. %, so that the sulphide melts should not contain C, as reflected by overall good totals of EPMA analyses.

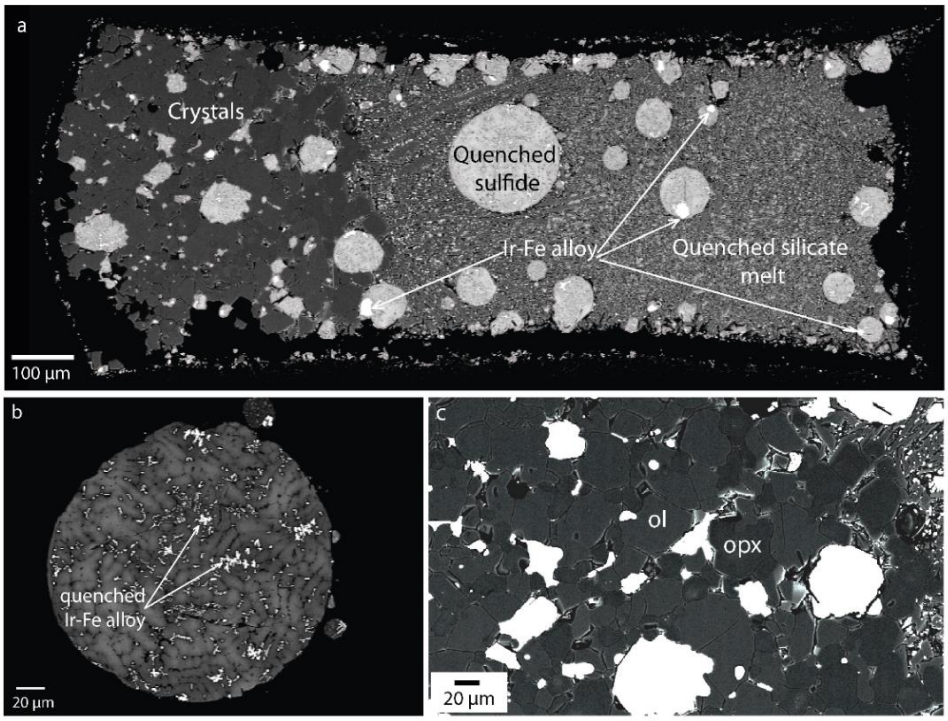

Figure 5.1: (a) Sample, Z1780 (5 GPa, 1450 °C), in a graphite capsule containing sulphide melt globules within both quenched silicate melt and crystals of a subsolidus peridotite assemblage. Ir-Fe alloy redox sensor is also present in some sulphide melts. This is a composite of two back scattered electron images with different brightness and contrast settings to show the textural characteristics of both silicate and sulphide phases. **(b)** A quenched sulphide globule showing a typical quench texture with crystallized sulphide (light grey), an interstitial oxygen-rich phase (dark grey), and quenched Fe-Ir alloy (white). **(c)** Silicate grains of olivine and orthopyroxene coexisting with quenched sulphide melt.

Sulphide melting relations are in good agreement with those of Zhang and Hirschmann (2016). Experiments Z1912 and Z1915 at 8 and 11 GPa and 1300 °C are likely subsolidus but their oxygen contents actually agree with the resulting temperature trend. As shown in Figure 5.2, the variation in excess O and S in the sulphide melts from this study, determined as the mole fractions of S+O-M, where M is the total mole fraction of metal atoms, varied from 0.03 to 0.12, which is a similar range to that found in many sulphide inclusions in diamonds (Davies et al. 1999; 2004). The highest sulphide oxygen concentration corresponds to 3.7 wt. % in sample Z1864 from 5 GPa and 1618 °C. When the O/(O+S) ratio is examined, along with

numerous other high-pressure studies from the literature, which also contained either coexisting olivine or silicate melts, there appears to be no clear dependence of O content on the excess anion content. Although some relationship probably exists, as seen in room pressure studies (Fonseca et al., 2008; Kress, 1997) it appears not to be a dominant factor at least for S+O-M>0. Although possibly arising from incomplete data coverage, it does appear that metal-rich samples have generally lower O contents and certainly the Ni-bearing samples appear to have consistently lower O contents, aside from a few outliers. Some of the Ni-bearing samples extend to metal-rich values as a result of adding Ni to the experiments as metal rather than NiS. This raises some uncertainty as to whether the low O contents may be related to high metal or high Ni contents.

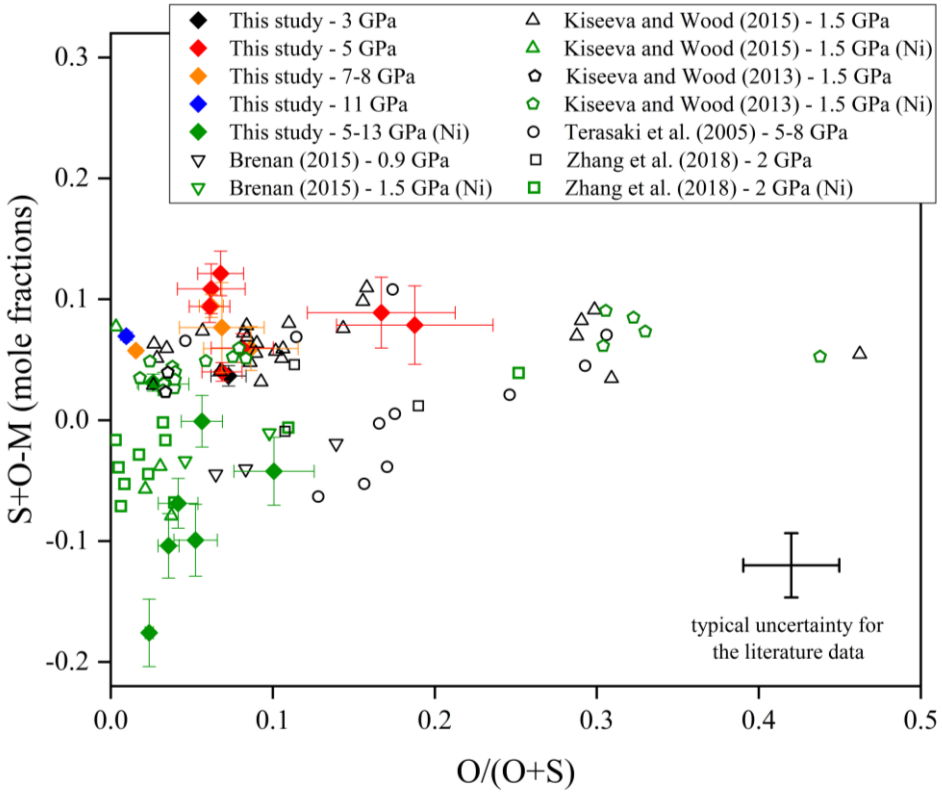

Figure 5.2: The variation of excess anions (mole fractions of sulphur + oxygen – metal) as a function of the normalized O content (expressed as oxygen/total anions) in sulphide. This study filled symbols and literature data open symbols. Green symbols (both open and filled) are Ni-bearing samples. Individual error bars are shown only for this study, with a typical uncertainty for literature data indicated.

The use of graphite capsules and the presence of carbonate-bearing melts in many of the experiments constrains the experimental oxygen fugacities to be below the enstatite-magnesite-

olivine-diamond (EMOD) buffer, defined by the equilibrium $MgSiO_3 + MgCO_3 = Mg_2SiO_4 + C + O_2$). Dilution of the carbonate component of the melt by silicate components lowers the fo_2 below EMOD. Using the expression given by Stagno and Frost (2010) the fo_2 can be estimated from the melt CO_2 content (supplementary Table A.2.3), which can, in turn, be approximated from the deficit in EPMA analysis totals (e.g. Stagno and Frost 2010). In four experiments sufficient Ir was added to saturate the sulphide phase and force the existence of an Ir-dominated alloy. The Fe content of this alloy is then sensitive to the oxygen fugacity (Woodland & O'Neill, 1997), which can be accurately calculated using the equilibrium $2Fe_2SiO_4 = 2FeSiO_3 + 2Fe + O_2$ and employing thermodynamic data given in Stagno and Frost (2010). All values are calculated relative to the FMQ buffer (Ballhaus et al., 1991) in order to remove *P* and *T* effects.

Table 5.2: Summary of experimental results

Run No.	*P* (GPa)	*T* (°C)	X_{Fe}^{Ol}	X_{Fe}^{En}	X_{FeO}^{Sul}	X_{NiS}^{Sul}	X_{Fe}^{Aly}	$X_{CO_2}^{Melt}$	log fo_2 (ΔFMQ)	
									A	*B*
H4662	3	1819	0.058(3)	0.06	0.08(1)			0.007(5)		-4.0(4)
Z1761	5	1735	0.071(5)	0.067(4)	0.07(1)			0.008(4)		-3.9(2)
Z1775	5	1450	0.11(1)	0.11(1)	0.09(2)			0.15(3)		-2.3(1)
Z1780	5	1450	0.11(1)	0.11(1)	0.08(2)		0.14(3)	0.07(2)	-2.0(3)	-2.7(1)
Z1788	5	1300	0.14(2)	0.13(1)	0.07(2)		0.14(3)		-1.8(1)	
Z1789	5	1600	0.09(1)	0.08(1)	0.07(1)			0.04(1)		-3.1(1)
Z1793	5	1562	0.19(3)	0.17(2)	0.19(5)		0.23(6)	0.05(2)	-2.3(2)	-2.9(2)
Z1864	5	1618	0.19(3)	0.17(2)	0.21(5)		0.30(9)	0.01(1)	-2.9(3)	-3.5(4)
H4958	5	1600	0.13(1)	0.12	0.04(1)	0.36(4)				
H4960	5	1480	0.17(2)	0.12(1)	0.03(1)	0.41(3)				
Z1960	5	1320	0.14(2)	0.13(1)	0.04(1)	0.33(2)				
H5560-1	5	1500	0.064(4)	0.17(4)	0.03(1)	0.14(1)		0.07(4)		-2.7(3)
H5560-2	5	1500	0.059(4)	0.054(4)	0.02(1)	0.53(5)		0.08(1)		-2.7(1)
H5561	5	1500	0.07(1)	0.065(4)	0.018(3)	0.73(5)		0.06(1)		-2.8(1)
Z2207	5	1500	0.25(4)	0.21(3)	0.09(2)	0.36(4)		0.04(2)		-3.0(3)
Z1778	7	1600	0.10(1)	0.09(1)	0.09(3)			0.09(3)		-2.9(1)
Z1869	8	1700	0.07(1)	0.07	0.07(3)			0.08(1)		-3.2(1)
Z1885	8	1500	0.10(1)	0.09(1)	0.07(1)			0.11(3)		-2.7(1)
Z1912	8	1300	0.05(1)	0.05	0.017(2)					
Z1915	11	1300	0.03(1)	0.03	0.01(1)					
Z1999	13	1520	0.06(1)	0.06(1)	0.03(2)	0.26(1)				

Notes. X_{Fe}^{Ol} and X_{Fe}^{En} are the molar Fe/(Fe+Mg) ratios of olivine and enstatite (enstatite values without uncertainties are estimated); X_{FeO}^{Sul} and X_{NiS}^{Sul} are mole fractions of FeO and NiS in sulphide melt. X_{Fe}^{Aly} is the molar Fe/(Fe+Ir) ratio of Ir–Fe alloy. $X_{CO_2}^{Melt}$ is the mole fraction of CO_2 in the silicate melt determined from the deficit in EPMA analysis totals. ΔFMQ is oxygen fugacity relative to the Fayalite–Magnetite–Quartz buffer (O'Neill 1987) calculated using, A, Fe-Ir alloy and B, the concentration of CO_2 in the silicate-carbonate melt (Stagno & Frost, 2010).

It is interesting to note that in comparison to room pressure experiments (Fonseca et al., 2011), much greater sulphide Ir contents are required to reach Ir-alloy saturation at 5 GPa. The solubility of Ir in room pressure sulphide melt has been shown to depend on temperature, sulphur fugacity and sulphide oxygen content but values are reported to be less than ~1 wt. % at temperatures up to 1400 °C (Fonseca et al. 2011). At 5 GPa, however, our experiments show that sulphide Ir concentrations varied between 3.8 and 19.9 wt. % at Ir-alloy saturation, which implies an important role of pressure on the exsolution of noble metal alloys from sulphides. The main cause of the Ir variation in the sulphide melt at these high-pressure conditions appears to be an inverse relationship with the sulphide oxygen content, which varied between 3.7 and 1.1 wt. %. This is a similar but stronger oxygen relationship to that found at room pressure (Fonseca et al., 2011). The mole fractions of Ir in the sulphide melt are still only ~ 0.05 at maximum, however, and there is no indication that this Ir concentration significantly influences the sulphide oxygen contents.

Oxygen fugacities calculated with both methods are reported in Table 5.2 and shown in Figure 5.3-a. Where both methods can be employed the carbonate-graphite equilibrium gives values which are consistently around 0.6 log units lower, which probably reflects inaccuracies in the CO_2 concentration estimated using the EMPA totals due to the presence of absorbed water and defects (Hughes et al., 2019). The experimental oxygen fugacities range from approximately 1.8 to 4.0 log units below the FMQ buffer, which is similar to the range obtained for the majority of peridotite xenoliths from the subcratonic lithospheric mantle (Stagno et al., 2013) and most likely covers the range relevant to diamond formation in the upper mantle. Within this range, which spans over 3 log units together with the results of Brenan (2015), there is no obvious dependence with the sulphide oxygen content. In contrast Kress (1997) and Fonseca et al. (2008) found sulphide oxygen contents to increase quite strongly with log fO_2 at room pressure conditions. In fact, the expression derived by Fonseca et al. (2008) for 1 bar sulphide melt oxygen contents, predicts an order of magnitude increase in oxygen over an equivalent range of fO_2, at constant fS_2 and temperature, as shown in Figure 5.3-a for a log fS_2 of -2 and a temperature of 1500 °C. A possible explanation is that the effect of fO_2 is subtler at high pressure conditions and not apparent in Figure 5.3-a due to the fact that the data are not collected at either constant fS_2 or temperature. Furthermore, as the fO_2 in this study is in most instances governed by the coexistence of graphite and carbonate-bearing melt, higher temperatures result in generally lower fO_2, as the melt carbonate component becomes diluted. Consequently, it is possible that effects of increasing temperature and decreasing fO_2 on the sulphide oxygen

contents cancel out to a certain extent, although the same effect is likely to occur in the mantle to some extent as volatile contents will always be diluted by silicate components at higher temperatures. The main factor apparently governing the oxygen contents of the two samples displaying the highest contents in Figure 5.3-a, however, is the FeO content of coexisting olivine.

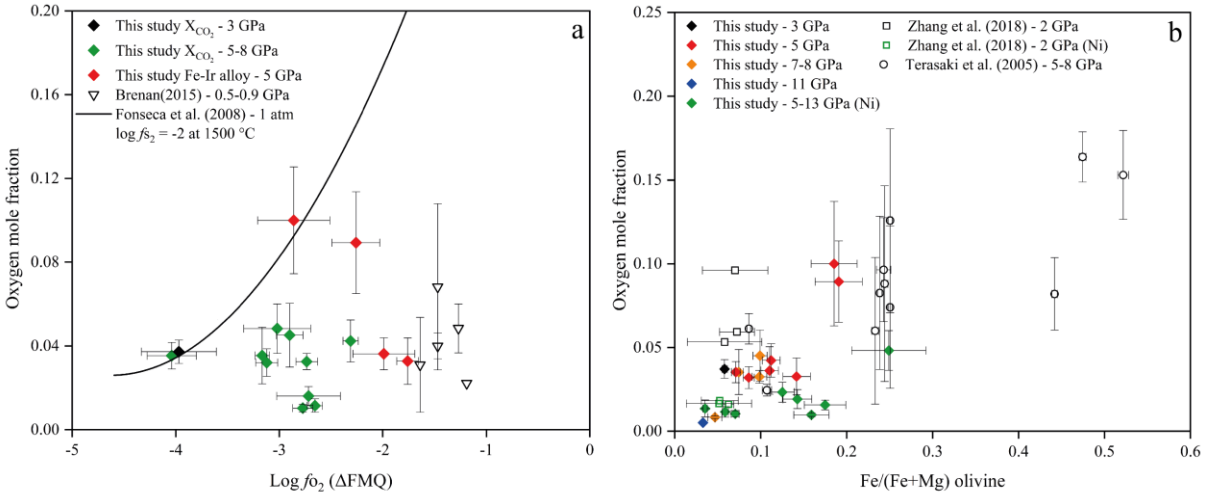

Figure 5.3: (a) Experimental oxygen contents (mole fraction) in sulphide melts as a function of oxygen fugacity normalized to the FMQ buffer. Experimental conditions – this study P = 3-8 GPa, T = 1300-1819 °C; Brenan (2015) P = 0.9-0.5 GPa, T = 1200-1300 °C. The curve is calculated from the 1 atmosphere oxygen equation of Fonseca et al. (2008) at a constant log fs_2 of -2 and at 1500 °C. (b) Experimental sulphide oxygen contents as a function of olivine molar Fe/(Fe+Mg) ratio. Uncertainties indicated are 1σ.

A correlation between the O content of sulphide melts and the FeO concentration in coexisting silicate melts has been previously reported (Boujibar et al., 2019; Kiseeva & Wood, 2013a, 2015). A broadly similar relationship can be observed in the results of this study when sulphide O contents are plotted as a function of the iron content of coexisting olivine, as shown in Figure 5.3-b. The increase in Fe/(Fe+Mg) ratio from approximately 0.03 to 0.25 results in a clear increase in the mole fraction of O in the sulphide melt from near zero to approximately 0.1. The experiments of Terasaki et al. (2005), which were performed up to an Fe/(Fe+Mg) ratio of over 0.5 are generally consistent with this trend. Nonetheless, for a given olivine Fe content there is still a considerable scatter in sulphide oxygen contents at least between 3 and 11 GPa. As will be seen, most of this variation can be explained by changing temperature. Previous experimental studies have proposed that the presence of Ni reduces the O content of sulphide

melts at otherwise comparable conditions (Boujibar et al., 2019; Fonseca et al., 2008; Kiseeva & Wood, 2015), this is also apparent in the current results, as discussed later. As peridotitic sulphide inclusions in natural diamonds have Ni contents in the range 12 to 60 wt. %, this effect is important.

Analysing the O content of diamond sulphide inclusions is inherently problematic due to potential heterogeneity in the distribution of oxides throughout the assemblage. One way around this would be to first rehomogenise the inclusions at high-temperature before break-out and analysis, following the procedure of McDonald et al. (2017). Another possibility would be to find a technique that allows the mineral proportions in the sulphide assemblage to be determined, ideally in a non-destructive manner before the diamond is even opened.

In order to test such a possibility a Mössbauer spectroscopy measurement was performed on a globule of quenched sulphide with a diameter of approximately 200 µm separated from the silicate melt of sample Z1778 (7 GPa, 1600 °C). The resulting spectrum of the Ni-free sulphide assemblage is dominated by a magnetic sextet signal from FeS, but a signal from magnetite is also clearly distinguishable (Fig. 5.4-a), from which a sample magnetite content of 8 ± 2 wt. % can be determined from the intensity ratios. This corresponds to an O content of 2.28 ± 0.55 wt. % which is within the error of the average EPMA measurement for this sample of 1.70 ± 0.49 wt. % (i.e. 6.16 ± 1.78 wt. % magnetite). The EPMA O value is an average of multiple analyses (30 points) distributed in several sulphide globules, whereas the Mössbauer measurement is from only a single globule. Thus, a level of inhomogeneity in the O concentration contributes to this mismatch. In order to confirm that O is only hosted by magnetite a TEM analysis was performed on another quenched sulphide assemblage, this time Ni-bearing, produced in a similar experiment (V1045) conducted at 3 GPa, 1400 °C (Armstrong, 2018). Selected area electron diffraction (SAED) and bright field imaging (Fig. 5.4-b), as well as high angle annular dark field imaging, and element maps (supplementary Fig. A.2.2) show that O is indeed hosted by quenched magnetite, which is closely associated with Fe-Ni alloy and surrounded by FeS. It is quite likely that the alloy and magnetite form from an (Fe,Ni)O component during quenching. In a Mössbauer spectrum metal alloy would contribute to the sextet from FeS (e.g., Lehlooh and Mahmood 2002) and would not interfere with the two outer lines of the magnetite sextet (e.g., Lyubutin et al. 2009).

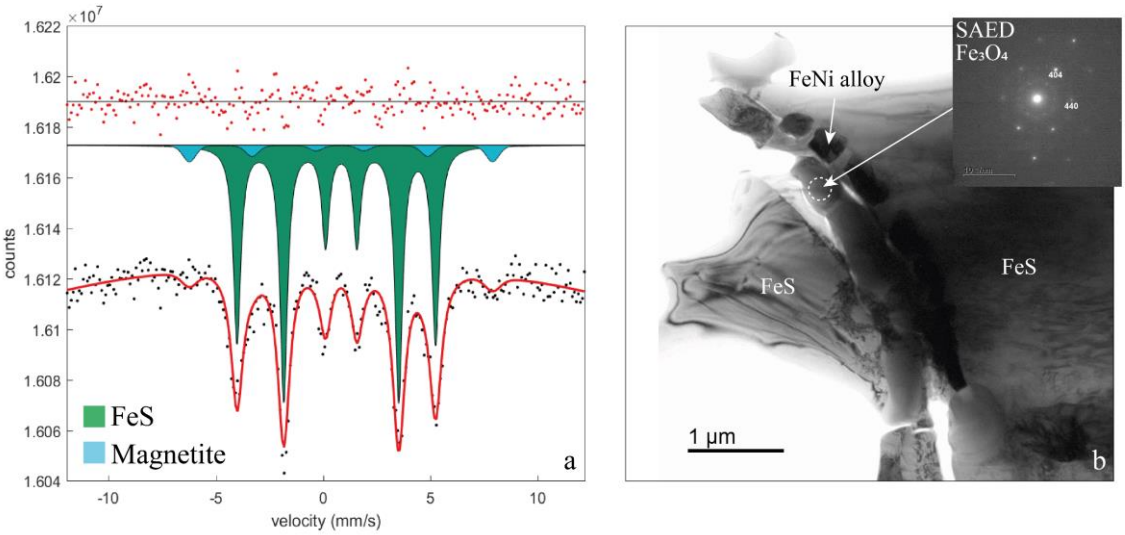

Figure 5.4: (a) Mössbauer spectrum collected for sample Z1778 (Ni free). The sextet in green is FeS and in blue is magnetite. **(b)** Bright field TEM image of a quenched sulphide melt assemblage (V1045) containing magnetite and Fe-Ni alloy. Inset in b is a selected area electron diffraction (SAED) pattern of magnetite.

Thus, Mössbauer measurements provide an effective and non-destructive method for determining the O concentration of sulphide assemblages. Although the current Mössbauer estimate has a large uncertainty, this could be reduced by using Synchrotron Mössbauer Source (SMS) spectroscopy, which has a much higher source flux (Potapkin et al., 2012; Rüffer & Chumakov, 1996). A high brilliance, small divergence beam would allow sulphide inclusions as small as 1 μm to be analysed for their magnetite, and therefore O, content while potentially still trapped in the diamonds. Although concentrations of other elements such as Ni and Cu would have to be determined independently, most likely through a chemical analysis of the exposed inclusion. Such a study would provide an estimate of the variability in oxygen contents among diamond sulphide inclusions.

5.4 Discussion

5.4.1 Thermodynamic model

In agreement with the results of Kiseeva and Wood (2015), an important control over the sulphide oxygen contents in our experiments comes from the FeO content of coexisting silicates. Given that at least at graphite saturation there does not appear to be a significant effect

of oxygen fugacity, it seems appropriate to describe the variation in sulphide oxygen content with the equilibrium:

$$\underset{\text{olivine}}{Fe_2SiO_4} = \underset{\text{orthopyroxene}}{FeSiO_3} + \underset{\text{sulphide melt}}{FeO} \quad (5.1)$$

and the corresponding FeO distribution coefficient, K_D:

$$K_D = \frac{X_{\mathrm{FeO}}^{\mathrm{Sul}} . X_{\mathrm{Fe}}^{\mathrm{Opx}}}{\left(X_{\mathrm{Fe}}^{\mathrm{Ol}}\right)^2} \quad (5.2)$$

where $X_{\mathrm{FeO}}^{\mathrm{Sul}}$ is the mole fraction of FeO in the sulphide melt and $X_{\mathrm{Fe}}^{\mathrm{Opx}}$ and $X_{\mathrm{Fe}}^{\mathrm{Ol}}$ are the molar $\mathrm{Fe}/(\mathrm{Fe}+\mathrm{Mg})$ ratios of orthopyroxene and olivine, respectively. The sulphide is described as a mixture of the components FeS, FeS_2 and FeO, in addition to Fe and NiS and other minor metal sulphides when necessary.

Figure 5.5 shows the dependence of K_D with temperature for the experiments in this study, with potentially a minor dependence also on pressure. Ni-bearing data show a greater variability due to the differences in Ni concentration. There are no previous experimental studies that we are aware of, that report sulphide oxygen contents and coexisting olivine and orthopyroxene compositions. However, both Terasaki et al. (2005) and Zhang et al. (2018) report sulphide oxygen contents coexisting with olivine and using the relationship between olivine and orthopyroxene Fe-Mg partitioning, we can estimate fictive orthopyroxene compositions. We do this also for a few experiments performed in this study where melting resulted in the loss of orthopyroxene from the solid assemblage. The study of Terasaki et al. (2005) was also performed using graphite capsules and for the study of Zhang et al. (2018) we only plot data where graphite capsules were employed, as it is possible that different oxygen dependencies occur at significantly higher fo_2. This compositional range, however, is at least consistent with most sulphide inclusions reported for lithospheric diamonds (Davies et al. 1999; 2004). Although most of the data from Terasaki et al. (2005) are in good agreement with the trend from this study, even though they cover very large ranges of olivine Fe content, one data point is an outlier and the data of Zhang et al. (2018) from measurements at 2 GPa are also in poor agreement. It is difficult to understand how this variation arises, although one possibility might be that it is difficult to achieve an equilibrium oxygen concentration in the sulphide in the absence of a silicate-bearing melt phase in the experiments of Zhang et al. (2018).

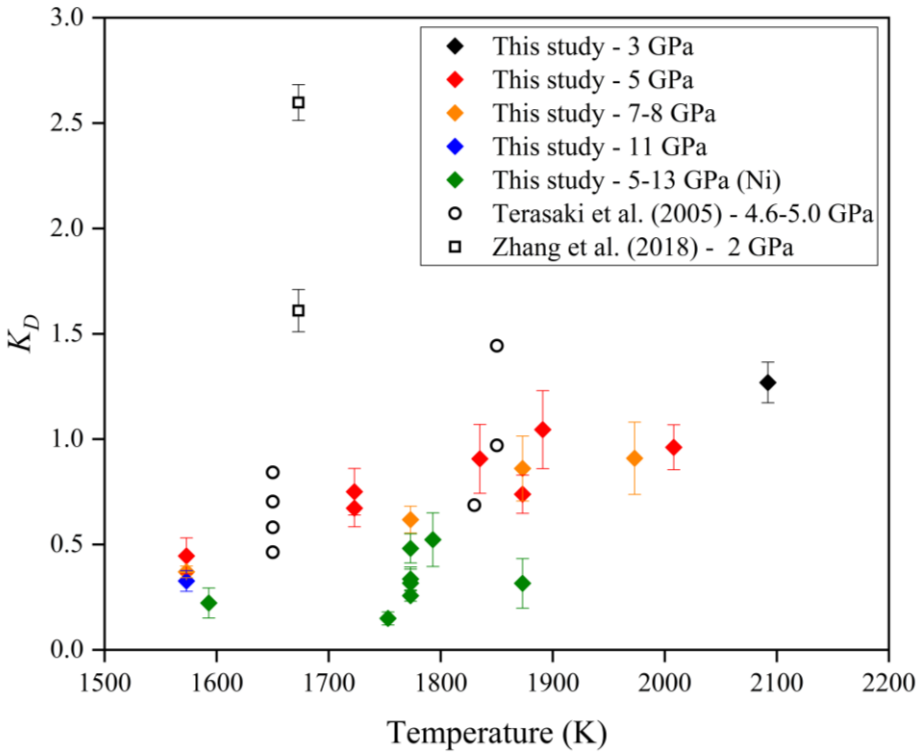

Figure 5.5: Distribution coefficient (K_D) dependence on experimental temperature. The K_D of FeO between the sulphide and silicate assemblage, calculated using equation 5.2, corelates positively with temperature. Literature data from experiments performed in graphite capsules.

We can describe the experimental K_D with a simple thermodynamic model where,

$$\Delta G^{o}_{(eq.1)} = \Delta H^{o} - T\Delta S^{o} + \Delta V(P-1) = -RT\ln K_D - RT\ln\frac{\gamma^{Sul}_{FeO}\ \gamma^{Opx}_{FeSiO_3}}{\gamma^{Ol}_{Fe_2SiO_4}} \qquad (5.3)$$

where γ^{Sul}_{FeO} is the activity coefficient for FeO in the sulphide melt and ΔH^{o}, ΔS^{o} and ΔV are the enthalpy, entropy, and volume changes, respectively, of the pure end members in equilibrium 5.1. We assume a symmetric mixing model for both olivine and enstatite solid-solutions, e.g.,

$$RT\ln\gamma^{Opx}_{Fe} = W^{Opx}_{Fe-Mg}\left(1 - X^{Opx}_{Fe}\right)^2 \qquad (5.4)$$

where W^{Opx}_{Fe-Mg} is a Margules interaction parameter. We find good agreement to the Fe-Mg partitioning data between olivine and orthopyroxene with interaction parameters for the two phases of 2000 and 1000 J/mol, respectively, on a single site basis (supplementary Fig. A.2.3).

The Fe-Mg partitioning data are in very good agreement with previous work (von Seckendorff and O'Neill 1993).

We examined different models for $\gamma_{\mathrm{FeO}}^{\mathrm{Sul}}$. Initially the effect of Ni was ignored and a simple binary mixing model was used that assumed the sulphide melt was simply a mixture of FeO and FeS i.e.,

$$RT \ln \gamma_{\mathrm{FeO}}^{\mathrm{Sul}} = W_{\mathrm{FeO-FeS}}^{\mathrm{Sul}} \left(1 - X_{\mathrm{FeO}}^{\mathrm{Sul}}\right)^2 \quad (5.5)$$

The value of $W_{\mathrm{FeO-FeS}}^{\mathrm{Sul}}$ was obtained by performing a least-squares fit to the Ni-free experimental data of this study, while simultaneously fitting ΔH^{o}, ΔS^{o} and ΔV in equation 5.3. No improvement in the quality of the fit was obtained by considering the presence of an FeS_2 component in the liquid and extending the mixing model to that of a symmetric ternary. To include the effects of Ni, however, a symmetric ternary model was employed i.e.,

$$RT \ln \gamma_{\mathrm{FeO}}^{\mathrm{Sul}} = W_{\mathrm{FeO-FeS}}^{\mathrm{Sul}} \left(1 - X_{\mathrm{FeO}}^{\mathrm{Sul}}\right)^2 + W_{\mathrm{FeO-NiS}}^{\mathrm{Sul}} \left(X_{\mathrm{NiS}}^{\mathrm{Sul}}\right)^2 + \left(1 - X_{\mathrm{FeO}}^{\mathrm{Sul}}\right) X_{\mathrm{NiS}}^{\mathrm{Sul}} \times \left(W_{\mathrm{FeO-FeS}}^{\mathrm{Sul}} + W_{\mathrm{FeO-NiS}}^{\mathrm{Sul}} - W_{\mathrm{FeS-NiS}}^{\mathrm{Sul}}\right) \quad (5.6)$$

where the first term is taken from the fit of equation 5.5. Ni-bearing data where S+O-M was significantly below zero were not included in the fitting to ensure that we only consider the effect of Ni, rather than the S/M ratio, which limited the Ni-bearing data to only four data points (H5560-1, H5560-2, H5561 and Z1999). The Ni data were then fitted to obtain $W_{\mathrm{FeO-FeS}}^{\mathrm{Sul}}$. Attempts to fit $W_{\mathrm{FeS-NiS}}^{\mathrm{Sul}}$ always returned a value of zero. Figure 5.6 shows the value of ΔG^{o} calculated for each experimental data point using equation (5.3) and the terms given in Table 5.3. The resulting fitting of these data using the values of ΔH^{o}, ΔS^{o} and ΔV given in Table 5.3 is shown calculated at 3 and 11 GPa in Figure 5.6.

Table 5.3: Thermodynamic model parameters

Parameter	Value
$W_{\mathrm{Fe-Mg}}^{\mathrm{Opx}}$	1.0 ± 0.3 kJ/mol
$W_{\mathrm{Fe-Mg}}^{\mathrm{Ol}}$	2.0 ± 0.2 kJ/mol
ΔH	-37.4 ± 8.3 kJ/mol
ΔS	-25.08 ± 1.4 J/mol/K
ΔV	-0.51 ± 0.02 kJ/GPa
$W_{\mathrm{FeO-FeS}}^{\mathrm{Sul}}$	14 ± 4 kJ
$W_{\mathrm{FeO-NiS}}^{\mathrm{Sul}}$	2.8 ± 0.3 kJ

Although the majority of the Ni-bearing data were not used in the fitting due to the data extending to values of S+O-M that were significantly less than zero, in Figure 5.7-a, it can be seen that when the resulting model is compared with these data and with those from the study of Zhang et al. (2018), there is a generally good agreement. However, it should be noted that here again there are multiple outliers, which are in poor agreement with the model and for which no explanation can be currently found.

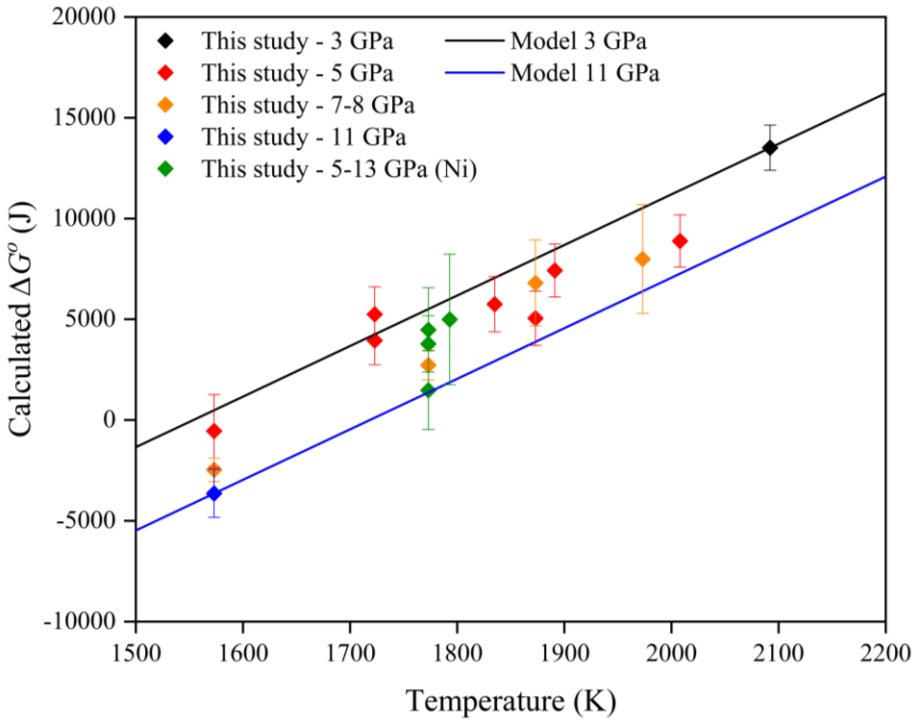

Figure 5.6: Calculated $\Delta G^{o}_{(eq.1)}$ of all experiments plotted as a function of the temperature. The lines show the *P* and *T* dependent fit of equation 5.3. Uncertainties calculated from the 1σ errors on the X^{Sul}_{FeO} determinations.

By substituting equations 5.2 and 5.6 into equation 5.3 and rearranging, we can obtain an expression for the temperature in terms of pressure, X^{Ol}_{Fe}, X^{Opx}_{Fe} $X^{Sul}_{FeO}$and X^{Sul}_{NiS} i.e.,

$$T = \{W^{Opx}_{Fe-Mg}(1 - X^{Opx}_{Fe})^2 + W^{Sul}_{FeO-FeS}\left(1 - X^{Sul}_{FeO}\right)^2 + W^{Sul}_{FeO-NiS}\left(X^{Sul}_{NiS}\right)^2 + \left(1 - X^{Sul}_{FeO}\right)X^{Sul}_{NiS}\left(W^{Sul}_{FeO-FeS} + W^{Sul}_{FeO-NiS}\right) - 2W^{Ol}_{Fe-Mg}\left(1 - X^{Ol}_{Fe}\right)^2 - \Delta H^{o} - \Delta V * P\}/\{-\Delta S^{o} - 8.314\ln(X^{sul}_{FeO}\, X^{Opx}_{Fe}/(X^{Ol}_{Fe})^2)\} \quad (5.7)$$

where *T* is in K and *P* in GPa. For convenience X^{Opx}_{Fe} can be replaced by (0.0039+0.8833X^{Ol}_{Fe}). In Figure 5.7-b the temperature calculated using this equation is compared to the experimental

temperatures. For the Ni-free experiments the largest deviation between the model and the experiments is 74 K, while for the Ni-bearing samples the highest deviation among the low S+O-M samples is 135 K, although this sample is from the highest pressure investigated of 13 GPa. The largest uncertainty arises from the sulphide oxygen contents, with typical uncertainties of approximately 80 K. However, when sulphide oxygen contents drop below 1 wt. %, i.e. $X_{FeO}^{Sul} < 0.05$, which corresponds to samples with low olivine Fe content (Fe/[Fe+Mg] <0.05), uncertainties start to rise and approach 300 K as O contents reach approximately 0.2 wt %, i.e. $X_{FeO}^{Sul} \sim 0.01$. Much of the variation in the oxygen standard deviation arises from the inhomogeneity of the oxygen distribution in the samples, which is an inevitable consequence of analysing samples that crystallise on quenching. Uncertainties arising from the olivine or enstatite chemical compositions are small and at most 20 K and similar to assuming a pressure uncertainty of 1 GPa.

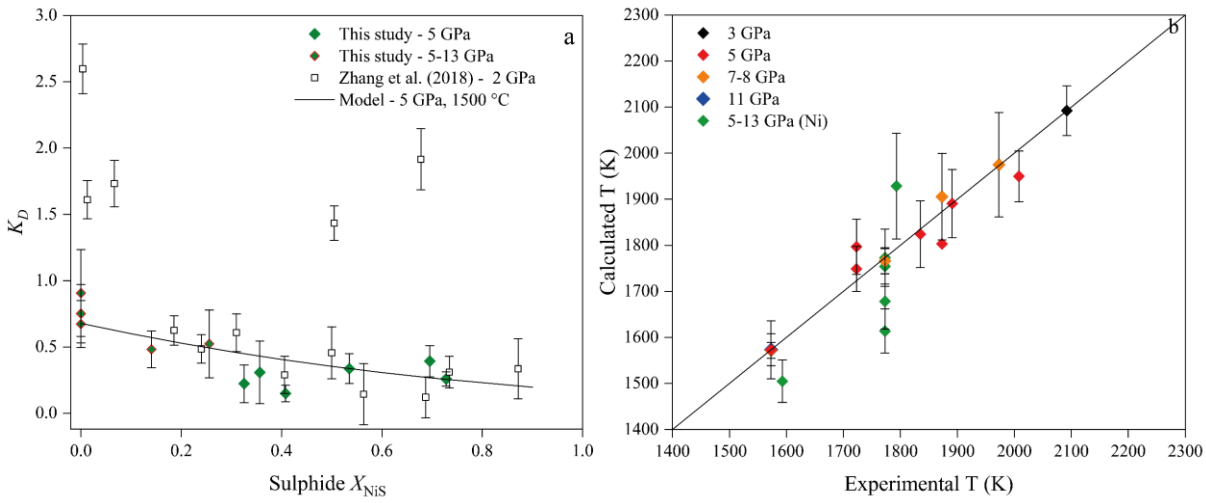

Figure 5.7: (a) Distribution coefficients (K_D – equation 5.2) as a function of Ni mole fraction in sulphide melt. Diamonds with red outline indicate data from this study between 5 and 13 GPa, 1400-1600 °C, that were used in the fitting procedure due to having S+O-M greater than or close to zero. Other Ni-bearing data with S+O-M<0 are shown in green. Small black squares are from Zhang et al. (2018) experiments at 2 GPa and 1400 °C. The black curve is calculated from the model at 5 GPa and 1500 °C. Uncertainties reported are 2σ. **(b)** Comparison between the experimental temperatures and those calculated using equation 5.7. Only Ni-bearing data where S+O-M close to 0 are plotted. Uncertainties are propagated from the errors on the sulphide melt FeO contents.

The effect of Ni introduces a large uncertainty because only data points with quite low Ni contents have S+O-M values close to or above zero. This appears to be also the case for the

majority of literature data, as shown in Figure 5.2, i.e. whenever Ni is added to such experiments, the excess metal cation content increases. This seems to have little to do with the way Ni is added to the experiments as we also added Ni as NiS. Although the model reproduces the O concentrations of samples with higher Ni contents, there is considerable scatter and some uncertainty remains as to whether the Ni or the excess metal cation content controls the O concentration. Sulphides in diamond inclusions do not show the same relationship between Ni and excess metal content as seen in the experiments (Davies et al. 1999; 2004). If we make the rather extreme alternative assumption that Ni does not affect the O content at all for samples with S+O-M>0, then for a sulphide with Ni/(Ni+Fe) ratio of 0.5 the temperature calculated with equation 5.7 would change by approximately 250 K.

5.4.2 The variation in oxygen content of sulphide melts in the mantle

We can use our model to calculate the O concentration that we expect for a sulphide melt in equilibrium with peridotite along a typical mantle adiabat within the top 200 km of the mantle. The main factor affecting the change in O content with depth is the sulphide Ni concentration, which can be determined from the sulphide-olivine Fe-Ni exchange experiments of Zhang et al. (2018). Zhang et al. (2018) propose a series of equations to describe this exchange, which results in the mantle sulphide Ni/(Ni+Fe) ratio reaching a maximum of approximately 0.65 at a depth of around 100 km and then subsequently decreasing to a value of approximately 0.3 at around 180 km. Zhang et al. (2018) proposed that the Ni/(Ni+Fe) ratio decreases as a result of a decrease in the fO_2 of the mantle and approaches 0.3 as the mantle fO_2 approaches ΔFMQ-3.

Figure 5.8 shows the sulphide O concentrations in wt. % calculated for a bulk silicate Earth composition (McDonough & Sun, 1995) along a 1320 °C mantle adiabat, using the mantle oxygen fugacity profile of Stagno et al. (2013), which results in a mantle fO_2 of ΔFMQ -3 at approximately 230 km. The curvature results purely from the change in sulphide Ni concentration and although it might appear that the O content would rise further, beyond this depth the metal cation content of the sulphide is likely to increase as the mantle fO_2 is projected to drop further (Z. Zhang et al., 2018) and the O model developed here may no longer be valid. For comparison, the dotted line in Figure 5.8 shows the O content if the Ni effect is ignored, which provides a prudent estimate of the uncertainty. Over this depth interval, typical peridotite rocks would not be expected to contain sulphides with oxygen contents greater than approximately 0.5±0.3 wt. %. At depths shallower than 100 km, graphite is likely exhausted

from a typical mantle assemblage (Stagno et al., 2013) and our model may also not hold at the resulting higher oxygen fugacities, potentially explaining higher oxygen contents in sulphide melts found inside olivines from some mantle xenoliths (Aulbach et al., 2004b). Although the variation in sulphide oxygen contents throughout this depth range is small, the results of Kiseeva and Wood (2015) imply that even this change would have a significant effect on the partitioning between sulphide and silicate melts of elements with high charges in the silicates such as Ga and Ge.

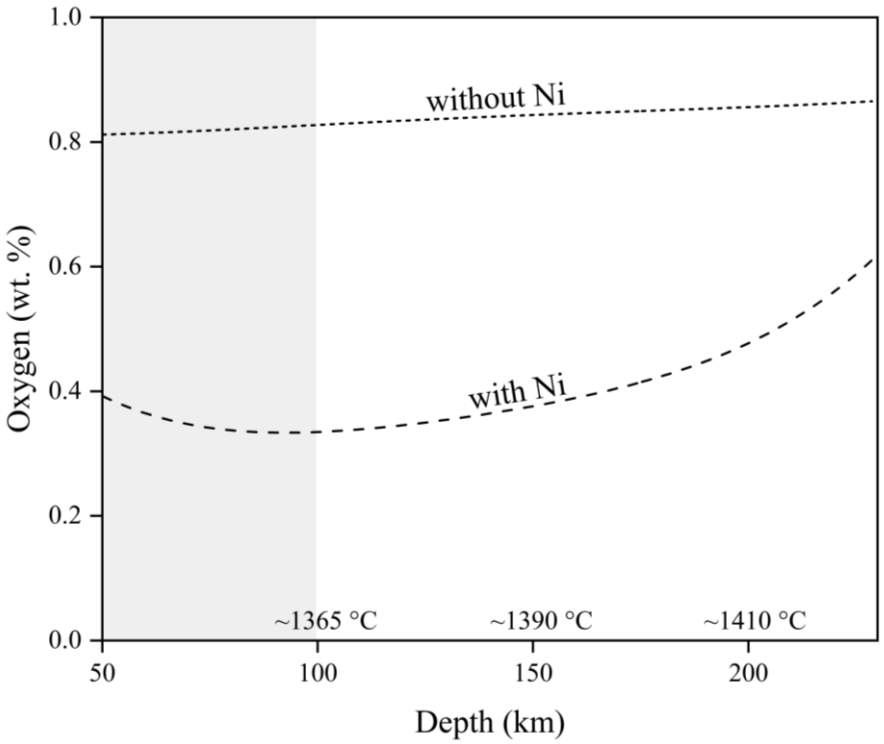

Figure 5.8: Variation in sulphide melt oxygen contents in equilibrium with mantle peridotite. Depth variation is mainly due to changing Ni concentrations in sulphide (dashed curve) due to partitioning with olivine. The dotted curve shows the same calculation if the Ni in sulphide is ignored. The calculation is made along a 1320 °C mantle adiabat, with the mantle f_{O2} decreasing with depth to reach FMQ -3 at approximately 230 km depth (Stagno et al. 2013). In the shaded area (<100 km depth) graphite may no longer be stable (Stagno et al. 2013) and the higher oxygen fugacities could lead to higher oxygen concentrations in sulphide melts.

5.4.3 The interpretation of oxygen contents of natural sulphide assemblages

Although the experiments in this study were performed principally to determine the factors important in controlling mantle sulphide O contents, we can use the model described above to

interpret variations in sulphide O contents reported for natural samples. The best measurements of mantle sulphide O contents should come from inclusions in diamond, which are not only chemically isolated but also have an upper-limiting constraint on the oxygen fugacity imposed by carbon saturation, as in our experiments. Unfortunately, analyses of such inclusions rarely include O contents, and in some instances do not even report sulphur contents, which are instead often determined by stoichiometry (Aulbach et al., 2009; Westerlund et al., 2006). Many studies simply dissolve sulphides broken out of diamonds in order to perform Re-Os age determinations. Nevertheless, a few sulphide inclusion O contents have been reported from diamonds recovered from the *Lac de Gras* kimberlite field (central Canadian Slave Craton; Davies et al. 1999; 2004). Oxygen contents range from 0.27 to 12 wt. % in these sulphides, which have been divided into both peridotitic and eclogitic parageneses, based on their Ni contents.

There are significant uncertainties in using published sulphide inclusion O concentrations. It cannot be determined, for example, whether cracks have exposed the inclusions to post entrapment alteration. Furthermore, the assemblage may have been coarse grained, making a determination of the average composition difficult, as surfaces may not represent bulk compositions. Taken at face value, however, the published O concentrations are those expected for sulphide liquids rather than MSS. The range is also consistent, in a qualitative fashion, with our experimentally produced sulphide melts, apart from two samples with oxygen contents above 4 wt. %, which may well have been oxidized post entrapment (Aulbach et al., 2004b). In order to apply our model to the peridotitic samples of Davies et al. (1999; 2004) we assume the sulphides were in equilibrium with mantle rocks of a particular olivine Fe content, adding further uncertainty. Olivine inclusions are also found in the diamonds studied by Davies et al. (1999, 2004), with Fe contents of $X_{\mathrm{Fe}}^{\mathrm{Ol}}$ = 0.075±0.01. This quite narrow range is in good agreement with measurements made on mantle xenoliths from the central Slave Craton (Kopylova & Caro, 2004) and corresponds to a temperature uncertainty from equation 5.7 of 100 K.

As shown in Figure 5.9 many high Ni peridotite-associated inclusions (NiS > 0.6) give calculated temperatures at 6 GPa, which are unrealistically high. However, based on the expected Ni-Fe exchange coefficient between olivine and sulphide melt (Z. Zhang et al., 2018) these sulphides have Ni concentrations too high to be in equilibrium with typical peridotitic olivines, such as those found as inclusions in the same diamonds or in xenoliths from the Slave

craton lithosphere. The high Co contents (up to 14.7 wt. %) of several of these inclusions also imply dis-equilibrium with typical mantle assemblages. If the O concentrations are reliable, then the anomalously high temperatures calculated were in equilibrium with mantle rocks enriched in both Ni and Fe. No experiments performed have accessed the compositions and conditions required to produce the simultaneously high Ni and O contents of these samples and contrary to Ni-rich experiments, the inclusions all have positive values of S+O-M. The inclusions may, therefore, have fractionally crystallized from sulphides that were far from equilibrium with mantle silicates.

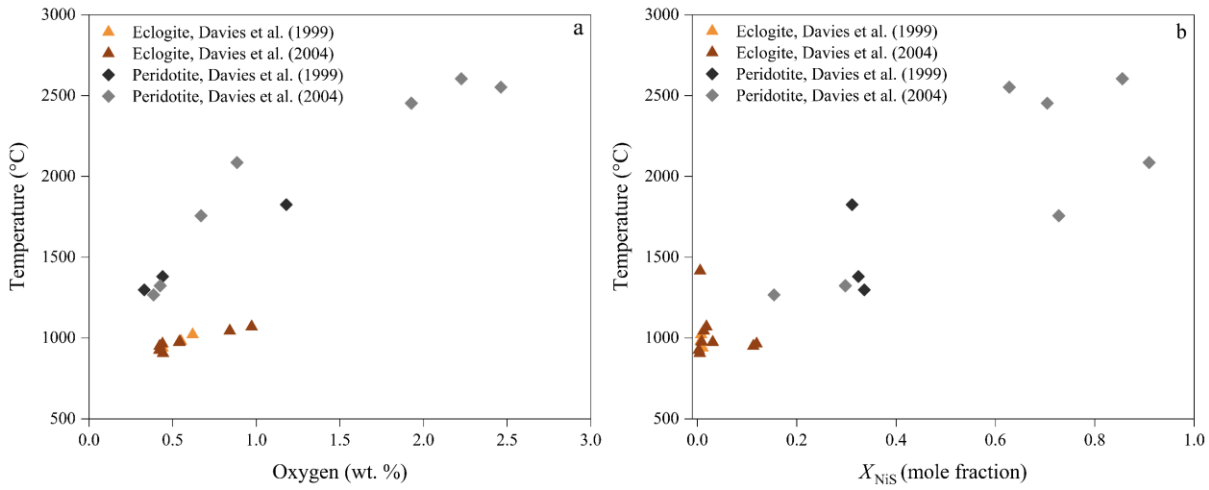

Figure 5.9: Equilibration temperatures calculated (equation 5.7) from oxygen concentrations reported in natural sulphide inclusions in diamonds from the Slave Craton, Canada (Davies et al. 1999; 2004) as a function of **(a)** oxygen concentration and **(b)** mole fraction of NiS, in sulphide inclusions.

Five peridotitic sulphide inclusions reported by Davies et al. (1999; 2004) do have Ni contents close to what would be expected for typical mantle, however, (Zhang et al. 2018) and although one of these gives an anomalously high temperature (1825 °C), the other four give a narrow range of temperatures with an average of 1318±48 °C. This is plausible for lithospheric diamond formation (Nimis, 2002; Stachel & Harris, 2009), is above the nominal FeS solidus (Z. Zhang & Hirschmann, 2016), and also agrees with the upper temperature limit obtained by Davies et al. (2004), using garnet-clinopyroxene inclusions in the same diamonds, which yield temperatures between 1040 and 1300 °C (Ellis & Green, 1979).

Half of the sulphide inclusions reported by Davies et al. (1999; 2004) are of eclogitic paragenesis and experiments in eclogitic compositions would be required to interpret the O contents of these samples. However, although our model cannot be applied directly to such

assemblages, we can very tentatively calculate fictive olivine and opx iron contents using a model for olivine-garnet Fe-Mg exchange (O'Neill & Wood, 1979) and then apply our model. Eclogitic garnet inclusions from the same diamonds have an average Fe/(Fe+Mg+Ca) ratio of 0.30 ± 0.04, from which an equivalent olivine Fe/(Fe+Mg) ratio of approximately 0.20 ± 0.08 can be calculated, depending on temperature. When this fictive assemblage of olivine and opx is combined with the O contents of the eclogitic sulphide inclusions, a narrow range of entrapment temperatures is calculated, 978 ±50 °C, which is close to the minimum temperature of entrapment of 1040 °C determined by Davies et al. (2004) using garnet-clinopyroxene inclusion pairs. This temperature is, however, below the FeS solidus and would require an additional sulphide component, such as H_2O or H_2 (Shibazaki et al., 2011; Wykes & Mavrogenes, 2005), to further depress the melting temperature. To get temperatures compatible with the FeS solidus would require the silicate assemblage to have an FeO content similar to peridotitic values.

5.5 Summary and Conclusions

In order to understand the factors that control the O concentration of sulphide melts in the upper mantle, sulphide liquids were experimentally equilibrated with mantle peridotite assemblages with varying FeO and NiO contents at *P, T* conditions between 3 and 13 GPa and from 1300 to 1819 °C, mainly in graphite capsules. Carbonates were added as a flux, which allowed oxygen fugacities to be estimated from the concentration of CO_2 in the resulting carbonate-silicate melts in equilibrium with graphite (Stagno et al. 2010). In some experiments, an additional saturating Ir-Fe alloy was added to provide fo_2 determinations from the proportion of iron in the alloy. Sulphide O contents varied from 0.2 to 3.7 wt. %, which is in qualitative agreement with the range reported for some sulphide inclusion assemblages in diamonds (Davies et al. 1999; 2004). The resulting silicate assemblage comprised mainly olivine and orthopyroxene with olivine Fe/(Fe+Mg) in the range 0.04–0.25. Neither variation in the sulphur to metal ratio nor fo_2, over a range from 1.8 to 4.0 log units below the FMQ buffer, appear to influence the sulphide melt O content. Rather, the FeO content of coexisting silicates and the temperature and pressure appear to be the main controlling factors. Further experiments show that Ni appears to lower the oxygen content of sulphide melts, although all Ni-bearing experiments, and those in the literature, also show a decrease in the sulphur/metal ratio as Ni is added that is hard to separate from the effect of Ni alone and thus causes some uncertainty.

A thermodynamic model was developed based on the exchange of FeO between olivine, orthopyroxene and sulphide melt (equilibrium 5.1). The calculated standard state Gibbs free energy ΔG^{o} for equilibrium (5.1) shows a clear correlation with temperature and pressure. The decrease in O with sulphide Ni content is accounted for through the inclusion of a non-ideal FeO-NiS interaction parameter. The resulting relationship reproduces the experimental temperatures ±74 K for Ni-free experiments and ±135 K for Ni- bearing samples. The increased uncertainty for the Ni-bearing data may be an indication that other factors such as the sulphur/metal ratio may also influence the O content. Applying this model, the expected O contents of sulphide melts in equilibrium with typical peridotite along a mantle adiabat between 100 and 200 km depth is determined to be in the range 0.4–0.6 wt. %.

Temperatures can be estimated for a series of peridotitic sulphide inclusions in diamonds from the Lac de Gras kimberlite field (Davies et al., 1999, 2004), from their O contents using our thermodynamic model. It is assumed that the inclusions were in equilibrium with a silicate assemblage with an olivine Fe/(Fe+Mg) ratio of 0.075±0.01, which is the average value of olivine inclusions found in the same diamonds and is typical for these xenoliths (Davies et al. 1999, 2004; Kopylova and Caro 2004). A group of peridotitic inclusions with NiS mole fractions < 0.6, give plausible temperatures (1318±48 °C) for lithospheric diamond formation. Unrealistically high temperatures are found for other inclusions, however, which have NiS mole fractions >0.6, which is higher than expected for sulphides in equilibrium with peridotites with typical mantle Ni concentrations (Zhang et al. 2018). These sulphides have much higher than expected O contents and may have equilibrated with silicates with very high Ni and Fe contents or fractionally crystallised from sulphide melts that were no longer in equilibrium with mantle silicates.

Temperatures for eclogitic sulphide inclusions in diamonds from the same locality were calculated by using Fe-Mg partitioning data to calculate fictive olivine and orthopyroxene iron contents assuming a typical eclogitic garnet iron content. These calculations result in entrapment temperatures, 978 ±50 °C, far below the sulphide solidus temperature, although other components such as H_2 or H_2O may have lowered the sulphide solidus or these inclusions were in equilibrium with assemblages with lower iron contents, i.e. more similar to peridotites, that would yield temperatures above the sulphide solidus.

The model produced here is preliminary and further work is required to ensure that the effect of Ni on the O contents has been suitably described, for which it would be necessary to produce

Ni-bearing sulphide assemblages that do not also have low sulphur/metal ratios. Although the temperatures calculated for some sulphide assemblages from diamonds appear reasonable, this could simply be a coincidence and the inclusions themselves may contain O as a result of post entrapment (epigenetic) alteration or the O analyses might not be representative of the entire inclusion as a result of a heterogeneous distribution of phases. Therefore, perhaps the most important further step would be to study sulphide inclusions to determine whether the O contents are epigenetic, to examine if they are captured melts or fractionally crystallised products from melts and to obtain representative O analyses. Mössbauer spectroscopy is shown to be a useful non-destructive method to determine the O content in sulphide inclusions. Synchrotron source Mössbauer spectroscopy, in particular, could be used to obtain at least a first approximation of O contents for many sulphide inclusions, potentially while they are still trapped inside the host.

Acknowledgements

We would like to thank Detlef Krausse and Anke Potzel for help with EPMA analyses, Hubert Schulze, Raphael Njul and Alexander Rother for sample preparation and Heinz Fischer for machining high-pressure cell assembly parts. We appreciate the very thorough reviews of Kate Kiseeva, John A. Mavrogenes, and editorial handling by Dante Canil. This project was conducted under the "Deep volatile cycles – International Research Training Group" funded by German Research Foundation (Deutsche Forschungsgemeinschaft – DFG, GRK 2156/1) and DFG grant FR1555/11.

Supplementary data

See appendix A.2 for supplementary figures (A.2.1, A.2.2 and A.2.3) and tables (A.2.1 and A.2.2). Supplementary tables A.2.3 and A.2.4 are available as electronic materials at: https://doi.org/10.6084/m9.figshare.21253536.v1

References

Alard O, Lorand JP, Reisberg L, et al (2011) Volatile-rich metasomatism in montferrier xenoliths (Southern France): Implications for the abundances of chalcophile and highly siderophile elements in the subcontinental mantle. J Petrol 52:2009–2045. doi: 10.1093/petrology/egr038

Armstrong K (2018) Redox Evolution of the Early Earth's Mantle. Doctoral dissertation, University of Bayreuth

Ashchepkov I V, Pokhilenko NP, Vladykin N V, et al (2010) Structure and evolution of the lithospheric mantle beneath Siberian craton, thermobarometric study. Tectonophysics 485:17–41. doi: 10.1016/j.tecto.2009.11.013

Aulbach S, Griffin WL, Pearson NJ, et al (2004) Mantle formation and evolution, Slave Craton: Constraints from HSE abundances and Re-Os isotope systematics of sulfide inclusions in mantle xenocrysts. Chem Geol 208:61–88. doi: 10.1016/j.chemgeo.2004.04.006

Aulbach S, Stachel T, Creaser RA, et al (2009) Sulphide survival and diamond genesis during formation and evolution of Archaean subcontinental lithosphere : A comparison between the Slave and Kaapvaal cratons. Lithos 112:747–757. doi: 10.1016/j.lithos.2009.03.048

Ballhaus C, Berry RF, Green DH (1991) High pressure experimental calibration of the olivine-orthopyroxene-spinel oxygen geobarometer: implications for the oxidation state of the upper mantle. Contrib to Mineral Petrol 107:27–40. doi: 10.1007/BF00311183

Bockrath C, Ballhaus C, Holzheid A (2004) Fractionation of the platinum-group elements during mantle melting. Science 305:1951–1953. doi: 10.1126/science.1100160

Boujibar A, Righter K, Bullock ES, et al (2019) Segregation of Na , K , Rb and Cs into the cores of Earth , Mars and Vesta constrained with partitioning experiments. Geochim Cosmochim Acta 269:622–638. doi: 10.1016/j.gca.2019.11.014

Brenan JM (2015) Se – Te fractionation by sulfide – silicate melt partitioning : Implications for the composition of mantle - derived magmas and their melting residues. Earth Planet Sci Lett Vol 422:45–57

Bulanova GP (1995) The formation of diamond. J Geochemical Explor 53:1–23. doi: 10.1016/0375-6742(94)00016-5

Bulanova GP, Griffin WL, Ryan CG, et al (1996) Trace elements in sulfide inclusions from Yakutian diamonds. Contrib to Mineral Petrol 124:111–125. doi: 10.1007/s004100050179

Davies RM, Griffin WL, O'Reilly SY, Doyle BJ (2004) Mineral inclusions and geochemical characteristics of microdiamonds from the DO27, A154, A21, A418, DO18, DD17 and Ranch Lake kimberlites at Lac de Gras, Slave Craton, Canada. Lithos 77:39–55. doi: 10.1016/j.lithos.2004.04.016

Davies RM, Griffin WL, Pearson NJ, et al (1999) Diamonds from the deep: pipe DO27, Slave craton, Canada. In: Gurney JJ, Gurney JL, Pascoe MD, Richardson SH (eds) 7th international Kimberlite conference. Red Roof Designs, pp 148–155

Davis FA, Tangeman JA, Tenner TJ, Hirschmann MM (2009) The composition of KLB-1 peridotite. Am Mineral 94:176–180. doi: 10.2138/am.2009.2984

Deines P, Harris JW (1995) Sulfide inclusion chemistry and carbon isotopes of African diamonds. Geochim Cosmochim Acta 59:3173–3188. doi: 10.1016/0016-7037(95)00205-E

Delpech G, Lorand JP, Grégoire M, et al (2012) In-situ geochemistry of sulfides in highly metasomatized mantle xenoliths from Kerguelen, southern Indian Ocean. Lithos 154:296–314. doi: 10.1016/j.lithos.2012.07.018

Doyle CD, Naldrett AJ (1987) The oxygen content of sulfide magma and it's effect on the partitioning of nickel between coexisting olivine and molten ores. Econ Geol 82:208–211

Eggler DH, Lorand JP (1993) Mantle sulfide geobarometry. Geochim Cosmochim Acta 57:2213–2222. doi: 10.1016/0016-7037(93)90563-C

Ellis DJ, Green DH (1979) An experimental study of the effect of Ca upon garnet-clinopyroxene Fe-Mg exchange equilibria. Contrib to Mineral Petrol 71:13–22. doi: 10.1007/BF00371878

Fonseca ROC, Campbell IH, O'Neill HSC, Fitzgerald JD (2008) Oxygen solubility and speciation in sulphide-rich mattes. Geochim Cosmochim Acta 72:2619–2635. doi: 10.1016/j.gca.2008.03.009

Fonseca ROC, Mallmann G, O'Neill HSC, et al (2011) Solubility of Os and Ir in sulfide melt: Implications for Re/Os fractionation during mantle melting. Earth Planet Sci Lett 311:339–350. doi: 10.1016/j.epsl.2011.09.035

Frost DJ (2003) $Fe2^{+}$ -Mg partitioning between garnet, magnesiowüstite, and $(Mg,Fe)_2SiO_4$ phases of the transition zone. Am Mineral 88:387–397

Gaetani GA, Grove TL (1999) Wetting of mantle olivine by sulfide melt: Implications for Re/Os ratios in mantle peridotite and late-stage core formation. Earth Planet Sci Lett 169:147–163. doi: 10.1016/S0012-821X(99)00062-X

Graham J, Bennett CEG, Van Riessen A (1987) Oxygen in pyrrhotite: 1. Thermomagnetic behavior and annealing of pyrrhotites containing small quantities of oxygen. Am Mineral 72:599–604

Graham J, McKenzie CD (1987) Oxygen in pyrrhotite: 2. Determination of oxygen in natural pyrrhotites. Am Mineral 72:605–609

Gunn SC, Luth RW (2006) Carbonate reduction by Fe-S-O melts at high pressure and high temperature. Am Mineral 91:1110–1116. doi: 10.2138/am.2006.2009

Harvey J, Warren JM, Shirey SB (2016) Mantle Sulfides and their Role in Re-Os and Pb Isotope Geochronology. Rev Mineral Geochemistry 81:579–649

Hernlund J, Leinenweber K, Locke D, Tyburczy JA (2006) A numerical model for steady-state temperature distributions in solid-medium high-pressure cell assemblies. Am Mineral 91:295–305. doi: 10.2138/am.2006.1938

Holwell DA, Mcdonald I (2010) A review of the behaviour of platinum group elements within

natural magmatic sulfide ore systems. Platin Met Rev 54:26–36. doi: 10.1595/147106709X480913

Hughes, E. C., Buse, B., Kearns, S. L., Blundy, J. D., Kilgour, G., & Mader, H. M. (2019). Low analytical totals in EPMA of hydrous silicate glass due to sub-surface charging: Obtaining accurate volatiles by difference. Chemical Geology, 505, 48–56. https://doi.org/10.1016/j.chemgeo.2018.11.015

Jacob DE, Piazolo S, Schreiber A, Trimby P (2016) Redox-freezing and nucleation of diamond via magnetite formation in the Earth's mantle. Nat Commun 7:11897. doi: 10.1038/ncomms11891

Kiseeva ES, Fonseca ROC, Smythe DJ (2017) Chalcophile elements and sulfides in the upper mantle. Elements 13:111–116. doi: 10.2113/gselements.13.2.111

Kiseeva ES, Wood BJ (2015) The effects of composition and temperature on chalcophile and lithophile element partitioning into magmatic sulphides. Earth Planet Sci Lett 424:280–294. doi: 10.1016/j.epsl.2015.05.012

Kiseeva ES, Wood BJ (2013) A simple model for chalcophile element partitioning between sulphide and silicate liquids with geochemical applications. Earth Planet Sci Lett 383:68–81. doi: 10.1016/j.epsl.2013.09.034

Kopylova MG, Caro G (2004) Mantle xenoliths from the Southeastern Slave craton: Evidence for chemical zonation in a thick, cold lithosphere. J Petrol 45:1045–1067. doi: 10.1093/petrology/egh003

Kress V (1997) Thermochemistry of sulfide liquids. I. the system O-S-Fe at 1 bar. Contrib to Mineral Petrol 127:176–186

Lehlooh A, Mahmood S (2002) Mössbauer Spectroscopy Study of Iron Nickel Alloys. Hyperfine Interact 139/140:387–392. doi: 10.1023/A

Lyubutin IS, Lin CR, Korzhetskit Y V, et al (2009) Mössbauer spectroscopy and magnetic properties of hematite / magnetite nanocomposites. J Appl Phys 106:. doi: 10.1063/1.3194316

McCammon CA, Chin IL, Gurney JJ, Mccallum ME (1998) Ferric iron content of mineral inclusions in diamonds from George Creek , Colorado determined using Mössbauer spectroscopy. Contrib to Mineral Petrol 133:30–37

McCammon CA, Mccammon C, Hutchison M, Harris J (1997) Ferric Iron Content of Mineral Inclusions in Diamonds from São Luiz : A View into the Lower Ferric Iron Content of Mineral Inclusions in Diamonds from São Luiz : A View into the Lower Mantle. Science (80-) 278:434–436. doi: 10.1126/science.278.5337.434

McDonald I, Hughes HSR, Butler IB, et al (2017) Homogenisation of sulphide inclusions within diamonds: A new approach to diamond inclusion geochemistry. Geochim Cosmochim Acta 216:335–357. doi: 10.1016/j.gca.2017.04.039

McDonough WF, Sun S s (1995) The composition of the Earth. Chem Geol 120:223–253. doi: 10.1016/0009-2541(94)00140-4

Naldrett AJ (1969) A portion of the system Fe-S-O between 900 and 1080 °C and its

application to sulfide ore magmas. J Petrol 10:171–201. doi: 10.1093/petrology/10.2.171

Nimis P (2002) The pressures and temperatures of formation of diamond based on thermobarometry of chromian diopside inclusions. Can Mineral 40:871–884. doi: 10.2113/gscanmin.40.3.871

O'Neill HSC (1987) Quartz-fayalite-iron and quartz-fayalite-magnetite equilibria and the free energy of formation of fayalite (Fe_2Si0_4) and magnetite (Fe_30_4). Am Mineral 72:67–75

O'Neill HSC, Canil D, Rubie DC (1998) Oxide- metal equilibria to 2500 °C and 25 GPa: Implications for core formation and the light component in the Earth's core. J Geophys Res 103:12239–12260

O'Neill HSC, Wood BJ (1979) An experimental study of Fe-Mg partitioning between garnet and olivine and its calibration as a geothermometer. Contrib to Mineral Petrol 70:59–70. doi: 10.1007/BF00371872

Palyanov YN, Borzdov YM, Bataleva Y V, et al (2007) Reducing role of sulfides and diamond formation in the Earth's mantle. Earth Planet Sci Lett 260:242–256. doi: 10.1016/j.epsl.2007.05.033

Pearson DG, Shirey SB, Bulanova GP, et al (1999) Re-Os isotope measurements of single sulfide inclusions in a Siberian diamond and its nitrogen aggregation systematics. Geochim Cosmochim Acta 63:703–711. doi: 10.1016/S0016-7037(99)00042-3

Pearson DG, Shirey SB, Harris JW, Carlson RW (1998) Sulphide inclusions in diamonds from the Koffiefontein kimberlite, S Africa: Constraints on diamond ages and mantle Re-Os systematics. Earth Planet Sci Lett 160:311–326. doi: 10.1016/S0012-821X(98)00092-2

Potapkin V, Chumakov AI, Smirnov G V, et al (2012) The 57 Fe Synchrotron Mössbauer Source at the ESRF. J Synchrotron Radiat 19:559–569. doi: 10.1107/S0909049512015579

Richardson SH, Shirey SB, Harris JW (2004) Episodic diamond genesis at Jwaneng, Botswana, and implications for Kaapvaal craton evolution. Lithos 77:143–154. doi: 10.1016/j.lithos.2004.04.027

Rubie DC (1999) Characterising the sample environment in multianvil high-pressure experiments. Phase Transitions 68:431–451. doi: 10.1080/01411599908224526

Rudnick RL, Eldridge CS, Bulanova GP (1993) Diamond growth history from in situ measurement of Pb and S isotopic compositions of sulfide inclusions. Geology 21:13. doi: 10.1130/0091-7613(1993)021<0013:DGHFIS>2.3.CO;2

Rüffer R, Chumakov AI (1996) Nuclear-resonance beamline at ESRF. Hyperfine Interact 97:589–604. doi: 10.1007/BF02458921

Sharp WE (1966) Pyrrhotite: a common inclusion in South African diamonds. Nature 211:402–403

Shibazaki Y, Ohtani E, Terasaki H, et al (2011) Effect of hydrogen on the melting temperature of FeS at high pressure: Implications for the core of Ganymede. Earth Planet Sci Lett 301:153–158. doi: 10.1016/j.epsl.2010.10.033

Shirey SB, Cartigny P, Frost DJ, et al (2013) Diamonds and the geology of mantle carbon. Rev Mineral Geochemistry 75:355–421. doi: 10.2138/rmg.2013.75.12

Shushkanova A V, Litvin YA (2008) Experimental evidence for liquid immiscibility in the model system $CaCO_3$-pyrope-pyrrhotite at 7.0 GPa: The role of carbonatite and sulfide melts in diamond genesis. Can Mineral 46:991–1005. doi: 10.3749/canmin.46.4.991

Smit K V, Shirey SB, Wang W (2016) Type Ib diamond formation and preservation in the West African lithospheric mantle: Re–Os age constraints from sulphide inclusions in Zimmi diamonds. Precambrian Res 286:152–166. doi: 10.1016/j.precamres.2016.09.022

Smith EE, Shirey SB, Nestola F, et al (2016) Large gem diamonds from metallic liquid in Earth's deep mantle Evan. Science (80-) 354:1403–1406

Stachel T, Harris JW (2009) Formation of diamond in the Earth's mantle. J Phys Condens Matter 21:. doi: 10.1088/0953-8984/21/36/364206

Stagno V, Frost DJ (2010) Carbon speciation in the asthenosphere: Experimental measurements of the redox conditions at which carbonate-bearing melts coexist with graphite or diamond in peridotite assemblages. Earth Planet Sci Lett 300:72–84. doi: 10.1016/j.epsl.2010.09.038

Stagno V, Ojwang D, McCammon CA, Frost DJ (2013) The oxidation state of the mantle and the extraction of carbon from Earth's interior. Nature 493:84–88. doi: 10.1038/nature11679

Taylor LA, Liu Y (2009) Sulfide inclusions in diamonds: not monosulfide solid solution. Russ Geol Geophys 50:1201–1211. doi: 10.1016/j.rgg.2009.11.018

Terasaki H, Frost DJ, Rubie DC, Langenhorst F (2005) The effect of oxygen and sulphur on the dihedral angle between Fe-O-S melt and silicate minerals at high pressure: Implications for Martian core formation. Earth Planet Sci Lett 232:379–392. doi: 10.1016/j.epsl.2005.01.030

von Seckendorff V, O'Neill HSC (1993) An experimental study of Fe-Mg partitioning between olivine and orthopyroxene at 1173, 1273 and 1423 K and 1.6 GPa. Contrib to Mineral Petrol 113:196–207. doi: 10.1007/BF00283228

Wendlandt RF (1982) Sulfide saturation of basalt and andesite melts at high pressures and temperatures. Am Mineral 67:877–885

Westerlund KJ, Shirey SB, Richardson SH, et al (2006) A subduction wedge origin for Paleoarchean peridotitic diamonds and harzburgites from the Panda kimberlite, Slave craton: Evidence from Re-Os isotope systematics. Contrib to Mineral Petrol 152:275–294. doi: 10.1007/s00410-006-0101-8

Wiggers de Vries DF, Pearson DG, Bulanova GP, et al (2013) Re-Os dating of sulphide inclusions zonally distributed in single Yakutian diamonds: Evidence for multiple episodes of Proterozoic formation and protracted timescales of diamond growth. Geochim Cosmochim Acta 120:363–394. doi: 10.1016/j.gca.2013.06.035

Woodland AB, O'Neill HSC (1997) Thermodynamic data for Fe-bearing phases obtained using noble metal alloys as redox sensors. Geochim Cosmochim Acta 61:4359–4366. doi: 10.1016/S0016-7037(97)00247-0

Wykes JL, Mavrogenes JA (2005) Hydrous sulfide melting: Experimental evidence for the solubility of H_2O in sulfide melts. Econ Geol 100:157–164. doi: 10.2113/100.1.0157

Yefimova ES, Sobolev N V, Pospelova LN (1983) Sulfide inclusions in diamonds and specific features of their paragenesis. Zap Vsesoyuznogo Mineral Obs 112:300–310

Zhang Z, Hirschmann MM (2016) Experimental constraints on mantle sulfide melting up to 8 GPa. Am Mineral 101:181–192. doi: 10.2138/am-2016-5308

Zhang Z, Hirschmann MM (2012) Carbon Solubility of Molten Sulfides at 2-3 GPa. In: American Geophysical Union, Fall Meeting 2012. p abstract id. DI13D-2454

Zhang Z, von der Handt A, Hirschmann MM (2018) An experimental study of Fe–Ni exchange between sulfide melt and olivine at upper mantle conditions: implications for mantle sulfide compositions and phase equilibria. Contrib to Mineral Petrol 173:. doi: 10.1007/s00410-018-1444-7

Chapter 6

Deuterium content and site occupancy in iron sulphide at high pressure and temperature using *in situ* neutron diffraction experiments

Sumith Abeykoon[1]✉, Christopher Howard[1], Serena Dominijanni[1], Lisa Eberhard[1], Alexander Kurnosov[1], Daniel J. Frost[1], Tiziana Boffa Ballaran[1], Hidenori Terasaki[2], Tatsuya Sakamaki[3], Akio Suzuki[3], Eiji Ohtani[3], Asami Sano-Furukawa[4], Jun Abe[5]

[1] Bayerisches Geoinstitut, University of Bayreuth, 95440 Bayreuth, Germany

[2] Department of Earth Sciences, Okayama University, Okayama, Japan

[3] Department of Earth and Planetary Material Sciences, Tohoku University, 980-8578, Sendai, Japan

[4] J-PARC Center, Japan Atomic Energy Agency, 2-4 Shirakata, Tokai, Naka, Ibaraki, 319-1195, Japan

[5] Neutron Science and Technology Center, Comprehensive Research Organization for Science and Society, Tokai, Naka, Ibaraki 319-1106, Japan

✉ sumith.abeykoon@uni-bayreuth.de

This chapter is currently under revision for publication in:
Journal of Geophysical Research – Solid Earth

Abstract

We have performed *in situ* time-of-flight neutron diffraction experiments to examine the uptake of deuterium in iron monosulphide at pressures up to 11.4 GPa and temperatures to 1300 K, using a multi-anvil device installed at a spallation neutron source. A D_2 fluid was formed in the experiments through the decomposition of ND_3BD_3, resulting in an oxygen fugacity, measured in parallel experiments, of approximately 1.2 log units below the iron-wüstite buffer. Deuterium positions and site occupancies were determined for the pyrrhotite polytype, referred to as FeS V, at high pressure and temperature conditions using Rietveld refinements of the

powder diffraction patterns. Our structural model indicates that two normally unoccupied sites in the *P*6$_3$/*mmc* FeS V structure, at Wyckoff positions *6h* and *4f*, are partially occupied by D atoms, with the latter being more dominant. The total D site occupancy (x) in $FeSD_X$ increases with both pressure and temperature over the experimental conditions explored, from 0.148(10) at 2.3 GPa and 787 K to 1.25(5) at 9.7 GPa and 1300 K. The unit-cell volume expansion per deuterium atom is found to be 1.53 ± 0.16 Å^3 at 6.9 GPa and 960 K, which is smaller than has been determined for deuteration of metallic iron phases at similar conditions. The variation in unit-cell volume indicates that most deuterium is lost from FeS V upon temperature quenching at high-pressures. By fitting the obtained FeS V deuterium site occupancies to a thermodynamic model, estimates for the hydrogen contents of iron monosulphide at conditions and oxygen fugacities consistent with the base of the cratonic lithosphere can be made that are in the range 1700–2700 ppm.

6.1 Introduction

Iron-nickel-rich mono-sulphides are found as accessory minerals in almost all mantle rocks and sulphide melts were also an important core-forming component during planetary differentiation (Harvey et al., 2016b; O'Neill, 1991; Rubie et al., 2016). Based on the depression of the FeS melting point, and in situ X-ray diffraction measurements of the unit-cell volume of FeS mineral phases, it has been proposed that iron sulphide minerals and melts can both dissolve a significant concentration of hydrogen (Piet et al., 2021; Shibazaki et al., 2011). This might be relevant to a number of planetary scenarios. Recent analyses of InSight seismic measurements, for example, are consistent with a lower than expected density for the Martian core (Stähler et al., 2021), too low, in fact, to be explained by the presence of sulphur as the only light alloying element, due to its limited cosmochemical abundance. This raises the possibility that hydrogen may also be present in a sulphur-rich Martian core. The highly siderophile element concentration of the Earth's mantle has been proposed to have also been established, in part, through the late stage separation of iron sulphide-rich melt to the core (Kiseeva & Wood, 2013b; Laurenz et al., 2016; O'Neill, 1991; Rubie et al., 2016; Wood & Halliday, 2005). If this melt were also to have removed hydrogen from an initially slightly water-bearing magma ocean, this might potentially explain how the Earth's mantle became more oxidised towards the end of core formation (Delano, 2001; Kasting, 1993), through the reaction (Ringwood, 1977; Z. D. Sharp et al., 2013),

$$H_2O + 2FeO = Fe_2O_3 + H_2 \quad (6.1)$$

Furthermore, iron sulphide minerals and melts might be important hosts for hydrogen in the mantles of the Earth and other planetary bodies. To clarify these possibilities, it is necessary to examine how hydrogen partitions between sulphides and silicate phases under different mantle conditions, and most importantly under different oxygen fugacities.

A critical obstacle in the study of hydrogen in high pressure and temperature fractionation processes, is that melt and mineral phases do not necessarily preserve hydrogen in quenched products recovered for analysis at ambient conditions. Mantle partial melt compositions, for example, can no longer be quenched to glasses in conventional high-pressure experiments performed above 3 GPa (Bondar et al., 2021; Tenner et al., 2009). This makes the analysis of hydrogen species unreliable because the quenched crystallised products do not necessarily retain the volatile inventory of the melt, either because the solubility is lower in the products or due to kinetic limitations causing fluid formation during quenching. This is compounded in studies on the behaviour of hydrogen during core formation processes, because metallic iron-rich melts not only crystallise on quenching but hydrogen is also lost from the quenched metal and hydride phases during recovery to room pressure (Antonov et al., 1998; Fukai & Suzuki, 1986; Iizuka-Oku et al., 2017; Okuchi, 1997). Sulphide minerals and melts are likely similar in this respect and may not preserve their high pressure and temperature hydrogen contents upon recovery to room temperature, at least above an as yet undetermined threshold.

There are several approaches that have been used to address the problem of hydrogen loss from metallic melts. Recent metal-silicate melt hydrogen partitioning experiments were performed with low bulk hydrogen contents (< 1000 wt. ppm H_2), assuming that the recovered quench-crystallised products retained hydrogen to ambient conditions, as a result of the concentrations being below the threshold where hydrogen would be lost from the products (Clesi et al., 2018; Malavergne et al., 2019). This may well be the case, but would be more convincing if the retention threshold were known and could be demonstrated to reproducibly preserve the melt concentration. Another possibility is to rapidly decompress and then quench hydrogen-bearing iron-liquids and estimate the initial hydrogen concentrations from the volume of the exsolved bubble network (Okuchi, 1997). This method suffers some uncertainties that are hard to gauge, such as those arising from the exact conditions, and therefore gas volume, at which exsolution occurs or the possibility of hydrogen loss without bubble formation. A final possibility is to quench metallic liquids at high-pressures and determine the hydrogen contents through *in situ*

methods before the pressure is removed (Tagawa et al., 2021). Such measurements use X-ray diffraction to estimate the metal hydrogen contents from the expansion in the unit cell volume, compared to hydrogen-free samples. Because hydrogen is essentially invisible to X-rays, this requires a calibration, using an independent method, for the effect of hydrogen on the unit cell volume of the solid phase in question.

From this discussion it is clear that a first step in understanding the hydrogen contents of metal and sulphide liquids is to be able to determine the hydrogen contents of sub-solidus phases. This is also required for the thermodynamic treatment of the effect of hydrogen on melting and provides information on the potential storage of hydrogen by such phases in planetary mantles and inner cores. In this study *in situ* time-of-flight (TOF) neutron powder diffraction measurements have been performed on samples of NiAs-type $Fe_{(1-x)}S$, (i.e. the FeS V structure as defined by Urakawa et al., 2004), at pressures between 2.3 and 11.4 GPa and temperature up to 1300 K, in order to quantify the position and solubility of deuterium in the crystal structure. NiAs-type $Fe_{(1-x)}S$, a polytype of pyrrhotite, remains the subsolidus mono-sulphide phase in the Fe–S system, throughout conditions of the upper mantle and transition zone (Shibazaki et al., 2011; Urakawa et al., 2004). The experiments are performed in a multi-anvil press installed at the J-PARC spallation neutron source in Japan. Atomic positions and site occupancies of deuterium in the FeS V structure are determined through Rietveld structure refinements.

6.2 Methods

6.2.1 Sample assemblage

High pressure and temperature experiments were performed using two cubic assemblies with (cubic) edge lengths (CEL) of 15.0 mm and 10.5 mm, for experiments at $P \leq 7$ GPa and $P > 7$ GPa, respectively. The starting material was a cold pressed cylindrical pellet of FeS powder (99.9% pure troilite – from "Chempur") with a height of either 5 or 4 mm depending on the size of assembly used. This was placed between two deuterated ammonia borane (ND_3BD_3) pellets, either 1.0 or 0.7-mm thick, and loaded into a NaCl capsule, with an inner diameter of either 3 or 4 mm. The capsule was closed with a 1 mm thick disk of NaCl. The NaCl was also used for *in situ* pressure measurements. The pellets of ND_3BD_3 undergo thermal decomposition into BN and D_2 upon heating above approximately 600 – 800 K at high-pressure (Nyĺn et al., 2009). Deuterium has a much higher scattering length/power (bound coherent scattering length

= 6.67 fm) than hydrogen (-3.74 fm), and smaller incoherent scattering (Dawidowski et al., 2013; Sears, 1992), resulting in a better signal to noise ratio in the collected diffraction patterns. At the same time, it is expected that D and H have similar solubilities in the FeS structure. NaCl is known to be an effective material for confining hydrogen at high *P* and *T* (Fukai et al., 2003; Machida et al., 2014; Sakamaki et al., 2009; Shibazaki et al., 2011). The capsules were placed inside a cylindrical graphite heater with graphite lids on the top and bottom which in turn was inserted inside a cylindrical hole drilled at the centre of a Cr_2O_3 doped MgO cube that served as a pressure transmitting medium. End caps, made out of ZrO_2 wrapped with molybdenum foil (for electrical conduction), were then placed in contact with both sides of the graphite resistance heater. The 15.0 mm and 10.5 mm CEL assemblies were compressed to target pressure between six tungsten carbide secondary anvils, with square truncations of edge lengths (TEL) 10 and 7 mm respectively. A diagram of the TEL 10 high-pressure cell assembly is shown in supplementary Figure A.3.1.

6.2.2 High-pressure neutron diffraction

High pressure and temperature time of flight neutron diffraction measurements were performed at the PLANET beamline (BL11) at the Material and Life Sciences Experimental Facility (MLF) in J–PARC, Japan (Hattori et al., 2015). The measurements were carried out using a six-ram multi-anvil high-pressure apparatus (ATSUHIME), where the rams are aligned along three perpendicular compression axes. Each of the six rams is capable of applying a load of 5000 kN (Sano-Furukawa et al., 2014) and is attached to an outer first-stage square faceted anvil. The rams are advanced simultaneously and compress an inner set of six square faceted second-stage tungsten carbide anvils, each inside a steal retaining ring. The second stage anvils are centered and initially held in place by an aluminium guide frame (see Iizuka-Oku et al., 2017 supplementary information). To eliminate neutron scattering from the assembly materials surrounding the sample, a set of incident slits and two sets of receiving radial collimators (each aligned with the 90 degree diffraction geometry) are placed as close as possible to the gaps between the second stage anvils (Hattori et al., 2015). The radial collimators are aligned so that only neutrons diffracted within the sample region that are perpendicular to the incident beam can reach the detectors. The slit size/beam sizes are chosen based on the assembly size and pressure and are reported in Table 6.1. Diffracted neutrons were collected using two detector banks, 1.5 m from the beam axis, comprised of 160 individual ^{3}He position-sensitive detectors (Hattori et al., 2015).

A diffraction measurement was taken before compression of each experiment for 10 minutes to confirm that the incident neutron beam was aligned over the sample. Another diffraction pattern was collected after compression to the target pressure to i) adjust any misalignment of the sample with respect to the neutron beam due to the compression of the whole assembly, ii) obtain diffraction from the NaCl pressure standard and iii) identify whether any phase transitions had occurred in the FeS sample during cold compression. Once the target pressure was reached, the sample was heated to the target temperature (Table 6.1) by supplying electrical power to the heater and using a previously calibrated power-temperature relation (supplementary Fig. A.3.2). This calibration has been performed with a similar experimental set up but employing a Pt–Pt 13% Rh thermocouple (error ±50 K; Ikuta et al., 2019). A total of six experiments were performed with pressures ranging from 2.3 to 11.4 GPa and temperatures between 787 and 1300 K (Table 6.1). Diffraction patterns were collected for up to 19 hrs and were monitored during this time every 30–60 minutes. The long collection times were required to obtain a good signal to noise ratio, especially at higher pressures where the sample and incident beam size are smaller.

6.2.3 Powder diffraction analysis

Intensity and background corrections were performed for all the diffraction profiles using the diffraction patterns of vanadium pellets and empty sample assemblies collected at the same conditions as those used for our measurements (see details in Hattori et al., 2015). A full profile analysis of the collected diffraction patterns was performed using the GSAS/EXPGUI software package (Larson & Von Dreele, 2004; Toby, 2001). Different FeS polymorphs (Table 6.1) were identified in the patterns collected during compression and decompression (Fig. 6.1). Moreover, cubic boron nitride (c BN) is present in the diffraction patterns collected after cooling in the two experiments at the highest pressures. This compound is produced after the decomposition of ND_3BD_3 to BN + D_2 at high-temperature, and the stability of cubic BN phase is consistent with the existing phase diagram (Solozhenko et al., 1999). Due to the smaller sample size of these two experiments, the top and the bottom of the sample, where the ND_3BD_3 pellet products resided, are also inside the neutron beam. Magnetite (Fe_3O_4) was observed in the experiment conducted without deuterium (blank experiment), likely due to the more oxidizing conditions compared to the deuterated experiments. At the target *P, T* conditions (Table 6.1), we observed the presence of FeS V, in agreement with previously reported phase diagrams (Fei et al., 1998; Kusaba et al., 1998; Shibazaki et al., 2011; Urakawa et al., 2004)

(Fig. 6.1). Also, the phases identified during the heating and cooling path agree with existing phase boundaries (Fig. 6.1). Rietveld refinements of the neutron diffraction patterns acquired at the highest *P* and *T* conditions of each experiment were performed to give insight into the deuterium position and occupancy inside the FeS V structure (as described in detail in the result section).

Pressures were determined from the unit-cell volume of NaCl obtained from the full profile analysis of the diffraction patterns. The equation of state of NaCl-B1 from Dorogokupets and Dewaele (2007) was used. Uncertainties in the pressure for each experiment were estimated using the error propagation equation explained in the supplementary Text A.3.1.

6.2.4 Chemical analyses

Three of the recovered experimental samples, A524, A526 and A527, were mounted in epoxy resin then sectioned and polished for chemical analysis with a JOEL JXA 8200 electron probe micro analyser in wavelength dispersive mode. The sulphide assemblage was analysed with a focused electron beam using a 20 kV acceleration voltage and 20 nA probe current. Oxygen in the sulphides was also measured using an LDE 1 (kα) crystal (Laurenz et al., 2016; Mann et al., 2012). Counting times were 20 s for sulphur and iron and 60 s for oxygen, with half of each counting time used for the respective backgrounds. Standards employed were FeS_2 for iron and sulphur and Fe_2O_3 for oxygen. Matrix corrections were performed using the "ZAF" method. The resulting analyses yielded an average composition of 37.29(0.19) % S, 61.85(0.23) % Fe and 0.46(0.41) % O, with no significant difference between the samples. Ignoring the minor oxygen content, this gives the sulphide stoichiometry $Fe_{0.963(6)}S$.

Table 6.1: Summary of the conditions at which the neutron diffraction experiments were performed and the run products obtained during compression and heating.

Run #	TEL/CEL (mm)	Heater material	Slit size W x H (mm)	Starting materials	Max. *P* (GPa)	Max. *T* (K)	Max. duration (hrs.)	Identified phases on heating/cooling path
A524-1	10/15	graphite	2 x 5	FeS + ND_3BD_3	2.3(2)	787	8	FeS I[a], IV[a], V
A524-2	10/15	graphite	2 x 5	FeS + ND_3BD_3	2.7(2)	940	8	FeS I[a], IV[a], V
A526	10/15	graphite	2 x 4	FeS + ND_3BD_3	6.9(4)	960	16	FeS I[b], IV[b], V
A593	7/10.5	graphite	2 x 4	FeS + ND_3BD_3	9.7(4)	1300	19	FeS III[a], V + c BN[b]
A527	7/10.5	TiC	2 x 4	FeS + ND_3BD_3	11.4(5)	1250	3	FeS V + c BN[b]
A595	7/10.5	graphite	2 x 4	FeS	7.3(4)	960	11	FeS III[a], V + Fe_3O_4 + Mo

Some NaCl capsule material was identified in all the experiments
A524-1 and A524-2 are two data points collected for the same experiment at different *P, T* conditions (first high T measurement).
TEL - truncation edge length, CEL - cube edge length.
At the *P* and *T* conditions reported for each experiment, the sample is FeS V phase. The other phases reported were either, [a] in the diffraction patterns acquired during compression (before heating), and [b] in the diffraction patterns acquired during cooling or decompression.
Neutron beam dimensions (slit sizes) are given as width (W) x height (H).

6.3 Results

6.3.1 Compressibility of the FeS V phase

During cold compression followed by heating, we observed four different high *P* and high *T* polymorphs of the $Fe_{0.96}S$ sample, described here using the following structure designations (Table 6.1, Fig. 6.1): FeS I (hexagonal - $\sqrt{3}a, 2c$), FeS III (monoclinic), FeS IV (hexagonal $2a, c$) and FeS V NiAs-type structure (a, c), where a and c are the unit-cell dimensions of the NiAs-type structure used to describe the FeS polymorphs (Kusaba et al., 2000; Urakawa et al., 2004). The FeS II (MnP-type orthorhombic) that has been reported between approximately 3.4 and 6.7 GPa at room temperature (Fei et al., 1995), was not detected during our measurements. After quenching, the high-pressure FeS V phase was preserved in most of the experiments and, therefore, its compressibility behaviour could be studied at room temperature during decompression (Table A.3.1, Fig. 6.2). In one run (#A526), we observed that FeS V transformed to FeS IV and then FeS I upon cooling and decompression. The reason for the back-transformation in this run might be due to the slower quench rate across the phase boundary; i.e., after data collection at 6.9 GPa and 960 K, the temperature was decreased to 450 K, resulting in the pressure dropping to 5.8 GPa due to thermal pressure effects. A similar back-transformation has previously been observed by Kusaba et al. (2000).

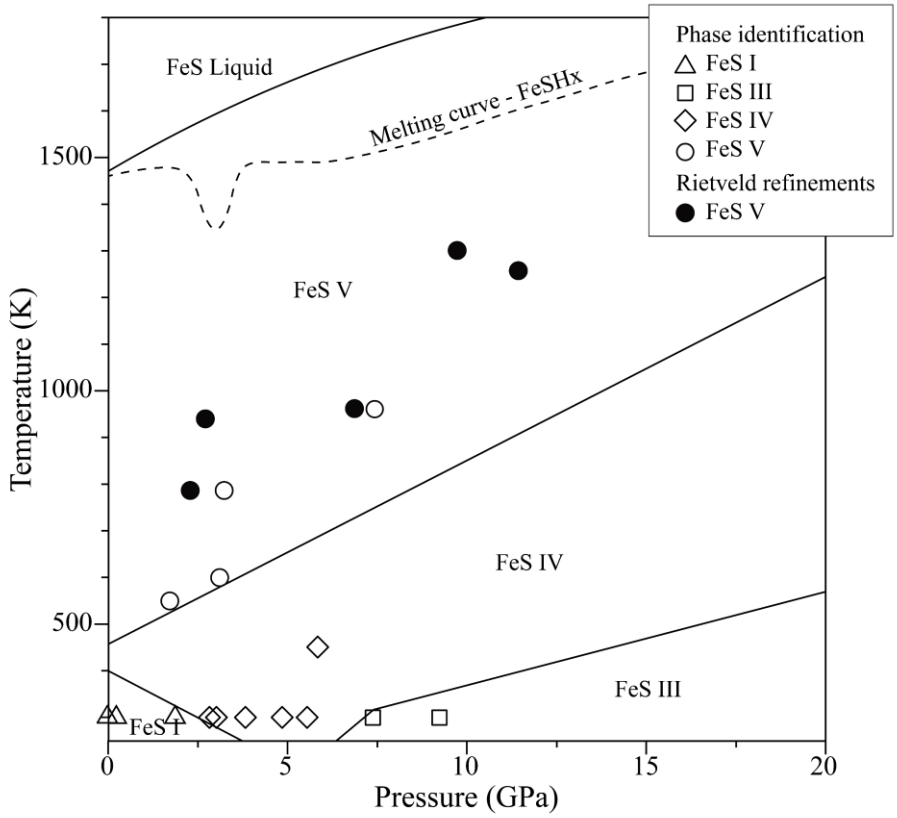

Figure 6.1: Observed high *P, T* polymorphs of FeS in this study (FeS I – triangles, FeS III – squares, FeS IV – diamonds and FeS V – circles) are shown on the existing phase diagram, where the solid lines show the phase boundaries from Urakawa et al. (2004). The dashed line shows the melting curve of $FeSH_X$ determined by Shibazaki et al. (2011). Filled circles (in the FeS V stability region) indicate the conditions where Rietveld refinements were performed to determine the deuterium site occupancy in FeS V. Open symbols indicate conditions where shorter diffraction measurements were performed for phase identification only. The FeS II (MnP-type orthorhombic) phase reported by Fei et al. (1995), is not shown here as it was not detected during our measurements. The unit-cell parameters of all observed phases are reported in the supplementary Table A.3.3.

The unit-cell volumes measured for FeS V during decompression and normalized with respect to the room-pressure volume, V_0 (60.08(1) Å^3 - measured in this study), show an anomalous increase starting from approximately 6.5 GPa (Fig. 6.2). This behaviour is likely due to a pressure-induced high-spin to low-spin phase transition, which must start around room-pressure but appears to be completed above 6.5 GPa. Such a transition has been observed by means of X-ray emission spectroscopy on a FeS troilite sample (Rueff et al., 1999). These authors reported the disappearance of the low-energy satellite in the Fe $K\beta$ emission spectrum of FeS above 6.3 GPa. Changes in the electronic state of Fe in FeS at the same pressures were

also reported in a high-pressure Mössbauer spectroscopy study (Kobayashi et al., 1997). Since Rueff et al. (1999) compressed troilite at room temperature, we may expect that the FeS sample had transformed to the FeS II orthorhombic structure above 3.4 GPa (Fei et al., 1995) and therefore, the spin transition observed at 6.3 GPa may have occurred in the same phase. The low-spin state of FeS was then observed up to 11.5 GPa in the same study (Rueff et al., 1999), i.e., in the stability field of the FeS III monoclinic polymorph (Nelmes et al., 1999). The pressure interval of the high-spin to low-spin transition observed from the X-ray emission spectra is very similar to the pressure at which, the anomalous change in the volume of FeS V is observed in this study (Fig. 6.2). This implies that the local environment of the Fe atoms in the different FeS polymorphs is very similar, causing the high-spin to low-spin electronic transition to occur over a similar pressure interval, which is seemingly independent from the precise structure topology. The interval between room pressure and 6.5 GPa can, therefore, be thought of as a region in which the Fe atoms in the FeS V structure have both high-spin and low-spin configurations. The anomalous decrease in volume is likely due to the change in the electronic state of an increasing number of Fe atoms. The same, seemingly anomalous volume behaviour, is observed in high pressure and temperature data for FeS IV and FeS V reported in the literature (Kusaba et al., 1998; Urakawa et al., 2004) (Fig. 6.2). These results in fact indicate that the completion of the high-spin to low-spin transition occurs at higher pressures as the temperature increases. At 1200 K, for example, the spin transition appears to be completed only above 11 GPa. Therefore, we can expect that at the target P and T of our experiments (Table 6.1), the electronic state of Fe in the FeS V analysed consists of a mixture of high- and low-spin states.

Due to the limited pressure range investigated in this study above 6.5 GPa, it is not possible for us to determine the room temperature equation of state of FeS V in the low-spin state. However, our data are in good agreement with the equation of state reported by Urakawa et al. (2004) for the low-spin FeS V structure (note that in the original paper the low-spin state of FeS V was referred to as the high-pressure phase, HPP, whereas the high-spin state was referred to as the low-pressure phase, LPP).

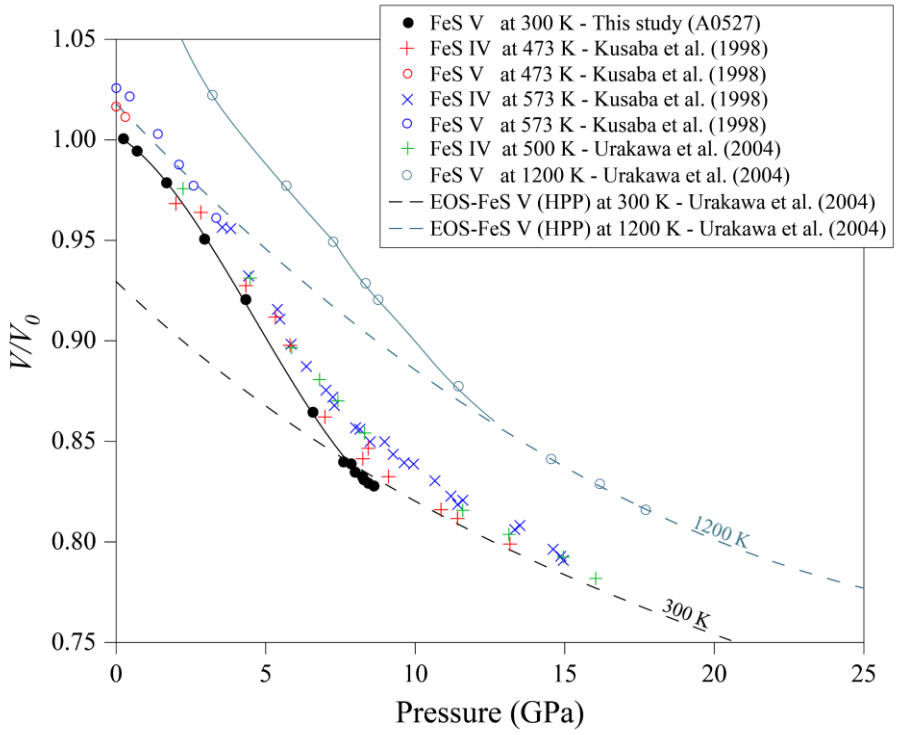

Figure 6.2: Unit-cell volumes (expressed as V/V_0) of FeS V during decompression at room-temperature in this study (filled black circles) are compared with isothermal compression curves (dashed lines) of low-spin, i.e. HPP, FeS V at 1200 K and 300 K (extrapolated), caluclated using the equation of state reported by Urakawa et al. (2004). The high *P* and *T* data of FeS IV and FeS V from previous studies (Kusaba et al., 1998; Urakawa et al., 2004) are also shown in coloured symbols. The inflection points at the FeS V–LPP to FeS V–HPP transition is moving to higher pressures with increasing temperature. The data plotted here in this study are given in supplementary Table A.3.1.

6.3.2 Deuterium incorporation in the FeS V structure

With the increasing temperature at high-pressure, the deuterium released from the ammonia borane (ND_3BD_3) pellets is expected to be incorporated into the FeS V structure and it should be possible to detect its presence from the collected time-of-flight powder neutron diffraction patterns. Rietveld refinement of the diffraction pattern collected for 16 h at 6.9(4) GPa and 960 K (A526, Table 6.1) was performed using the structural model of FeS V (Brand & Briest, 1965; Shibazaki et al., 2011) with Fe at the *2a* $\{0,0,0\}$ and S at the *2c* $\{1/3,2/3,1/4\}$ Wyckoff positions of the $P6_3/mmc$ space group. The occupancies of the two atoms were fixed to the values obtained from the chemical analysis, i.e., full occupancy for the S site and 0.963 occupancy for the Fe site. The isotropic displacement parameters of both atoms were free to

vary. All reflections in this diffraction pattern belonged either to the FeS V phase or to the NaCl capsule/pressure standard. No new diffraction lines were observed, indicating that the deuterium atoms randomly occupy the interstitial sites of the FeS V structure. The same observation was made by Shibazaki et al. (2011), who studied the hydrogenation of FeS V up to 16.5 GPa and 1723 K and did not report any change in symmetry for this compound based on powder X-ray diffraction patterns. Structural refinement of the FeS V phase in sample A526 shows a large discrepancy between the observed and the calculated diffraction pattern (supplementary Fig. A.3.4-a). A difference Fourier ('DELF') map was then generated and nuclear densities at the *6h* $\{x, 2x, 1/4\}$ and *12k* $\{x, 2x, z\}$ Wyckoff positions of the $P6_3/mmc$ space group were observed (supplementary Fig. A.3.3). Deuterium atoms were then added to the model at the two positions taken from the DELF map with a starting occupancy of 0.01. Rietveld refinements were then performed by either refining the deuterium atoms positions + occupancy or their isotropic displacement parameter (constrained to be equal to each other). During such refinements, the *6h* position was found to be very stable, while atoms in the *12k* equivalent positions became progressively closer to each other, suggesting a large dynamic disorder of the deuterium atom around an average atomic position, which can be described as a *4f* $\{1/3\,, 2/3\,, z\}$ Wyckoff position. By substituting the *4f* position as the second deuterium atom site it was possible to refine all atomic coordinates and isotropic displacements parameters, *U*iso, (with the D atoms being constrained to have the same *U*iso) as well as the occupancies of the deuterium atoms at the two sites. The resulting final refinement (supplementary Fig. A.3.4-b) shows a substantial improvement in the fit compared to the previous dry model (supplementary Fig. A.3.4-a), as reflected by the improvement of the "weighted R factor" (*wRp*) by 52.5% to a final value of 3.3% and of the Chi-square (χ^2) by 36.3% to a final value of 3.4. The calculated total deuterium occupancy per formula unit ($FeSD_X$) is 0.74(2) which equals to 1.71(8) wt.% of D. Our final structural model for deuterated FeS V (see deposited CIF, Table 6.2 and Fig. 6.3) is significantly different from what was proposed by Shibazaki et al. (2011) for hydrated FeS V based on first principle calculations. These authors suggested that octahedral interstitial sites are the most stable positions for the hydrogen atoms, whereas our results show that deuterium is instead partially occupying either a tetrahedral void (D–4*f*) or a position within the same layer defined by the S atoms (D–*6h*) (Fig. 6.3). Both deuterium positions are much closer to the S atoms than to the Fe atoms, with the shortest S···(D–4*f*) distance equal to 1.22(1) Å and S···(D–6*h*) distance equal to 1.23(1) Å versus the shortest Fe···(D–4*f*) distance of 2.207 Å and Fe···(D–6*h*) distance of 1.965 Å. These

short distances suggest that there may be a covalent bond between the S and D atoms as bond lengths in D_2S compounds are about 1.30 to 1.35 Å (Cockcroft & Fitch, 1990).

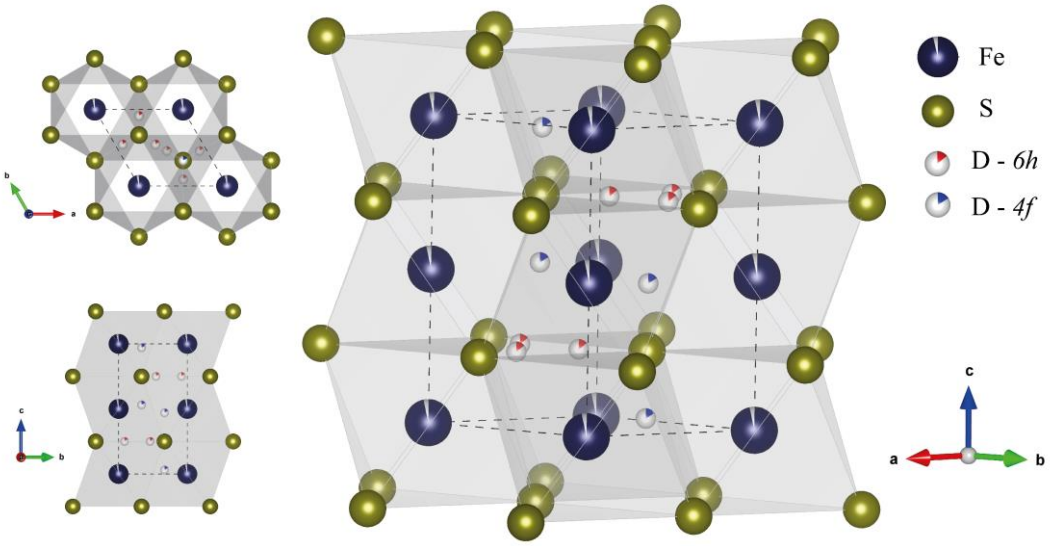

Figure 6.3: Final structural model of deuterated FeS V ($P6_3/mmc$, Z=2) at 6.9 GPa and 960 K. Refined occupancies of D are shown in red (for *6h*) and blue (for *4f*) as a percentage of each interstitial site. The atomic coordinates for the different atoms are: Fe: $\{0,0,0\}$; S: $\{1/3,2/3,1/4\}$; D-*6h*: $\{0{,}46(2),0.54(2),3/4\}$; and D-*4f*: $\{1/3,2/3,0.03(3)\}$. The dashed lines mark the unit-cell of FeS V, and the shaded polyhedrons are made with Fe as the centre of the octahedron. Section view along the *c*-axis and the *a*-axis of the structure are shown in the left side.

This final deuterated model was then used to refine the other diffraction patterns collected for at least 3 hours and up to 19 hours at the different *P* and *T* conditions (Table 6.1). The positions of the deuterium atoms were fixed to those obtained from the refinement at 6.9(4) GPa and 960 K to reduce the large correlations between deuterium positions, occupancies and displacement parameters, as this was the highest quality pattern due to having the largest sample size and a long collection time. The isotropic displacement parameters were constrained to be equal for the two deuterium positions. The diffraction pattern at 11.4(5) GPa and 1250 K was collected only for three hours due to the occurrence of a blowout, therefore, the signal to noise ratio was not sufficient for the refinement of all parameters. For this diffraction pattern, the isotropic displacement parameter was fixed to 0.5, i.e., the same value obtained in the refinements of the diffraction pattern collected at 9.7(4) GPa and at a similar temperature. Cubic-boron nitride (c-BN) is present in the experiments at 9.7(4) GPa and 11.4(4) (Table 6.1) due to the use of a smaller sample and assembly. Obtained "weighted R factor" (*wRp*) ranged between 3.2% and

5.0% and Chi-square (χ^2) values ranged between 1.3 and 6. Details of the structural refinements are reported in Table 6.2, whereas examples of the refined diffraction patterns are reported in Figure 6.4. The displacement parameters of deuterium appear to be correlated with temperature and are quite large for the highest-pressure experiments conducted at 1250 K and 1300 K, suggesting a large dynamic disorder of the deuterium atoms.

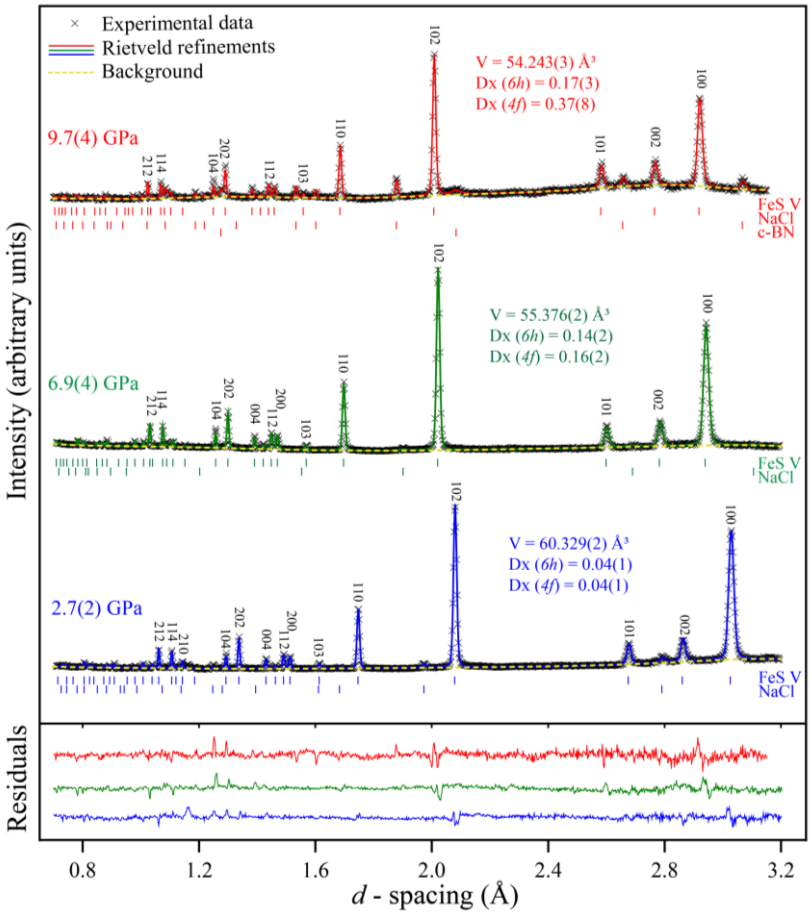

Figure 6.4: Rietveld refinements of neutron diffraction patterns at 2.7(2) GPa, 6.9(4) GPa and 9.7(4) GPa. Residuals to the fit are shown at the bottom of the figure in corresponding colours for each diffraction pattern. Cubic BN is identified in the diffraction pattern at 9.7(4) GPa, in addition to the FeS V and NaCl phases.

6.3.3 Volume variation due to deuteration

At a given pressure and temperature, the unit-cell volume of FeS V increases because of the incorporation of deuterium into the crystal structure. For example, at 6.9(4) GPa and 960 K, we observed a gradual increase of the unit-cell volume of FeS V over a period of 6 hours, until it became virtually constant (filled diamond symbols in Fig. 6.5). To clarify that the cause of

the unit-cell volume increase was purely due to deuteration, a second blank experiment was performed using an identical set-up but without the deuterium source; the conditions of this blank experiment were 7.3(4) GPa and 960 K. In contrast to the deuterated experiment, after a small volume expansion likely due to thermal adjustment of the cell assembly, there was no volumetric expansion observed over a period of 11 hrs (empty diamond symbols in Fig. 6.5). This verifies that the volume expansion (approximately 4.3%) observed in the deuterated experiment is a result of increasing deuterium. After 6 hours, the deuterated FeS V structure appears to have reached equilibrium, with a total occupancy of deuterium X_D=0.74(2) determined from Rietveld refinements (Table 6.2). The small difference in pressure between the non-deuterated (7.3±0.4 GPa) and deuterated (6.9±0.4 GPa) experiments is within the uncertainties and would produce no significant contribution to this volume difference, thus the difference in unit-cell volumes is mainly due to deuteration. The unit-cell volume expansion per one deuterium atom, ΔV(D), in the FeS V structure (Z=2) can be calculated as 1.53±0.16 $Å^3$ at 6.9 GPa, 960 K. This value is smaller compared to that proposed for Fe-metal hydrogenation (2.21 ± 0.04 $Å^3$ – Machida et al., 2014; 2.22 ± 0.36 $Å^3$ – Ikuta et al., 2019). This is most likely because for Fe-metal, hydrogen occupies octahedral interstitial sites within layers that are not occupied by Fe, whereas for FeS V hydrogen occupies sites in layers that are also occupied by Fe and S.

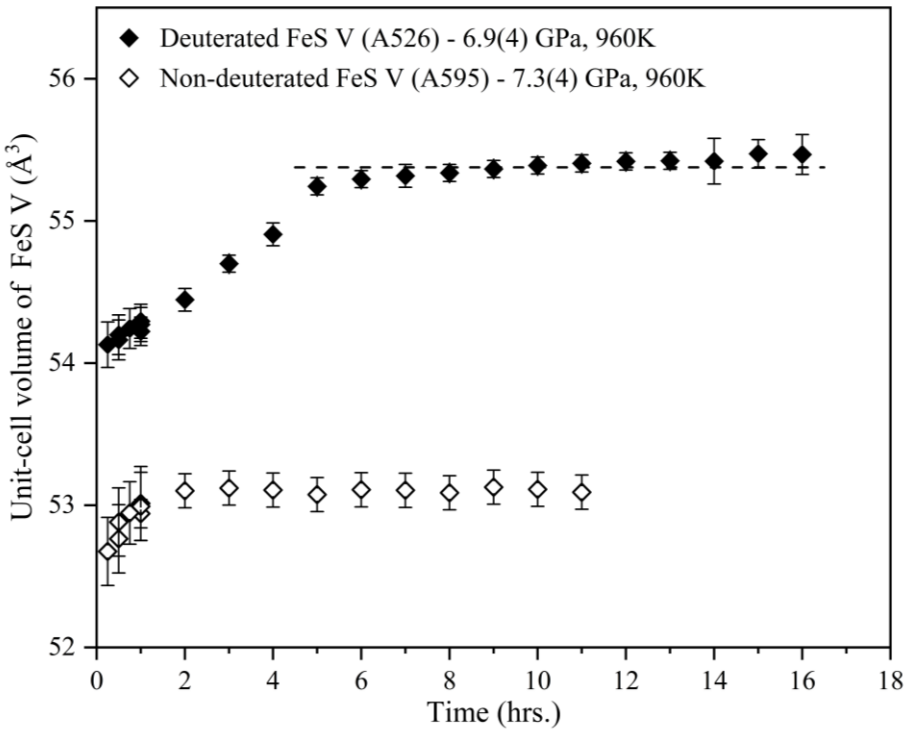

Figure 6.5: The unit-cell volumes of deuterated (filled diamonds–A526) and non-deuterated (empty diamonds–A595) FeS V plotted as a function of data collection time. The first hour of data collection was observed with higher (15–20 min.) time resolution. The dashed line indicates the unit-cell volume of FeS V once the dissolution of D_2 appears to be completed (55.376±0.002 Å^3), obtained by fitting the diffraction data collected during the last 10 hrs of heating. The average unit-cell volume of FeS V in non-deuterated experiment is 53.111±0.005 Å^3. Larger errors in the last three data points of A526 are caused by interruptions in the neutron source during the last 3 hours. The data plotted here are given in supplementary Table A.3.2.

The rate of deuterium uptake into the FeS V structure can be broken into three phases (Fig. 6.5) based on the unit-cell volume expansion rate of the experiment A526 at 6.9(4) GPa, 960 K. The first phase is completed within the time taken to heat to target temperature (approximately 15 minutes) and perform the first measurement (1 hour). Here, there is already a significant D content, which approaches X_D = 0.4 for a $FeSD_X$ stoichiometry, calculated using unit-cell volume expansion per deuterium atom (1.53 Å^3). Next, the rate of uptake decreases significantly over the next 5–6 hours until a virtually constant D occupancy (X_D = 0.74) is reached (Fig. 6.5).

In comparison with the 960 K experiment (A526), we observed faster deuterium equilibration in experiments at higher temperature (e.g. 1300 K – A593; supplementary Fig. A.3.5). The

total D content was obtained independently using the Rietveld refinement of the diffraction pattern, indicating a total deuterium content of 2.85 wt. %, which corresponds to the occupancy of 1.25(5) in $FeSD_X$ stoichiometry.

Table 6.2. Results of Rietveld structure refinements of FeS V

Experimental conditions				Unit-cell parameters of deuterated FeS V			Deuterium occupancies			
Run #	*P* (GPa)	*T* (K)	V_{NaCl} (Å^3)	*a* (Å)	*c* (Å)	*V* (Å^3)	6*h* site	4*f* site	*x* apfu	*U*iso
A524-1	2.3(2)	787	173.24(5)	3.4873(1)	5.7114(2)	60.151(2)	0.030(8)	0.029(9)	0.148(10)	0.24 (8)
A524-2	2.7(2)	940	173.36(11)	3.4908(1)	5.7168(2)	60.329(2)	0.036(10)	0.037(12)	0.182(11)	0.27 (9)
A526	6.9(4)	960	155.2(5)	3.3914(1)	5.5594(2)	55.376(2)	0.14(2)	0.16(2)	0.74(2)	0.38 (6)
A593	9.7(4)	1300	149.51(3)	3.3667(1)	5.5259(3)	54.243(3)	0.17(3)	0.37(8)	1.25(5)	0.49 (8)
A527	11.4(5)	1250	144.90(4)	3.3367(1)	5.4696(3)	52.739(3)	0.13(2)	0.25(3)	0.89(3)	0.5*

Note: Uncertainties on temperature are ± 50 K, all other uncertainties are given in parentheses. Isotropic atomic displacement parameters (*U*iso) are constrained to be equal in both deuterium occupied interstitial sites. * Not refined.

6.4 Discussion

6.4.1 P-T behaviour of the FeS V deuterium content and comparison with previous studies

By comparing the determined deuterium contents in the experiments at 2.7 and 6.9 GPa, at 940–960 K (A524–2 and A526), it appears that there is a clear increase in deuterium with increasing pressure (Fig. 6.7). The effect of temperature within the range of our experiments (787 – 1300 K) is harder to gauge, although with the exception of the experiment at 11.4 GPa, the results are consistent with an increase in deuterium with temperature. The experiment at 11.4 GPa (A527, Table 6.1), was interrupted by a blowout after the first three hours of heating, which might explain the seemingly lower than expected deuterium content as a result of the sample not fully equilibrating with D_2. The diffraction pattern is also of poorer quality than the others due to the use of a smaller sample and the short collection time. Comparing the volumes of the recovered samples, however, in Figure 6.6 indicates that deuterium is lost from the FeS V sample, or strongly reduced, as the temperature is quenched at high-pressures. Although the room temperature volume versus pressure curve is complicated by the change in iron spin state, it would appear that the temperature quenched samples all follow a very similar decompression curve, with the non-deuterated sample also falling, on this curve, albeit slightly on the lower

side. This implies that the majority of the deuterium is lost from the sample during temperature quenching, implying quite a strong temperature dependence to the deuterium content.

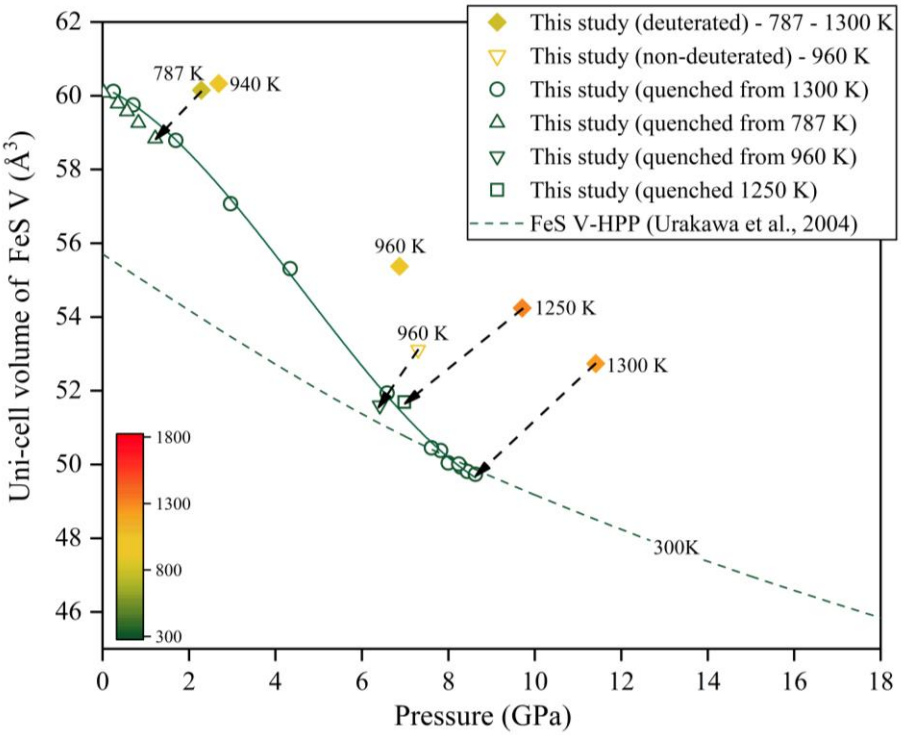

Figure 6.6: Absolute unit-cell volumes of experiments in this study plotted as a function of pressure. Open symbols indicate non-deuterated (yellow triangle) or quenched experiments from different conditions. Filled diamonds are deuterated experiments with colours representing the temperatures. Solid line shows the decompression trend and not a fit. The dashed line is an extrapolation of the Urakawa et al. (2004) equation-of-state of FeS V–HPP at 300 K. Arrows indicate the change in pressure as the samples were quenched to room temperature.

In the study of Shibazaki et al. (2011), FeS V hydrogen contents in an H_2 fluid, produced by thermal decomposition of $LiAlH_4$, were determined based on the increase in the unit-cell volume, assuming volume changes on hydrogenation based on dhcp–FeH_x measurements Badding et al. (1991). It should be noted that such a comparison between hydrogen-bearing and hydrogen-free FeS V unit cell volumes is complicated by the presence of the high-spin to low-spin iron transition, which prevents the application of a simple hydrogen-free FeS V equation of state over most of the conditions studied (Figure 6.2). Never the less, the hydrogen contents reported for solidus conditions by Shibazaki et al. (2011) are proposed to increase sharply between 2 and 3 GPa, from X_H = 0.02 to 0.2. They then increase to values of 0.4 by approximately 16.5 GPa. The results of our study, however, indicate, as Shibazaki et al. (2011)

also suspected, that volume changes on hydrogenation from FeH_x measurements are larger than for FeS V, implying that the X_H concentrations are underestimated and may well be consistent with our study.

Iizuka-Oku et al. (2021) used neutron diffraction experiments on a multi-phase system containing Fe, S, $MgSiO_3$ and D_2O, to study the uptake of deuterium by Fe-metal and FeS over similar conditions to those in our study. They concluded that the deuterium content in FeS is negligible. However, they proposed that the presence of only small amounts of FeS (added as ~ 5-10 % of S powder into Fe metal powder) reduced the extent of deuteration in coexisting Fe metal (the major phase in their system). The low FeS V deuterium contents, reported in this previous study, may result from potentially higher oxygen fugacities in the experiments, resulting from adding a D_2O source rather than D_2, resulting in a lower deuterium fugacities (fD_2). Additionally, the FeS V peaks appear to be not as strong or as well resolved as in our study, due to the patterns being dominated by fcc-Fe metal, which causes multiple peak-overlaps with FeS V, particularly at lower *d*-spacing.

Although the NiAs-structure of FeS V (Urakawa et al., 2004) is, in principle, the same as that of dhcp FeH_X, the accommodation of H is quite different, because in FeH_X hydrogen is on octahedral interstitial sites, which in FeS V host the S. The hydrogenation/deuteration of different iron-metal structures has been extensively examined, however, at high pressures and temperatures using neutron diffraction experiments (Iizuka-Oku et al., 2017; Ikuta et al., 2019; Machida et al., 2014, 2019), and the H/D site occupancies obtained are compared with our values for FeS V in Figure 6.7. Although the measurements are performed at different temperatures, there is a general agreement in the magnitude of H/D occupancy with increasing pressure. There is also no obvious difference between studies using H or D. Although in detail there are likely to be differences in H/D accommodation due to the different structures involved and for FeS due to the high-spin low-spin transition, the general increase in pressure implies that this may be at least partly coupled to an increase in hydrogen or deuterium fugacity.

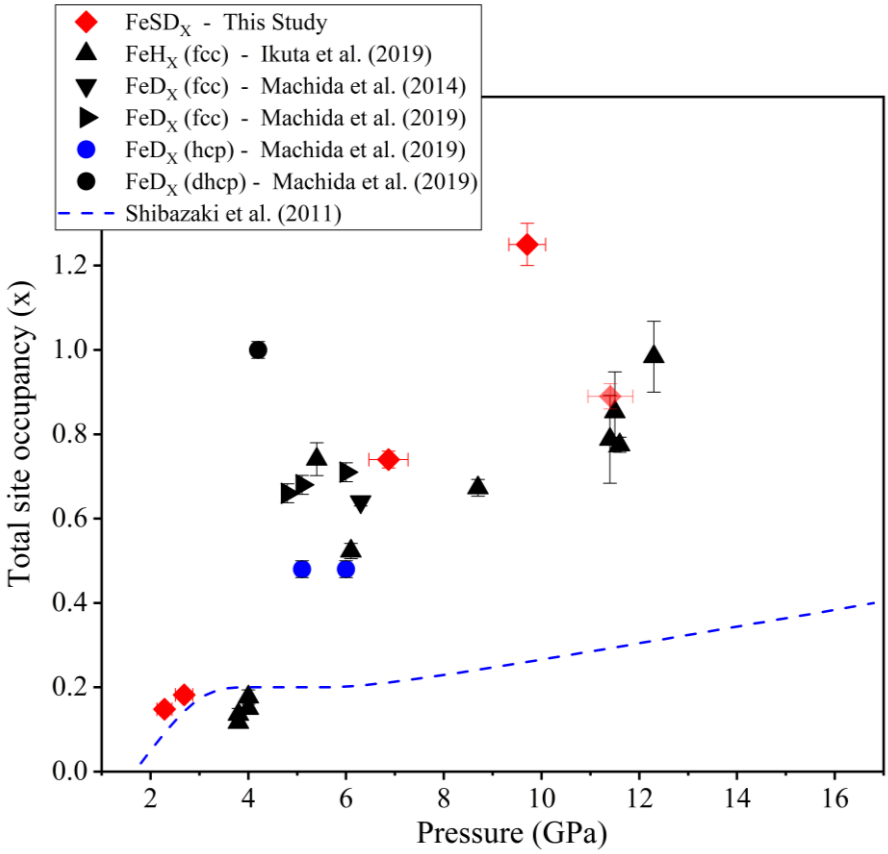

Figure 6.7: Total site occupancy of D/H in FeS V (red diamonds) as a function of pressure. Previous study data on iron hydride/deuteride are shown in triangles. The occupancy of the experiment at 11.4(5) GPa in this study (shaded red diamond symbol–#A527) may be underestimated because of not being fully equilibrated. The blue shaded line shows the increase in hydrogen occupancy with increasing pressure proposed by Shibazaki et al. (2011) using unit-cell volume relations.

6.4.2 The oxygen fugacity of the measurements and the nature of the coexisting fluid phase

Before considering the relationship between deuterium incorporation in FeS V and the deuterium fugacity, a further issue to consider is the experimental fo_2 and the composition of the coexisting fluid. The fo_2 should be controlled through the formation of a D_2-rich fluid from the breakdown of ND_3BD_3, because no other fo_2 buffering assemblage was employed. To examine the likely fo_2 conditions during the neutron diffraction measurements, a separate experiment was performed that replicated the sample environment of the *in situ* experiments but replaced the sample itself with a ferropericlase-based sliding redox sensor assemblage (J. R. Taylor et al., 1992). A 2.0 mm outer and 1.0 mm inner diameter NaCl capsule with a total sample length of 2.5 mm, was filled with two layers of deuterated ammonia borane, each of

~1.2 mm thickness, which were separated by a ~0.1 mm thick layer of $Fe_{0.2}Mg_{0.8}O$ ferropericlase, mixed with 2 wt. % of pure iron metal. The capsule was closed by a 0.5 mm thick NaCl lid. The experiment was performed using a 5000 t Kawai-type multi-anvil press installed at the Bayerisches Geoinstitut (Frost et al., 2004) using a 18/11 set up (18 mm edge length octahedral assembly with 11 mm truncations of secondary stage tungsten carbide cubes). A stepped graphite resistive heater was used with a thermally insulating ZrO_2 sleeve. The temperature was monitored using a type D ($W_{97}Re_3$–$W_{75}Re_{25}$) thermocouple inserted axially touching a very thin (<0.2 mm) MgO disk (to prevent any damage from thermocouple to the capsule) placed on top of the capsule. The redox sensor and ammonia borane layers were equilibrated at 1300 °C and 8 GPa for 2 hours. The recovered sensor was examined using the electron probe micro analyser and was comprised of ferropericlase with the composition $Fe_{0.13}Mg_{0.87}O$, in addition to iron metal and brucite. The fo_2 can be calculated using the equilibrium between the iron metal and ferropericlase FeO component and using thermodynamic properties given in (Stagno et al., 2011). This gives a value of 1.2 ± 0.2 log units below the iron wüstite (IW) oxygen buffer. It is possible to make a simple calculation for the H_2 content of an O–H fluid at these conditions, which should not be significantly different to D_2 (Tkacz & Litwiniuk, 2002), using the equilibrium,

$$H_2 + \frac{1}{2}O_2 = H_2O \tag{6.2}$$

and values for the equilibrium coefficient *K* from Holland & Powell (2011), where,

$$K = \frac{f_{H_2O}}{f_{H_2}.\left(f_{O_2}\right)^{0.5}} \tag{6.3}$$

Assuming ideal mixing in the H_2–H_2O fluid then,

$$f_{H_2} = P_T.X_{H_2}.\emptyset_{H_2} \tag{6.4}$$

where P_T is the total pressure, X_{H_2} the mole fraction and $\emptyset_{H_2}$ is the fugacity coefficient of pure H_2, determined here using the equations of state of Belonoshko & Saxena (1991). A similar expression can be written for H_2O and when this and equation (6.4) are substituted into equation (6.3) and the constraint that X_{H_2}= 1- X_{H_2O} is applied, then the combined expression can be solved to give X_{H_2} as a function of f_{O_2}. This is shown by the black curve in Figure 6.8, which indicates that at the experimental conditions and ΔIW -1.2, the fluid is calculated to be only 36

mol % H_2. The relatively high f_{O_2} obtained in the experiments is, therefore, apparently inconsistent with a D_2-dominated fluid, which should only comprise more than 90 % of the fluid at ΔIW -4.

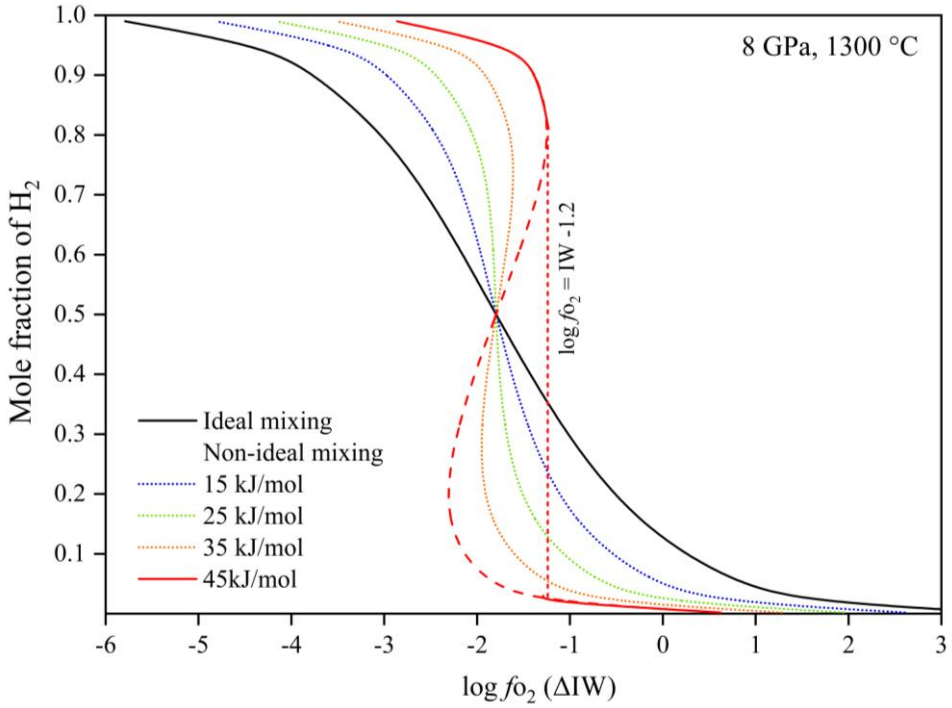

Figure 6.8: The proportion of H_2 in an H_2–H_2O fluid as a function of oxygen fugacity relative to the iron-wüstite oxygen buffer (ΔIW), calculated for the indicated pressure and temperature condition. The calculation uses the equation of state of Belonoshko & Saxena (1991), assuming both ideal mixing of H_2 and H_2O in the fluid (solid black curve) and for a series of non-ideal mixing Margules interaction parameters. As non-ideality increases, a back bend in the proportion of H_2 occurs, which indicates regions where immiscible H_2 and H_2O-rich fluids coexist at the same oxygen fugacity. For an interaction parameter of 45 kJ/mol this coexistence occurs at an oxygen fugacity consistent with the experimentally measure value. The vertical red dotted line indicates the coexisting immiscible fluid compositions for this oxygen fugacity.

It is unlikely that adsorbed H_2O would be sufficient to dominate over the significant amount of stoichiometric D_2 that would be released by ND_3BD_3, and it is more likely that the assumption of H_2–H_2O ideal mixing in the calculation is incorrect. Evidence for this comes from the recent observation of H_2–H_2O immiscibility (Bali et al., 2013), where separate, nearly pure, H_2 and H_2O fluids were found to coexist at conditions of IW. The critical temperature for closure of this solvus was found to increase quite strongly between 1.5 and 2.7 GPa, from approximately 800 to 1000 °C. Some idea of the consequences of H_2–H_2O non-ideal mixing can be obtained

by including a further activity coefficient, $\gamma_{H_2}^{H_2-H_2O}$, in equation 6.4, which can in turn be described using a Margules interaction parameter, *W*, i.e.,

$$RT\ln\gamma_{H_2}^{H_2-H_2O} = W_{H_2-H_2O}\left(1 - X_{H_2}\right)^2 \quad (6.5)$$

where *R* is the gas constant and *T* is temperature. As shown in Figure 6.8, increasing non-ideality reduces the range of fo_2 over which H_2O-rich fluids reduce to H_2-rich fluids. An H_2-dominated fluid can be stabilised at an fo_2 of ΔIW -1.2, coexisting with an immiscible H_2O dominated fluid, if the interaction parameter is approximately 45 kJ/mol. This is slightly larger than the value required to explain the observations of Bali et al. (2013) between 1 and 3 GPa, but the value should increase with pressure in line with the increase in the critical temperature. This indicates that the fo_2 determined in this study upon D_2 release is quite consistent with the observations of H_2O–H_2 immiscibility of Bali et al. (2013). In detail, the non-ideal interaction parameter may be asymmetric and require a more complex *P* and *T* fitting. This should not, however, change the main implications from Figure 6.8, that H_2-dominted fluids can be stable at higher fo_2 than might be expected and that because the transition between H_2O and H_2 dominated fluids occurs over a smaller fo_2 range, the mole fraction of H_2 in fluids at higher oxygen fugacities is most likely lower than would be expected if ideal mixing is assumed.

6.4.3 A model for the deuterium content of FeS V and extrapolation to mantle conditions

As there are two FeS molecules in the FeS V unit-cell, then there are two *4f* deuterium sites and three *6h* sites that could potentially be occupied for the FeS stoichiometry. However, the two sets of three *6h* sites in each unit cell are unlikely to be all deuterated at the same time, due to their close proximity, therefore, it seems more reasonable to assume only two of these sites can be deuterated in any unit-cell. For FeS this means a total possible occupancy of three deuterium atoms (one in the *6h* position and two in the *4f* position), i.e. a fictive fully deuterated endmember of $FeSD_3$. Assuming that the ND_3BD_3 source produces a pure D_2 fluid, which the calculations in the previous section seem to support, then the deuteration can be considered as,

$$FeS\square_3 + \frac{3}{2}D_2 = FeSD_3 \quad (6.6)$$

where □ indicates the vacant interstitial sites. If for simplicity we assume disorder over all three sites, then we can relate the concentration of deuterium, to the deuterium fugacity and the standard state Gibbs free energy change, ΔG^o, of reaction (6.6) through,

$$\ln\left(\frac{a\mathrm{FeSD}_3}{a\mathrm{FeS}\square_3.[fD_2]^{3/2}}\right)=\frac{-\Delta G^o}{RT} \quad (6.7)$$

Assuming ideal mixing of D in the FeS V structure, the activities are given by,

$$a\mathrm{FeSD}_3=\left[\frac{X_\mathrm{D}}{3}\right]^3 \quad (6.8)$$

and

$$a\mathrm{FeS}\square_3=\left[\frac{3-X_\mathrm{D}}{3}\right]^3 \quad (6.9)$$

where X_D is the deuterium site occupancy per FeS formula unit, given in Table 6.2. The experimental data can then be fitted by taking hydrogen fugacities from Belonoshko & Saxena (1991), and fitting ΔG^oas $\Delta H^o - T\Delta S^o + P\Delta V^o$. If the anomalous 11.4 GPa data is removed, the fitting parameters are ΔH^o=64.8 ± 13 kJ/mol, ΔS^o=-154 ± 19 J/(mol.K) and ΔV^o= 0.66 ± 0.11 J/bar. Given that four data points are being fit with three parameters it is perhaps not surprising that the fit is very good and the largest residual in X_D is only 0.04. The ΔV^o is larger than the value of 0.3 J/bar that can be estimated from the volume change on deuteration, ΔV(D), determined in this study, however, and if the $\Delta V^o$is fixed at 0.3 J/bar, the largest X_D residual increases to 0.22. It may not be reasonable to assume ideal mixing of D in the vacant site, however, and if we choose a single site Margules mixing parameter for D on the vacant site of -1.2 kJ/mol then fitting parameters can be obtained that give a ΔV^o that is in reasonable agreement, i.e. ΔH^o=112 ± 17 kJ/mol, ΔS^o=-145 ± 14 J/(mol.K) and ΔV^o= 0.35 ± 0.14 J/bar. Although these models are almost certainly over simplified and would require far more data to become robust, they do allow a basic qualitative exploration of how D/H uptake in FeS V is likely to change under different conditions. Firstly, both models predict that if equilibrium is maintained, the D content should drop to low levels on quenching to room temperature at high pressure, in agreement with the quenched FeS V unit cell volumes shown in Figure 6.6.

Secondly, by considering that,

$$f\mathrm{H}_2=P.\emptyset_{\mathrm{H}_2}.X_{\mathrm{H}_2}.\gamma_{\mathrm{H}_2}^{\mathrm{H}_2-\mathrm{H}_2\mathrm{O}} \quad (6.10)$$

as in equation 4, but adding a further activity coefficient to describe non-ideal mixing between H_2O and H_2 as defined in equation 6.5 and consistent with the observations of Bali et al. (2013), then the effect of lower H_2, fugacities, can be explored on the equilibrium FeS V hydrogen

contents. As Fe-Ni-rich monosulphides are the dominant inclusion found in diamonds, the relevant conditions to explore this relationship are those at which diamonds exist in the subcratonic lithospheric mantle. For a typical cratonic geotherm, with temperatures of 1300 °C at 6.5 GPa i.e. approximately 200 km depth, then FeS V would be subsolidus (Z. Zhang & Hirschmann, 2016) and in a pure H_2 fluid the two models predict an FeS X_H of 0.8–0.87, which is equivalent to approximately 1 wt. % hydrogen in the structure. However, diamond bearing peridotite mantle xenoliths at these conditions record typical values of fo_2, relative to the fayalite-magnetite-quartz oxygen buffer (FMQ), of ΔFMQ -3 ± 1 or ΔIW +1.8. As carbon at these conditions is mainly in the form of diamond (Shirey et al., 2013), an O–H mixing calculation similar to that described in section 6.4.2. at ΔFMQ of -3, predicts a H_2 fluid activity (i.e. $X_{H_2}.\gamma_{H_2}^{H_2-H_2O}$) of 0.02, which results in a predicted FeS X_H of 0.15–0.24 or 1700–2700 ppm hydrogen in the structure, depending on which FeS V fitting model is used. The hydrogen content would be half this value at ΔFMQ of -2. Of course, hydrogen activities may have been much lower than this during diamond formation and FeS inclusion capture, depending on the nature of the medium from which they are formed. This relatively simple calculation, however, appears to indicate that significant hydrogen contents could be accommodated by FeS inclusions in diamonds. If such diamonds were then brought to the surface, the reduction in temperature and pressure would cause the FeS inclusions to exsolve H_2, the analysis of which might give the false impression that the inclusions were captured at very reducing conditions. A further possibility is that this loss of hydrogen from the inclusions upon decompression, may cause hydrogen embrittlement of the diamond, as often encountered in diamond anvil cell experiments on hydrogen (Eremets & Trojan, 2009), which may then play a role in the development of the rosette like fracture systems often observed around sulphide inclusions in diamonds (Harris, 1972). This may also be promoted by the strong volume expansion that would occur due to the FeS V iron spin transition, as indicated in Figure 6.6.

It is also possible to estimate how much hydrogen could be stored in FeS monosulphide phases within the bulk mantle rocks at the base of the cratonic lithosphere. If these rocks contain on average approximately 400 ppm sulphur (Gehlen, 1992) accommodated at these conditions in FeS V, then provided that the rocks were in equilibrium with an O–H fluid at ΔFMQ = -3, this equates to 2–3 ppm H_2 hosted by sulphides in the bulk rock, which is equivalent to 16–26 ppm H_2O. This value would decrease at higher oxygen fugacities and at shallower depths in the cratonic lithosphere. At greater depths the oxygen fugacity of the mantle is expected to decrease

and the FeS V phase would also become molten which might both promote higher hydrogen contents in the sulphide phase, although this remains to be experimentally tested.

6.5 Summary

Time-of-flight powder neutron diffraction measurements at pressures up to 11.4 GPa and temperatures to 1300 K were performed to study the solubility of deuterium in the NiAs-structured FeS V polytype of pyrrhotite. Thermal decomposition of ND_3BD_3 was used to create a D_2 dominated fluid in the multi-anvil experiments. Rietveld structure refinements indicated the partial occupancy of deuterium on two normally unoccupied sites in the structure at Wyckoff positions *6h*: $\{0.46(2), 0.54(2), 3/4\}$ and *4f*: $\{1/3\,, 2/3\,, 0.03(3)\}$ at high pressure and temperature conditions, with the latter being more dominant.

The incorporation of deuterium in the crystal structure increases the unit-cell volume of FeS V by 4.3% at 6.9 GPa and 960 K and the unit-cell volume expansion per deuterium atom, $\Delta V(D)$, is 1.53±0.16 $Å^3$. This is smaller compared to that previously reported for the hydrogenation of Fe-metal phases at similar conditions (2.21±0.04 $Å^3$ – Machida et al., 2014). The structural model indicates that both deuterium sites are closer to the S atoms than to the Fe atoms, such that S and D may be covalently bonded, which may explain the smaller $\Delta V(D)$ value compared to Fe-metal phases. Previously reported hydrogen contents in FeS V, by means of X-ray diffraction volume relations are likely underestimated, due to the use of a $\Delta V(H)$ value estimated from results on hydrogenated Fe-metal phases (Shibazaki et al., 2011). The deuterium dissolved in FeS V at high-temperature is mainly lost during temperature quenching at high-pressure, as indicated by the decrease in unit-cell volumes of the quenched experiments.

Refinements of all diffraction patterns collected indicate that the D content in FeS V increases with both pressure and temperature. The total deuterium content, X in FeSDx, increases from 0.148(10) at 2.3 GPa and 787 K to 1.25(5) at 9.7 GPa and 1300 K. A comparison between FeSDx and FeHx/FeDx measurements at similar conditions shows that there is a general similarity in the magnitude of H/D occupancy with increasing pressure.

A parallel multi-anvil experiment was conducted to determine the oxygen fugacity of samples exposed to the D_2 fluid produced by the breakdown of ND_3BD_3, indicating an oxygen fugacity of 1.2 ± 0.2 log units below the iron wüstite (IW) oxygen buffer. This is much higher than would be expected for an O-H fluid dominated by H_2 if ideal mixing of H_2–H_2O is assumed. It

is consistent, however, with the degree of non-ideal mixing implied by the recent observation of immiscibility between H_2 and H_2O-rich fluids (Bali et al., 2013).

The D_2 solubilites are fitted to a thermodynamic model which confirms that FeS V hydrogen contents should drop to low levels on temperature quenching at high-pressure. The model is extrapolated to the lower H_2 fugacities consistent with the higher oxygen fugacities at the base of the cratonic lithosphere. At these conditions FeS V could still contain significant amounts of hydrogen, in the range 1700–2700 ppm. Loss of hydrogen from diamond hosted FeS V during decompression, could play a role in the development of the rosette like fracture systems often observed around sulphide inclusions in diamonds (Harris, 1972). Based on an average mantle sulphur content of 400 ppm (Gehlen, 1992), then at the base of the cratonic lithosphere a bulk mantle H_2 content of 2–3 ppm could be hosted by mantle sulphides. At greater depths lower oxygen fugacities and melting of FeS V may lead to higher hydrogen contents in sulphides.

Finally, it may be possible to study the partitioning of deuterium between sulphide melts and silicate melts and minerals at high pressure and temperature conditions, by quenching the sulphide melts to temperatures where the deuterium content of the crystallised FeS V assemblage is still below the D_2 solubility. The deuterium contents in the quenched FeS V assemblage would then be determined using the same type of *in situ* neutron diffraction measurement, whereas the silicates would be recovered to room pressure for analysis.

Acknowledgements

We would like to thank Raphael Njul, Alexander Rother and Heinz Fischer for their technical assistance. Dr. Takanori Hattori is thanked for scheduling the experiments at J-PARC and for valuable discussion. Dr. Florian Heidelbach and Dr. Shin Ozawa are thanked for their help with the analysis of some experimental samples and we thank Dr. Nicolas Walte for constructive discussions. This project was conducted as a part of the "Deep volatile cycles" – International Research Training Group funded by the German Research Foundation (Deutsche Forschungsgemeinschaft – DFG, GRK 2156/1) and through DFG grant FR1555/11.

Supplementary materials

See appendix A.3 for supplementary text, figures and tables. The deposited CIF can be found as electronic supplementary materials available at:
https://doi.org/10.6084/m9.figshare.21253968.v1

References

Antonov, V. E., Cornell, K., Fedotov, V. K., Kolesnikov, A. I., Ponyatovsky, E. G., Shiryaev, V. I., & Wipf, H. (1998). Neutron diffraction investigation of the dhcp and hcp iron hydrides and deutendes. *Journal of Alloys and Compounds*, *264*(1–2), 214–222. https://doi.org/10.1016/S0925-8388(97)00298-3

Badding, J. V., Hemley, R. J., & Mao, H. K. (1991). High-Pressure Chemistry of Hydrogen in Metals: In Situ Study of Iron Hydride. *Science*, *253*(5018), 421–424.

Bali, E., Audétat, A., & Keppler, H. (2013). Water and hydrogen are immiscible in Earth's mantle. *Nature*, *495*(7440), 220–222. https://doi.org/10.1038/nature11908

Belonoshko, A., & Saxena, S. K. (1991). A molecular dynamics study of the pressure-volume-temperature properties of supercritical fluids: II. CO_2, CH_4, CO, O_2, and H_2. *Geochimica et Cosmochimica Acta*, *55*(11), 3191–3208.

Bondar, D., Fei, H., Withers, A. C., Ishii, T., Chanyshev, A., & Katsura, T. (2021). A simplified rapid-quench multi-anvil technique. *Review of Scientific Instruments*, *92*(11). https://doi.org/10.1063/5.0062525

Brand, V. P., & Briest, J. (1965). Das quasi-binäre System NiAs-Ni1,5Sn. *Zeitschrift Für Anorganische Und Allgemeine Chemie*, *337*(3–4), 209–213.

Clesi, V., Bouhifd, M. A., Bolfan-Casanova, N., Manthilake, G., Schiavi, F., Raepsaet, C., et al. (2018). Low hydrogen contents in the cores of terrestrial planets. *Science Advances*, *4*(3), e1701876.

Cockcroft, J. K., & Fitch, A. N. (1990). The solid phases of deuterium sulphide by powder neutron diffraction. *Zeitschrift Fur Kristallographie - New Crystal Structures*, *193*(1–2), 1–19. https://doi.org/10.1524/zkri.1990.193.1-2.1

Dawidowski, J., Granada, J. R., Santisteban, J. R., Cantargi, F., & Palomino, L. A. R. (2013). *Neutron Scattering Lengths and Cross Sections*. *Experimental Methods in the Physical Sciences* (Vol. 44). Elsevier Inc. https://doi.org/10.1016/B978-0-12-398374-9.09989-7

Delano, J. W. (2001). Redox history of the Earth's interior since ~3900 Ma: Implications for prebiotic molecules. *Origins of Life and Evolution of the Biosphere*, *31*(4–5), 311–341. https://doi.org/10.1023/A:1011895600380

Dorogokupets, P. I., & Dewaele, A. (2007). Equations of state of MgO, Au, Pt, NaCl-B1, and NaCl-B2: Internally consistent high-temperature pressure scales. *High Pressure Research*, *27*(4), 431–446. https://doi.org/10.1080/08957950701659700

Eremets, M. I., & Trojan, I. A. (2009). Evidence of maximum in the melting curve of hydrogen at megabar pressures. *JETP Letters*, *89*(4), 174–179.

Fei, Y., Charles, T., Prewitt, C. T., Mao, H., & Bertka, C. M. (1995). Structure and Density of FeS at High Pressure and High Temperature and the internal Structure of Mars. *Science*, *268*, 1892–1894.

Fei, Y., Prewitt, C. T., Frost, D. J., Parise, J. B., & Brister, K. (1998). Structures of FeS polymorphs at high pressure and temperature. *The Review of High Pressure Science and Technology*, *7*, 55–58.

Frost, D. J., Poe, B. T., Trønnes, R. G., Liebske, C., Duba, A., & Rubie, D. C. (2004). A new large-volume multianvil system. *Physics of the Earth and Planetary Interiors*, *143*(1–2), 507–514. https://doi.org/10.1016/j.pepi.2004.03.003

Fukai, Y., & Suzuki, T. (1986). Iron-Water Reaction under High Pressure and Its implication in the evolution of the Earth, *91*(B9), 9222–9230.

Fukai, Y., Mori, K., & Shinomiya, H. (2003). The phase diagram and superabundant vacancy formation in Fe-H alloys under high hydrogen pressures. *Journal of Alloys and Compounds*, *348*(1–2), 105–109. https://doi.org/10.1016/S0925-8388(02)00806-X

Gehlen, K. von. (1992). Sulfur in the Earth's Mantle—A Review. *Early Organic Evolution*, 359–366.

Harris, J. W. (1972). Black material on mineral inclusions and in internal fracture planes in diamond. *Contributions to Mineralogy and Petrology*, *35*(1), 22–33.

Harvey, J., Warren, J. M., & Shirey, S. B. (2016). Mantle sulfides and their role in Re–Os and Pb isotope geochronology. *Reviews in Mineralogy and Geochemistry*, *81*(1), 579–649.

Hattori, T., Sano-Furukawa, A., Arima, H., Komatsu, K., Yamada, A., Inamura, Y., et al. (2015). Design and performance of high-pressure PLANET beamline at pulsed neutron source at J-PARC. *Nuclear Instruments and Methods in Physics Research, Section A: Accelerators, Spectrometers, Detectors and Associated Equipment*, *780*, 55–67. https://doi.org/10.1016/j.nima.2015.01.059

Holland, T. J. B., & Powell, R. (2011). An improved and extended internally consistent thermodynamic dataset for phases of petrological interest, involving a new equation of state for solids. *Journal of Metamorphic Geology*, *29*(3), 333–383.

Iizuka-Oku, R., Yagi, T., Gotou, H., Okuchi, T., Hattori, T., & Sano-Furukawa, A. (2017). Hydrogenation of iron in the early stage of Earth's evolution. *Nature Communications*, *8*, *14096*. https://doi.org/10.1038/ncomms14096

Iizuka-Oku, R., Gotou, H., Shito, C., Fukuyama, K., Mori, Y., Hattori, T., et al. (2021). Behavior of light elements in iron-silicate-water-sulfur system during early Earth's evolution. *Scientific Reports*, *11*(1), 12632. https://doi.org/10.1038/s41598-021-91801-3

Ikuta, D., Ohtani, E., Sano-Furukawa, A., Shibazaki, Y., Terasaki, H., Yuan, L., & Hattori, T. (2019). Interstitial hydrogen atoms in face-centered cubic iron in the Earth's core. *Scientific Reports*, *9*(1), 1–8. https://doi.org/10.1038/s41598-019-43601-z

Kasting, J. F. (1993). Earth's Early Atmosphere. *Science*, *259*(5097), 920–926. Retrieved from http://www.jstor.org/stable/1698323

Kiseeva, E. S., & Wood, B. J. (2013). A simple model for chalcophile element partitioning between sulphide and silicate liquids with geochemical applications. *Earth and Planetary Science Letters*, *383*, 68–81. https://doi.org/10.1016/j.epsl.2013.09.034

Kobayashi, H., Sato, M., Kamimura, T., Sakai, M., Onodera, H., Kuroda, N., & Yamaguchi, Y. (1997). The effect of pressure on the electronic states of FeS and Fe_7S_8 studied by Mössbauer spectroscopy. *Journal of Physics Condensed Matter*, *9*(2), 515–527. https://doi.org/10.1088/0953-8984/9/2/019

Kusaba, K., Syono, Y., Kikegawa, T., & Shimomura, O. (1998). High pressure and temperature behavior of FeS. *Journal of Physics and Chemistry of Solids*, *59*(6–7), 945–950. https://doi.org/10.1016/S0022-3697(98)00015-8

Kusaba, K., Utsumi, W., Yamakata, M., Shimomura, O., & Syono, Y. (2000). Second-order phase transition of FeS under high pressure and temperature. *Journal of Physics and Chemistry of Solids*, *61*(9), 1483–1487. https://doi.org/10.1016/S0022-3697(00)00005-6

Larson, A. C., & Von Dreele, R. B. (2004). General Srtucture Analysis System (GSAS). Los Alamos National Laboratory Report LAUR, University of California.

Laurenz, V., Rubie, D. C., Frost, D. J., & Vogel, A. K. (2016). The importance of sulfur for the behavior of highly-siderophile elements during Earth's differentiation. *Geochimica et Cosmochimica Acta*, *194*, 123–138. https://doi.org/10.1016/j.gca.2016.08.012

Machida, A., Saitoh, H., Sugimoto, H., Hattori, T., Sano-Furukawa, A., Endo, N., et al.

(2014). Site occupancy of interstitial deuterium atoms in face-centred cubic iron. *Nature Communications*, *5*, 2–5. https://doi.org/10.1038/ncomms6063

Machida, A., Saitoh, H., Hattori, T., Sano-Furukawa, A., Funakoshi, K. ichi, Sato, T., et al. (2019). Hexagonal Close-packed Iron Hydride behind the Conventional Phase Diagram. *Scientific Reports*, *9*(1), 1–9. https://doi.org/10.1038/s41598-019-48817-7

Malavergne, V., Bureau, H., Raepsaet, C., Gaillard, F., Poncet, M., Surble, S., et al. (2019). Experimental constraints on the fate of H and C during planetary core-mantle differentiation. Implications for the Earth. *Icarus*, *321*, 473–485.

Mann, U., Frost, D. J., Rubie, D. C., Becker, H., & Audétat, A. (2012). Partitioning of Ru, Rh, Pd, Re, Ir and Pt between liquid metal and silicate at high pressures and high temperatures - Implications for the origin of highly siderophile element concentrations in the Earth's mantle. *Geochimica et Cosmochimica Acta*, *84*, 593–613. https://doi.org/10.1016/j.gca.2012.01.026

Nelmes, R. J., McMahon, M. I., Belmonte, S. A., & Parise, J. B. (1999). Structure of the high-pressure phase III of iron sulfide. *Physical Review B*, *59*(14), 9048–9052.

Nyĺn, J., Sato, T., Soignard, E., Yarger, J. L., Stoyanov, E., & Häussermann, U. (2009). Thermal decomposition of ammonia borane at high pressures. *Journal of Chemical Physics*, *131*(10). https://doi.org/10.1063/1.3230973

O'Neill, H. S. C. (1991). The origin of the moon and the early history of the earth-A chemical model. Part 2: The Earth. *Geochimica et Cosmochimica Acta*, *55*, 1159–1172. https://doi.org/10.1016/0016-7037(91)90168-5

Okuchi, T. (1997). Hydrogen partitioning into molten iron at high pressure: Implications for earth's core. *Science*, *278*(5344), 1781–1784. https://doi.org/10.1126/science.278.5344.1781

Piet, H., Leinenweber, K., E, G., Prakapenka, V. B., & Shim, S. H. (2021). Effects of Hydrogen on the Phase Relations in Fe-FeS at Pressures of Mars-Sized Bodies.pdf. *Journal of Geophysical Research-Planets*, *126*(11).

Ringwood, A. E. (1977). Composition of the core and implications for origin of the earth. *Geochemical Journal*, *11*, 111–135.

Rubie, D. C., Laurenz, V., Jacobson, S. A., Morbidelli, A., Palme, H., Vogel, A. K., & Frost, D. J. (2016). Highly siderophile elements were stripped from the Earth's mantle by iron sulfide segregation. *Science*, *353*(6304), 1141–1144.

Rueff, J. P., Kao. C. C., Struzhkin, V. V., Badro, J., Shu, J., Hemley, R. J., & Mao, H. K. (1999). Pressure-induced high-spin to low-spin transition in FeS evidenced by X-ray emission spectroscopy. *Physical Review Letters*, *82*(16), 3284–3287. https://doi.org/10.1103/PhysRevLett.82.3284

Sakamaki, K., Takahashi, E., Nakajima, Y., Nishihara, Y., Funakoshi, K., Suzuki, T., & Fukai, Y. (2009). Melting phase relation of FeHx up to 20 GPa: Implication for the

temperature of the Earth's core. *Physics of the Earth and Planetary Interiors*, *174*(1–4), 192–201. https://doi.org/10.1016/j.pepi.2008.05.017

Sano-Furukawa, A., Hattori, T., Arima, H., Yamada, A., Tabata, S., Kondo, M., et al. (2014). Six-axis multi-anvil press for high-pressure, high-temperature neutron diffraction experiments. *Review of Scientific Instruments*, *85*(11). https://doi.org/10.1063/1.4901095

Sears, V. F. (1992). Neutron scattering lengths and cross sections. *Neutron News*, *3*(3), 26–37. https://doi.org/10.1080/10448639208218770

Sharp, Z. D., McCubbin, F. M., & Shearer, C. K. (2013). A hydrogen-based oxidation mechanism relevant to planetary formation. *Earth and Planetary Science Letters*, *380*, 88–97. https://doi.org/10.1016/j.epsl.2013.08.015

Shibazaki, Y., Ohtani, E., Terasaki, H., Tateyama, R., Sakamaki, T., Tsuchiya, T., & Funakoshi, K. ichi. (2011). Effect of hydrogen on the melting temperature of FeS at high pressure: Implications for the core of Ganymede. *Earth and Planetary Science Letters*, *301*(1–2), 153–158. https://doi.org/10.1016/j.epsl.2010.10.033

Shirey, S. B., Cartigny, P., Frost, D. J., Keshav, S., Nestola, F., Nimis, P., et al. (2013). Diamonds and the geology of mantle carbon. *Reviews in Mineralogy and Geochemistry*, *75*(1), 355–421. https://doi.org/10.2138/rmg.2013.75.12

Solozhenko, V. L., Turkevich, V. Z., & Holzapfel, W. B. (1999). Refined Phase Diagram of Boron Nitride. *Journal of Physical Chemistry B*, *103*(15), 2903–2905. https://doi.org/10.1021/jp984682c

Stagno, V., Tange, Y., Miyajima, N., McCammon, C. A., Irifune, T., & Frost, D. J. (2011). The stability of magnesite in the transition zone and the lower mantle as function of oxygen fugacity. *Geophysical Research Letters*, *38*(19), 1–5. https://doi.org/10.1029/2011GL049560

Stähler, S. C., Khan, A., Banerdt, W. B., Lognonné, P., Giardini, D., Ceylan, S., et al. (2021). Seismic detection of the martian core. *Science*, *373*(6553), 443–448.

Tagawa, S., Sakamoto, N., Hirose, K., Yokoo, S., Hernlund, J., Ohishi, Y., & Yurimoto, H. (2021). Experimental evidence for hydrogen incorporation into Earth's core. *Nature Communications*, *12*(1), 1–8. https://doi.org/10.1038/s41467-021-22035-0

Taylor, J. R., Wall, V. J., & Pownceby, M. I. (1992). The calibration and application of accurate redox sensors. *American Mineralogist*, *77*(3–4), 284–295.

Tenner, T. J., Hirschmann, M. M., Withers, A. C., & Hervig, R. L. (2009). Hydrogen partitioning between nominally anhydrous upper mantle minerals and melt between 3 and 5 GPa and applications to hydrous peridotite partial melting. *Chemical Geology*, *262*(1–2), 42–56.

Tkacz, M., & Litwiniuk, A. (2002). Useful equations of state of hydrogen and deuterium. *Journal of Alloys and Compounds*, *330–332*, 89–92. https://doi.org/10.1016/S0925-8388(01)01488-8

Toby, B. H. (2001). EXPGUI, a graphical user interface for GSAS. *Journal of Applied Crystallography*, *34*(2), 210–213. https://doi.org/10.1107/S0021889801002242

Urakawa, S., Someya, K., Terasaki, H., Katsura, T., Yokoshi, S., Funakoshi, K. ichi, et al. (2004). Phase relationships and equations of state for FeS at high pressures temperatures and implications for the internal structure of Mars. *Physics of the Earth and Planetary Interiors*, *143*(1–2), 469–479. https://doi.org/10.1016/j.pepi.2003.12.015

Wood, B. J., & Halliday, A. N. (2005). Cooling of the Earth and core formation after the giant impact. *Nature*, *437*(7063), 1345–1348. https://doi.org/10.1038/nature04129

Zhang, Z., & Hirschmann, M. M. (2016). Experimental constraints on mantle sulfide melting up to 8 GPa. *American Mineralogist*, *101*(1), 181–192. https://doi.org/10.2138/am-2016-530

Appendix A

Appendix A.1

The single-crystal diamond trap (SCDT): a new method to determine the composition of high-P–T fluids

Supplementary Figures and Tables

Figure A.1.1 – Minerals recovered from the SCDT eclogite experiment

Table A.1.1 – LA-ICP-MS analyses of the MnO-doped Li_2B_4O

Table A.1.2 – LA-ICP-MS analyses of the epoxy

Table A.1.3 – Composition of minerals before and after melting

Table A.1.4 – LA-ICP-MS analyses of the volatility test with GSE-1G glass

Supplementary Figure A.1.1: Minerals recovered from the SCDT eclogite experiment

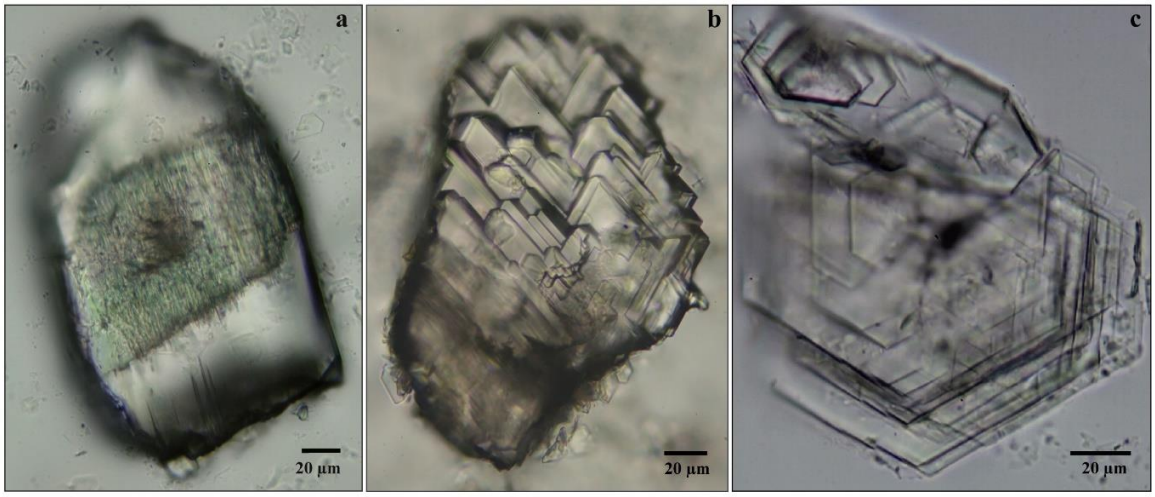

Supplementary Figure A.1.1: Mineral grains recovered from an experiment conducted with eclogitic starting material at 2.8 GPa and 700 °C for 15 hrs. a) Pyroxene crystal with an old core and new overgrowth. b) Garnet crystal with new overgrowth on the surface; c) Newly formed mica crystal.

Supplementary Table A.1.1: LA-ICP-MS analyses of major and trace element concentrations in the MnO-doped $Li_2B_4O_7$

Element/oxide	Measured value	Unit
Li_2O	22.9 ± 0.1	wt. %
B_2O_3	74.3 ± 0.1	wt. %
MnO	2.38 ± 0.04	wt. %
SiO_2	0.37 ± 0.03	wt. %
K_2O	< 0.039	wt. %
CaO	< 0.82	wt. %
FeO_{tot}	< 0.023	wt. %
Al	36.1 ± 3.4	µg/g
Ti	19.7 ± 7.3	µg/g
Na	8.8 ± 4.3	µg/g
Mg	6.9 ± 1.6	µg/g
Sr	0.5 ± 0.1	µg/g
Pb	0.5 ± 0.2	µg/g
Zr	0.5 ± 0.1	µg/g
Nb	0.3 ± 0.2	µg/g
Cs	< 0.2	µg/g
U	< 0.4	µg/g
La	< 0.4	µg/g
Th	< 0.5	µg/g
Rb	< 0.5	µg/g
Y	< 0.6	µg/g
W	< 0.8	µg/g
Ag	< 1.2	µg/g
Co	< 1.4	µg/g
Ba	< 1.5	µg/g
Mo	< 2.2	µg/g
As	< 2.3	µg/g
Cd	< 2.4	µg/g
Cu	< 2.6	µg/g
Sn	< 6.1	µg/g
Cr	< 31.7	µg/g
Se	< 89.5	µg/g
P	< 205	µg/g

Supplementary Table A.1.2: LA-ICP-MS analyses of the epoxy

Element/oxide	Epoxy	Unit
CaO	< 0.14	wt. %
SiO_2	< 0.10	wt. %
Al	3.4 ± 0.6	µg/g
Na	2.1 ± 1.1	µg/g
Fe	< 35.83	µg/g
K	< 28.44	µg/g
Ti	< 2.85	µg/g
Mg	< 0.71	µg/g
Pb	< 0.03	µg/g
La	< 0.04	µg/g
U	< 0.04	µg/g
Th	< 0.05	µg/g
Sr	< 0.06	µg/g
Nb	< 0.06	µg/g
Ag	< 0.07	µg/g
Tl	< 0.08	µg/g
Cs	< 0.08	µg/g
Y	< 0.08	µg/g
Zr	< 0.08	µg/g
Rb	< 0.10	µg/g
Co	< 0.12	µg/g
Cu	< 0.17	µg/g
W	< 0.21	µg/g
Mo	< 0.22	µg/g
Ba	< 0.33	µg/g
B	< 0.42	µg/g
As	< 0.69	µg/g
Cd	< 0.92	µg/g
Sn	< 0.93	µg/g
Mn	< 1.33	µg/g
Li	< 2.59	µg/g
Se	< 6.48	µg/g
P	< 15.19	µg/g

Supplementary Table A.1.3: Composition of minerals before and after melting them in the presence of lithium tetraborate

Oxide (wt%)	Garnet pellet	Garnet SCDT	Epidote pellet	Epidote SCDT-1	Epidote SCDT-2	Tourmaline pellet	Tourmaline SCDT	Albite crystal	Albite SCDT
Na_2O	0.0±0.0	0.7±0.2	3.2±0.0	3.1±0.5	3.0±0.3	2.3±0.0	2.4±0.1	11.5±0.1	11.6±1.0
MgO	2.6±0.0	2.8±0.3	1.8±0.2	1.6±0.5	1.8±0.4	2.3±0.0	2.8±0.0	<0.0	<0.0
Al_2O_3	18.4±0.1	19.3±1.6	12.8±0.4	12.9±1.6	12.3±0.7	31.9±0.1	38.6±1.4	19.4±0.3	19.1±0.7
SiO_2	42.7±0.1	42.7	63.6±0.1	63.6	63.6	40.0±0.0	40.0	69.1±0.2	69.1
K_2O	0.0±0.0	1.4±0.2	2.7±0.1	3.2±0.6	4.6±0.9	0.1±0.0	0.8±0.1	0.2±0.0	4.0±1.2
CaO	0.7±0.0	1.1±1.6	9.8±0.1	9.6±1.7	11.1±0.6	0.2±0.0	1.2±0.4	<0.4	<6.1
TiO_2	0.2±0.0	0.2±0.1	0.8±0.0	0.8±0.3	0.8±0.3	0.2±0.0	0.3±0.0	<0.0	<0.0
FeO_{tot}	34.7±0.1	33.4±3.2	5.2±0.2	4.6±0.9	5.2±0.5	11.4±0.0	12.3±0.1	<0.0	0.3±0.2

All these tests were performed by filling small amounts of mineral powders into laser-drilled holes within diamonds, subsequently melting them in the presence of MnO-doped $Li_2B_4O_7$, filling the remaining space of the holes with epoxy, and ultimately analyzing the entire holes with LA-ICP-MS. The reference values were obtained by LA-ICP-MS analysis of densely pressed powder pellets, except for the albite, where larger piece of the same starting material was used.

Supplementary Table A.1.4: LA-ICP-MS analyses of major and trace elements of the volatility test with GSE-1G glass

Element/oxide	Unit	Reference value	Measured	Deviation (%)
SiO_2	wt. %	53.7	53.7 ± 0.0	int. std.
MgO	wt. %	3.5	3.5 ± 0.1	-1
Al_2O_3	wt. %	13.0	12.8 ± 0.5	-2
CaO	wt. %	7.4	7.7 ± 0.8	+4
TiO_2	wt. %	0.1	0.1 ± 0.0	-4
FeO_{tot}	wt. %	12.7	13.9 ± 0.9	+10
Na_2O	wt. %	3.9	5.7 ± 0.6	+47
K_2O	wt. %	2.6	6.0 ± 0.6	+130
Pb	µg/g	378	396 ± 100	+5
As	µg/g	260	264 ± 16	+1
Ba	µg/g	427	417 ± 44	-2
Sr	µg/g	447	428 ± 35	-4
Co	µg/g	380	357 ± 39	-6
Sn	µg/g	280	254 ± 18	-9
Zr	µg/g	410	359 ± 35	-12
Nb	µg/g	420	357 ± 22	-15
Rb	µg/g	356	301± 60	-15
La	µg/g	392	328 ± 22	-16
Y	µg/g	410	340 ± 32	-17
Mo	µg/g	390	316 ± 39	-19
U	µg/g	420	321 ± 16	-24
Th	µg/g	380	291 ± 22	-24
W	µg/g	430	324 ± 24	-25
Cs	µg/g	310	200 ± 48	-35
Cu	µg/g	380	114 ± 74	-70
Ag	µg/g	200	<26	>-113
Cd	µg/g	160	<76	>-147

Volatility test for SCDT method, performed by filling GSE-1G powder and MnO-doped $Li_2B_4O_7$ powder at a ~2:1 weight ratio into laser-drilled holes within the diamond, subsequently melting the mixture at 1000 °C for 10 minutes, and then filling the remaining space with epoxy resin before the LA-ICP-MS analysis.

Appendix A.2

An experimental investigation of factors controlling the oxygen content of sulphide melts in the Earth's mantle

Supplementary Figures and Tables

Figure A.2.1 – Cross-section view of high-pressure multi-anvil cell assembly

Figure A.2.2 – (a) TEM high angle annular dark field (HAADF) image (b) EDX element map

Figure A.2.3 – Fe-Mg exchange between coexisting olivine and orthopyroxenes

Table A.2.1 – Compositions of starting silicate mixtures used in the experiments

Table A.2.2 – Summary of EPMA standards and secondary standards used for the analyses

Table A.2.3 – Summary of silicate crystals and melt composition analysis by EPMA *

Table A.2.4 – Summary of sulphide analysis by EPMA *

* Available as electronic materials at: https://doi.org/10.6084/m9.figshare.21253536.v1

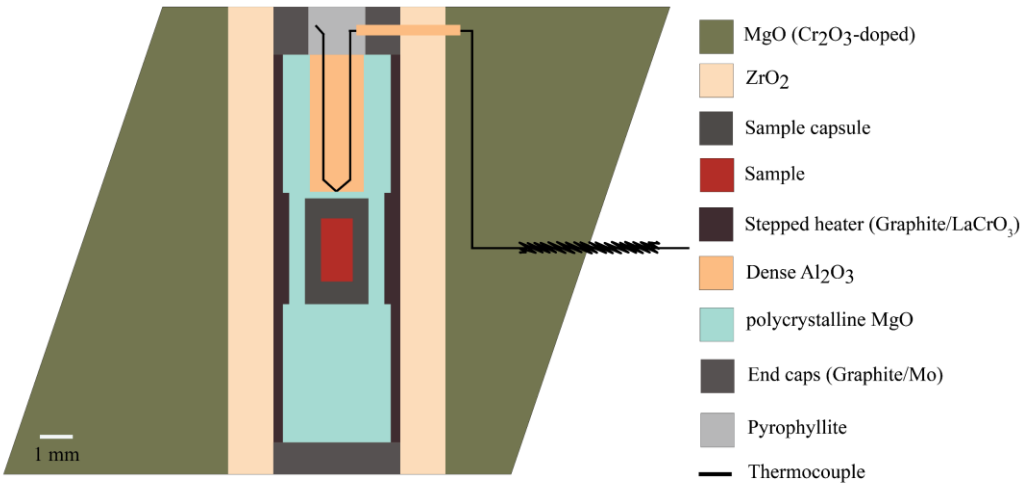

Supplementary Figure A.2.1: Cross-section through the octahedron cell assembly with an edge length of 18 mm, used for high-P-T multi-anvil experiments. The truncation edge length of WC cubes used were 11 mm.

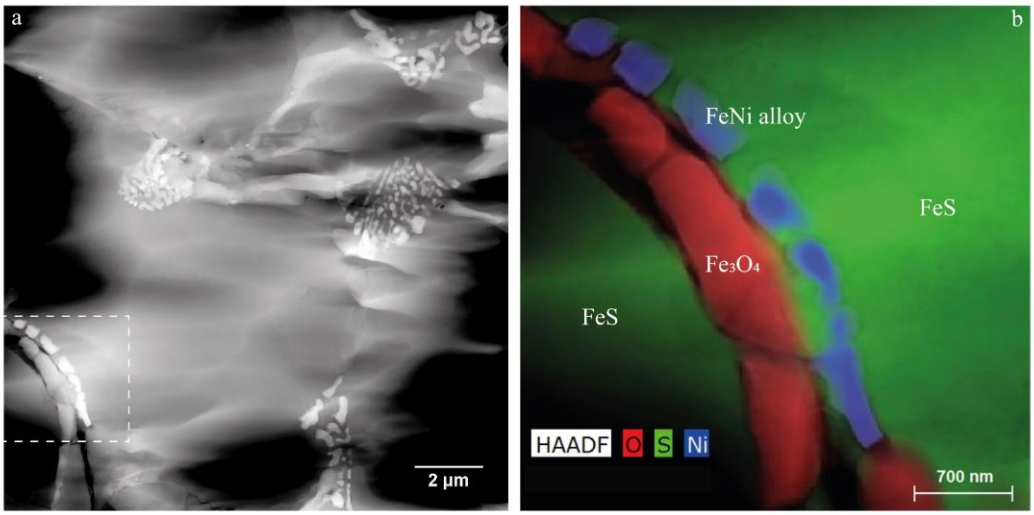

Supplementary Figure A.2.2: (a) High angle annular dark field (HAADF) scanning TEM image of the sulphide assemblage showing the atomic number (Z) contrast of different phases (sample V1045; 1400 °C). (b) EDX element map of area (dashed square in the image) showing the presence of different compositions

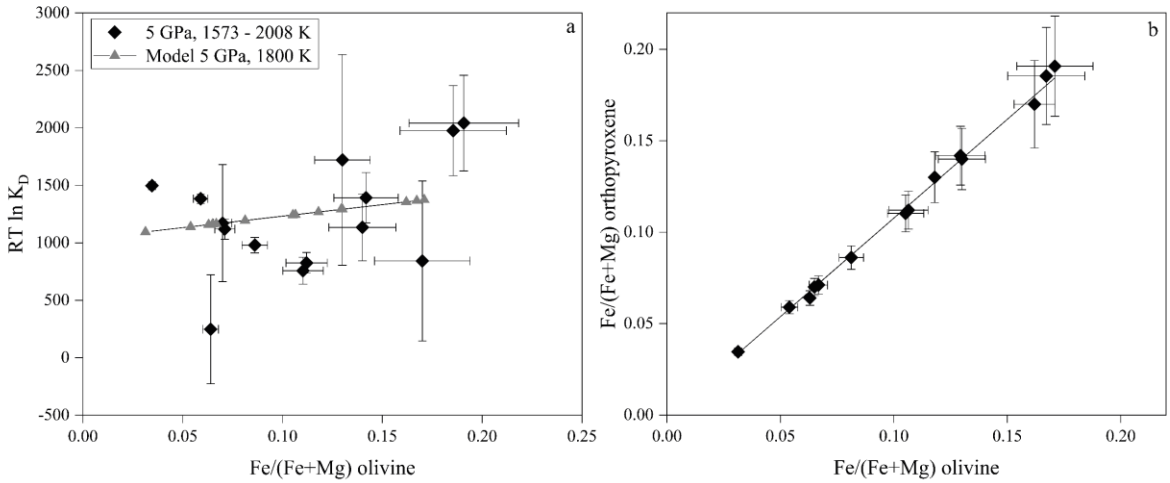

Supplementary Figure A.2.3: Fe-Mg exchange between coexisting olivine and orthopyroxenes. (a) The exchange coefficient (K_D) expressed as RT ln K_D as a function of Fe content (molar Fe/(Fe+Mg)) of olivine. Calculated fit through the experimental data is shown as the black line at 5 GPa, 1800 K. The scatter is partly due to the variation of the temperature. (b) Fe content (Fe/(Fe+Mg)) in coexisting orthopyroxene and olivine crystals. The black line through the data is calculated using free energy of endmembers and is not a linear fit to the data points. Uncertainties are 1σ standard deviation.

Supplementary Table A.2.1: Compositions of starting silicate mixtures used in the experiments.

wt. % oxide	A	B	C	D	E	F
SiO_2	44.05	43.20	41.29	39.47	48.70	40.61
TiO_2	0.11	0.11	0.10	0.10	-	
Al_2O_3	3.45	3.38	3.23	3.09	-	
Cr_2O_3	0.31	0.31	0.29	0.28	-	
FeO	8.06	9.83	13.81	17.61	3.97	25.72
MnO	0.12	0.12	0.11	0.11	-	
MgO	38.82	38.07	36.39	34.79	46.03	33.67
CaO	3.02	2.96	2.83	2.70	1.32	
Na_2O	0.29	0.29	0.28	0.26	-	
K_2O	0.02	0.02	0.02	0.02	-	
V_2O_5	1.76	1.72	1.65	1.58	-	
Total	100.00	100.00	100.00	100.00	100.00	100.00

A, B, C, D – Modified KLB 1 composition after Davis et al. (2009). The total FeO ranges from 8.06 – 17.61 wt. %.

E – simplified olivine + clino-enstatite mixture

F – Fe rich olivine $(Mg_{0.7}Fe_{0.3})_2SiO_4$ + 5 % SiO_2 starting mixture

Supplementary Table A.2.2: EPMA standards and secondary standards used for the analyses of experimental silicate and sulphide run products

Silicates analysis (oxides)	Standard	Crystal	X-ray line	Counting times (S)	
				peak	background
SiO_2	Olivine/Andradite	TAP	Kα	20	10
TiO_2	$MnTiO_3$	LIF	Kα	60	30
Al_2O_3	Spinel	TAP	Kα	20	10
Cr_2O_3	Cr_2O_3	LIFH	Kα	60	30
FeO	Olivine	LIF/LIFH	Kα	20	10
MnO	$MnTiO_3$	LIF	Kα	60	30
MgO	Enstatite/Olivine	TAP	Kα	20	10
CaO	Andradite	PETJ	Kα	20	10
Na_2O	Albite	TAP	Kα	10	5
K_2O	Orthoclase	PETJ	Kα	10	5
V_2O_5	V metal	LIFH	Kα	60	30
Sulphide/alloy analysis (elements)					
Fe	FeS_2/Fe metal	LIF/LIFH	Kα	20	10
S	FeS_2	PETJ	Kα	20	10
O	Fe_2O_3	LDE1	Kα	60	30
Ir	Ir metal	LIF/LIFH	Lα	20	10
Ni	Ni metal	LIFH	Kα	20	10
V	V metal	LIFH	Kα	20	10
Cu	Cu metal	LIFH	Kα	20	10
Mo	Mo metal	LIFH	Kα	20	10
Cr	Cr_2O_3	LIFH	Kα	60	30
Si	FeSi alloy	TAP	Kα	60	30
Secondary standards measured for background oxygen levels					
Fe metal					
FeSi alloy					
FeS_2					
Pyrrhotite					

All analyses were performed using JEOL JXA 8200 electron probe micro analyser in Bayerisches Geoinstitut, Bayreuth, Germany. Matrix corrections method for silicates is "φρ-z" and for sulphide/alloy is "ZAF" method.

Appendix A.3

Deuterium content and site occupancy in iron sulphide at high pressure and temperature using *in situ* neutron diffraction experiments

Supplementary Text, Figures and tables

Text A.3.1 – Error propagation of experimental pressure

Figure A.3.1 – High pressure cell assembly

Figure A.3.2 – Power vs. temperature calibration curves

Figure A.3.3 – positive nuclear densities observed in difference Fourier map of FeS V

Figure A.3.4 – Results of refinned diffraction patterns showing dry (a) and final deuterated (b) models

Figure A.3.5 – Overview of the unit-cell volume expansion of FeS V of each experiment

Table A.3.1 – Unit-cell parameters upon room temperature decompression of quenched FeS V phase

Table A.3.2 – Unit-cell parameters of deuterated (A526) and blank (A595) experiments

Table A.3.3 – Unit-cell parameters of identified high *P*, *T* polymorphs of FeS

Text A.3.1: Calculating the uncertainties of experimental pressure

The uncertainties in pressure were estimated using the following error propagation equation, combining both unit-cell volume and temperature errors (±50 °C) on the NaCl-B1 equation of state reported by Dorogokupets and Dewaele (2007).

$$\text{Uncertainty of } P = \sqrt{\left\{\frac{\sigma_V}{V} \times \frac{(P^V_{\max} + P^V_{\min})}{2}\right\}^2 + \left\{\frac{\sigma_T}{T} \times \frac{(P^T_{\max} + P^T_{\min})}{2}\right\}^2}$$

where σ_V is the error of unit-cell volume, $P^V_{\max}$ and $P^V_{\min}$ are pressures calculated at $V + \sigma_V$ and $V - \sigma_V$ respectively, σ_T is the error on temperature (±50 °C), $P^T_{\max}$ and $P^T_{\min}$ are pressures calculated at $T + \sigma_T$ and $T - \sigma_T$ respectively.

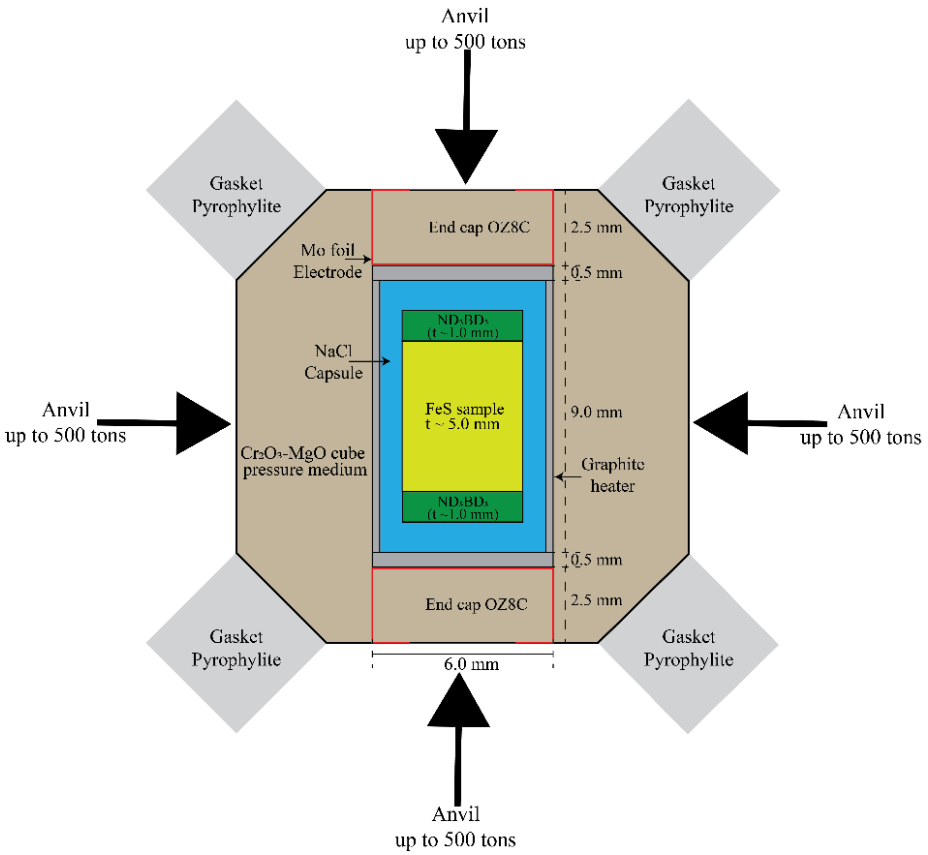

Figure A.3.1: A cross-section through the high pressure cell assembly of TEL 10 cell (cube edge length is 15.0 mm) used for experiments at $P \leq 7$ GPa. The TEL 7 cell used for the experiments at $P > 7$ GPa has the same design with a cube edge length of 10.5 mm. The deuterium source, ND_3BD_3 pellets, are placed on the top and bottom of the troilite sample pellet in a NaCl capsule.

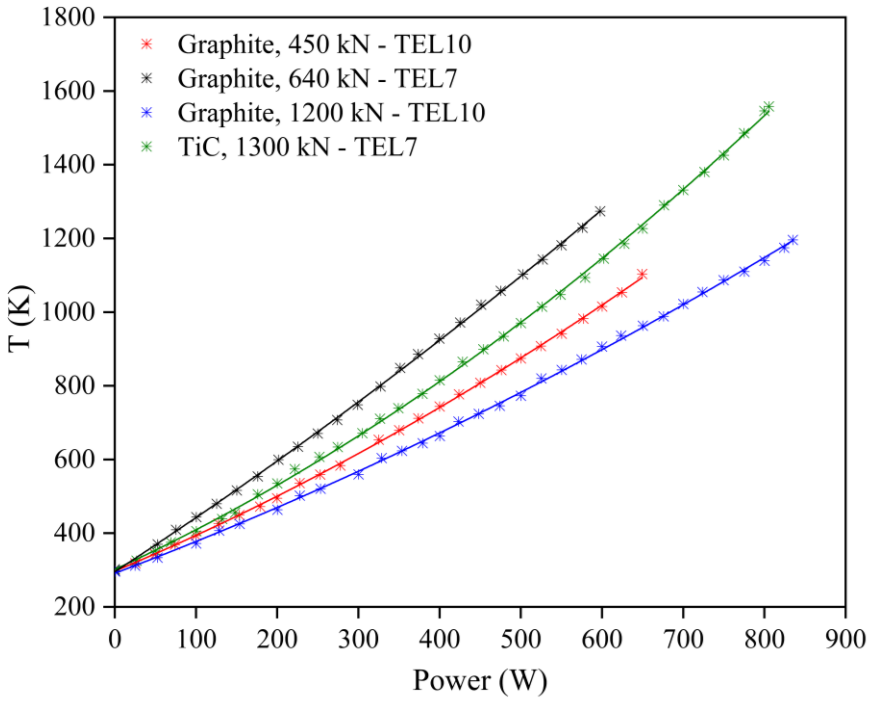

Figure A.3.2: Measured temperatures employing Pt-Pt 13% Rh thermocouples as a function of electrical power (W) in four different calibration experiments. These power-temperature calibrations were later used for determining the required electrical power to reach target temperatures during the *in situ* experiments.

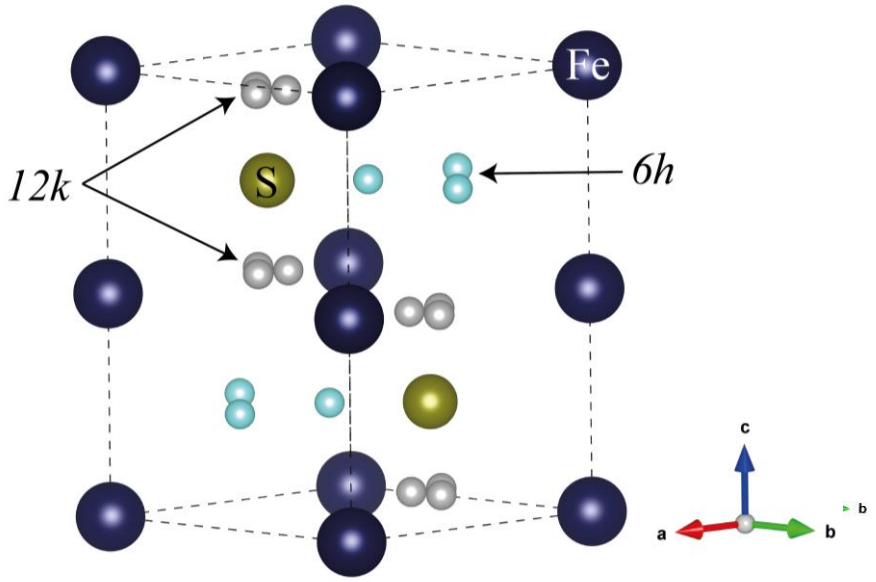

Figure A.3.3: The structure model of the FeS V ($P6_3/mmc$, Z=2) at 6.9 GPa, 960 K showing the *6h* (light blue) and *12k* (light grey) Wyckoff positions, where positive nuclear densities were observed in the difference Fourier map (DELF).

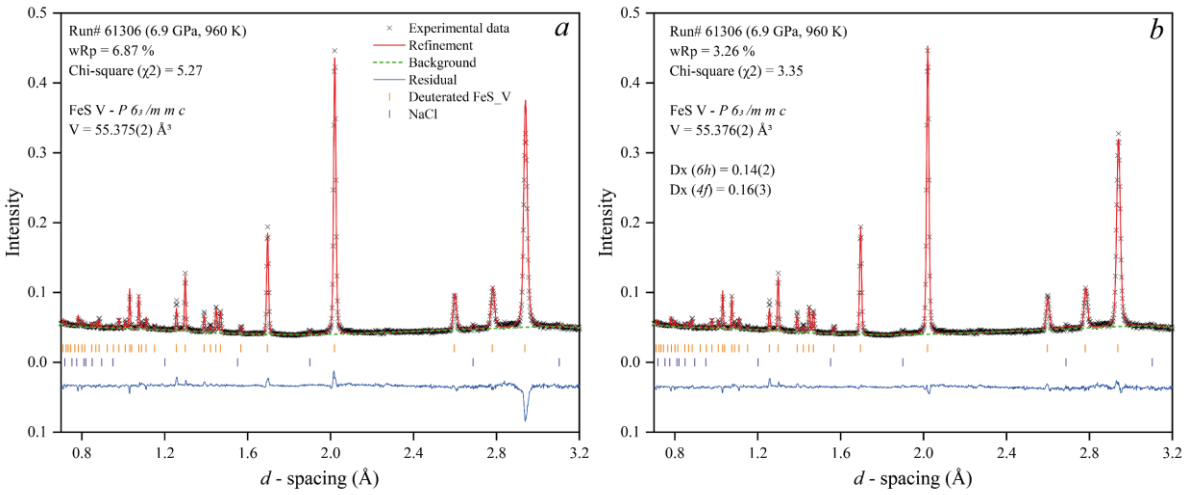

Figure A.3.4: Neutron diffraction - Rietveld structure refinement of NiAs-type FeSV structure (hexagonal–P$6_3/mmc$, Z=2) of run number A526 (data file #61306) at 6.9 GPa, 960 K. Two different models represent; **a** refinement with no D in the structure–dry model (residuals are observed), **b** final structural model implies two interstitial sites - *6h* and *4f (3m)*, are partially occupied by deuterium. The weighted R factor (*wRp*) of the final model in panel "b" is 3.26 %, which is an 52.5 % improvement compared to the dry model in panel "a".

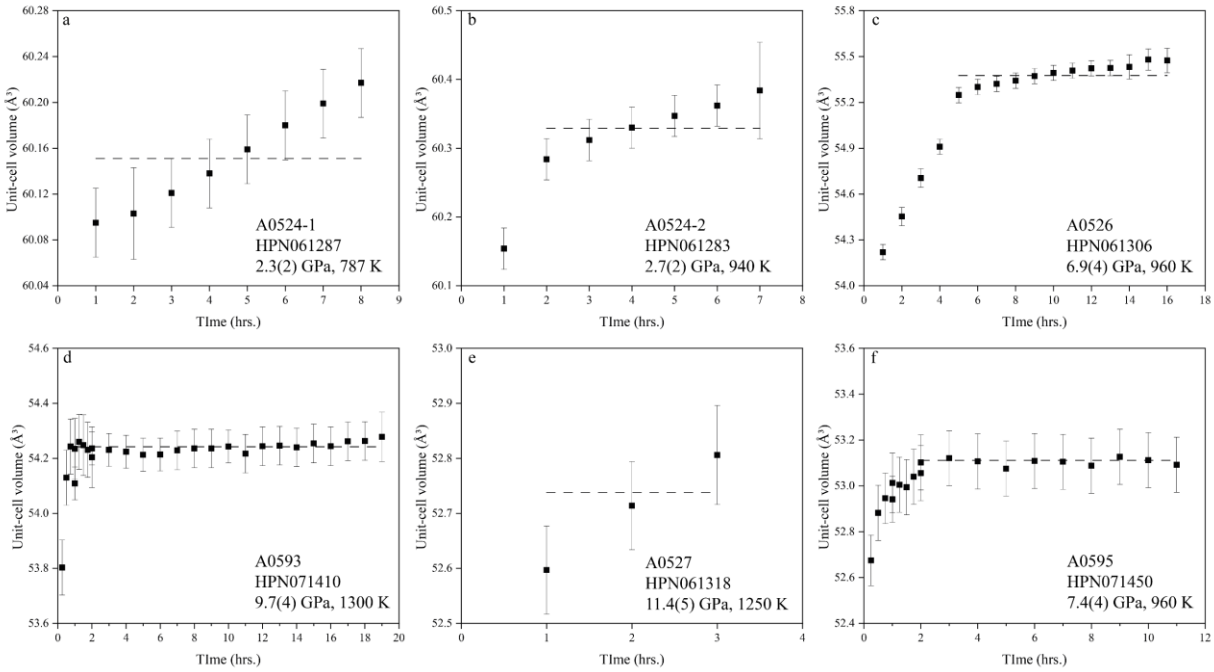

Figure A.3.5: The unit-cell volume expansion of FeS V over the run duration of each experiment. The dashed lines represent the unit-cell volumes obtained (see table 2) by fitting the diffraction patterns excluding the first 1-5 hrs. The experiment A527 (panel-e) was terminated before the equilibration (only ~3 hrs.). Panels a and b represent the same experiment (A524) where two diffraction data collections were done at 940 K and 787 K. Panel-f shows the blank experiment. Note that all experiments (except the blank run without deuterium source) show a slight continuous increase of unit-cell volume until the end of data collection. This is more prominent in panel-a (with a short-range y-axis) because the data collection (T = 787 K) was done after the first stage of unit-cell volume increase is completed at a higher temperature (940 K in panel-b). Uncertainty of temperatures can be up to ~50 °C.

Table A.3.1: Unit-cell parameters of quenched FeS V phase upon room temperature decompression (data plotted in the Figure 6.2) – experiment A527

Data#	P (GPa)	V_{NaCl} (Å^3)	Unit-cell parameters of FeS V			V/V$_0$
			a (Å)	*c* (Å)	V (Å^3)	V$_0$ = 60.081(6) Å^3
61332	0.3(3)	177.52(4)	3.4527(2)	5.8229(7)	60.117(8)	1.00
61331	0.7(4)	174.52(5)	3.4469(3)	5.8073(8)	59.755(9)	0.99
61330	1.7(3)	168.86(5)	3.4291(3)	5.7734(9)	58.790(9)	0.98
61329	3.0(3)	162.83(4)	3.3969(5)	5.7114(14)	57.075(14)	0.95
61328	4.3(3)	157.33(6)	3.3648(5)	5.6411(13)	55.312(13)	0.92
61327	6.6(3)	150.24(5)	3.3187(5)	5.4453(14)	51.938(14)	0.86
61326	7.6(2)	147.47(4)	3.2970(4)	5.3596(12)	50.454(11)	0.84
61325	8.2(2)	145.88(5)	3.2881(4)	5.3420(13)	50.016(12)	0.83
61324	8.6(2)	144.95(3)	3.2816(3)	5.3327(9)	49.734(8)	0.83
61323	8.4(4)	145.39(7)	3.2822(7)	5.3393(19)	49.814(18)	0.83
61322	8.3(3)	145.79(4)	3.2831(5)	5.3494(15)	49.934(13)	0.83
61321	8.0(4)	146.45(5)	3.2883(5)	5.3444(15)	50.045(15)	0.83
61320	7.8(4)	146.91(6)	3.2926(5)	5.3659(14)	50.378(12)	0.84

Table A.3.2: Unit-cell parameters of one-hour data slices in deuterated experiment – A526 (6.9(4) GPa, 960 K) and blank experiment – A595 (7.3(4) GPa, 960 K). these data correspond with the Figure 6.5.

Time (hrs.)	Unit cell parameters of FeS V					
	Deuterated experiment (Run# A526)			Blank experiment (Run# A595)		
	a (Å)	*c* (Å)	V (Å^3)	*a* (Å)	*c* (Å)	V (Å^3)
1	3.3703(2)	5.5121(5)	54.223(5)	3.3463(4)	5.4591(11)	52.941(10)
2	3.3745(2)	5.5208(4)	54.445(4)	3.3496(4)	5.4652(13)	53.102(12)
3	3.3791(1)	5.5316(3)	54.699(3)	3.3493(4)	5.4680(13)	53.121(12)
4	3.3824(1)	5.5415(4)	54.905(4)	3.3494(4)	5.4661(13)	53.107(12)
5	3.3888(1)	5.5548(3)	55.243(3)	3.3477(4)	5.4684(13)	53.075(12)
6	3.3897(1)	5.5569(4)	55.294(3)	3.3490(4)	5.4676(13)	53.109(12)
7	3.3901(1)	5.5577(4)	55.316(3)	3.3489(4)	5.4676(13)	53.105(12)
8	3.3906(1)	5.5581(4)	55.337(3)	3.3492(4)	5.4648(13)	53.088(12)
9	3.3912(1)	5.5589(3)	55.365(3)	3.3492(4)	5.4689(13)	53.127(12)
10	3.3916(1)	5.5602(3)	55.389(3)	3.3490(4)	5.4682(13)	53.112(12)
11	3.3920(1)	5.5605(3)	55.405(3)	3.3484(4)	5.4679(13)	53.092(12)
12	3.3924(1)	5.5605(3)	55.418(3)			
13	3.3924(1)	5.5607(3)	55.422(3)			
14	3.3925(3)	5.5607(9)	55.423(8)			
15	3.3932(2)	5.5630(5)	55.471(5)			
16	3.3935(3)	5.5616(7)	55.467(7)			

Table A.3.3. Unit-cell parameters of identified high-*P*–*T* polymorphs of FeS. These data correspond to the points plotted in the FeS phase diagram (Figure 6.1)

Run#	Data#	P (GPa)	T (K)	V_{NaCl} (Å^3)	Phase	Unit-cell parameters				
						a (Å)	*b* (Å)	*c* (Å)	V (Å^3)	β
A0524	61278	0.0(-)	298	179.65(4)	FeS I	5.9684(3)	5.9684(3)	11.7577(14)	362.72(4)	
A0526	61313	0.2(3)	298	177.83(6)	FeS I	5.9679(8)	5.9679(8)	11.749(2)	362.39(7)	
A0524	61289	1.7(3)	550	172.72(5)	FeS V	3.4676(1)	3.4676(1)	5.7376(3)	59.749(3)	
A0526	61312	1.8(3)	298	168.05(4)	FeS I	5.9246(5)	5.9246(5)	11.3858(16)	346.11(5)	
A0526	61311	2.8(2)	298	163.47(4)	FeS IV	6.7801(5)	6.7801(5)	5.7388(13)	228.47(5)	
A0524	61278	3.0(3)	298	162.72(5)	FeS IV	6.7531(7)	6.7531(7)	5.7187(17)	225.86(7)	
A0524	61280	3.1(4)	600	165.98(7)	FeS V	3.4182(8)	3.4182(8)	5.545(2)	56.107(19)	
A0524	61281	3.2(4)	787	167.97(6)	FeS V	3.4478(4)	3.4478(4)	5.6260(11)	57.919(11)	
A0526	61310	3.8(2)	298	159.32(3)	FeS IV	6.7354(5)	6.7354(5)	5.7273(9)	225.01(4)	
A0526	61309	4.8(2)	298	155.60(3)	FeS IV	6.6954(5)	6.6954(5)	5.7108(10)	221.71(4)	
A0526	61308	5.5(2)	298	153.38(3)	FeS IV	6.6724(4)	6.6724(4)	5.7061(10)	220.01(4)	
A0526	61307	5.8(7)	447	153.70(4)	FeS IV	6.6902(6)	6.6902(6)	5.6939(15)	220.71(6)	
A0595	71449	7.4(2)	298	148.11(4)	FeS III	8.0332(16)	5.5402(12)	6.2530(10)	277.99(8)	92.651(18)
A0593	71409	9.3(2)	298	143.47(5)	FeS III	8.0064(13)	5.5021(13)	6.1742(12)	271.60(6)	93.052(12)

(Eidesstattliche) Versicherungen und Erklärungen

(§ 9 Satz 2 Nr. 3 PromO BayNAT)

Hiermit versichere ich eidesstattlich, dass ich die Arbeit selbstständig verfasst und keine anderen als die von mir angegebenen Quellen und Hilfsmittel benutzt habe (vgl. Art. 64 Abs. 1 Satz 6 BayHSchG).

(§ 9 Satz 2 Nr. 3 PromO BayNAT)

Hiermit erkläre ich, dass ich die Dissertation nicht bereits zur Erlangung eines akademischen Grades eingereicht habe und dass ich nicht bereits diese oder eine gleichartige Doktorprüfung endgültig nicht bestanden habe.

(§ 9 Satz 2 Nr. 4 PromO BayNAT)

Hiermit erkläre ich, dass ich Hilfe von gewerblichen Promotionsberatern bzw. -vermittlern oder ähnlichen Dienstleistern weder bisher in Anspruch genommen habe noch künftig in Anspruch nehmen werde.

(§ 9 Satz 2 Nr. 7 PromO BayNAT)

Hiermit erkläre ich mein Einverständnis, dass die elektronische Fassung meiner Dissertation unter Wahrung meiner Urheberrechte und des Datenschutzes einer gesonderten Überprüfung unterzogen werden kann.

(§ 9 Satz 2 Nr. 8 PromO BayNAT)

Hiermit erkläre ich mein Einverständnis, dass bei Verdacht wissenschaftlichen Fehlverhaltens Ermittlungen durch universitätsinterne Organe der wissenschaftlichen Selbstkontrolle stattfinden können.

……..

Ort, Datum, Unterschrift